

Multi-laser powder bed fusion using 808nm sources



Mohammed T. Alsaddah

Department of Mechanical
Engineering

The University of Sheffield

This dissertation is submitted for the degree of

Doctor of Philosophy

August 2023

Abstract

Laser Powder Bed Fusion (LPBF) is a disruptive manufacturing technique widely used in aerospace, automotive, and energy industries, enabling the creation of intricate structures from various metallic alloys with minimal waste. However, LPBF systems face limitations in processing efficiency, scalability, and thermal control.

The main constraint is single-fibre laser productivity, hindering large-scale adoption due to galvo-scanning method limitations. Multi-laser integration shows potential but presents challenges in design and control complexity. Innovations are sought to effectively incorporate multiple lasers while ensuring efficiency and scalability.

LPBF systems use high-power fibre lasers at 1064 nm wavelength, but their low material-specific absorption efficiency (<60%) demands high laser power, resulting in challenges in processing high-performance alloys with limited weldability and high crack susceptibility. Enhanced thermal management with in-situ control and slower cooling rates are necessary to mitigate these issues, although they increase production costs and time.

On the other hand, low-power diode lasers are emerging as a promising alternative. They are compact, energy-efficient, and durable and emit shorter wavelengths ranging from 450 nm to 3300 nm, making them suitable for various industrial processes. Research efforts are currently focused on developing Diode Area Melting (DAM) systems where multiple diode lasers selectively melt powder beds, offering a high-resolution and energy-efficient solution. However, challenges still exist in beam quality, power output, and system design.

Integrating multi-fibre coupled diode lasers as a 2D array in LPBF can offer significant advantages, including improved productivity, enhanced material absorption, and reduced energy consumption. The ability to individually control each laser allows for customized intensity distributions, enabling the fabrication of complex parts. Further research is needed to optimize system design, increase power output, and explore scalability to larger write areas suitable for production environments. The use of fibre-coupled diode laser and optical systems can potentially create efficient and scalable LPBF systems that can enhance the microstructure of final parts. This, in turn, can significantly improve the mechanical properties at an industrial level without incurring excessive costs or time investment.

This research investigates the influence of laser wavelength on the efficiency and scalability of the Powder Bed Fusion (PBF) process using a 2D array head

comprising a scalable, low-power (4.5 W) 808 nm fibre-coupled diode laser. The individual control of multiple short wavelengths (808 nm) diode lasers enhances absorption and processing efficiency, enabling the fabrication of intricate parts with better thermal control. The research delves into how beam profiles, laser power, scanning speed, and wavelength affect microstructure, mechanical properties, and melt pool morphology when manufacturing three-dimensional Ti6Al4V parts.

The study reveals that low-power diode lasers generate energy densities comparable to traditional selective laser melting due to shorter laser wavelengths, increasing metallic powder absorption, and enhancing processing efficiency. Moreover, the investigation highlights the impact of laser wavelength on keyhole formation, melt pool characteristics, and microstructural evolution. The 2D array laser head produces parts with mechanical properties akin to those manufactured using selective laser melting systems, indicating the potential of this technique to optimize PBF manufacturing efficiency. These findings are valuable to researchers and industry professionals seeking to enhance the quality, scalability, and cost-effectiveness of the PBF process.

Acknowledgements

In the name of God, the most gracious most merciful

I would like to extend my gratitude to my supervisor **Dr Kamran Mumtaz**, who first introduced me to the world of Additive Manufacturing, and his inputs regarding the areas in which the literature review should be done. I thank him for his guidance and encouragement throughout my research project. Also, I would express my gratitude to my second supervisor **Dr Kristian Groom** for his support and insight into the project and his inputs regarding the basic understanding of the principles, applications, and limitation of the lasers.

Thanks to **Dr. Ashfaq Khan** for his advice on metallurgical and assistance with the optical analyses. **Abdullah Alharbi** for his encouragement and guidance.

Thanks to all members of IDC who assisted me throughout my research journey, especially **Clare Clarke** and **Adele Blinston**.

My final and biggest thanks go to my lovely family, especially my mother "**Malak**," my wife "**Wasam**", **Abdullah**, **Mayar**, **Maria**, and **Mira**.

NOMENCLATURE

AM	Additive Manufacturing
SLM	Selective laser melting
3D	Three Dimensions
DAM	Diode Area Melting
EBM	Electron Beam Melting
PBF	Powder Bed Fusion
DLD	Direct laser Deposition
SLS	Selective laser sintering
CAD	Computer Aided Design
DLD	Direct Laser Deposition
DiAM	Diode-based Additive Manufacturing
Nd: YAG	Neodymium-doped Yttrium Aluminium Garnet
Yb laser	Ytterbium Laser
NA	Numerical aperture
LENS	Laser Energy Net Shaping
CW	Continuous Wave
ST	Scanning Strategy
M^2	Beam Quality Factor
BPP	Beam Parameter Product (mm·mrad)
λ	Wavelength (nm)
θ	Total beam divergence (degrees, mrad)
w_0	Beam Waist (mm, μm)
f	Focal length (mm)
P	Laser Power (W)
A	Absorption (%)
R	Reflection (%)
r_B	Beam Radius (mm, μm)

L_t	Layer Thickness (μm)
S_v	Scanning velocity (mm/min)
H_d	Hatch Distance (μm)
LED	Linear Energy Density (J/mm)
SED	Surface Energy Density (J/mm ²)
VED	Volumetric Energy Density (J/mm ³)
NED	Normalised energy density (%)
k	Thermal Conductivity (W/m ⁻¹ K ⁻¹)
D	Thermal Diffusivity (m ² s ⁻¹)
γ_{LV}	surface tension (N/m)
T_m	Material Melting Temperature (K)
T_0	Initial Temperature (K)
C_p	Specific Heat Capacity (J kg ⁻¹ k ⁻¹)
ρ	Density (kg m ⁻³)
P^*	Normalised laser power (-)
h^*	Normalised Hatch Spacing (-)
E^*_0	Normalised required energy density (-)
E^*	Normalised Volumetric energy density (-)
v^*	Normalised scanning velocity (-)
l^*	Normalised Layer Thickness (-)
v	Beam velocity (m/s)
l	Layer thickness (m)
h	Hatch spacing (m)

Contents

Abstract.....	i
Acknowledgements.....	iii
NOMENCALATURE.....	iii
List of Figure	xi
List of tables	xxii
List of Publications	xxiv
1. Chapter 1: Introduction	1
1.1 Motivation	1
1.2 Novelty Statement.....	2
1.3 Research Aims and Objectives.....	4
1.4 Thesis Outline	6
2. Chapter 2: Literature Review.....	9
2.1 Additive Manufacturing: Overview	10
2.2 Selective Laser Melting (SLM)	12
2.3 Challenges associated with the SLM process.....	14
2.3.1 Part porosity and balling defects.....	15
2.3.2 Residual stresses and cracks (warping/buckling).....	20
2.3.3 Separation/delamination	23
2.3.4 Evaporation and Spattering.....	24
2.3.5 Absorption, thermal conductivity of powder	26

2.3.6	Environment during the SLM process	32
2.4	Material characteristics in the PBF process	34
2.4.1	The influence of particle size.....	34
2.4.2	Microstructure in SLM parts.....	35
2.4.3	Ti6AL4V Microstructure in PBF	37
2.5	Laser types and applications.....	41
2.5.1	CO2 laser	42
2.5.2	Solid-state laser (Nd: YAG).....	42
2.5.3	Yb-Doped Fibre Laser	43
2.5.4	Diode laser	44
2.5.4.1	Multi-Emitter Diode Lasers: Power Enhancement and Limitations	48
2.5.4.2	Different Approaches for Improving Beam Quality: Free Distance Optics vs Fiber Optics Delivery.....	49
2.5.4.3	Multimode print-head optical fibers as a potential solution	59
2.5.5	The State-of-the-Art use of Diode Lasers in traditional LPBF	63
2.6	Process Parameters Associated with Energy Input	65
2.6.1	Laser power	65
2.6.2	Scanning speed	66
2.6.3	Layer thickness.....	67
2.6.4	Hatch distance and scanning pattern.....	68
2.7	Productivity and Scalability.....	71

2.8	Energy Density Overview	74
2.8.1	Linear energy density	75
2.8.2	Surface energy density	77
2.8.3	Volumetric energy density (VED).....	78
2.8.4	Normalised energy density (NED)	82
2.9	Literature Review Conclusions	84
3.	Chapter 3: Experimental Methodology	87
3.1	Introduction.....	88
3.2	Brief description of the Diode area melting system.....	89
3.3	Brief description of the Diode Area Melting process.....	91
3.4	Diode Area Melting System Development	93
3.4.1	Movement stages	93
3.4.2	Powder handling unit.....	94
3.4.3	cooling system.....	98
3.4.3.1	Test the Stability of the cooling system.....	102
3.4.3.2	Effect of heat on the optical output.....	105
3.4.3.3	Effect of heat on Conversion Efficiency	106
3.4.4	Laser driver unit.....	107
3.5	Laser characterisation	110
3.5.1	Single laser	110
3.5.2	Multiple individually addressable laser sources (CTP)	113

3.6	Material	119
3.7	Characterisation.....	120
3.7.1	Archimedes Density Test.....	120
3.7.2	Optical 3D Microscope (Surface Roughness).....	120
3.7.3	Samples Preparation	120
3.7.4	Scanning Electron Microscopy (SEM) and Energy Dispersive X-ray Analysis (EDX) 121	
3.7.5	X-Ray Diffraction Analysis.....	121
3.7.6	Nanoindentation Test	121
4.	Chapter 4: The impact of wavelength on Absorbance	122
4.1	Introduction.....	123
4.2	Experimental procedure.....	124
4.3	Results and Discussions.....	125
4.3.1	Effect of the Wavelength on the Materials	125
4.3.2	Comparative Analysis of Laser Absorption in Copper and Ti6Al4V Powders with Different Particle Sizes	126
4.3.3	Comparative Analysis of Laser Absorption in Copper and Ti6Al4V Powders with Different Particle Sizes	128
4.4	Conclusions	132
5.	Chapter 5: Efficient Energy Absorption with 450-808 nm DL in Ti6Al4V	133
5.1	Introduction.....	134
5.2	Experimental procedure.....	134

5.2.1	Stage-1: Single-track laser processing and characterisation.....	134
5.2.2	Stage-2: Normalisation:.....	135
5.3	Results and discussions	138
5.3.1	Influence of wavelength on surface temperature	138
5.3.2	Influence of the wavelength on the morphology of single laser tracks	140
5.3.3	Melt pool top surface morphology.....	141
5.3.4	Morphology of cross-sectioned tracks.....	144
5.3.5	Multilayer Fabrication	147
5.3.5.1	Processing regions for 450-808nm powder bed fusion of Ti6Al4V.....	147
5.3.5.2	Part density	151
5.3.5.3	Microstructure (XRD).....	152
5.3.5.4	Nanoindentations (hardness & elastic modulus).....	155
5.4	Conclusions.....	156
6.	Chapter 6: Multi-beam 808nm Laser Melting of Ti6Al4V.....	158
6.1	Introduction.....	159
6.2	Experimental procedure.....	159
6.3	Results and discussion.....	160
6.3.1	Single line scanning.....	160
6.3.2	Single layer scanning.....	164
6.3.2.1	Effect of laser beam profiles	164
6.3.3	Effect of laser power and scanning speed	169

6.3.4	Normalized processing windows for Ti6Al4V (multilayer)	170
6.3.5	Density evaluation.....	172
6.3.6	Surface Roughness	174
6.3.7	Microstructure	176
6.3.8	XRD.....	181
6.3.9	Nanoindentation	182
6.4	Conclusions.....	185
7.	Chapter 7: Conclusions & Future Work	186
7.1	Conclusions:.....	186
7.1.1	system control development.....	189
7.1.2	Enhancing Efficiency and Material Processing with Shorter Wavelengths (450nm).....	190
7.1.3	New Multi-laser Integrated System for the 3D Printing Process	191
7.1.4	Modelling and process monitoring.....	193
7.2	Final recommendations	193
8.	References.....	195

List of Figure

Figure 1.1: visual flow diagram of the present research.	8
Figure 2.1: Cost comparison using AM over conventional technologies in term of number of parts and complexity of part [31].	11
Figure 2.2: Illustrating the sequences of operations in selective laser melting (SLM) [36].	13
Figure 2.3: Type of porosity, including (a) Entrapped gas pores and (b) Lack of fusion pores (Gas porosity) [39].	15
Figure 2.4: Optical image showing the lack of fusion defect within the layers' boundary, exhibiting unmelted particles [44].	17
Figure 2.5: The optical microscope reveals multiple single-track morphologies under varying processing parameters: (a) scanning speeds, (b) laser power, and (c) layer thickness (with layer thickness gradually increasing from left to right) [43].	17
Figure 2.6: Acceptance (a) contact angle between liquid and surface (b) ratio of the cylindrical melt pool before breakup [45].	18
Figure 2.7: Marangoni flow (A) Outer Convection Currents Caused by Negative Surface Tension Gradients, (B) Inner Currents Driven by Positive Surface Tension Gradients [48].	19
Figure 2.8: Defects in the SLM process caused by residual stress include (a) crack formation and (b) warpage [53].	20
Figure 2.9: Residual stress during (a) heating and (b) cooling [52].	22
Figure 2.10: shows the final SLM parts with and without support structures, illustrating the importance of support structures in reducing warping during the Selective Laser Melting (SLM) process [54].	22

Figure 2.11: Samples produced using the SLM process showing cracks, base plate separation and warpage [60].	23
Figure 2.12 Side view of samples produced using SLM process under various substrate temperatures: (a) 100°C, (b) 150°C, (c) 200°C, (d) 250°C [62].	24
Figure 2.13: Shows high-speed images during the scanning of single tracks at different scanning speeds: (a) 50 W at 0.1 m/s and (c) 100 W at 0.5 m/s, where the vaporized material emerging from the irradiation zone in the form of a vapour jet (spatter), which is influenced by the geometry of the melt pool [65].	25
Figure 2.14: illustrates the interaction of the laser with a powder particle, which can be either absorbed or reflected.	27
Figure 2.15: Absorptivity of different materials [73].	28
Figure 2.16: The absorption of a flat 316L varies according to the power of the laser at scanning speeds of 100, 500, and 1500 mm/s [72].	30
Figure 2.17: Absorptivity during SLM process at (a) low-power laser 100W/cm ² and (b) high-power 200W/cm ² [72].	31
Figure 2.18: The effect of oxygen content during the SLM process influences balling formation at three levels: (a) 0.1%, (b) 2%, and (c) 10% [43].	32
Figure 2.19: Demonstrates the general trends in SLM microstructures. While these grains are typically equiaxed in the build plane, they exhibit significant elongation along the build direction due to epitaxial development, leading to a pronounced anisotropic microstructure [82].	36
Figure 2.20: Two distinct crystal structures: a hexagonal close-packed (HCP) structure and a body-centred cubic (BCC) structure [87].	37
Figure 2.21: α and β stabilizers along with the associated phase diagrams for Ti6Al4V [87].	38

Figure 2.22: Shows the Influence of Cooling Rate on Phase Transformation in Ti6Al4V. (a) Phase diagram of Ti6Al4V [90]. (b) Phase transformation as a function of cooling rates [89].	39
Figure 2.23: Microstructures of samples produced using SLM (a-c) and EBM (d-f) [93].	39
Figure 2.24: XRD pattern for samples of (a) SLM and (b) EBM [94].	40
Figure 2.25: Schematics of different types of lasers with different gains (a) Gas (b) Solid State (c) fibre laser [19].	41
Figure 2.26: The foundation of the CO ₂ laser module consists of a back mirror, a gas power supply to excite the gas, and a front mirror [19].	42
Figure 2.27: Fundamental of Nd: YAG laser module [19].	43
Figure 2.28: Concept of Ytterbium fibre laser module [19].	43
Figure 2.29: Structure of diode laser [102].	44
Figure 2.30: Diagram showing diode laser characteristics and operational fundamentals [102].	44
Figure 2.31: Typical single bar of multiple emitters of high-power diode laser [104].	48
Figure 2.32 Multi-mode diode lasers stack [103].	49
Figure 2.33: laser profile(a) near-field, (b) mid-field, (c) far-field [103].	50
Figure 2.34: Different approaches for collection and focusing Diode lasers (a) free distance optics (microlenses array) and (b) fibre optics delivery [107].	50
Figure 2.35: Illustration of the beam characteristics from a single emitter in two directions: the fast axis ($\theta \perp$ FWHM), and the slow axis ($\theta \parallel$ FWHM), The fast axis is perpendicular to the active layer, while the slow axis runs parallel to the active layer [102].	51

Figure 2.36: (a) Microlens array (FAC) and (SAC) [24], (b) The dimensions of a typical FAC aspherical cylindrical micro-lens [104].	52
Figure 2.37 Lens setup for focusing the fast and slow beam modes [24].	54
Figure 2.38: Illustration of the optical system used by Zavala et al. to correct the 19 emitters of a high-power diode laser bar and the general beam path[24].	55
Figure 2.39 Typical construction of a fiber-coupled diode laser, which consists of diode bar lasers, FAC microlenses, a fiber bundle, and a fiber ferrule assembly [108].	56
Figure 2.40: Illustration of Laser Beam Propagation within an Optical Fiber [109].	56
Figure 2.41 Beam characterisation for different lasers: (a) at same beam waist (b) at same beam angle.	58
Figure 2.42: Illustrates different transverse electromagnetic modes (TEM) [111].	58
Figure 2.43: Illustration of 1D Array Configuration of Multi Fibre-Coupled Diode Lasers in a Laser Head [107].	59
Figure 2.44: Front view of multi-fibre-coupled diode lasers attached to a V-groove substrate [107].	60
Figure 2.45 Schematic of multiple edge-emitting lasers coupled into V-groove fibers Array, developed by Karp et al. [110].	61
Figure 2.46: Demonstrate the effect of increasing the laser power under constant scanning speed within the range of (400 mm/s to 2000 mm/s) on the morphology of forming single tracks at different laser powers: (a) 100 W, (b) 200 W, (c) 300 W, (d) 400 W, and (e) 500 W, in order to investigate the limitations of using VED (Volumetric Energy Density) [114].	66
Figure 2.47 Surface morphology at different hatch distances (a) 75 μm (b) 100 μm (c) 150 μm (d) 200 μm .	68

Figure 2.48: Different techniques of scanning strategies: (a) island (b) single line (g) spiral (in-out) (h) spiral (out-in).....	70
Figure 2.49: Shows the changes in the optimal processing window resulting in a consistent single track using two different laser powers: (a) 50 W and (b) 25 W [112].	76
Figure 2.50: Relative density under (a) same laser power with different scanning speeds (b) Same VED by varying (power/speed) [114].....	79
Figure 2.51: Single track morphology at the same VED (242 J/mm ³) under different processing parameters.	80
Figure 2.52 Normalised Energy Density for various EBM materials developed by Tomas et al. [146].....	83
Figure 3.1 Schematic of the main component of the diode area melting (DAM) used in this research project.....	90
Figure 3.2: Step-by-Step Breakdown of the Diode Area Melting Process.....	92
Figure 3.3: View of the Processing Area, Illustrating Integral Components within the Inert Chamber, including Laser Head, Build Area, Powder Wiper, Air Flow Gas, and X-Y Gantry.	94
Figure 3.4 Lack of fusion (adherent) and balling phenomena under different scanning speeds (A) 25 mm/min (B) 50 mm/min (C) 75 mm/min (D) 150 mm/min (E) deposited second layer.	96
Figure 3.5: The images demonstrate the enhancements achieved when employing a substrate with holes: (A) stage one, where the material is melted inside the holes, (B) stage two, involving the deposition of a second layer, (C) after multiple layers, a smooth melt is observable on the area covered by holes while balling occurs on the flat surface, (D) a top view of the final multi-layer samples, and (E) a side view where warping is apparent on the area not covered by holes.....	97

Figure 3.6: Substrate configuration employed in the current study.....	98
Figure 3.7 Schematic of the cooling system setup used for controlling the temperature of the diode laser shown (computer, TEC controller, TEC ,and fan heat seatsink).....	99
Figure 3.8: Final cooling system design to control up to 12 lasers.....	100
Figure 3.9: The Cooling System: (a) The exterior view of the cooling system shows the temperature control unit, (b) The internal assembly of all cooling components.	102
Figure 3.10: Setup Employed for Testing the Stability of the Laser Temperature and the Cooling System: (1) Laser Temperature Controller, (2) Laser Power Supply, (3) Beam Profile, (4) Laser Power Meter, (5) Laser Module, (6) Cooling Unit.....	103
Figure 3.11: The temperature measurement of six diode lasers operating at maximum power for 1 minute, demonstrating stable temperature at 18°C when integrated into the cooling system.....	104
Figure 3.12: Thermal Image of Single Diode Laser assessing temperature stability after 5 Hours of Maximum Power Operation.	104
Figure 3.13: Demonstrate the effect of temperature on the output laser power (Power-Current curve, P-I) at four temperature levels (15°C, 20°C, 25°C ,and 30°C), where the laser power decreases as the temperature increases.....	105
Figure 3.14: Shows the conversion efficiency of the laser (electrical to optical power), which is significantly influenced by the laser's operating temperature within the range of 15°C to 30°C.	106
Figure 3.15: The laser power supply used to control each laser module individually..	108
Figure 3.16: P-I-V chart for 4 different lasers shows the stability of the output power.	109
Figure 3.17: Schematic illustration of the optical system for the single diode laser [25].	110

Figure 3.18: The setup of the beam profiler to characterise the laser beam using different optical setups.....	111
Figure 3.19: Beam profiles and Gaussian fit of (a) 808 nm and (b) 450 nm.....	112
Figure 3.20: (a) Schematic of DAM (b) configuration of laser head beam profile (c) schematic of melt pool [151].....	114
Figure 3.21: The setup of the beam profiler used to characterise the 2D array laser head.	115
Figure 3.22: shows the measured beam profiles for ten activated laser fibers within the 2D laser head array (LP1), illustrating their shape and beam specifications [151].	116
Figure 3.23: Shows the measured beam profiles for ten activated laser fibers within the 1D laser head array configuration (beam spacing 76.2 μm), which propagate a single stripe beam called (LP2) [151].....	117
Figure 3.24: shows the measured beam profiles for ten activated laser fibers within the 1D laser head array configuration, with a single fiber spacing (one on/one off- beam spacing 152.5 μm), propagating individual single beam spots called (LP2) [151].	118
Figure 3.25: (a) Ti-6Al-4V powder morphology; (b) particle size distribution.....	119
Figure 4.1: Absorption and Reflection of laser beam from a Powder Bed.....	123
Figure 4.2 The optical absorption of Ti6Al4V, AlSi12 and Cu within the 400 to 1100 nm wavelength range.....	126
Figure 4.3: The optical absorption of Ti6Al4V and copper using different average particle sizes and distributions within the 400 to 1100 nm wavelength range.	127
Figure 4.4: Illustration of the laser beam interaction with powder (a) fine particles and (b) large particles.....	128
Figure 4.5: Illustration of the interaction between the laser and oxidised surface particle.	130

Figure 4.6: The optical absorption of (oxidised /new) Ti6Al4V, Cu within the 400 to 1100 nm wavelength range.....	131
Figure 5.1: Normalised energy density of Ti6Al4V from literature.	137
Figure 5.2: The maximum temperature measured during laser processing at various scanning speeds for 808 nm and 450 nm wavelengths.	138
Figure 5.3: Temperature measurement at a speed of 50 mm/min.	139
Figure 5.4: Top surface morphology under different scanning speeds for 808 nm and 450 nm wavelength laser processing.....	143
Figure 5.5: Effect of scanning speed on melt pool width for both lasers (808 nm, 450 nm).	144
Figure 5.6: Cross-section morphology of melt pool at different scanning speeds.....	146
Figure 5.7 Variation of melt pool (a) depth and (b) width with scan speed for 450 and 808nm lasers.	147
Figure 5.8: Normalised diagram showing the location of the experimental parameters and the visible region for given laser power.....	148
Figure 5.9: The effect of the scanning speed on the specimen's top surface.	149
Figure 5.10 The effect of hatch distance on the top surface of the specimens (a) Hatch distance of 200 μm increases the separation between the tracks. (b) 157 μm is the optimal value to provide a better joint. (c) 100 μm reduces the processing efficiency and excessive energy.....	150
Figure 5.11: Density of parts fabricated using (a) 808 nm and (b) 450 nm.	151
Figure 5.12: Top surface porosity of specimen fabricated using (a) 808 nm and (b) 450 nm.	152
Figure 5.13: XRD profile for 808 nm and 450 nm, showing the presence of β phase.	153

Figure 5.14: Ti6Al4V microstructure at the top surface of the samples shown β when processed using diode lasers (a)808 nm,and (b)450 nm.....	155
Figure 5.15: Ti6Al4V mechanical properties (a) Elastic modulus (b) Hardness.....	156
Figure 6.1: Illustration of the dual laser configurations employed for single track.....	160
Figure 6.2: (a) Beam profile of Channels 1&2 ($dp= 38.1 \mu\text{m}$), (b) Morphology of single tracks.	161
Figure 6.3 (a) Beam profile of Channels 1&3 ($dp= 76 \mu\text{m}$), (b) Morphology of single tracks.	161
Figure 6.4 (a) Beam profile of Channels 1&5 ($dp= 153 \mu\text{m}$), (b) Morphology of single tracks.	162
Figure 6.5 (a) Beam profile of Channels 1&7 ($dp= 228 \mu\text{m}$), (b) Morphology of single tracks.	162
Figure 6.6 (a) Beam profile of Channels 1&9 ($dp= 305 \mu\text{m}$), (b) Morphology of single tracks.	163
Figure 6.7: Surface morphologies of Ti6Al4V under different processing parameters using LP1 configuration (each track was formed using x5 lasers).....	165
Figure 6.8: Surface morphologies of Ti6Al4V under different processing parameters using LP2 configuration (each track was formed using x5 lasers).....	166
Figure 6.9: Surface morphologies of Ti6Al4V under different processing parameters using LP3 configuration (each track was formed using x5 lasers).....	166
Figure 6.10: Cross-section morphology for a single layer produced using LP1, LP2, and LP3 at different overlap distances.....	167
Figure 6.11: Effect of laser power and scanning speed on melt pool depth for 3.5W and 4.5W laser powers.	170

Figure 6.12: Normalized energy input showing the location of the experimental parameters and the optimal region for LP1 and LP2.....	172
Figure 6.13:Variation of density with speed and normalised energy density for LP1 and LP2.....	173
Figure 6.14: The effect of scanning speed on the top surface and cross-section for LP1.	173
Figure 6.15: The effect of scanning speed on the top surface and cross-section for LP2.	174
Figure 6.16 Surface roughness for different speeds and profiles, with corresponding r.m.s roughness Ra.	175
Figure 6.17: Ti6Al4V microstructural variation with speed and laser beam profile.....	177
Figure 6.18: Temperature comparison at scanning speed of 75 mm/min for LP1 and LP2.	178
Figure 6.19: EBSD analysis of XY-plane (top surface) from the samples at processing parameters (a) IPF for LP1 at 75 mm/min (b) IPF for LP2 at 75 mm/min (c) IPF for LP1 at 200 mm/min (d) IPF for LP2 at 200 mm/min.	179
Figure 6.20: Average grain size (a) for LP1-75 mm/min (b) for LP2-75 mm/min (c) for LP1-200 mm/min (d) for LP2-200 mm/min.	180
Figure 6.21: Corresponding pole figure (a) (PF) for LP1 at 75 mm/min (b) (PF)for LP1 at 200 mm/min (c) (PF)for LP2 at 75 mm/min (d) (PF) for LP2 at 200 mm/min	181
Figure 6.22: XRD graphs for LP1 and LP2 at different speeds using 4.5 W [151].	182
Figure 6.23: Nano hardness and elastic modulus comparison for LP1 and LP2 at different scanning speed.....	183
Figure 6.24: Nanoindentation and material composition for LP1 and LP2 at 75 mm/min.	184

Figure 6.25: P-h Curves for samples produced at 75 mm/min for LP1 and LP2.	184
Figure 7.1: Development of Multiple Zarray for better processing efficiency and microstructure control.	191
Figure 7.2: Heat effect zone as a result of the slow processing speed.....	192
Figure 7.3: Integration of high-power fiber galvo scanning fiber laser (Contour Scan) with multi-laser DAM head for component infill.	192

List of tables

Table 2.1: ASTM International classification of AM Technologies [28].	12
Table 2.2 The absorptivity of various materials in PBF systems.	27
Table 2.3: Commonly used semiconductor materials and their central wavelengths [103].	45
Table 2.4: Summarizing laser types and specifications used in different PBF systems [19]:	47
Table 2.5: A different mathematical approach to identify the Energy Input.	75
Table 2.6: Summarises the optimal processing parameters from previous work.	81
Table 2.7 Summary of Systems and Limitations in the State-of-the-Art of Diode Lasers in Traditional Laser Powder Bed Fusion (LPBF).	86
Table 3.1 Impact of processing parameters (different scanning speeds) on the adhesion of the first layer in the PBF process.	95
Table 3.2 TEC data provided from supplied (Thorlabs).	100
Table 3.3: Specifications of Diode lasers used in this research investigation [25].	113
Table 3.4: The chemical composition and properties of Ti-4Al-4V.	119
Table 5.1 SLM processing parameters for single-track formation.	135
Table 5.2: Summary of processing parameters for SLM of Ti6Al4V from literature.	136
Table 5.3 A summary of single-track processing parameters and resultant melt pool characteristics.	140
Table 5.4: Experimental parameters investigated for Ti6Al4V.	148
Table 5.5 A comparison of cooling rate and corresponding microstructures of Ti6Al4V processed using SLM, EBM and DAM.	154

Table 6.1 : Comparison between a single laser and multi-laser array 4.5 watts, x5 lasers approach for a single layer ($10 \times 10 \text{ mm}^2$)	168
Table 6.2: Processing parameters using x10 diode lasers of Ti6Al4V to normalize energy density.....	170

List of Publications

- *Alsaddah, M., Khan, A., Groom, K. et al. Use of 450-808 nm diode lasers for efficient energy absorption during powder bed fusion of Ti6Al4V. Int J Adv Manuf Technol 113, 2461–2480 (2021). <https://doi.org/10.1007/s00170-021-06774-4>*
- *Alsaddah M, Khan A, Groom K, Mumtaz K. Diode area melting of Ti6Al4V using 808 nm laser sources and variable multi-beam profiles. Mater Des 2022;215:110518. <https://doi.org/10.1016/j.matdes.2022.110518>.*

Chapter 1: Introduction

1.1 Motivation

Advanced manufacturing technologies, such as powder bed fusion (PBF), including selective laser melting (SLM) and electron beam melting (EBM), are now considered disruptive and viable alternatives to traditional manufacturing methods. PBF is increasingly employed in aerospace, automotive, and energy industries to manufacture high-value end-use components. The growing utilization and acceptance of PBF in the industry can be attributed to its ability to produce customized, geometrically efficient structures and reduce material waste from various metallic alloys. These alloys would otherwise be challenging or impossible to produce using conventional manufacturing technologies.

The LPBF process, exemplified by SLM, employs high-performance fiber lasers (usually 200-1000 W) with a spot size of approximately 40-100 μm in diameter to melt a thin layer of metallic powder feedstock layer by layer. These lasers utilize mechanical galvo mirrors to selectively melt sections of powder beds based on sliced 3D CAD data [1,2]. The final product produced using SLM can achieve near-full density without requiring additional processes. The mechanical properties of built components are comparable to those created using traditional manufacturing methods. Moreover, the mechanical properties of SLM components can be customized as needed by adjusting process parameters, influencing the final microstructure of the components. Overall, SLM offers several advantages over conventional manufacturing techniques.

Similarly, non-laser-based powder bed fusion methods, such as electron beam melting (EBM), utilize vacuum electron guns (3-6.5 kW) to scan and melt the powder bed. Compared to other PBF technologies, EBM produces fewer residual thermal stresses because it is possible to pre-heat the surface with the electron beam. Additionally, EBM boasts a higher manufacturing rate due to its ability to scan faster and split/control multiple electron beams on the powder bed.

However, EBM is typically more expensive than SLM systems and yields components with lower resolution and surface finish. For this reason, Selective Laser Melting (SLM) is the most prevalent and researched metal additive manufacturing technology, renowned for its versatility in processing a broad range of materials.

The methodology for manufacturing components using LPBF has not fundamentally evolved in over two decades. The use of high-power fibre laser sources, creating high-intensity laser spots that rapidly deflect across the powder bed using galvo-mirrors, creates a number of challenges for SLM. These challenges include limitations for processing efficiency, scalability, thermal/microstructural control and range of processable alloys [3,4]. Therefore, any method that increases the build rate will likely find some commercial applications. Likewise, delivering a technology that reduces costs and overcomes the drawbacks of SLM technology is also expected to be welcomed.

1.2 Novelty Statement

The lasers employed in SLM systems are primarily chosen for their high power and beam quality, regardless of the absorption spectrum of the material being processed. The current laser systems utilize fiber lasers operating at wavelengths of approximately 1070 nm. Depending on the material being processed at this wavelength, only a portion of the laser energy is absorbed or converted to heat. This further contributes to energy loss due to the high reflectivity of metals at this wavelength[5]. Current SLM lasers are already inefficient, typically 20-30% wall-plug efficiency, requiring higher power to process the more reflective materials such as copper and aluminium [5,6].

The galvo-scanning method, which involves the deflection of fiber laser sources over a limited working area, has inherent implications for system productivity and scalability. Low productivity has been identified as one of the limiting factors preventing the wider adoption of SLM by the industry, especially when manufacturing in higher volumes or when serial production is required [7].

The build rate of SLM is between 2-40 cm³/h for a single laser, depending on the material being processed [8]. Literature suggests that optimizing processing parameters for a single laser source generates limited practical productivity increases for LPBF [9]. Because the LPBF approach uses fast-moving (up to 7000 mm/s), highly focused melting sources, the process generally exhibits poor thermal control over the melt pool with high cooling rates (up to 10⁷°C/s), generating microstructures that are fine dendritic and difficult to alter in-situ. The rapid cooling rate also creates significant thermal residual stresses within the manufactured part that need to be relieved post-process [10]. Occasionally, the stress can be so significant that it causes a part to crack or geometrically distort/fail within a build. Rapid solidification can limit material processability, making it challenging to process high-performance, intermetallic forming alloys that exhibit limited weldability, leading to a high crack susceptibility (e.g., CM247LC, TiAl, Al6000 series) [11-13].

To overcome SLM productivity limitations, system manufacturers (e.g., Renishaw, EOS, SLM Solutions) have developed systems that include up to four high-power (500-1000 W) fiber lasers (with one system having up to twelve lasers, SLM Solutions NXG XII 600), leading to increased build speeds but also significant increases in hardware costs, energy consumption, and overall system size [7,8,14-16].

The use of multiple galvo-scanning systems has future potential to enhance in situ thermal control. However, this control enhancement is likely to be small, with only marginally altered cooling rates due to the continued use of highly focused, rapidly scanning laser beams. It has been reported that the build rate for Ti6Al4V of a four-laser SLM system is 105 cm³/h compared with 18 cm³/h for a single-laser system.

A cost model developed by Kopf et al. [17] showed that implementing 27 lasers of 1 kW power each would increase the build platform from 1400 cm² to 3540 cm², therefore, reducing the production cost by 43% compared to a system with two lasers of 700 W. However, the authors state that implementing such a large number of lasers is not technically feasible. Integrating multiple fiber lasers involves practical space considerations, as each laser requires an individual galvo-scanning mirror, cooling system, optics, and control.

Essentially, the cost of an SLM system scales super-linearly with the number of lasers, while the scanning speed of each laser is still restricted by the mechanical movement of the galvo-mirror system. Furthermore, the processing area is limited by the ability of the F-theta lens to provide a consistent beam profile and laser power across the processing area. Lasers consume approximately 68% of the electrical energy in SLM systems due to the low conversion efficiency of electrical to optical energy, which is at least 30% [18,19].

High-Power Diode Lasers (HPDL) are being explored as alternative laser sources for use within LPBF; they are more compact and energy-efficient than fiber lasers and have longer lifetimes [20]. HPDL has the capability to emit short wavelengths ranging from 450 nm to 3300 nm with a wall-plug efficiency of up to 60%. As a result, it has been used for material processing applications, including soldering, cutting, surface treatments, and welding [18,19]. Recently, research has tried to overcome the limitations of PBF by utilizing diode lasers for multiple spot processing [21-27]. However, these attempts have not successfully produced high-density metallic parts due to poor beam quality.

Furthermore, high laser power (ranging from 50 W to 5 kW) is still being used, as none of the studies considered using a short wavelength (808 nm - 450 nm) to increase the absorptivity of the metallic powder. This gives the ability to use a low-power laser, therefore improving the process efficiency. Fibre-coupled diode

lasers are a superior option to HPDLs due to their excellent beam quality, flexibility, and scalability. Optical fibers ensure a uniform output, enhancing cooling capacity for improved efficiency and reliability. Additionally, multiple modules can be combined to increase power output and scalability without adding complexity.

The direct use of fibre-coupled laser diode sources has not been explored. This work presents developing, testing, and investigating a new methodology for processing metallic powder using a multi-laser array head that implements fibre-coupled diode laser sources with a short wavelength and low power. To investigate the feasibility of utilizing up to ten low-power diode lasers, each with a power of less than 5 W, in a scalable configuration to achieve large write areas without compromising speed, resolution, or causing deformation in final samples. A short laser wavelength of 808 nm is used to achieve high absorption and processing efficiency. Furthermore, individual control of each laser allows the management of intensity distributions across the linear array of laser beams, enabling complex custom-made parts to be built. The work aims to realise a high-resolution and high-energy-efficiency AM system with improved process thermal control, which has the potential to be scalable to write areas of the appropriate dimension for production.

1.3 Research Aims and Objectives

This research aims to develop a novel PBF approach to overcome SLM limitations using a commercial fibre-coupled diode laser (low power 4.5 W, short wavelength 808 nm - 450 nm). In order to achieve this goal, a new powder bed system has been designed, developed, and built for conducting experimental studies. Additionally, the research involves developing and characterizing the laser head that combines several diode lasers in linear arrays to create a high-resolution, energy-efficient PBF system. The objective is to enhance processing efficiency, thermal gradient, and scalability. The specific objectives are:

1. Develop solid knowledge about the laser characteristics and the effect of the absorptivity of wavelength spectrum on the process efficiency.
2. Design, develop and build a novel diode area system to conduct the experimental research.
3. Characterise the multi-laser array head and identify the optimal beam configuration to enhance the process efficacy.
4. Adopt the normalised energy density approach to identify the processing windows and develop this approach for multiple laser processes.

5. Optimise the processing parameters and understand the effects of the process on built components by investigating their mechanical and structural properties.
6. Evaluate the Diode Area Melting (DAM) processes to make recommendations for next-generation systems of PBF.

1.4 Thesis Outline

Chapter2:

This chapter delves into the constraints of Powder Bed Fusion (PBF) in terms of efficiency, productivity, and scalability, beginning with an understanding of Additive Manufacturing. It discusses the limitations of traditional PBF systems and highlights the significant role of wavelength in process efficiency. The adoption of diode lasers in PBF systems is emphasized, illustrating how they enhance process efficiency. The chapter further covers Energy Density in the PBF process and its role in defining the processing area through an in-depth review.

Chapter3:

This chapter outlines the methodology and setup of a research study. Introducing the innovative Diode Area Melting (DAM) approach using multiple fibre-coupled diode lasers 2D arrays with short wavelengths and low-power. The chapter details the characteristics of laser systems, single-diode modules, and multi-laser heads. It also outlines modifications to the system and requisite equipment for DAM processing. The chapter concludes by overviewing characterisation techniques employed to analyse the mechanical and microstructural properties of the final manufactured parts.

Chapter4:

This chapter investigates key factors influencing metallic powder characteristics (material type, particle size, and quality) to optimize process efficiency in PBF. It presents absorptivity measurements conducted on copper, Ti6Al4V, and AlSi12 with varied particle sizes and quality levels.

Chapter5:

This chapter investigates the influence of low-power, short-wavelength single fiber-coupled diode lasers (808 nm and 450 nm) on material absorption and processing efficiency using a Diode Area Melting (DAM) approach with Ti6Al4V. Highlighting the impact of wavelength on absorption rates, it focuses on the increased efficiency achieved with shorter wavelengths.

Chapter6:

This chapter focuses on using multiple addressable fibre-coupled diode lasers (808nm) to improve the efficiency and scalability of Powder Bed Fusion (PBF). Investigate the effect of 3 different beam profiles using a 2D laser head array on resolution, processing efficiency, and scalable PBF system for precise, repeatable parts production with desired mechanical characteristics.

Chapter7

This chapter summarises and concludes this research project (thesis) and provides limitations and recommendations for future studies.

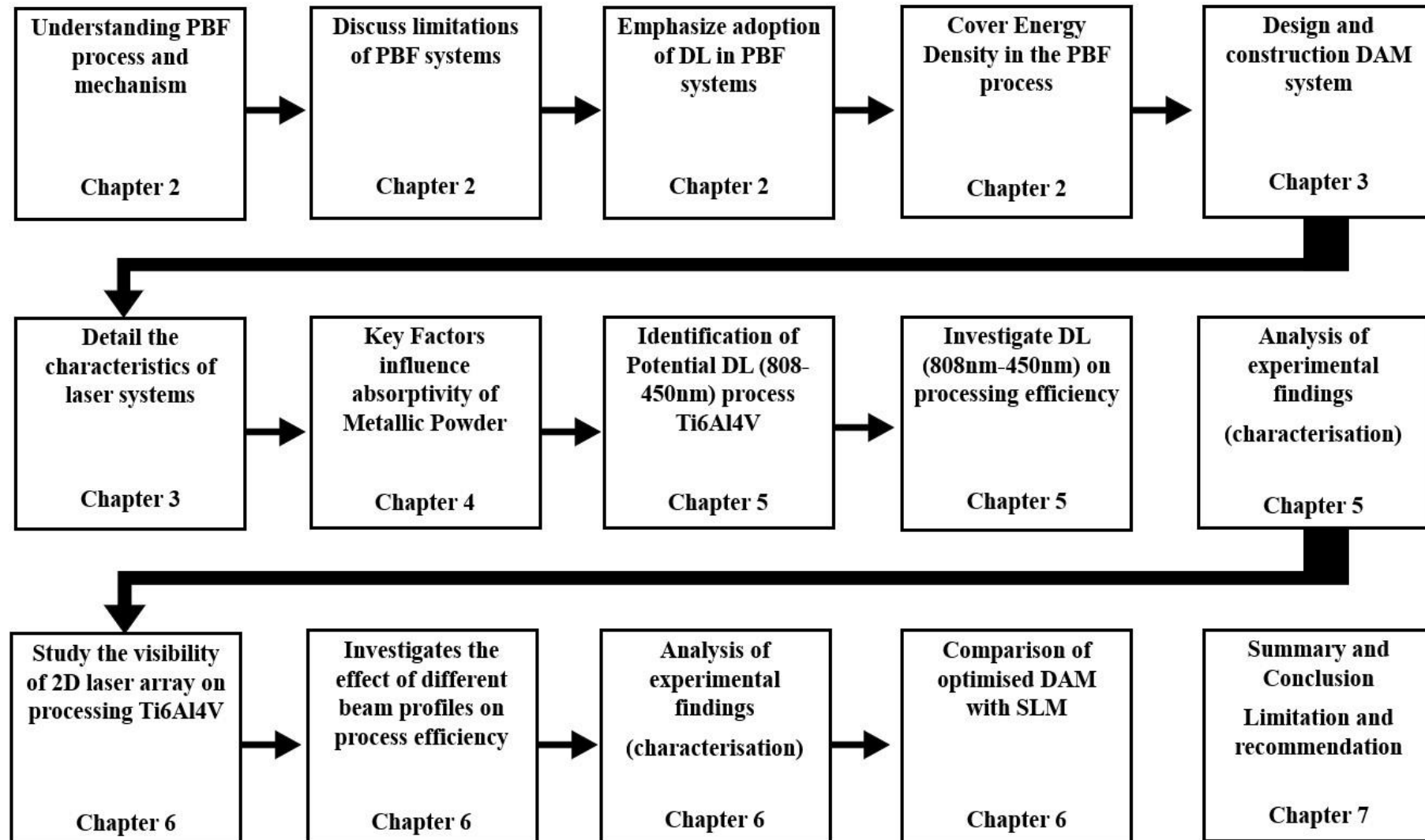


Figure 1.1: visual flow diagram of the present research.

Chapter 2: Literature Review

Summary

This chapter presents a comprehensive literature review of the limitations in process efficiency, including productivity and scalability, associated with Powder Bed Fusion (PBF). It begins with a fundamental understanding of Additive Manufacturing (AM) technologies, focusing on conventional PBF systems and their associated limitations. Next, it explains the importance of wavelength and highlights the adoption of diode lasers in PBF systems to improve the efficiency of the process.

The review elaborately explores the enduring factors related to productivity and scalability in the PBF process. A concise introduction to additive manufacturing sets the stage, followed by a detailed discussion of the challenges within the PBF process. The chapter then explores various laser systems employed in PBF, presenting their benefits and drawbacks.

Special emphasis is placed on Diode lasers, discussing their properties and cutting-edge applications in PBF. The chapter elaborates on how efficiency can be improved by integrating a fiber-coupled diode laser as a multi-diode array package, providing a solution to PBF limitations.

Lastly, the chapter covers the concept of Energy Density, a crucial aspect of the PBF process. The discussion explores how energy density is utilized to determine the processing area.

2.1 Additive Manufacturing: Overview

Additive Manufacturing (AM) is a general term that encompasses a variety of processes used to create three-dimensional (3D) parts directly from a computer-aided design (CAD) model [28]. In a typical AM process, a part is formed by applying a layer of material upon another layer in the vertical direction. Unlike conventional manufacturing techniques (e.g., casting, forging, and machining), AM technologies use solid CAD model data to build multiple thin cross-sectional layers [28]. This has several advantages over conventional processes, such as manufacturable complex part geometries, fully functionally graded materials, and improved and tailorable mechanical properties [29].

AM is an efficient process in terms of material usage due to the small amount of raw material used during manufacturing and the recyclability of leftover material. Another advantage of AM is that no special tooling is required, reducing manufacturing time, design iterations, cost, and material waste while increasing the flexibility of production volume [29,30]. AM eliminates most physical manufacturing restrictions, enabling the production of parts that were virtually impossible to manufacture before [29]. AM has seen a significant improvement in product development because it does not require special tools. For instance, the total development cost of a mould decreases as the production rate increases, making it costly for low production volumes using conventional technologies. In contrast, there are no tooling costs for using AM technologies, and the build volume of the machine can contain several parts with different geometries and sizes, reducing cost further (as shown in Figure 2.1) and aiding product development by increasing design freedom compared with conventional technologies [31].

The freedom of design given by building with sequential layers is another significant benefit of AM. It is as easy to build a geometrically complex design as it is to build simple cubes, offering a financial benefit over standard techniques where the component is difficult to produce and thus expensive, as shown in Figure 2.1.

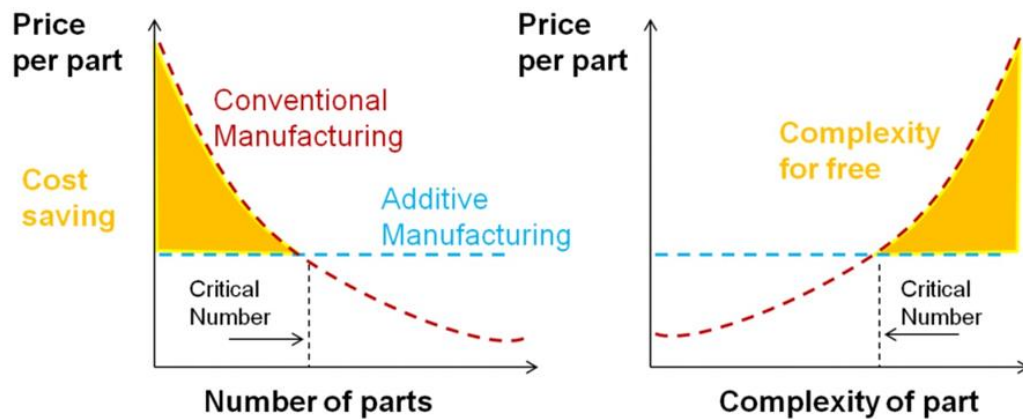


Figure 2.1: Cost comparison using AM over conventional technologies in terms of number of parts and complexity of part [31].

Therefore, it opens up a new avenue for the optimization and deliverance of organic shapes (i.e., customized biomedical implants), weight reduction (i.e., aerospace components), better performance (i.e., heat exchangers), and a wide variety of material selection like polymers (nylon 12 and nylon 66), ceramics (yttria-stabilized zirconia and silicon carbide), and metals (different grades of steel, titanium, and nickel-based superalloys) [30,32].

These features have attracted significant attention and led major industries (i.e., aerospace, automotive, and healthcare) to invest in AM. AM technologies are classified into seven categories, according to ASTM [28], as illustrated in Table 2.1.

Table 2.1: ASTM International classification of AM Technologies [28].

CATEGORIES	TECHNOLOGIES	PRINTED "INK"	POWER SOURCE	STRENGTHS / DOWNSIDES
Material Extrusion	Fused Deposition Modeling (FDM)	Thermoplastics, Ceramic slurries, Metal pastes	Thermal Energy	<ul style="list-style-type: none"> Inexpensive extrusion machine Multi-material printing Limited part resolution Poor surface finish
	Contour Crafting			
Powder Bed Fusion	Selective Laser Sintering (SLS)	Polyamides /Polymer	High-powered Laser Beam	<ul style="list-style-type: none"> High Accuracy and Details Fully dense parts High specific strength & stiffness Powder handling & recycling Support and anchor structure Fully dense parts High specific strength and stiffness
	Direct Metal Laser Sintering (DMLS)	Atomized metal powder (17-4 PH stainless steel, cobalt chromium, titanium Ti6Al-4V), ceramic powder		
	Selective Laser Melting (SLM)			
	Electron Beam Melting (EBM)		Electron Beam	
Vat Photopolymerization	Stereolithography (SLA)	Photopolymer, Ceramics (alumina, zirconia, PZT)	Ultraviolet Laser	<ul style="list-style-type: none"> High building speed Good part resolution Overcuring, scanned line shape High cost for supplies and materials
Material Jetting	Polyjet / Inkjet Printing	Photopolymer, Wax	Thermal Energy / Photocuring	<ul style="list-style-type: none"> Multi-material printing High surface finish Low-strength material
Binder Jetting	Indirect Inkjet Printing (Binder 3DP)	Polymer Powder (Plaster, Resin), Ceramic powder, Metal powder	Thermal Energy	<ul style="list-style-type: none"> Full-color objects printing Require infiltration during post-processing Wide material selection High porosities on finished parts
Sheet Lamination	Laminated Object Manufacturing (LOM)	Plastic Film, Metallic Sheet, Ceramic Tape	Laser Beam	<ul style="list-style-type: none"> High surface finish Low material, machine, process cost Decubing issues
Directed Energy Deposition	Laser Engineered Net Shaping (LENS) Electronic Beam Welding (EBW)	Molten metal powder	Laser Beam	<ul style="list-style-type: none"> Repair of damaged / worn parts Functionally graded material printing Require post-processing machine

2.2 Selective Laser Melting (SLM)

Among the various AM techniques, Selective Laser Melting (SLM), classified as a powder bed fusion process (PBF), is the most widespread process for metal industries and has been in high demand in recent years [33]. This can be attributed to the high accuracy (down to $\sim 70\text{-}100\ \mu\text{m}$) and excellent surface finish compared with Electron Beam Melting (EBM) or Direct Laser Deposition (DLD) [32,34]. SLM is capable of melting metallic powders to produce fully dense parts without the need for expensive post-processing, such as heat treatment and/or infiltration, which is the case with Selective Laser Sintering (SLS), more than detaching the parts and the support structure from the platform [35].

The design of the part is provided in a CAD model, and then it is divided into a series of two-dimensional layers to prepare for construction. The feedstock spreads a thin layer of metallic powder at a thickness of $50\ \mu\text{m}$. The primary laser then moves over the powder bed to selectively melt and bind the required two-dimensional geometry to the previous surface. After that, the processing substrate is lowered to a distance equal to the thickness of the layer, and the process is repeated until all layers are processed, and the three-dimensional part is made, as shown in Figure 2.2. SLM can produce a dense part comparable to bulk material mechanical properties.

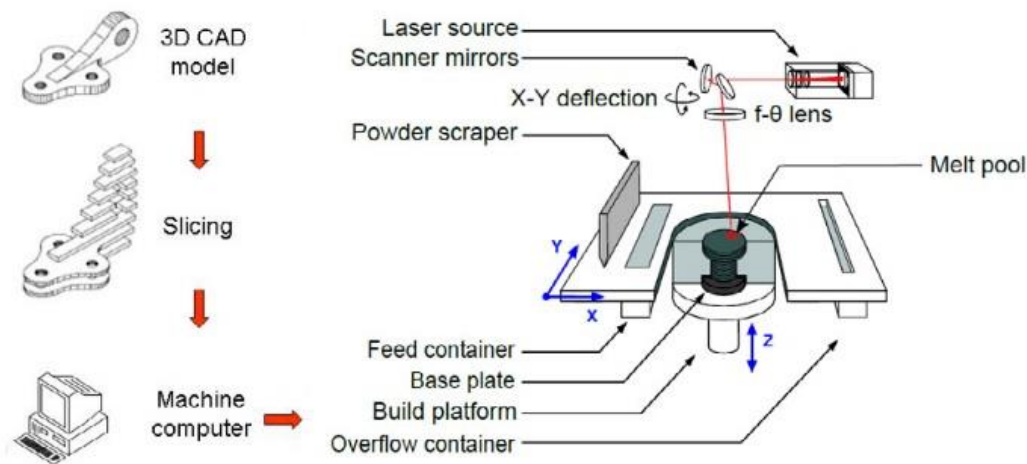


Figure 2.2: Illustrating the sequences of operations in selective laser melting (SLM) [36].

In SLM systems, the laser is the heat source fusing metallic powder. The technology concept was commercialized in 1993 using a CO₂ laser with a wavelength of 10.6 μm, which could not produce metallic parts without lengthy and costly post-processing. SLS sinters the mixture of plastic as a binder with metallic powder to create a green part [35]. The green part requires additional post-process treatment, including heat treatment to remove the plastic binder and then infiltration to produce metallic-based parts. Researchers later realized the importance of the effect of the wavelength spectrum on the absorptivity of the materials, which increases in metals with shorter wavelengths. Therefore, SLM was developed to be equipped with an Nd: YAG fiber laser with a wavelength of 1.06 μm. Using a short wavelength has contributed to reducing the amount of power needed to melt metal powders from kilowatts in SLS to watts in SLM. Nd: YAG fiber laser delivers enough high-intensity energy to melt the metallic powder and produce fully dense, precise, and reliable parts compared with other metal AM techniques or conventional processes. The mechanical properties (e.g., ultimate tensile strength, hardness), surface quality, and processing time of SLM parts can be customized by changing key parameters such as laser power, scanning speed, hatching, and layer thickness. As a result, SLM is one of the most promising AM technologies for metal manufacturing in the aerospace, automotive, and healthcare sectors, and it is of special interest to researchers and developers [30].

Nevertheless, SLM has several disadvantages that inhibit its wider industry adoption [34]. The SLM system's laser source determines the final part's mechanical properties, geometric precision, and internal residual stresses. Usually, there is a compromise between build rate and feature size. This may involve adjusting the laser power, scan speed, layer thickness, and other parameters to achieve the desired balance between build rate and feature size.

For mass production, SLM is relatively slow, expensive, and has a rough surface finish compared with conventional machining. In terms of scalability, although SLM systems are large, giving the impression that the machine should be able to produce huge parts, the build volume is still limited (maximum build $600 \times 400 \times 500 \text{ mm}^3$) and requires high power, resulting in high energy consumption [14]. This limitation arises because SLM systems use a single laser, which is constrained by the galvo scanner's ability to cover a limited processing area. A multiple-beam galvo scanning methodology has been introduced to address this scalability issue. However, implementing the additional galvo-laser system results in a significant increase in system and operational costs.

Furthermore, the high power and low wall plug efficiency of the lasers used in the SLM system lead to more extraordinary operational expenses. The surface finish is low on a level of mechanical properties compared to machined parts. The fabricated parts suffer from internal stresses, resulting in reduced mechanical properties. The use of high-powered lasers and the physical properties of materials induce rapid melting and subsequent solidification, leading to undesirable defects such as cracking, warpage, and residual stress [37]. SLM is still behind conventional methods in terms of productivity, production costs and surface quality.

2.3 Challenges associated with the SLM process.

SLM consists of multiple parameters affecting productivity, repeatability, and quality, such as energy, absorption, thermodynamic microstructural changes, fluid dynamics, evaporation, and chemical reactions. Understanding the causes and effects of physical aspects associated with the SLM process will help optimise processing parameters, minimise defects in parts, and increase their density and dimensional precision. SLM-manufactured components can suffer from localized inconsistencies, leading to undesirable voids and poor mechanical properties. These inconsistencies can be caused by various factors, including balling, cracks, the heat-affected zone (HAZ), atmospheric conditions, and remaining stress. It is essential to carefully investigate these challenges to improve the quality and lifespan of SLM-produced parts.

2.3.1 Part porosity and balling defects.

Porosity in SLM is defined as voids within the fabricated part, which reduces the part's mechanical properties and quality [38]. Figure 2.3 shows two types of pores found in samples: gas-trapped and lack-of-fusion pores [39]. Gas pores are dispersed randomly within the material and often have a spherical or elliptical shape, ranging in diameter from 5-20 μm , as shown in Figure 2.3 (b). These pores form when gas is trapped in the molten pool and fails to escape in time, becoming trapped within the bulk material. Optimizing the packing density of the deposited layer and fine-tuning processing parameters, such as scanning speed and power, can reduce porosity. Even though decreasing the incidence of gas pores by slowing down the scan speed and increasing laser power is possible, eliminating them remains a significant challenge.

In contrast, lack-of-fusion pores are typically larger and present an irregular wedge or band shape with pointed tips on either end with a typical size of 50-500 μm , as shown in Figure 2.3 (a). These pores are often found at the boundary between two contiguous layers, creating thin, flat interfacial fractures. Lack-of-fusion pores primarily result from deviations from ideal melting conditions, such as inadequate laser energy in melting an excess of powders. This leads to insufficient melting and poor interlayer bonding. The minor axis of these pores is typically oriented in the building direction. Under loading, particularly uniaxial tensile loading parallel to the building direction, the pointed tips of these pores are susceptible to concentrated local stresses, which may cause premature material failure [40,41].

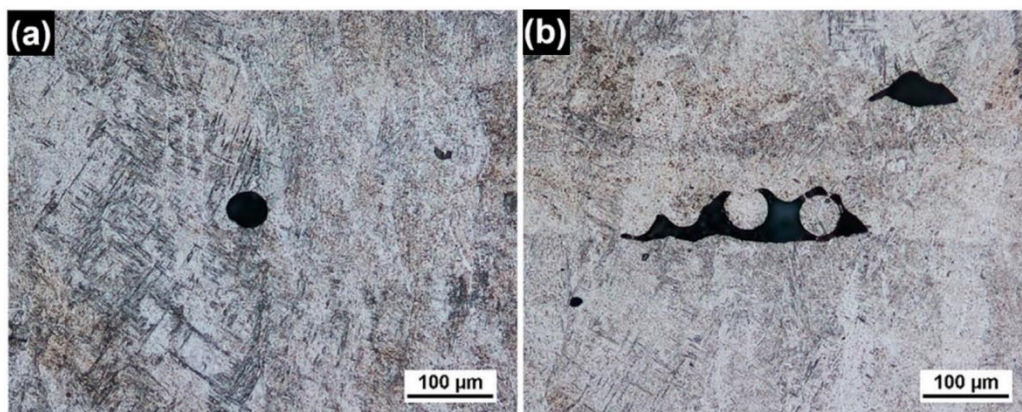


Figure 2.3: Type of porosity, including (a) Entrapped gas pores and (b) Lack of fusion pores (Gas porosity) [39].

Kasperovich et al. [40] carried out a study to examine the effect of process parameters on the porosity characteristics of SLM-processed Ti6Al4V. The experimental results revealed that the scan speed was the most crucial factor, followed by laser power, which significantly impacted the process, where the hatch distance was found to have the most negligible influence. They confirmed that the impact of energy density on SLMed samples showed two main types of porosity defects. Circular pores are formed when excessive energy is supplied, attributed to the keyhole effect. These pores have a fine ribbed surface due to surface tension forces. However, insufficient energy leads to the formation of elongated voids that are perpendicular to the build direction. These voids are over 100 μm long and are caused by incomplete melting of the metallic powders, also known as the balling effect.

On the other hand, balling is known as the formation of discontinuous molten material (droplets) during laser scanning. Porosity and balling have similar causes, and porosity can usually be considered symptomatic of balling [42]. There are two factors responsible for the formation of balling in the SLM; one is the lack of fusion with the previous surface due to a lack of wettability, as shown in Figure 2.4, and the second is related to the Marangoni effect, where the molten material has high surface tension and low viscosity during the SLM process [42]. During the interaction between laser radiation and metallic powder, capillary force is manifested in the molten powder, resulting in the redistribution, conduction, and fusion of powder particles. Capillary forces play a crucial role in achieving a consistent and homogeneous melt accumulation and ensuring the proper flow of molten material between powder particles or/and the substrate. This consequently affects the mechanical properties of the finished part, the level of its porosity and overall quality. Balling occurs due to insufficient energy or/and time factors related to laser radiation and properties of powder layers, such as particle size, layer thickness, and powder size distribution, causing an unstable melt pool [43]. Low laser power may lead to limited liquid formation and insufficient cooling of the melt pool, resulting in the formation of balls with high roughness and weak structures. Also, a high scanning speed may result in instability in the melting capillaries, causing the melting caused by the laser to be scattered and a large number of small balls along the laser scanning path. If not optimised, laser energy and time variables (scanning speed/hatch distance), as well as powder properties (particle size, layer thickness, powder size distribution), and processing environment (oxygen level, ambient temperature) cause balling, resulting in an insufficient distribution of the energy input as shown in Figure 2.5 [38].

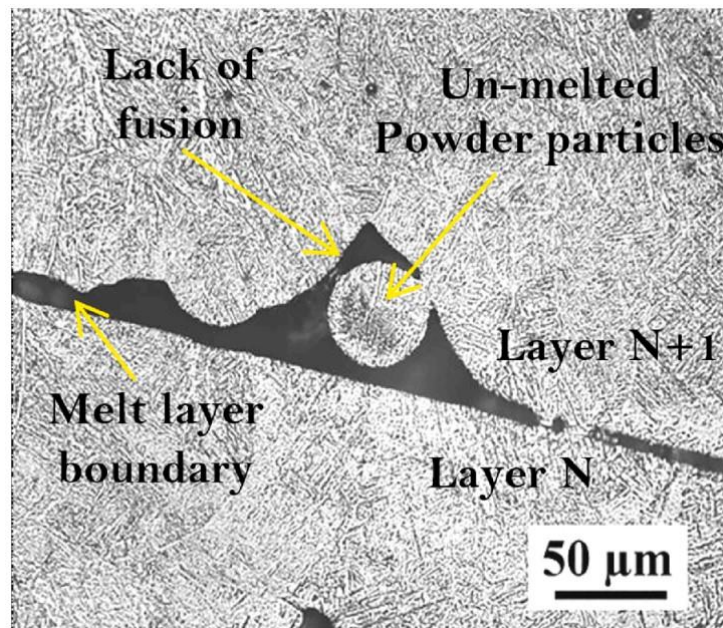


Figure 2.4: Optical image showing the lack of fusion defect within the layers' boundary, exhibiting unmelted particles [44].

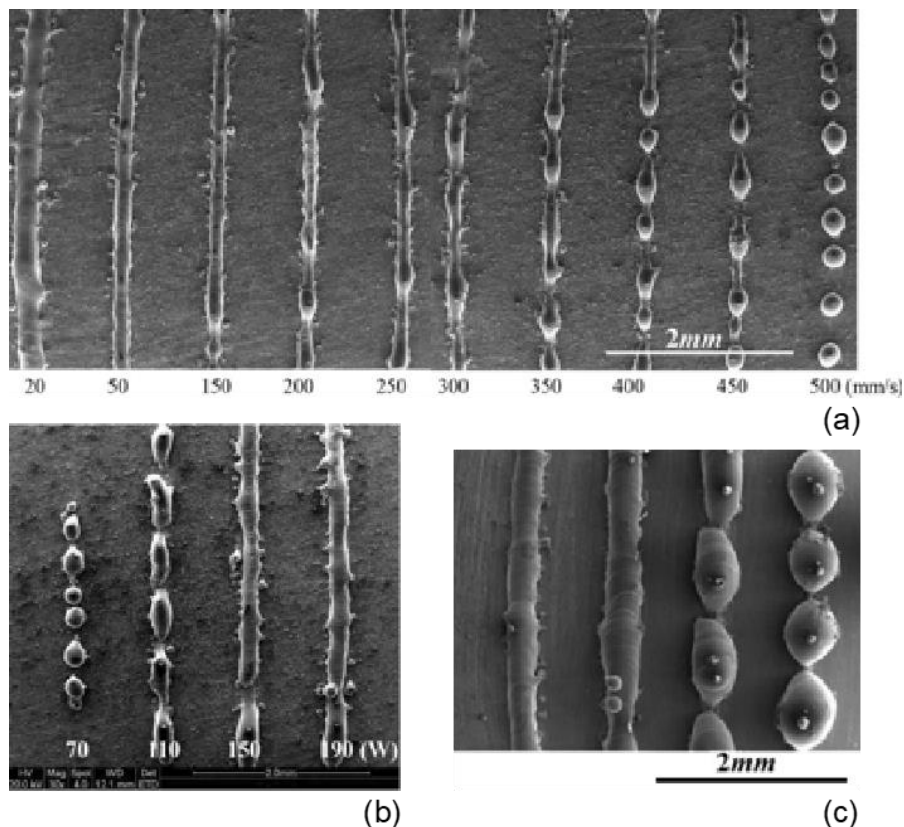


Figure 2.5: The optical microscope reveals multiple single-track morphologies under varying processing parameters: (a) scanning speeds, (b) laser power, and (c) layer thickness (with layer thickness gradually increasing from left to right) [43].

Balling occurs when the melted metallic powder fails to fuse with the previous layer. In this case, spherical droplets tend to form due to surface tension effects, particularly high surface tension. Balling can also be induced by using a high scanning speed, creating unstable melting pools that fail due to Rayleigh instabilities. Rayleigh instabilities cause the cylindrical solidified melt pool to disintegrate in an attempt to minimize surface energy. This phenomenon typically occurs when the length-to-radius ratio exceeds approximately 2.1 [45], as shown in Figure 2.6.

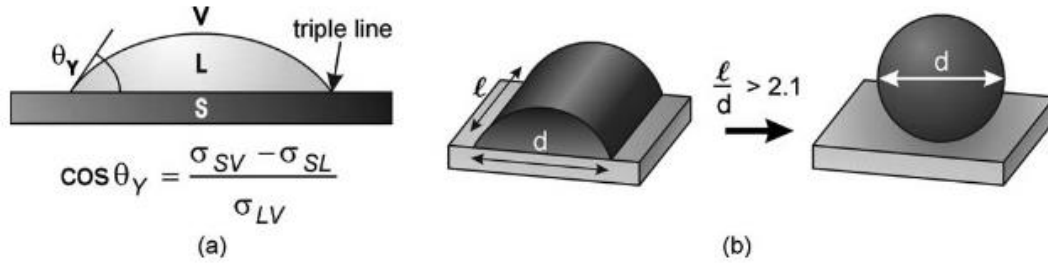


Figure 2.6: Acceptance (a) contact angle between liquid and surface (b) ratio of the cylindrical melt pool before breakup [45].

Rombouts et al. [46] concluded that balling is a process that depends on time, which means if solidification can take place faster than breakup time, the propensity of balling can be reduced. The author used Equation 2.1, which identifies the minimum time to break, to calculate the minimum time for Fe before its breakup, where r represents the cylinder radius, γLV represents surface tension, and ρ represents the material density.

$$t_{\text{break}} = \left\{ 0.3433 \sqrt{\frac{\gamma LV}{\rho r^3}} \right\}^{-1} \quad (2.1)$$

Assuming a diameter of 0.4 mm, they calculated the breakup time (0.5 ms), which was significantly lower than the time required for solidification. They concluded that the melting pool could be stabilised by reducing the length-to-cycle ratio or increasing the contact between the melting pool and the previous layer (wettability). Furthermore, wetting can improve when the oxygen level inside the processing environment is reduced.

The Marangoni flow is defined as the minimisation of surface energy in the event of surface tension gradients, resulting in melt flow from regions with low surface tension to regions with high surface tension, as shown in Figure 2.7 [47].

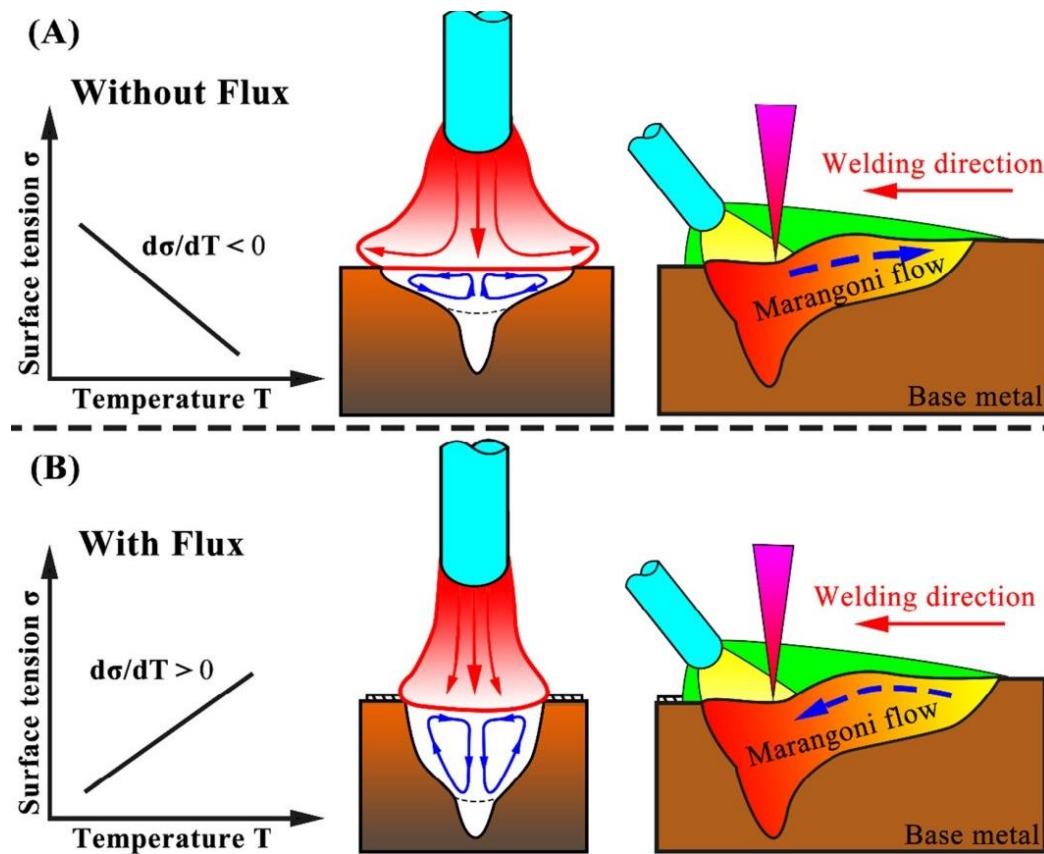


Figure 2.7: Marangoni flow (A) Outer Convection Currents Caused by Negative Surface Tension Gradients, (B) Inner Currents Driven by Positive Surface Tension Gradients [48].

Generally, melt flows from the centre, where laser irradiation reduces the surface tension, towards the edges of the melt pool, where the surface tension remains high. This dynamic results in a broad, shallow melt pool with limited penetration, as demonstrated in Figure 2.7 (A), a phenomenon called "outward flow". In contrast, an "inward flow", illustrated in Figure 2.7 (B), leads to a deep, narrow melt pool [48].

The gradient of surface tension in relation to temperature is typically negative for pure metals and several alloys. However, alloys containing a significant number of elements that influence the surface show a positive gradient. For example, iron with high concentrations of sulphur or oxygen exhibits this characteristic [46]. The introduction of oxygen can reverse this gradient, subsequently altering the direction of convection within the melt pool. In research conducted by Niu et al. [49], it was observed that steel powders processed at high laser speeds and containing 0.10 wt% of oxygen had a heightened propensity for balling compared to those with only 0.02 wt%. This tendency towards balling was ascribed to a more dominant inward Marangoni flow, stemming from the increased surface tension gradient in Fe with higher dissolved oxygen concentrations.

To prevent balling, selecting an appropriate balance between power and scanning speed and monitoring the oxygen concentration during the process is essential, ensuring sufficient energy input to the material while considering each material's processing window [45].

2.3.2 Residual stresses and cracks (warpage/buckling)

SLM parts are more likely to be subject to high residual stresses and distortion owing to high thermal gradients and fast heating and cooling. In the Selective Laser Melting (SLM) process, metal powders are melted and solidified rapidly by a laser. This causes a high cooling rate of up to 10^7 °C/s [10], resulting in significant residual thermal stress and a steep temperature gradient in the final product. Residual stresses tend to increase as more layers are added, with the highest stress values often occurring at or near the surface of the final layer. The residual stress profile usually contains high levels of tensile stress in the upper part of the workpiece, which can reach values equal to the yield strength of the part [50]. The methodology of building parts layer upon layer in SLM and the length of the track significantly impact the residual stress level. A study shows residual stresses are higher in the scanning direction than in the perpendicular direction due to the more significant thermal gradient in the former [51]. This results in a non-uniform distribution of stress in the final piece. Moreover, the increase in scan length leads to an amplification of residual stresses [52].

Residual stresses are known to considerably impact the development of cracks and warping in a component. This often leads to the detachment of builds from the build plate and the emergence of cracks in the final products, Figure 2.8 (a).

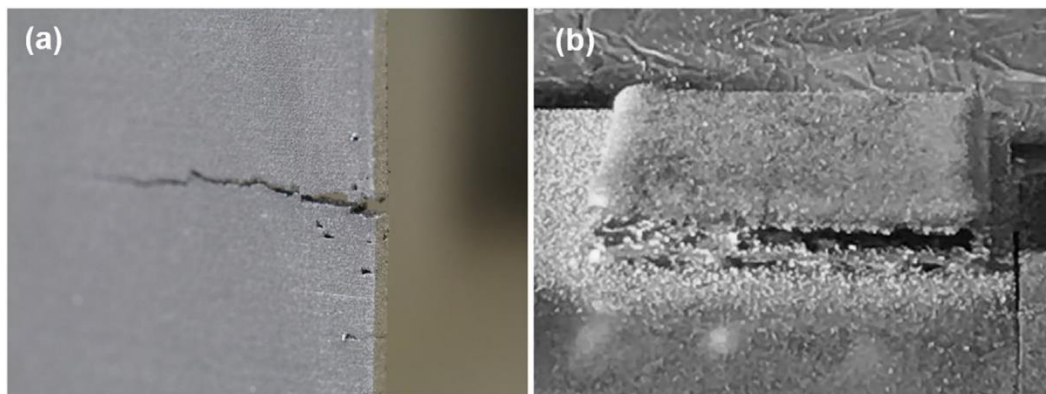


Figure 2.8: Defects in the SLM process caused by residual stress include (a) crack formation and (b) warpage [53].

Cracks often form and grow in the finished piece, particularly from partially melted metal powders on the as-built surface. The microstructure on both sides of the crack reveals elongated crystal grains that suggest a transgranular cracking

mode. This is especially problematic for materials with low thermal conductivity and high thermal expansion coefficient, like stainless steel and nickel-based superalloys.

On the other hand, Warpage and buckling defects occur due to the thermal gradient between the layers and the rapid variation in temperature gradient (heating/cooling) during the process [45], as shown in Figure 2.8 (b). This kind of aberrances results from differential cooling, contributing to thermal stress. Specifically, the cooling rate at the higher end of the part is not the same as the cooling rate at the lower end, which is typically the result of localised rapid heating by laser. Given these considerations, it is clear that processing parameters and material properties significantly influence thermal disruption and stress in the final part [52]. During cooling, elastic deformations restrain (rest), but the plastic deformations remain, causing residual stress, as shown in Figure 2.9. These stresses accumulate during the build, layer by layer [45]. However, they can be reduced by reducing the cooling rate by heating the substrate or preheating the powder feeder using an optical heat source [42,52,54]. It has been reported that reducing the accumulated stress during the build helps to relieve stress and reduce part curl [54].

Recently, several researchers used multiple high-powered lasers (simultaneously laser processing) to heat the surface[55]. This helped to reduce stress, control grain growth, or avoid recrystallisation. Another approach is to use two lasers in series to reduce the cooling rates, which helps reduce the thermal stresses and enhance the mechanical properties or improve productivity by reducing the required energy input [56].

A research project addressing thermal stress indicated that re-melting nickel alloy parts lowered stress by 33.6% [57]. The scanning strategy, where surface geometries are divided into small areas, notably reduces thermal stress [58].

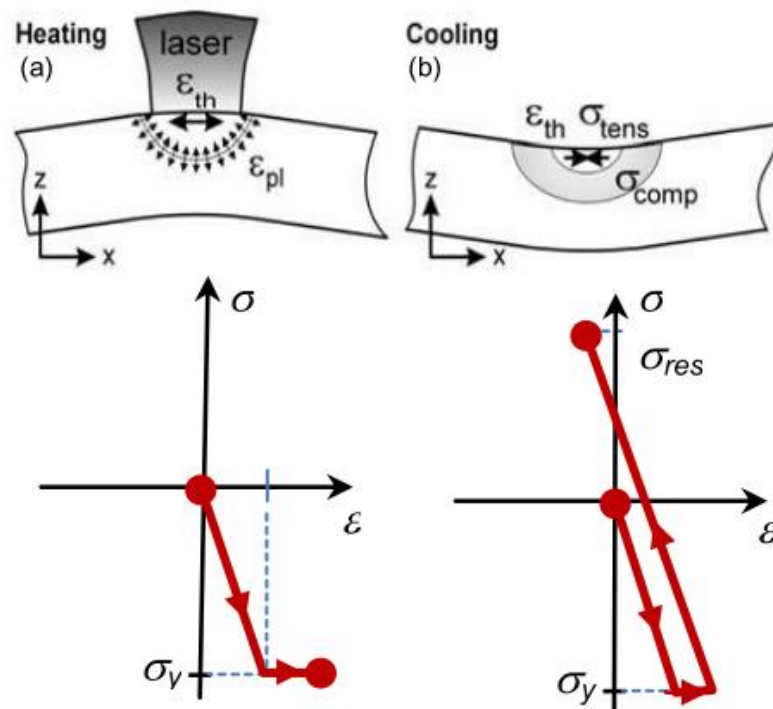


Figure 2.9: Residual stress during (a) heating and (b) cooling [52].

In addition to reducing the geometric quality of the part, thermal stress can cause warpage, which leads to failure to complete the build because the wiper fails to pass over the warped layer. Warpage can be prevented by attaching parts to the substratum during building (anchorless) [54], as shown in Figure 2.10.

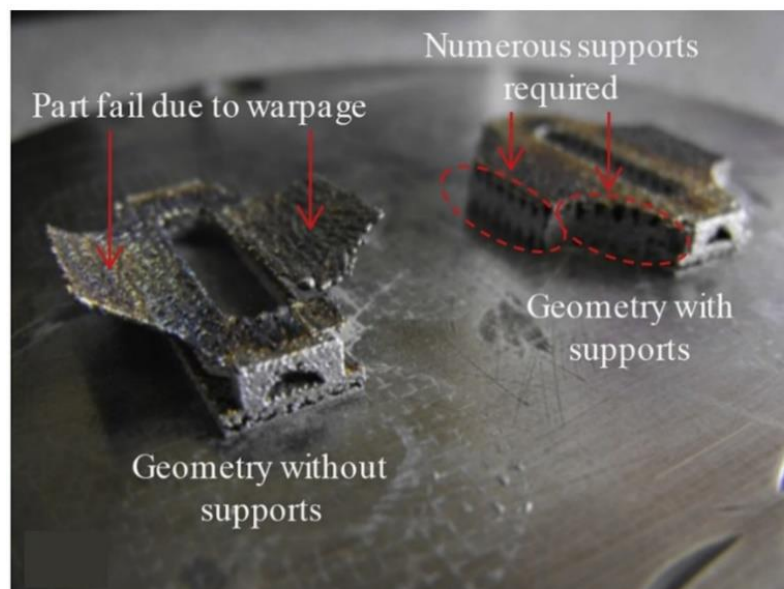


Figure 2.10: shows the final SLM parts with and without support structures, illustrating the importance of support structures in reducing warping during the Selective Laser Melting (SLM) process [54].

2.3.3 Separation/delamination

In addition to previous defects, cracks, and gaps within the layers lead to delamination, causing separation in the horizontal direction of the build, as shown in Figure 2.11. Separation (delamination) occurs between the layers (horizontal direction of the build). The low scanning speed of the laser over a thick layer ($>100\ \mu\text{m}$) of metallic powder leads to heat dissipation on the surface of the powder, causing more of an increase in the heat-affected surface than penetration through the layer, which, in turn, increases stress than the tendency of separation (delamination) between layers. Hence, a thin layer ($<50\ \mu\text{m}$) produces more extensive bonding between layers [59].

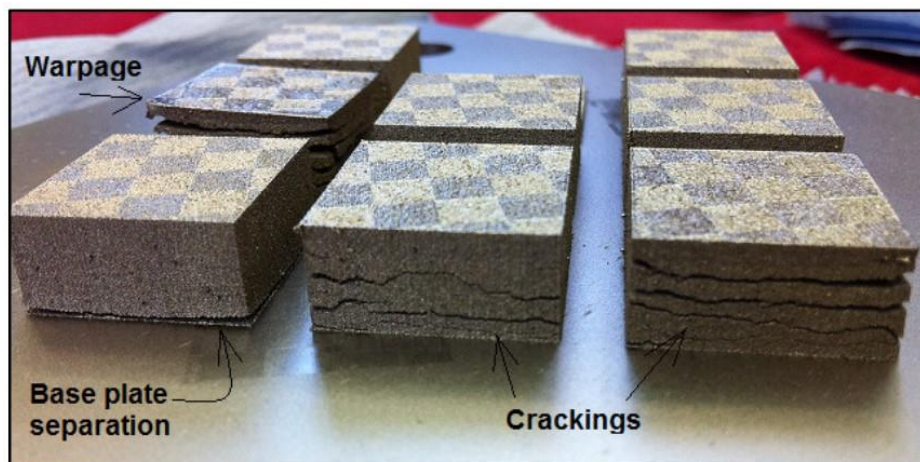


Figure 2.11: Samples produced using the SLM process showing cracks, base plate separation and warpage [60].

In order to achieve a clear surface melting between the melt and the previously consolidated material to enhance the wettability, it is important to re-melt the previous layer to break down and remove any oxide layer to produce a clean surface for the new melting process. According to research conducted by Osakada and Shiomi, it was found that implementing rescanning techniques led to a 55% reduction in thermal stress for nickel alloy parts [61].

Preheating the base plate has emerged as a highly effective approach for mitigating cracking and enhancing densification during the SLM process. A study by Liu et al. [60] has shown a significant improvement in crack formation, eliminating the separation during the process. By preheating the base plate to temperatures of approximately 200°C , Liu et al. significantly reduced thermal gradients between the molten metal and the surrounding solidified material. Consequently, this reduction in thermal gradients leads to a decrease in the magnitude of residual stresses generated. Similar results have been reported by Ji et al. [62]. Figure 2.12 demonstrated a considerable reduction inside cracks and delamination when the base plate was preheated to temperatures ranging from

100 to 250°C, compared to lower preheating temperatures of around 100°C. In conclusion, implementing base plate preheating offers an effective strategy for minimizing the detrimental effects of residual stresses.

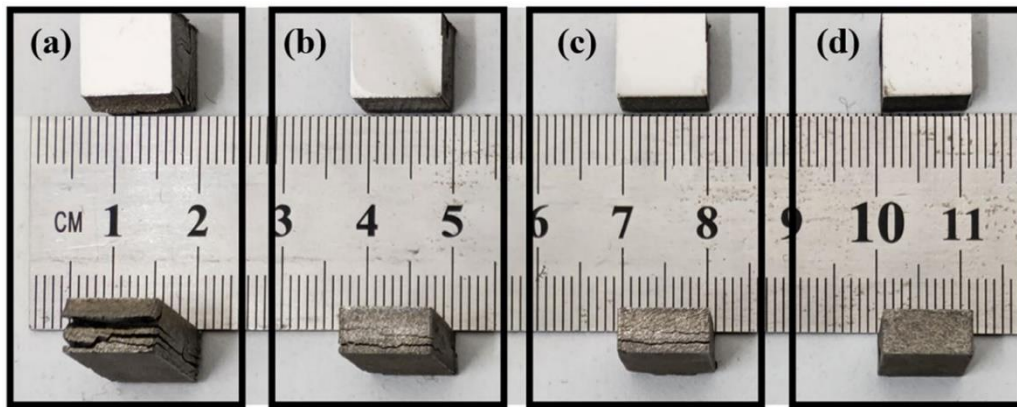


Figure 2.12 Side view of samples produced using SLM process under various substrate temperatures: (a) 100°C, (b) 150°C, (c) 200°C, (d) 250°C [62].

2.3.4 Evaporation and Spattering

In selective laser melting (SLM), a highly focused laser beam rapidly and intensely heats the material, causing a portion of it to reach boiling temperature and leading to evaporation as a significant driving force in the SLM process. This significantly impacts the characteristics of the melt pool and spattering [45]. The quality and integrity of the final product during the selective laser melting (SLM) process can be significantly impacted by vibrations. Vibrations cause spattering, the ejection of molten particles from the melt pool, resulting in defects such as porosity and surface roughness [63]. Additionally, vibrations can disrupt the stability of the melt pool, leading to inconsistent heat distribution and inadequate fusion between layers, ultimately reducing the mechanical properties of the printed part [64].

The main cause of evaporation is the high intensities generated by the laser beam, typically around 10^8 W/cm², leading to intense and localized evaporation. This creates pressure pushing down on the surface of the melt pool, which can be more than five times atmospheric pressure (5 bar). This pressure creates a keyhole shape, mainly influenced by laser power and scan speed. The evaporated material exits the irradiation zone as a vapour jet, with its direction determined by the shape of the melt pool, as shown in Figure 2.13 [65]. Bidare et al. [65] observed from single-line scans indicate that particle ejection paths shift forward to backwards as laser power and scan speed increase. The ejection direction becomes entirely backwards at higher speeds and laser power, disrupting the underlying powder layer. The upward motion of particles draws them towards

the laser spot due to the aerodynamic drag effect. Upon approaching the plume, particles experience sintering or melting, followed by ejection, depending on the heat and momentum they have gathered. After multiple layers, powder availability is less impacted by denudation compared to the first layer due to the increased thickness and roughness of the powder layer [66]. Due to the Bernoulli effect, the vapour jet generates a strong flow within the surrounding gas, with velocities reaching 10 m/s or higher [67]. This gas flow causes powder particles near the melt pool to be displaced or even drawn into the vapour jet and accelerated up to 10^8 m/s². Three types of spatter particles are commonly distinguished melt pool spatter, cold powder spatter, and hot powder spatter.

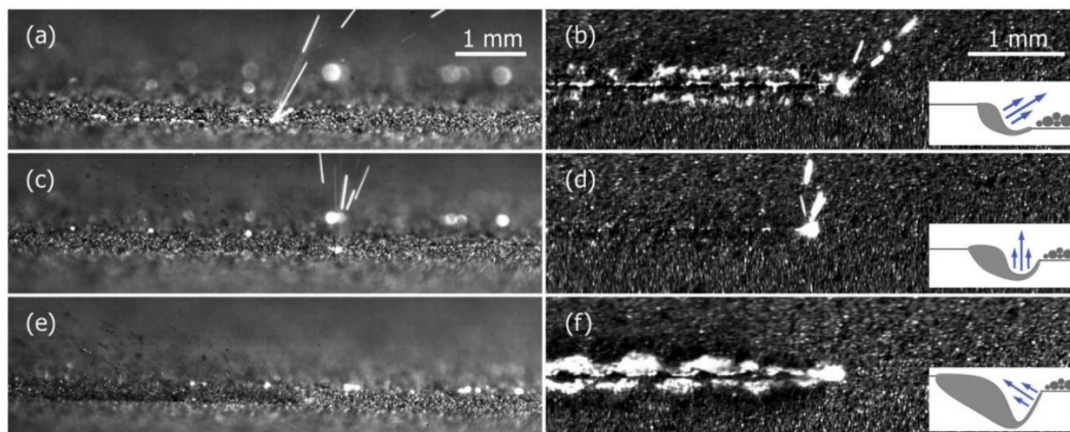


Figure 2.13: Shows high-speed images during the scanning of single tracks at different scanning speeds: (a) 50 W at 0.1 m/s and (c) 100 W at 0.5 m/s, where the vaporized material emerging from the irradiation zone in the form of a vapour jet (spatter), which is influenced by the geometry of the melt pool [65].

Melt pool spatter consists of droplets that escape due to high fluid flow velocities; they are significantly larger than the original powder and can cause issues when redeposited into the powder bed. Cold powder spatter consists of loose powder particles from around the melt pool that get entrained into the vapour jet-induced gas flows. A hot powder spatter is a powder that gets sucked into the high-speed vapour jet itself, causing rapid, intense heating, and can be problematic when redeposited. Spatter particles can become oxidized or have altered grain structures, disrupting the powder bed. By altering laser power profiles and optimizing build chamber pressure, spatter generation can be reduced, and its related effects minimized. In summary, controlling and minimizing spatter is essential in the SLM process.

Ly et al. [67] have determined that the spatter produced during selective laser melting (SLM) mainly comprises 60% hot powder spatter, 25% cold powder spatter, and 15% melt pool spatter. The velocity of these spatter particles is influenced by various factors, including particle size, particle type, and the strength of the vapour jet, which, in turn, is affected by different process

parameters. Previous studies [63,67,68] have reported that cold powder spatters can reach velocities below 5 m/s while melt pool spatters can reach up to 10 m/s. On the other hand, a hot powder spatter can reach velocities as high as 20 m/s due to its smaller size than a melt pool spatter. Studies conducted by Simonelli et al. [69] and Liu et al. [70] have focused on spatter particles' shape and chemical composition. It was found that spatter particles of materials that contain alloying elements prone to oxidation tend to develop oxide layers on their surfaces, despite efforts to reduce residual oxygen levels. These oxide layers are typically found on the outer surface of the particles, while the core can experience changes such as larger grain sizes due to the relatively slow cooling during the particle's flight in the gas atmosphere. Most spatter particles maintain a spherical shape, though some particles may have small satellites on the outside as a result of collisions during mid-air or when landing on the powder bed.

Minimizing vibrations during SLM is crucial to ensure high-quality and reliable components. Several strategies can be employed to minimize the adverse effects of vibrations and spattering in Selective Laser Melting (SLM). These include optimizing processing parameters by reducing the volumetric energy density via increasing the laser spot size [71]. Alternatively, employing a multi-beam strategy, where a defocused laser beam for remelting follows a processing laser, which, as reported, heating the powder after it has melted can reduce the tendency for spattering [16,56].

2.3.5 Absorption, thermal conductivity of powder

SLM is considered to be a thermomechanical process. The interaction of the laser emission and material powder, which always includes a complex thermodynamic activity, is the first step towards creating a path, layer or even a complete part production. Thus, material thermal properties such as absorption and thermal conductivity are important parameters that affect laser absorptivity, melting formation and other processes related to heat transfer mechanisms [42]. Compared with bulk materials, powder particles have comparatively high absorbability due to the voids between the packed powder particles, allowing the laser source to penetrate the powder bed with multi-propagation effects [72]. In other words, when the high-power laser interacts with packed powder on the substrate, the laser beams divide into a multi-beam consisting of the transmitted beam through the material, the reflected beam (forward/backwards), and the absorbed beam by the powder particles and the substrate, as shown in Figure 2.14.

Table 2.2 The absorptivity of various materials in PBF systems.

Material	Nd: YAG laser (1.06 μ m)	CO ₂ laser (10.6 μ m)
Metals		
Cu	59%	26%
Fe	64%	45%
Sn	66%	23%
Ti	77%	59%
Pb	79%	-
Ceramics		
ZnO	2%	94%
Al ₂ O ₃	3%	96%
CuO	11%	76%
SiC	78%	66%
TiC	82%	46%
WC	82%	48%
Polymers		
Polytetrafluoroethylene	5%	73%
Polymethyl acrylate	6%	75%
Epoxy polyether polymer	9%	94%

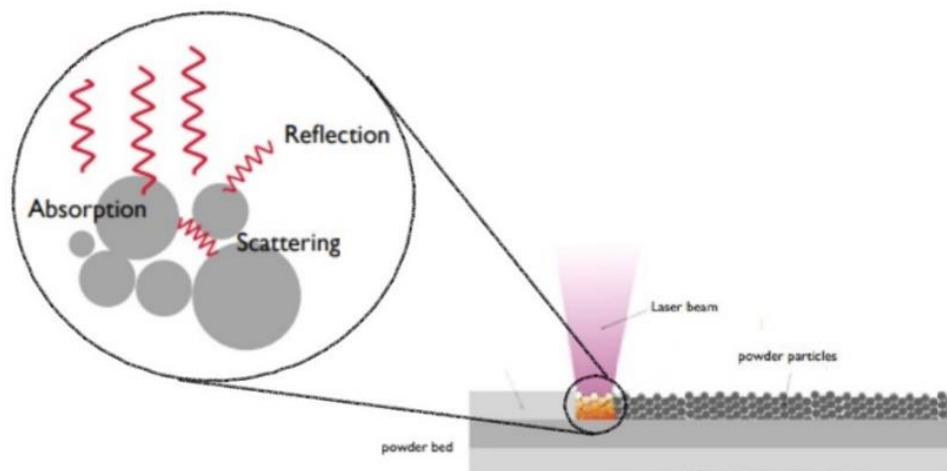


Figure 2.14: illustrates the interaction of the laser with a powder particle, which can be either absorbed or reflected.

The beam transmission in metals is neglected; thus, the total light spectrum will be absorbed (A) or reflected (R). The absorption phenomenon occurs if the spectrum wavelength of light and absorptivity properties of the atom are compatible. Therefore, depending on the level of compatibility, the unabsorbed beam will be reflected. Metal generally shows a strong reflection to the infrared and visible spectrum wavelengths, where it transmits the light of the ultraviolet wavelength. SLM metal powders have better absorptivity under shorter wavelengths (Nd: YAG laser), as shown in Table 2.2. compared to long wavelength laser (CO₂ laser), which is suitable for non-metallic powder (polymers and ceramics). As illustrated in Figure 2.15, the shorter wavelength improves the absorptivity of metallic powder during the SLM process.

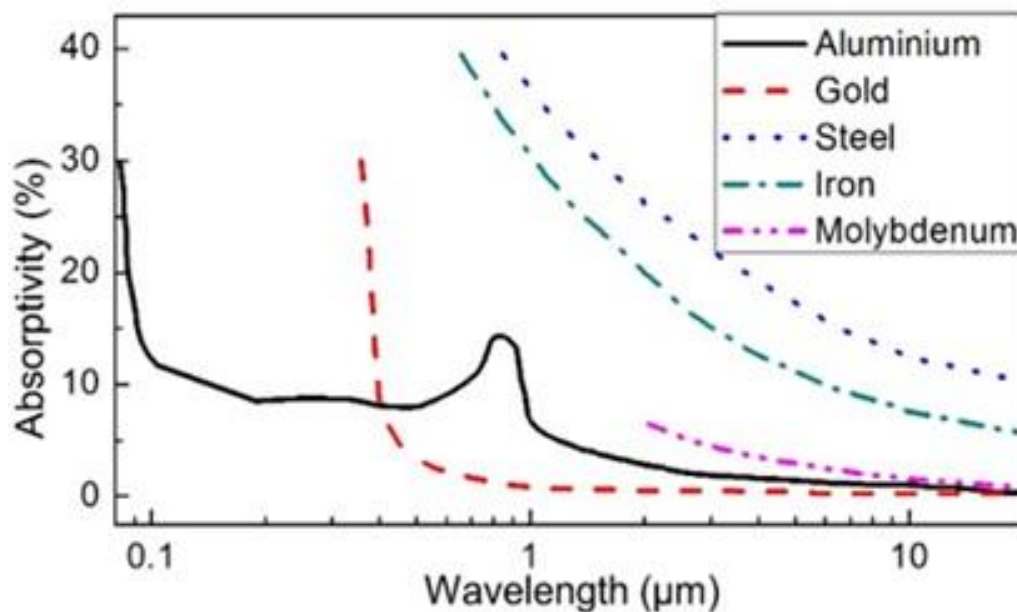


Figure 2.15: Absorptivity of different materials [73].

However, the material setup in SLM, i.e., the powdered material deposited on a previously solidified layer with a specific packing density, makes it challenging to use the known absorptivity of bulk materials. This implies that not only the thickness of the layer and absorption of the bulk are important, but they also require more significant consideration of influenced parameters such as material morphology, powder particle size, packaging densities, and material evaporated, as well as spatter. For that reason, previous works conducted to measure thermal absorptivity were mostly complicated and costly to be repeated. Even with numerical simulations such as Ray tracing, which helped predict the thermal absorptivity behaviour in SLM processes, the accuracy was limited when simulating powder materials with high surface roughness or where oxidation was present.

Recently, Rubenchik et al. [74] developed an experimental measurement to validate the Ray tracing model using a calorimetric method to measure the absorptivity of several materials (316L SS, Ti64-Al-V4, Al) under different powder distribution and layer thicknesses comparable to SLM systems. The experiment was conducted on a thin refractory disk coated with the targeted powder, where thermocouples measured the temperature changes during exposure to a 50 W VCSEL laser at a wavelength of 1 μm . The results were reported to be well in accordance with the Ray tracing model for 316L SS, while there was a 15% and 5% variation with Ti64-Al-V4 and pure aluminium, respectively, due to surface oxides.

Similarly, Trapp et al. [72] used an improved calorimetric method to study the effect of laser absorptivity over various SLM processing parameters, which included two levels of laser power (30-540 W) and three levels of scanning speed (100, 500, 1500 mm/s) with 316L SS and aluminium.

Trapp et al. concluded that in the case of laser power, the absorptivity increases until it reaches complete melt and increases once again when the beam penetrates through the molten track to create a keyhole because of the increases in the scattering of the beam inside the keyhole. The initial absorptivity is significantly higher in the case of a powder layer compared with the bulk material. The author reported that the absorptivity of 316L SS was constant (0.6-0.7) when using the same SLM energy input until the melt pool solidified. To summarize the previous works of literature which help implement these findings when using energy density:

- A short wavelength will increase the absorption of metallic powder; therefore, the required laser power is reduced.
- Thermodynamics in the melt pool is influenced by the material's properties (absorption, thermal conductivity) and material morphology (packing density, particle size, particle average range).
- Multiple reflections during the SLM process increase the absorptivity in metallic powder two times higher than in bulk metals. For that reason, materials with a reasonable absorption spectrum (such as nickel alloys, titanium, and steel) are less likely to increase the absorptivity during laser processing than more reflective metals, such as aluminium, copper and silver.
- The absorptivity is influenced significantly by layer thickness and powder morphology. Hence, increasing the thickness and powder packing and reducing the particle size leads to improved absorptivity [74].
- The fluctuation of absorptivity during the SLM process can be reduced using a wide range of particle sizes.

- Considering the energy input during the SLM process, absorptivity is classified into three regions. In low energy input (<35 W), absorptivity remains constant due to the absence of melt pool formation. In the case of medium to high energy input (85–210 W), absorptivity increases significantly due to the formation of a keyhole, resulting in increased absorption from multiple reflections within it. Absorptivity reaches its maximum value at high energy inputs, primarily because of the reflections inside the keyhole, as shown in Figure 2.16 [72].

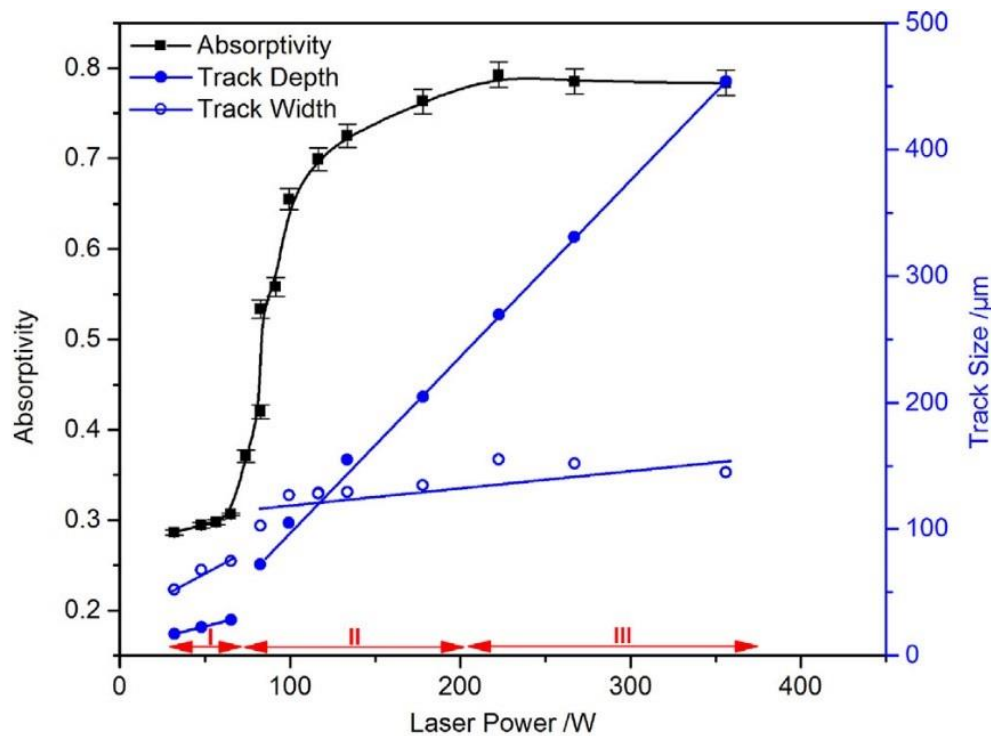


Figure 2.16: The absorption of a flat 316L varies according to the power of the laser at scanning speeds of 100, 500, and 1500 mm/s [72].

- In SLM, absorptivity fluctuation is found to be time-dependent, categorised into two distinct phases based on the energy density level. As shown in Figure 2.17, the first phase involves the laser beam penetrating the powder bed, leading to multi-reflection. This process increases absorptivity until it peaks. Subsequently, the specific energy density plays a role: a lower energy density induces a heat equilibrium, halting the melting and stabilising absorptivity in the second phase. Conversely, with high energy density, the fusion persists, and the growing presence of porosity and keyholes elevates absorptivity. This continues until there is a reduction in porosity, culminating in complete solidification and a corresponding decrease in absorption [72].

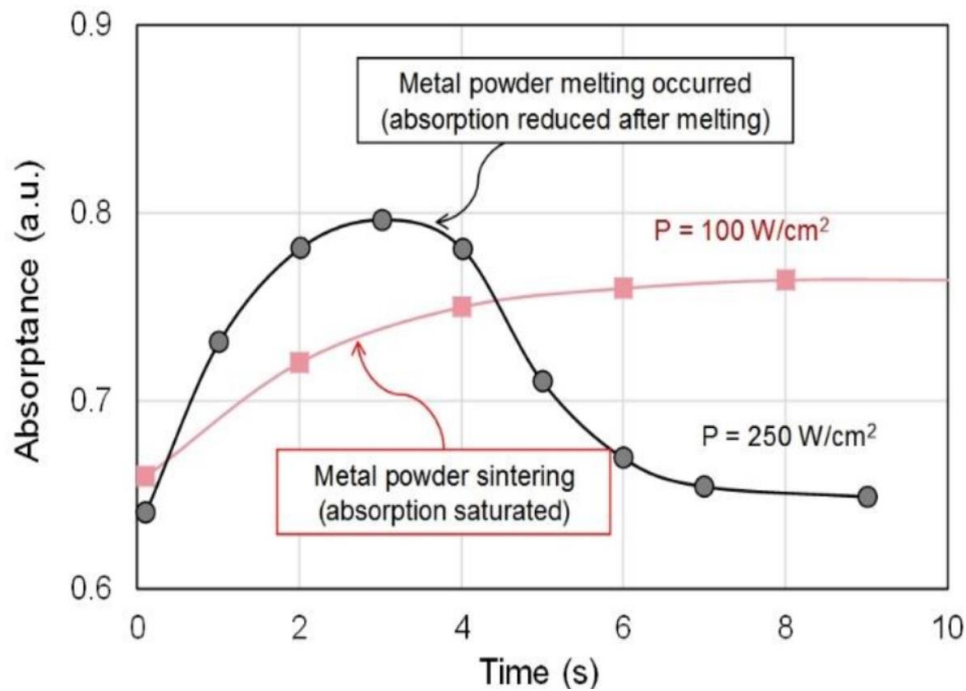


Figure 2.17: Absorptivity during SLM process at (a) low-power laser 100 W/cm^2 and (b) high-power 200 W/cm^2 [72].

Thermal conductivity is the ability of a material to transfer heat efficiently between the particles when exposed to the intense heat generated by the laser in SLM or the electron beam in EBM. This property plays a crucial role in determining the temperature distribution within the material during the process, affecting the final parts' overall quality. Materials with high thermal conductivity can effectively disperse heat and reduce the likelihood of thermal gradients, warping, and defects. On the other hand, materials with low thermal conductivity require more thermal energy, making the process less efficient [75]. Thermal conductivity differs significantly from absorptivity. Thermal conductivity increases notably in bulk materials compared to powders. Porosity in the material or low packing density can reduce thermal conductivity due to limited particle contact.

Because of differences in thermal conductivity between loose powder and solidified material, the conductivity of a powder bed significantly affects the development of high thermal gradients during the melting process. In powder bed fusion systems, effective thermal conductivity depends primarily on the quality of powder packing density. However, powder beds with irregular particles and wide size distribution tend to be more conductive at the same density as regular spherical particles.

2.3.6 Environment during the SLM process

The quality and repeatability of fabricated parts in SLM depend highly on the processing environment, including factors such as gas flow through the building area and the platform's heating. To mitigate the formation of oxidation during the interaction between the laser and the material, the processing chamber should be filled with an inert gas [43,46,76]. Generally, oxygen reacts with molten metal, producing a thin oxide surface that negatively impacting wettability, bonding, and the final part's properties. Oxidation reduces the wettability of molten material, hindering sufficient fusion within the tracks and between layers leading to defects like porosity, balling, delamination, and tearing due to surface stress [43].

Maintaining oxygen levels below 0.2% during the process is recommended to minimize oxygen reactions within the melting pool. This ensures a stable convection flux of Marangoni and promotes strong bonding between the melted particles [76]. In addition to an oxygen-free atmosphere, a continuous flow of inert gas over the processing area is essential to prevent residual melting, including vaporized material. Residual melting can affect laser characteristics, reducing power intensity and absorptivity during the process.

A detailed study on balling behaviour in SLM by Li et al. [43] revealed a significant increase in oxygen content in fabricated parts when the oxygen level was raised from 0.1% to 10% during the SLM process, as depicted in Figure 2.18.

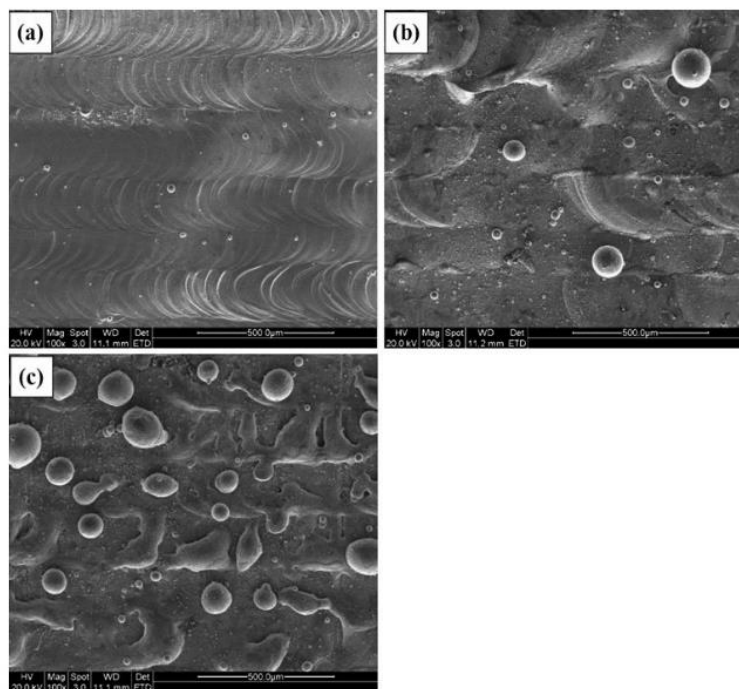


Figure 2.18: The effect of oxygen content during the SLM process influences balling formation at three levels: (a) 0.1%, (b) 2%, and (c) 10% [43].

Different types of inert gases, such as argon (Ar), nitrogen (N₂), helium (He), or carbon dioxide (CO₂), have been used to reduce oxygen levels during metal processing. The choice of gas is crucial, as some gases have the potential to react with alloy elements, leading to undesirable defects. For example, titanium, manganese, vanadium, and chromium can react with nitrogen to form nitrides or cause micro-porosity when used with carbon steel [77]. Understanding the properties of gases is also important; gases with a lower mass than air, such as helium and nitrogen, are lighter than air, making it challenging to protect the processing area in SLM. Consequently, many SLM systems preferentially use argon due to its cost-effectiveness, lack of reactivity, and heavier-than-air properties.

Another environmental aspect researchers consider positively influencing surface roughness, thermal distortion, and the required energy input is heating the platform during the SLM process [55]. However, some studies indicate that heating the substrate may not necessarily enhance the part properties since the heating is limited to 100-250°C, while the melting temperature of metals exceeds 1000°C [42]. Nonetheless, heating the platform does improve powder flowability by reducing moisture content in the powder. The spreading behaviour can also be slightly improved due to the low-temperature variation between the substrate and melt pool.

2.4 Material characteristics in the PBF process

2.4.1 The influence of particle size

The rapid development and growth of powder bed fusion systems have made metal powder the largest material group in continuous development, among other materials [78]. SLM technology started by processing pure materials such as aluminium, titanium, iron, silver, and copper; the processed material has recently expanded to include composite alloys such as nickel, aluminium, and iron alloys. Most of the metal powder is directly suitable for producing fully functional parts; however, processing difficulties may arise and increase with highly reflective metals such as copper and silver. Therefore, the process parameters should be optimised before processing, as powder characteristics, such as the packing density, melting temperature, energy absorptivity, thermal properties, and particulate size, significantly affect the process and, therefore, the quality and mechanical properties of fabricated parts. The most important factor in powder properties is the morphology and distribution of particle powder [79]. It significantly impacts packing density and flowability over the powder bed. Furthermore, the density and surface quality of produced parts, as well as the resolution of layer thickness, are affected by particle size distribution. A high-quality packing density can be achieved with a wide range of particle distribution since the fine particles can fill gaps between bigger particles. Using a broad distribution range, smaller than ($<37\ \mu\text{m}$) or bigger than ($>140\ \mu\text{m}$), leads to the production of highly defective structures with pores and rough surfaces [79].

Niu et al. [79] found that oxidation was more likely when a finer particle size ($<38\ \mu\text{m}$) was used. As a result of oxidation, an incomplete fusion between the layers and tracks occurs, which leads to increased porosity. The material type and powder composition also contribute significantly to the development of oxidation during the process; for instance, aluminium is more susceptible than steel to forming an oxide surface when processed by laser. Therefore, improving wettability can only be achieved if the energy input is increased to disrupt oxidation.

On the other hand, using large particles reduces heat transfer into the powder layer; thus, more energy input is needed to penetrate and melt. The particles' size and morphology directly impact the powder bed packaging density, which, in turn, will impact the absorptivity and thermal conductivity of the powder bed, as discussed in section 2.3.5.

It has been reported that an average particle size distribution of $20\text{-}50\ \mu\text{m}$ can accomplish the necessary acceptance level of fully functional, dense components in SLM. Generally, the small particle size distribution helps reduce the stair-

stepping effect in SLM because it can deposit and process thin layers. Furthermore, it allows a small beam diameter (50 μm) to be used, which helps to increase the intensity and precision of the SLM process [27,80,81].

2.4.2 Microstructure in SLM parts

As many physical and mechanical characteristics are structurally sensitive, it is essential to understand the development of the microstructure in a material during the SLM process, i.e., grain size, grain formation, phase distribution, and volume fraction in a systematic manner. Several studies on the fundamental effects associated with the microstructural formation and features of SLM components are reviewed below. In the SLM process, the microstructure of the produced part is determined by solidification conditions such as the cooling rate. When the laser moves away from the melt pool, disordered material in liquid-phase changes into an orderly solid phase, accompanied by a thermal energy discharge. Crystalline nuclei develop and grow as thermal energy is removed during solidification procedures. As a general rule, few crystalline nuclei form independently at random points in the bulk of the molten metal. However, fast cooling rates in SLM procedures decrease the time to form nuclei and can create non-equilibrium nucleation. Several materials have more than one crystal structure. The temperature change is, indeed, capable of effectively managing the crystal structure. This can change material properties as various crystal structures have different mechanical properties. Rapid cooling rate (10^7C/s) high-temperature gradients reinforce SLM component microstructure [82], forming fine grains in the solidified structure. Although they are usually equiaxed in the build plane, such grains display extreme elongation along the build direction, owing to epitaxial development, resulting in a strong anisotropic microstructure, as shown in Figure 2.19.

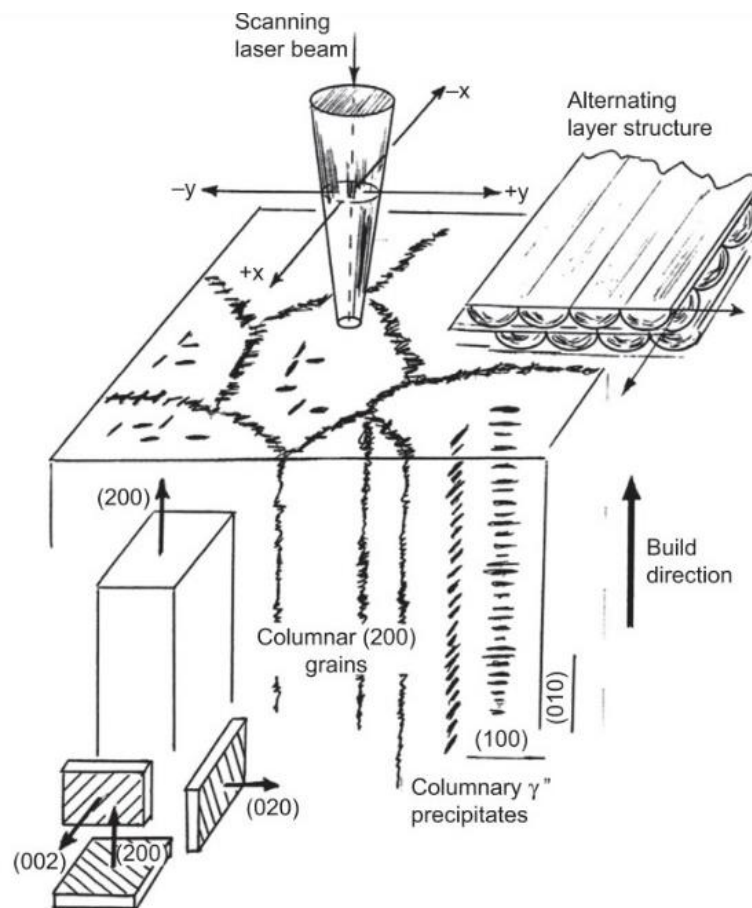


Figure 2.19: Demonstrates the general trends in SLM microstructures. While these grains are typically equiaxed in the build plane, they exhibit significant elongation along the build direction due to epitaxial development, leading to a pronounced anisotropic microstructure [82].

This behaviour was addressed by Riemer et al. [83] on stainless steel 316L. The columnar development of grains across several layers was demonstrated, and the minimisation of this anisotropy via heat treatment was explored. Due to grain development, the anisotropy grade was increased by heat treatment at 650°C for two hours, whilst anisotropy was markedly diminished when the grain structure was reorganised owing to a hot isostatic pressing (HIP) treatment at 1150°C and 1000 bar. The impact of process parameters on stainless steel 316L microstructure was examined by Niendorf et al. [84]. Results indicated that greater layer thicknesses and higher energy densities promoted columnar development of grains. Due to non-equilibrium solidification at high cooling speeds and high-temperature gradients, the shift in liquidus and solidus temperatures and a significant increase in the in-between temperature range make it more likely for minor alloying elements to separate [85]. Thijs et al. [86] demonstrated that columnar development for AlSi10Mg occurred from the melt pool edges to the middle of the superior surface of the melt pool, where an equiaxed grain was present. This hindered columnar development across multiple layers with a powerful parallel to the build direction. Such features of

microstructure determine mechanical properties. The part's orientation in the build chamber depends on part properties owing to anisotropy. Young's modulus and yield strength are lower, while elongation at break is higher when loading is applied along the direction of the elongated grains. The opposite is true when loading is applied at right angles to the elongated direction, but since SLM parts have smaller grain dimensions on average, the yield strength is higher, and elongation at break is lower, as in the case of cast material. The implementation of HIP treatment as a post-processing phase helps to attenuate such anisotropic mechanical behaviour. Hence, as indicated by some studies, it is possible to achieve mechanical properties similar to cast components.

2.4.3 Ti6Al4V Microstructure in PBF

Ti6Al4V is well-known as $\alpha+\beta$ titanium alloy that finds widespread use in various industrial applications such as aerospace, automotive, and medical fields due to its excellent properties. These include a high strength-to-weight ratio, competent fatigue and fracture resistance, biocompatibility, high-temperature resistance, and corrosion resistance.

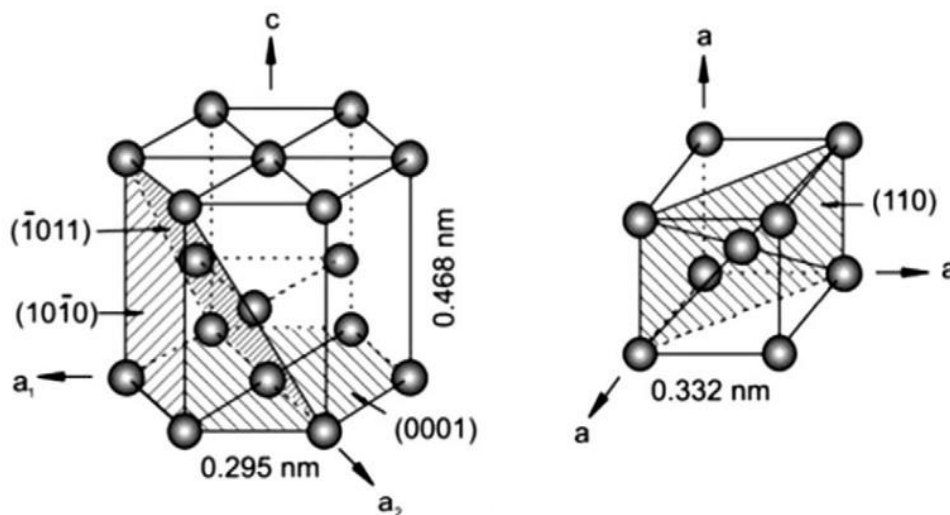


Figure 2.20: Two distinct crystal structures: a hexagonal close-packed (HCP) structure and a body-centred cubic (BCC) structure [87].

At room temperature, titanium is in its α -phase, which is a hexagonal, close-packed (HCP) structure (91%) and (9%) of β phase. However, when the temperature reaches above 900°C, known as the β transus temperature, the titanium atoms rearrange themselves into the β phase with a body-centred-cubic (BCC) structure, Figure 2.20 [87,88]. The transformation temperature and stability regions can be modified by adding stabiliser alloying metals. For instance, aluminium can act as an α stabilizer, increasing the transformation temperature from α to β , while vanadium can serve as a β stabilizer, reducing the transformation temperature, as shown in Figure 2.21.

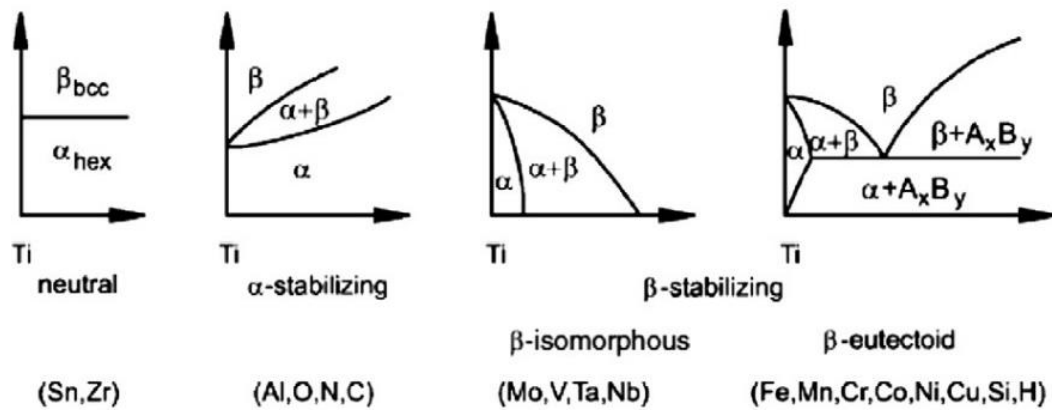


Figure 2.21: α and β stabilizers along with the associated phase diagrams for Ti6Al4V [87].

Based on the phase diagram in Figure 2.22 (a), the martensite (M_s) temperature starts ranges between 800°C and 575°C. It is the temperature at which β fully transforms to $\alpha+\beta$ during a slow cooling rate. However, rapid cooling in the PBF process leads to the non-equilibrium martensitic α phase formation instead of the equilibrium $\alpha+\beta$ phases [89].

The influence of cooling rate on the phase transformation of Ti6Al4V was investigated by Ahmad et al. At cooling rates above 410°C/s, a mainly martensitic α microstructure is produced. At the same time, cooling rates between 410-20°C/s yield a microstructure to form both α martensite and $\alpha + \beta$ phases, as shown in Figure 2.22 (b) [89].

In contrast, a slow cooling rate of less than 20°C/s results in a significant time to permit diffusional processes to occur, allowing the decomposition of β to the equilibrium $\alpha + \beta$ lamellar microstructure. Ultimately, by reducing the cooling rate to the lowest value investigated in this study, 1.5°C per second, the grain boundary Widmanstätten α plates continued to grow towards the grain centres. This led to the development of the 'basketweave' Widmanstätten pattern.

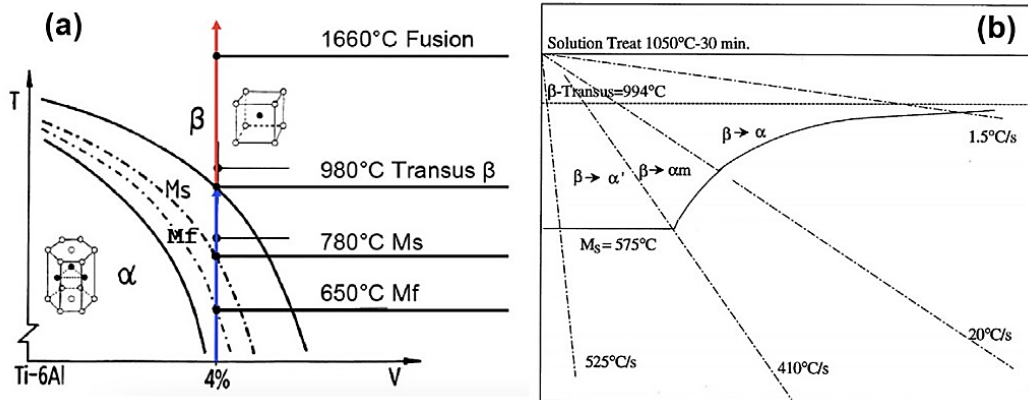


Figure 2.22: Shows the Influence of Cooling Rate on Phase Transformation in Ti6Al4V. (a) Phase diagram of Ti6Al4V [90]. (b) Phase transformation as a function of cooling rates [89].

The comparative analysis of the microstructure of Ti6Al4V fabricated by SLM) and EBM reveals a pronounced divergence arising from the varied thermal conditions within each process [53,91-93]. In SLM, the rapid cooling rates of ~ 104 - 107°C/s foster a martensitic microstructure dominated by fine α martensitic microstructure. Conversely, EBM has a lower cooling rate (103 - 105°C/s) due to a higher build temperature (600 - 750°C), resulting in α + β microstructure. The α phase appears in a lamellar or basketweave morphology within the β phase matrix, with larger grains and a coarser microstructure (0.4 - $1.4\ \mu\text{m}$) than SLM (0.1 - $0.4\ \mu\text{m}$), as shown in Figure 2.23. The microstructural phases strongly correlate with hardness and mechanical properties. α martensite provides the highest strength, while α + β offers a better balance of strength and elongation.

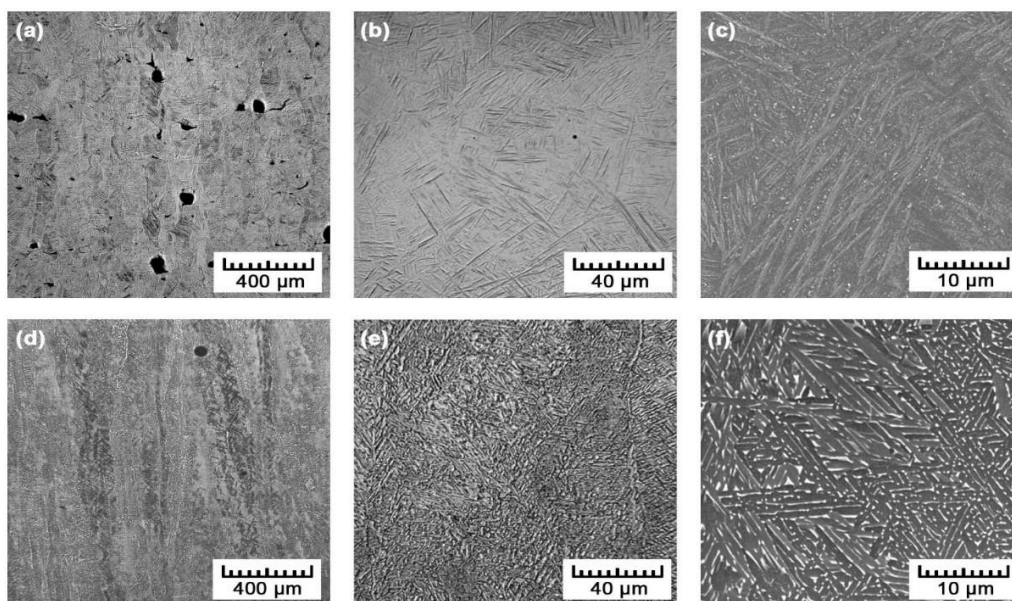


Figure 2.23: Microstructures of samples produced using SLM (a-c) and EBM (d-f) [93].

The research carried out by Zaho et al. [94], utilising X-Ray Diffraction (XRD) analysis, provides experimental support to the previous discussion on the microstructure of Ti-6Al-4V fabricated via SLM and EBM. Figure 2.24 demonstrates that most peaks are attributed to the α/α' phase for both manufacturing techniques. Nevertheless, a discernible difference is identified with the detection of a peak commensurate with the body-centred cubic (bcc) β phase in the EBM samples, indicating the presence of a degree of β phase within the microstructure of the samples. When comparing the width of the α/α' peaks between the SLM and EBM samples, it was found that the peaks were broader in the SLM samples. This suggests that SLM produces a finer grain size for the α' phase.

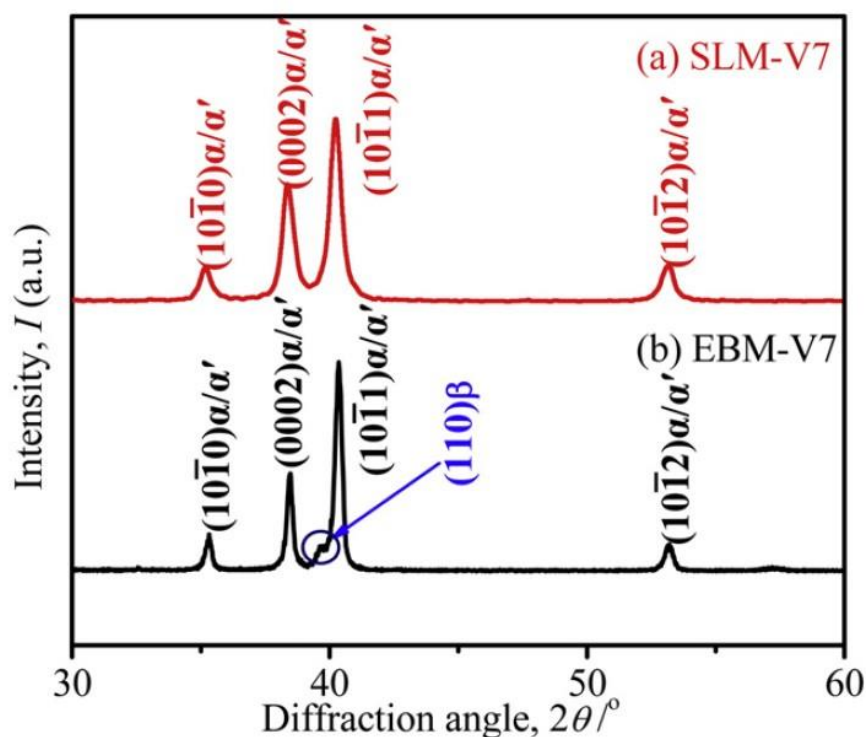


Figure 2.24: XRD pattern for samples of (a) SLM and (b) EBM [94].

SLM and EBM Ti6Al4V's microstructure and mechanical performance can be improved in various ways by optimizing the building temperature, reducing the cooling rate, optimizing the scan pattern, or/ and applying hot isostatic pressing (HIP), and annealing heat treatments [89,93,95,96]. These strategies aim to control microstructural features like grain size and α lath thickness and eliminate defects, improving the balance of strength, ductility, and fatigue life for the PBF process.

2.5 Laser types and applications

In SLM, the laser beam is the primary thermal energy source responsible for melting the metal powder [8]. Providing high beam quality ensures efficient, precise, and high-quality material deposition during the process. The laser quality depends on beam properties, which are affected by many variables, including wavelength, spot size, mode, beam profile and transfer medium. In most SLM systems, the laser wavelength is fixed to 1064 nm. However, specific parameters can be adjusted based on the processed material to achieve high-density parts, depending on the selected laser mode (continuous or pulsed). Continuous mode systems adjust parameters such as spot size, focal plane, and laser power, while pulse systems offer adjustable parameters like peak power, frequency, spot size, and pulse duration [97]. The laser characterisation is determined by three significant elements engaged in producing laser light: the active medium (gain), the pumping energy source and the optical resonator [98]. The laser beam is generated by amplifying the light emanating from the active medium which is placed inside the optical generator using pumping energy. Therefore, the laser is classified by a gain medium to a solid state, gas lasers, liquid lasers, and semiconductors, as shown in Figure 2.25. Gas lasers (CO₂) and solid-state lasers (Nd: YAG laser, Yb-doped fibre laser) are the most extensively used in SLM [8,99].

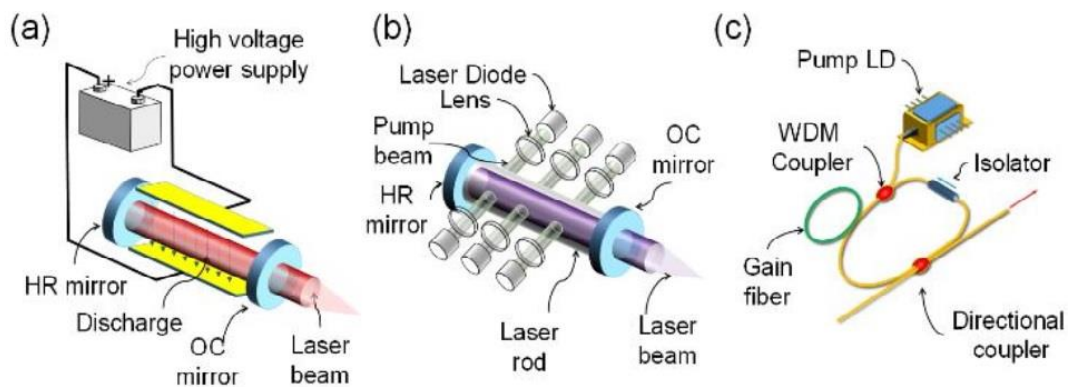


Figure 2.25: Schematics of different types of lasers with different gains (a) Gas (b) Solid State (c) fibre laser [19].

2.5.1 CO₂ laser

The earliest gas laser, the CO₂ laser, was developed in 1964 [100]. CO₂ is used as a gain medium inside a discharge tube, which is activated using an electrical pump source and amplified using optics (mirrors and lenses), as shown in Figure 2.26.

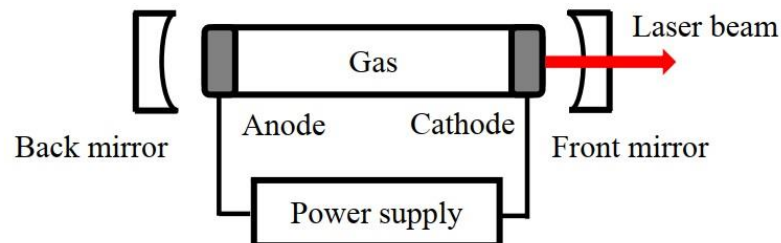


Figure 2.26: The foundation of the CO₂ laser module consists of a back mirror, a gas power supply to excite the gas, and a front mirror [19].

This process generates an infrared wavelength from 9.0 up to 11 μm . Due to its efficiency (5%-25%) and the power ranges (0.1-20 kW), the CO₂ laser is used widely in material processing (such as cutting, welding, surface treatment and drilling) where the power quantity, not the quality, is important. The CO₂ laser is considered a workhorse of precision manufacturing due to its low cost, reliability, and simplicity. However, the long wavelength of CO₂ limits the material processing, especially with metals, due to the lack of absorption coefficient. In AM, a wavelength of 10.5 μm is the most commonly used in SLA systems to process polymers or a mixture of metal with polymer due to high absorptivity by polymers. Another obstruction is the beam quality of the CO₂ laser, which cannot be improved or delivered by an optical fibre [19]. Another downside of the CO₂ laser is the output power instability caused by thermal expansion due to the massive heat generated by pumping energy into a large volume of CO₂ gas. In addition, the optics must be examined every 2000 hours for fatigue [19].

2.5.2 Solid-state laser (Nd: YAG)

The Nd: YAG laser (Neodymium-Doped yttrium aluminium garnet laser) is a type of crystal used as a gain medium in a solid-state laser [19]. In addition to CO₂ lasers, the industry ordinarily uses these two types of lasers as high-power sources [101]. However, one of the advantages over CO₂ lasers is that Nd: YAG lasers are near-infrared (NIR), with a wavelength of 1064 nm, which can be delivered using fibre optics. Nd: YAG lasers have output power of up to 20 kW in continuous mode and 120 J in pulsed mode. Nd: YAG uses a flash lamp as an

energy pump source, which is the primary factor responsible for poor beam quality [19], as shown in Figure 2.27.

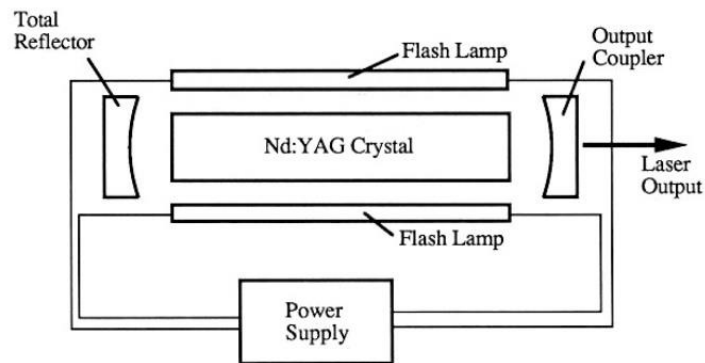


Figure 2.27: Fundamental of Nd: YAG laser module [19].

As a result of the low power conversion (electrical to optical), the unabsorbed energy is dissipated as heat, which affects the beam quality. Another weakness is the short lifetime of the flash lamp, which can be improved using a diode-pumped solid-state (DPSS) as an energy pump source to lead to better beam quality and longer laser lifetime, five times more than before [19]. In SLM systems, the Yb-laser has replaced Nd: YAG to achieve higher efficiency. However, the accessibility of the Nd: YAG laser means researchers commonly use it to study the parametric and optimising key factors of AM.

2.5.3 Yb-Doped Fibre Laser

Rare-earth-doped fibre lasers are used as an active medium in a fibre laser. In the earliest years of fibre lasers, their output power performance was limited compared to bulk lasers. The use of a diode laser (950-980 nm) as a pumping source, as illustrated in Figure 2.28, improves beam quality, efficiency, and produces near -IR laser beams (1030-1070 nm) [19].

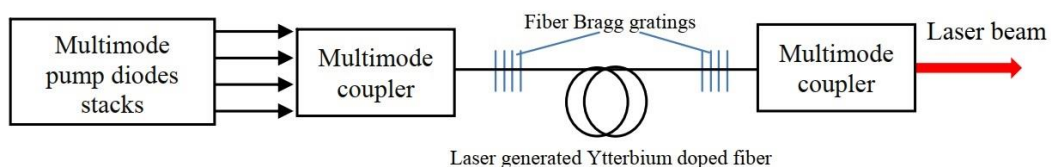


Figure 2.28: Concept of Ytterbium fibre laser module [19].

Yb-fibres have the ability to produce high power due to their high stable efficiency (94%) compared with the other types of rare-earth-doped fibres. Yb-fibre-lasers can produce constant energy of several kilowatts with a high beam efficiency optical to optical output (70-80%) and an electrical to optical effectiveness of up

to 30% [19]. Optical fibre allows the Yb-fibre laser to deliver the beam to a longer distance or connect to a movable optical system without affecting the original beam characterisation (beam quality, output power) and improve system compactness. Yb-fibre lasers are extensively applied in the material process and have almost displaced Nd: YAG lasers in SLM systems [19].

2.5.4 Diode laser

A diode laser is classified as a solid-state laser where electrical power is converted into optical energy. The diode laser consists of a thin layer of semiconductor material (P-N junction) sandwiched between the identical semiconductor material on both sides of the junction, as shown in Figure 2.29 (a).

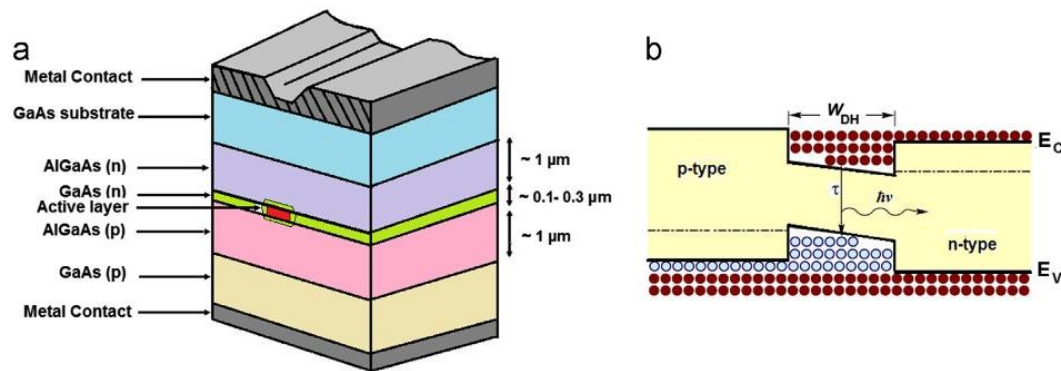


Figure 2.29: Structure of diode laser [102].

The internal surfaces of the junction are highly polished to be a mirrored surface, where the back is coated to a highly reflective surface, and the front is also partially coated to allow the laser module to emit light. Once the current starts flowing by applying the voltage, the depletion region narrows, and the P-N Fermi level becomes excited to generate radiation ($h\nu$) Figure 2.29 (b).

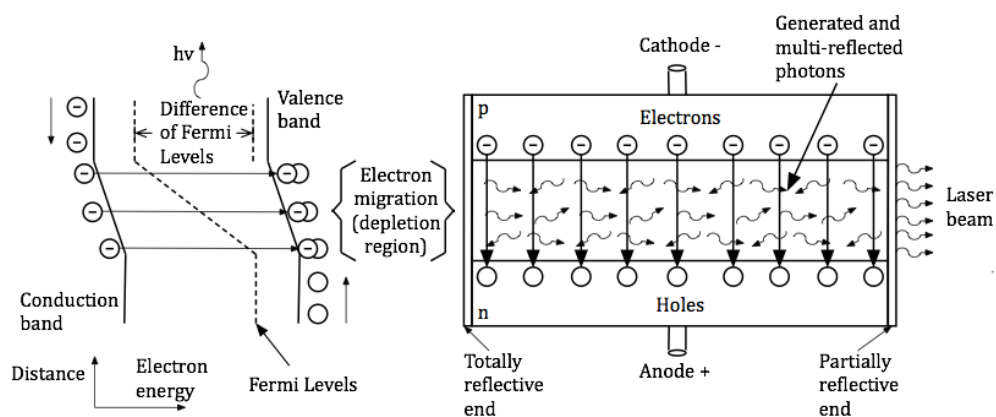


Figure 2.30: Diagram showing diode laser characteristics and operational fundamentals [102].

Because of current flows through the P-N junction, the N region injects electrons, and the P region injects holes into the depletion region, which increases the population of the photons by the inversion due to mirror recombination and stimulation in the depletion region, as shown in Figure 2.30. Photons start emitting at a specific wavelength from the partially coated surface, creating a monochromatic laser beam [102]. A combination of factors, including the band gap energy, cavity length, and refractive index of the semiconductor material, determines the wavelength of a diode laser. As a result, it is subject to variations depending on the material, temperature, and driving current. High-power diode lasers operating in the IR spectrum typically utilize AlGaAs and InGaAs semiconductor material, as in Table 2.3 [103].

Conversely, a shorter wavelength (ultraviolet to infrared) can be achieved by combining two different materials, known as heterostructural laser diodes. These diodes have a gain profile that varies depending on the semiconductor material used. The table below displays the gain profiles for the most commonly used material combinations. High-power diode lasers generally have wider wavelength bands than CO₂ and Nd: YAG lasers [103].

Table 2.3: Commonly used semiconductor materials and their central wavelengths [103].

Materials	Central Wavelengths (nm)
AlGaAs	720-880
InGaAs	940-990
AlGaInP	630-690
GaN/InGaN, GaN/AlGaIn	0.3-0.5
GaAs/GaAlAs	0.52-0.98
InP/InGaAsP	0.9-1.65

The diode offers wavelength ranges of 375–3500 nm, offering a notable advantage over CO₂ or Nd: YAG lasers in that many metallic materials commonly used in industry (such as Al, Cu, Ag and Au) have a higher absorption coefficient in this wavelength spectrum. They are commonly powered by a continuous current source with low voltage, making them electrically efficient as laser sources. HPDL have an electrical to optical conversion efficiency of 20-30%, with a maximum of 65%, exceeding other high-power lasers such as CO₂ lasers (10-15%), Nd: YAG lasers (lamp pump: 1-3% /diode pump: 10-20%), and Yb-fibre laser (30%). Table 2.4 summarises the technical characteristics of laser sources used in

PBF [19]. In comparison to alternative laser sources, diode lasers stand out as the superior choice owing to their remarkable electrical efficiency, compact size of millimetres, long lifetime, low operating costs, and wide range of wavelengths employed in the laser processing industries [102]. The advantages of diode lasers have encouraged their widespread adoption in material processing applications, including soldering, cutting, surface treatments, and welding. However, diode lasers face two main challenges: limitations on output power and poor beam quality. These limitations obstruct the widespread adoption of diode lasers in PBF manufacturing processes [103].

Table 2.4: Summarizing laser types and specifications used in different PBF systems [19]:

Laser	CO ₂ laser	Nd: YAG laser	Yb-fibre laser	Diode laser
AM Applications	SLA, SLM, SLS, LENS	SLM, SLS, LENS	SLM, SLS, LENS	SLM
Operation wavelength	10.6 μm	1.06 μm	1.07 μm	375 nm to 3500 nm
Efficiency	15 %	Lamp pump: 1-3 % Diode pump: 20-30 %	30 %	65%
Laser power	Up to 25 kW	Up to 16 kW	Up to 8 kW	Average power 50 W
Pump source	Direct electrical source	Flashlamp or laser diode	Laser diode	Direct electrical source
Operation mode	CW & Pulse	CW & Pulse	CW & Pulse	CW & Pulse
Beam quality factor (mm·mrad)	3 to 5	0.4 to 20	0.3 to 17	10 to 60
Fibre delivery	Not possible	Possible	Possible	Possible (105 μm to 400 μm)
Maintenance periods	2000 hrs	200hrs (lamp life) 10,000 hrs (diode life)	(25,000 hrs)	Maintenance free (1000000 hrs)
Industrial Applications	Cutting, welding, surface treatments, material processing (AM-polymers-Ceramics)	Metal marking, drilling, welding (robotics), Materials processing (AM-Metallics)	Cutting, welding, (AM-Metallics)	Medical, soldering, marking, Micro-soldering, heat treatment, pump source.
Disadvantages	Beam cannot deliver using Fibre. Not suitable for metallic application. not compactness (need more space). Requires constant maintenance	Poor beam quality Not suitable for non- metallic application.	High cost to operate and install	Low average power Poor beam quality Poor coherent

2.5.4.1 Multi-Emitter Diode Lasers: Power Enhancement and Limitations

Typically, the output power of a single laser diode generates a few watts (max 5 W). Additional carriers and photons are required to increase the power of single-laser. Achieving this involves increasing the volume of the active layer. However, it is important to maintain a high carrier density within the active layer to ensure high lasing efficiency. Therefore, increasing the thickness of the active layer is not a feasible option. Instead, the most straightforward approach to increasing laser power is to increase the width of the active layer. Laser diodes usually do not exceed a power of a few milliwatts because they have active layer widths ranging from tens to hundreds of microns, as illustrated in Figure 2.31. Alternatively, to increase the output power to around 100 W, multi-emitters are combined on the top of a substrate as a single bar [103].

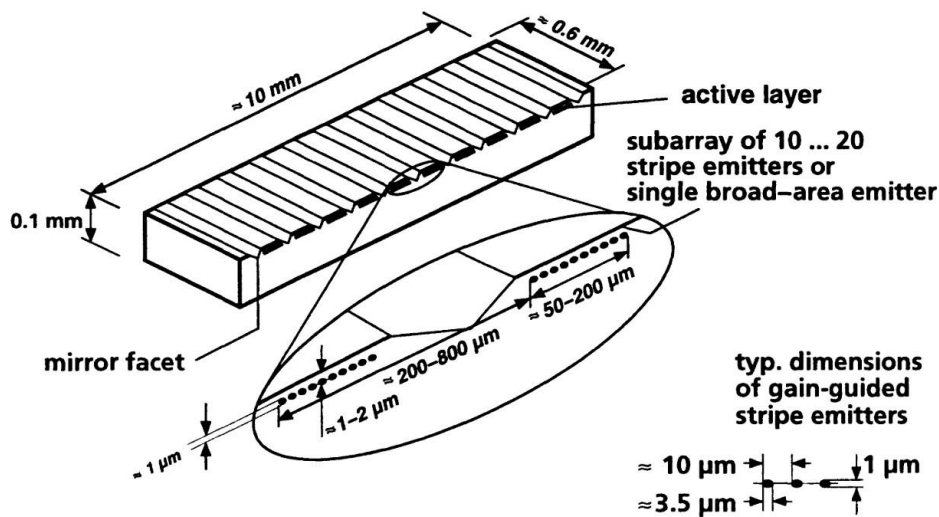


Figure 2.31: Typical single bar of multiple emitters of high-power diode laser [104].

As shown in Figure 2.31, a diode bar linear array typically consists of 20-50 subarrays, with each subarray containing 10-20 individual emitters. Another possible configuration is a linear setup of 20-50 broad-area active layer emitters with widths varying between 50-200 μm [104]. Several HPDL modules can be stacked horizontally or vertically to increase the output power to Kilowatts, as shown in Figure 2.32. Therefore, high-power diode laser (HPDL) stacks have no limit to the maximum power, which has been reported to be a 4 kW continuous laser as direct output or a 2.5 kW fibre-coupled diode laser [105].

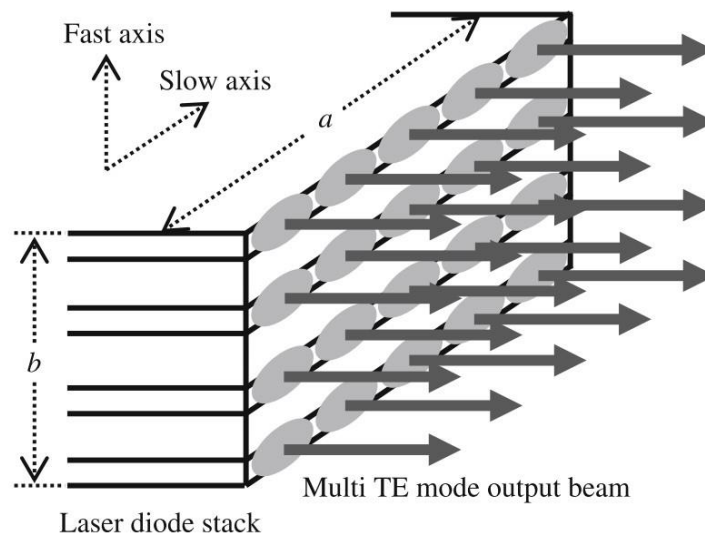


Figure 2.32 Multi-mode diode lasers stack [103]

Vidal et al. [106] demonstrated a welding system that utilised a one-dimensional diode laser consisting of 19 emitters ($W_{\text{emitter}}=150 \mu\text{m}$; $D_{\text{pitch}}=500 \mu\text{m}$; 2.5 watts), radiating a total power of 60 W [106]. The diode laser module was integrated into a welding machine with a horizontal x-y table and a vertical carriage mechanism to position the laser head. A similar approach has been demonstrated by Zavala et al. for BPF processing. Zavala et al. [24] used an 808 nm single diode module (19 emitters/ 2.5 W) to create a single stripe processing area of 4.75 mm x 0.25 mm with a total power of 50 W. Nonetheless, these studies do not demonstrate the ability to focus the laser beam to a spot size equivalent to those in SLM systems or control each laser spot independently; due to the high divergence of diode lasers, the beam quality can be poor, which limits the potential to print small features, such as micron-scale lattice-like structures, compared to SLM laser systems.

2.5.4.2 Different Approaches for Improving Beam Quality: Free Distance Optics vs Fiber Optics Delivery.

When the beam travels away a few microns from the emitter, the size of every single mode diverges until it combines and creates a multi-mode beam. As the beams travel farther away (distance $< 100 \mu\text{m}$) from the diode bar, the laser beams diverge significantly, resulting in an incoherent rectangular beam profile and a 70% loss of power [103]. The beam profile distribution of five emitters at three different locations (Near-field, Mid-field, and Far-field) is shown in Figure 2.33. It can be observed that each emitter radiates a single-mode beam, exhibiting coherent propagation and uniform power intensity distribution at the diode laser output. However, as the beams travel away, the size of each mode expands, and they merge (Figure 2.33 b). Eventually, the intensity distributions of the five single modes combine to create a multi-mode single laser beam (Figure

2.33 c). Due to this, the diode laser has poor beam quality, causing the beam to diverge significantly after exiting the laser module. This limits its direct use in material applications, including PBF technologies.

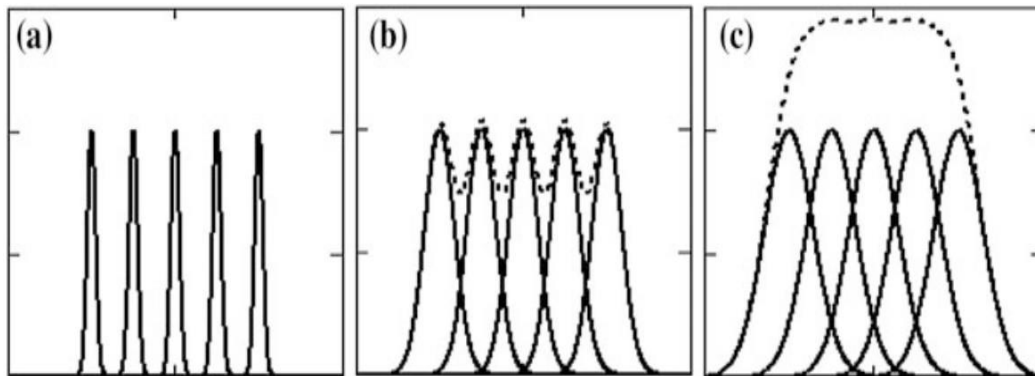


Figure 2.33: laser profile(a) near-field, (b) mid-field, (c) far-field [103].

Increasing the power density and improving the beam quality can be done using two different optical methods: free distance optics (microlenses array) or fibre optics delivery, as shown in Figure 2.34.

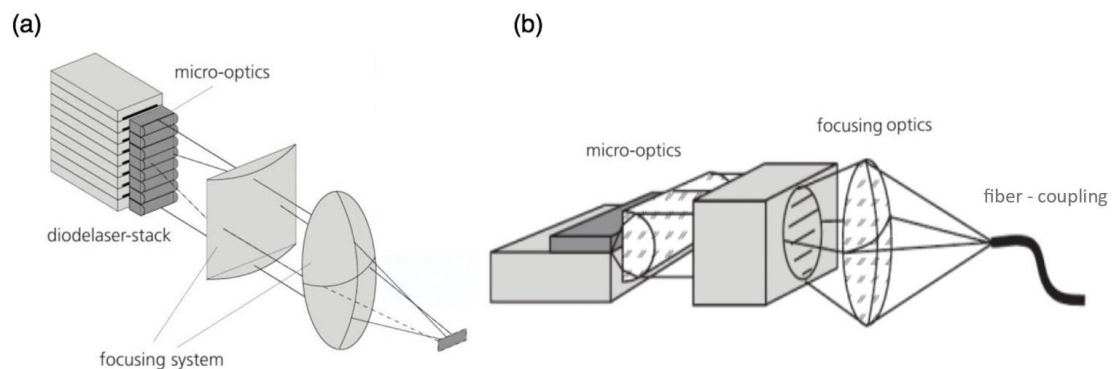


Figure 2.34: Different approaches for collection and focusing Diode lasers (a) free distance optics (microlenses array) and (b) fibre optics delivery [107].

Commercial diode lasers (DLs) employed in material processing typically have a beam quality factor (M^2) ranging between 10 and 60 [19]. The emitted laser beam is generated when a part of the laser field passes through one facet of the active layer. Even though the active layer is rectangular, some of the laser radiation will escape due to limited confinement, leading to an elliptical-shaped beam instead of a circular shape compared to other laser sources.

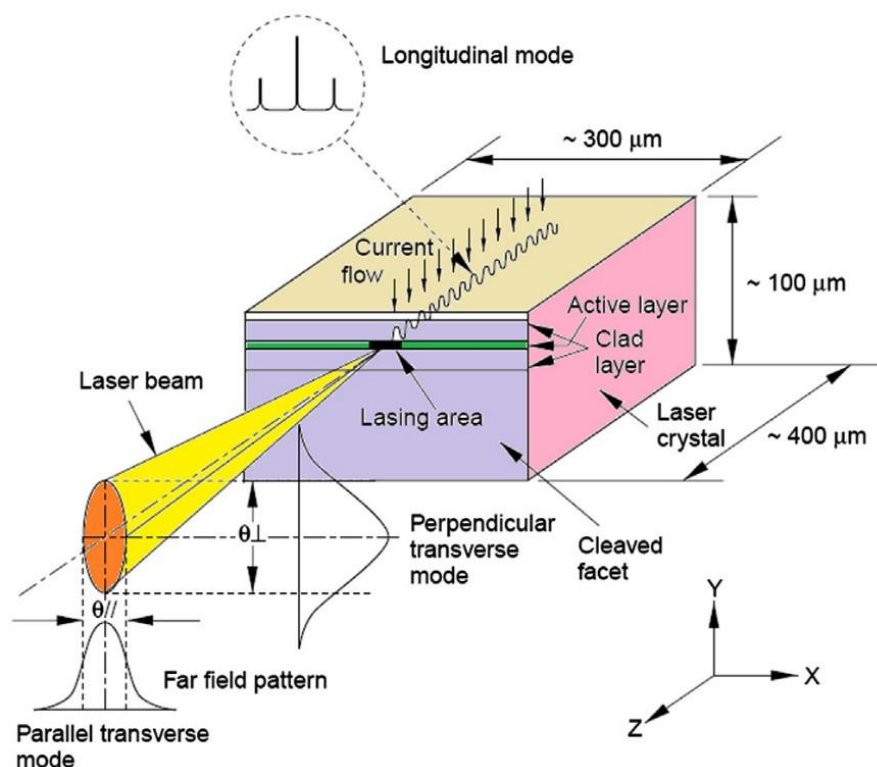


Figure 2.35: Illustration of the beam characteristics from a single emitter in two directions: the fast axis ($\Theta_{\perp\text{FWHM}}$), and the slow axis ($\Theta_{\parallel\text{FWHM}}$). The fast axis is perpendicular to the active layer, while the slow axis runs parallel to the active layer [102].

Figure 2.35 showcases how the output beam of a single emitter is split into two directions: the fast axis and the slow axis. The fast axis, or perpendicular transverse mode ($\Theta_{\perp\text{FWHM}}$), is perpendicular to the active layer. On the other hand, the slow axis, or parallel transverse mode ($\Theta_{\parallel\text{FWHM}}$), runs parallel to the active layer and displays 2.5 - 6 times less divergence than the fast axis [103]. The beam size at the emitter is roughly $1\ \mu\text{m}$ on the fast axis and several microns on the slow axis. The full-width half magnitude (FWHM) divergent angle typically measures around 15° to 40° and 6° to 12° in the fast and slow axis directions, respectively. In terms of $1/e^2$ intensity divergence, these values are approximately 26° to 68° and 10° to 20° for the fast and slow axis directions, respectively [103].

Due to the high M^2 factor, utilising a microlens array with a short focal length, which restricts the distance between the lens and the processing area, is important. Achieving high beam quality and maximum laser irradiance depends mainly on the optical performance of the fast-axis collimator (cylindrical microlenses). Collimation optics convert a divergent beam $\Theta_{\perp} \times \Theta_{\parallel}$ into a collimated beam while maintaining its Gaussian intensity distribution and elliptical beam profile with collimated diameters.

The M^2 factor for beam quality is inconsistent between the two transverse modes. In order to collimate a highly divergent diode laser beam, a cylindrical fast axis collimator (FAC) and slow axis (SAC) microlens are required, as shown in Figure 2.36 (a). Attaching the fast axis first is imperative due to its higher divergence. Figure 2.36 (b) shows the geometry of a typical FAC micro-lens, where the Plano-concave lens has an aspherical contour that is precisely proportioned to the diode bar. P1 and P2 represent the thick lens's paraxial principal planes. The paraxial focal length is represented by f , while d represents the beam waist, shows radial beam divergence of the fast axis is given, and r represents the radius of curvature of the paraxial sphere. The ideal collimation would indicate that $\alpha = 0$ for a non-extended source. The first principal plane is situated at a distance of t/n from the laser emitter, where t represents the centre thickness of the lens, and n is the refractive index. As a result of the plane entrance surface, the second principal plane is located at the lens exit. However, the minimum divergence of a collimated beam is limited by diffraction. Therefore, the Gaussian beam divergence ϑ_{\perp} and waist d are affected [104]. The slow axis divergence can be reduced by employing a slow axis collimator (SAC), which is a monolithic array of cylindrical micro-lenses, Figure 2.36 (a). The collimated beam diameter, given at the intensity of 13.5% ($1/e^2$), is determined by the focal length (f) of the collimating lens and the divergence of the laser diode.

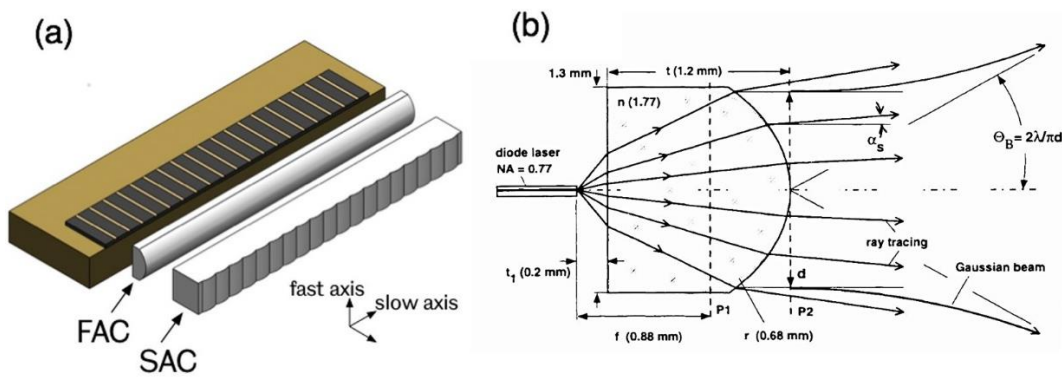


Figure 2.36: (a) Microlens array (FAC) and (SAC) [24], (b) The dimensions of a typical FAC aspherical cylindrical micro-lens [104].

For diode lasers where the M^2 value is large, reducing the lens's focal length is necessary to achieve a smaller spot diameter and higher energy density. The diameter of the collimated beams for both transverse modes $\varnothing_{\perp} \times \varnothing_{\parallel}$ can be calculated using Equation 2.2 for FAC and Equation 2.3 for SAC, where f is the focal length of the collimation lens.

$$\varnothing_{\perp} = 2f \sin\left(\frac{1}{2} \theta_{\perp \text{FWHM}} 1.7\right) \quad (2.2)$$

$$\varnothing_{\parallel} = 2f \sin\left(\frac{1}{2} \theta_{\parallel \text{FWHM}} 1.7\right) \quad (2.3)$$

A collimated beam is characterized by parallel light waves with minimal divergence, resulting in limited divergence as they propagate over a distance. The beam diameter and radiation wavelength influence the divergence of the collimated beam. Therefore, the divergence of diffraction-limited Gaussian beams is equal to twice the beam's half-angle divergence, which is represented by $\theta=2\vartheta$. Equation 2.4 can calculate the total divergences of the fast and slow transverse modes, whereas Equation 2.5 can determine the focused spot diameters of the elliptical beam produced [103].

$$\vartheta_{\perp,\parallel} = \frac{\lambda}{\pi \phi_{\perp,\parallel}} \quad (2.4)$$

$$d_{\perp,\parallel} = \frac{4M^2\lambda f}{\pi\phi_{\perp,\parallel}} \quad (2.5)$$

Following the collimation of the fast and slow axis, the resulting beams with diameters of $\phi_{\perp, \parallel}$ and total beam divergences $\vartheta_{\perp, \parallel}$ (radial beam divergence $\vartheta=\theta/2$) must be focused by two cylindrical Plano-convex lenses. These lenses, corresponding to each transverse mode, are necessary to create high-intensity focused beams. Due to astigmatism and the divergences of the fast and slow axis, the lenses are employed to focus both modes at different focal lengths (f), as seen in Figure 2.37. The focal length of the lens and the beam quality factor, M^2 , play crucial roles in determining the diameter of the focused beam, d . A smaller d results from lower values of M^2 and shorter focal lengths, which leads to high beam intensity.

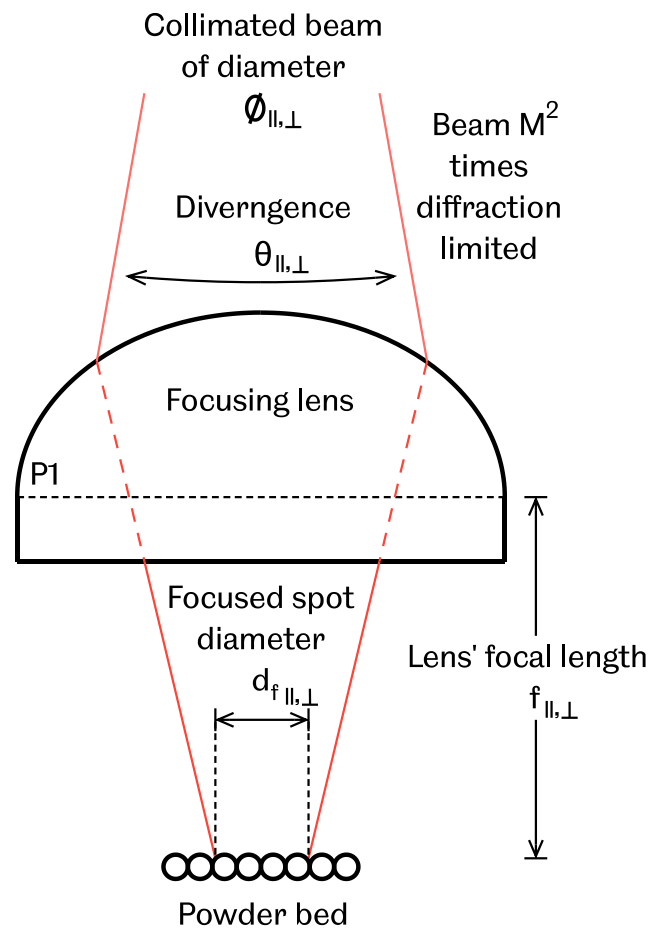


Figure 2.37 Lens setup for focusing the fast and slow beam modes [24].

Zavala et al. [24] developed a diode laser system utilizing bulk optics for (PBF) process. Their study employed a diode module that operates at a 50 W power output with a laser wavelength of 808 nm. The module comprises 19 emitters, each spanning a width of 135 μm pitch distance of 500 μm . The lasers show high divergence in the fast-axis direction (FWHM of 27°) and the slow-axis (FWHM of 7°), creating an elliptical beam with significant asymmetry. To manage this, the authors incorporated a Fast-Axis Collimating (FAC) and a Slow-Axis Collimating (SAC) micro-lens, as shown in Figure 2.38. Using short focal length micro-lenses during the collimation process, they achieved 2.73° and 0.097° divergences for the fast and slow axes, respectively. The focal lengths for focusing were 50 mm and 25 mm, resulting in 1 mm and 0.5 mm beam diameters. The focused spot diameters for both axes were 0.25 mm, enabling a processing area of 4.75 mm x 0.25 mm and generating a total power of 47.5 W.

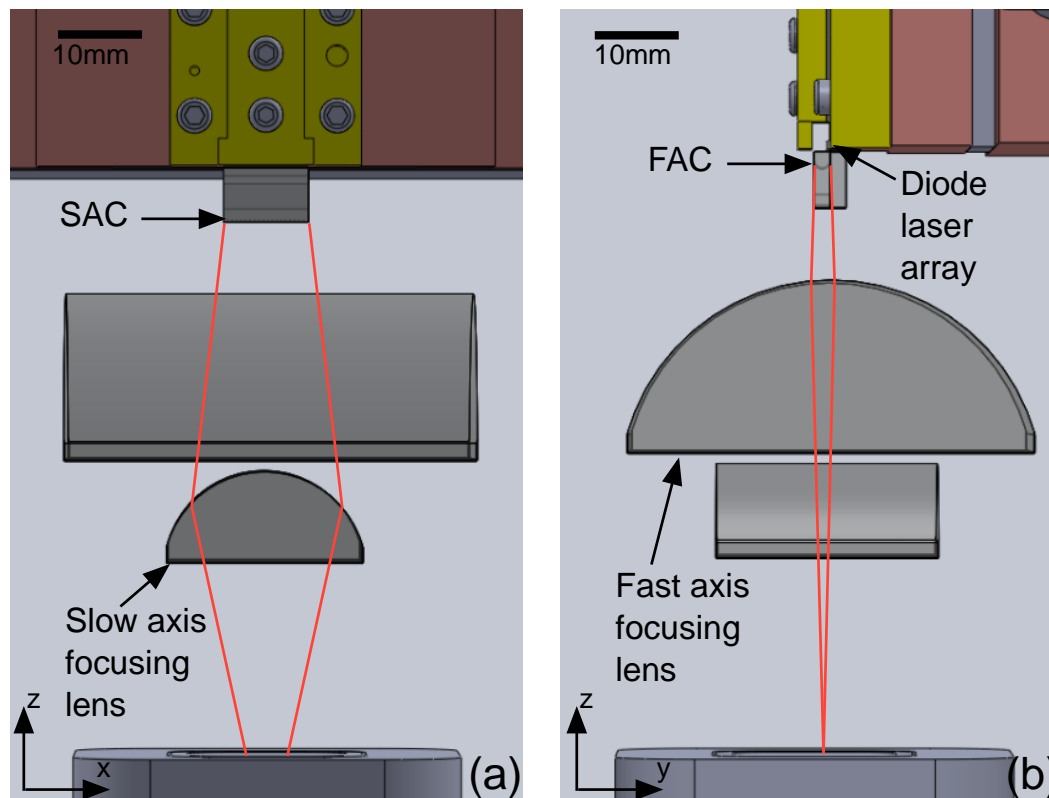


Figure 2.38: Illustration of the optical system used by Zavala et al. to correct the 19 emitters of a high-power diode laser bar and the general beam path[24].

DAM presented the ability to produce a dense single layer of steel 316L at a scanning speed of 1 mm/s. However, the PBF process generates a high-temperature inside the chamber (70°C to 200°C) to reduce the thermal stress in the fabricated parts, which is considered one of the challenges of operating the diode laser using free distance optics. The short focal distance in DAM increases the potential of damaging the optics and increases the operation costs due to the need for a highly efficient cooling system to avoid wavelength shifting. Additionally, the standard spacing of commercial diode modules is an important factor limiting the focus mechanism by using the bulk optics approach. As Zavala et al. reported, the free distance optics have a limited working distance, non-uniform Gaussian profile, and lack of individual control over every emitter [27].

Figure 2.39 shows the structural layout of the fiber-coupled multimode diode laser. Fiber-coupled modules with multiple emitters generally consist of multiple individual emitters, an optical system, and a pigtail. These focusing lenses facilitate efficient light capture and guidance through the optical fiber, ensuring the accurate delivery of laser energy to the powder bed. The diode laser output is directed into the glass tube (fiber) by utilising fibre optic delivery, allowing for remote positioning over long distances and typically resulting in a circular spot just a few millimetres in size.

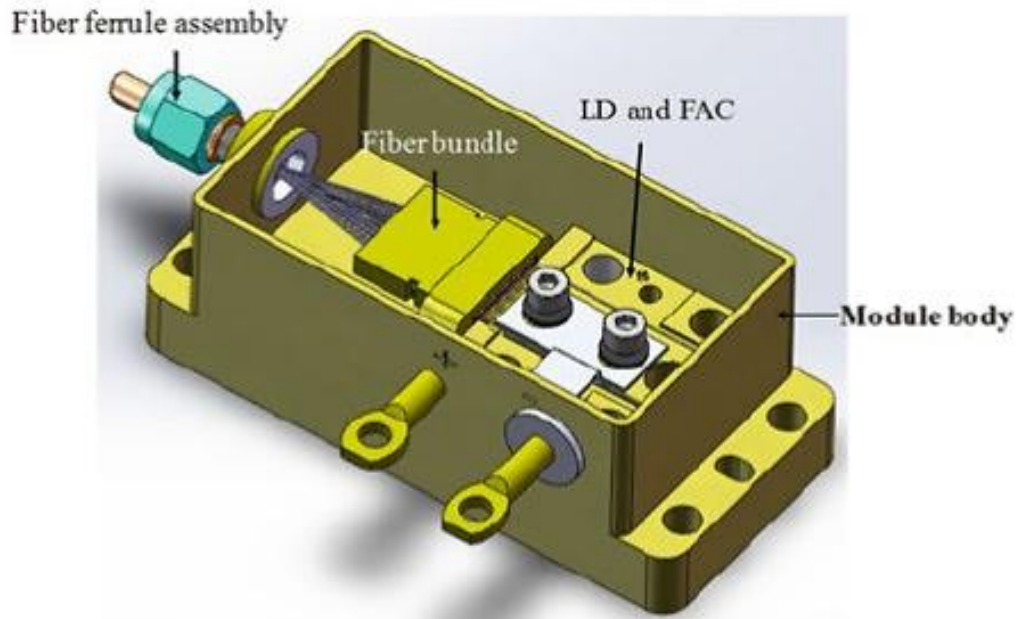


Figure 2.39 Typical construction of a fiber-coupled diode laser, which consists of diode bar lasers, FAC microlenses, a fiber bundle, and a fiber ferrule assembly [108].

The main role of the optical system is to improve the beam quality and support the coupling of laser beams into an optical fiber. The fiber coupling process involves fast-axis and slow-axis collimation lenses to minimize divergence and focus the multimode beam (n) into a spot smaller than the fiber core (n_1), as shown in Figure 2.40.

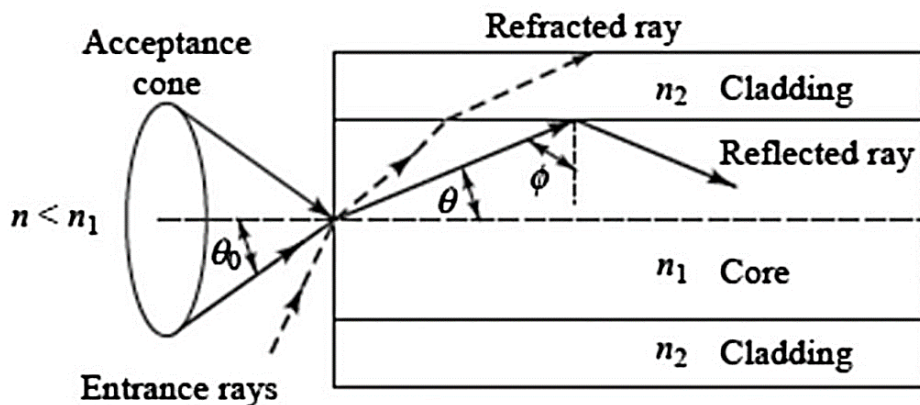


Figure 2.40: Illustration of Laser Beam Propagation within an Optical Fiber [109].

A key aspect of this process is the Numerical Aperture (NA) [109], which indicates the light-gathering capacity of a lens or optical fiber. The NA is calculated as the product of the refractive index of the medium in which the light travels (n ,

approximately 1 for air) and the sine of the half-angle (θ) of the maximum light cone that can enter fiber, as shown by Equation 2.6.

$$NA = n \sin(\theta) \quad (2.6)$$

A larger NA corresponds to a wider light cone, implying that the optical fiber system can accept or emit more laser modes. This, however, is not without challenges. For instance, an optical fiber with a high NA can guide more light into the fiber, but it might also lead to a higher mode volume, causing increased modal dispersion in multimode fibers. When applied to the Powder Bed Fusion (PBF) process that utilizes a diode laser, the NA can impact the focusing of the beam in several ways. A large NA value (as high as 0.6) can lead to high beam divergence at the fiber's exits, which affects the focusability of the beam and, therefore, the precision of the PBF process. In addition, it impacts the working distance, defined as the space between the focusing lens and the focal spot. Typically, a larger NA equates to a shorter working distance, which could influence the design and operation of the PBF setup. As suggested by Karp et al. [110], it is optimal to have a lower Numerical Aperture (NA), typically around 0.1 to 0.22, as this range is an efficient coupling of the laser light into the fiber, ensuring a more precise and effective PBF process. Furthermore, accept sufficient laser power, a critical aspect for the successful execution of the PBF process. Using an optical set at the end of the fibre helps to increase the power density and ensure precise processing over the powder bed processing area.

The beam quality of fibre coupled diode laser is typically characterised by the beam parameter product (BPP) [20], which is defined as the results of the beam radius and the beam divergence half-angle, calculated at the beam waist and in the far field, respectively, and is expressed in millimetres times milliradians (mm·mrad), as shown in Equation 2.7 [111].

$$BPP = w_0 \theta = \frac{\lambda}{\pi} = \text{constant} \quad (2.7)$$

BPP significantly correlates with power density and impacts manufacturing resolution, as low BPP is equivalent to higher intensity and perfect Gaussian distribution. Wavelength determines the minimum BPP limit, as shown in Equation 2.7 [111], representing the diffraction limit dictated by the operating wavelength. For example, the minimum value of the BPP for the CO₂ laser (wavelength 10.6 μm) is 3.3 mm·mrad, and for Nd: YAG laser (wavelength 1.064 μm) is 0.3 mm·mrad, which means the laser with shorter wavelengths will result in higher focusability, thus, higher intensity, as shown in Figure 2.41.

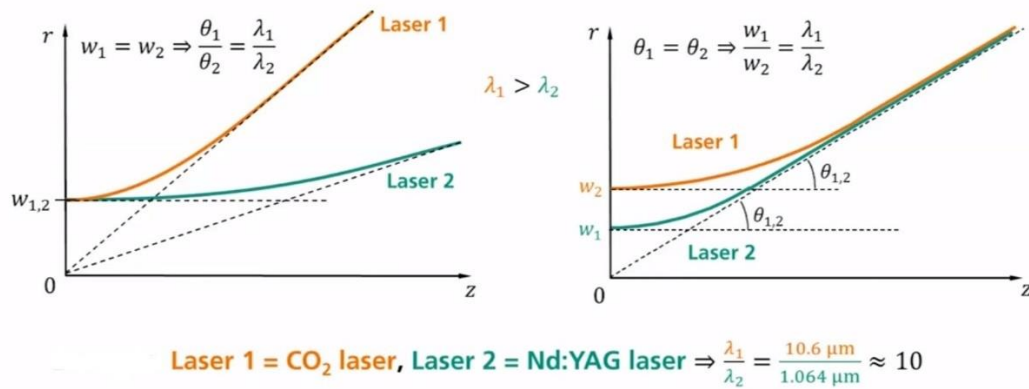


Figure 2.41 Beam characterisation for different lasers: (a) at same beam waist (b) at same beam angle.

Power distribution is an important factor that demonstrates the beam's quality and ensures the delivery of a uniform distribution of power over the powder bed. By the Transversal Electromagnetic modes (TEM) of the cavity, the intensity distribution of the laser is specified as shown in Figure 2.42 [111]. The Gaussian distribution is the most popular laser intensity distribution model used to define the laser intensity throughout the laser beam with symmetrical distribution [19].

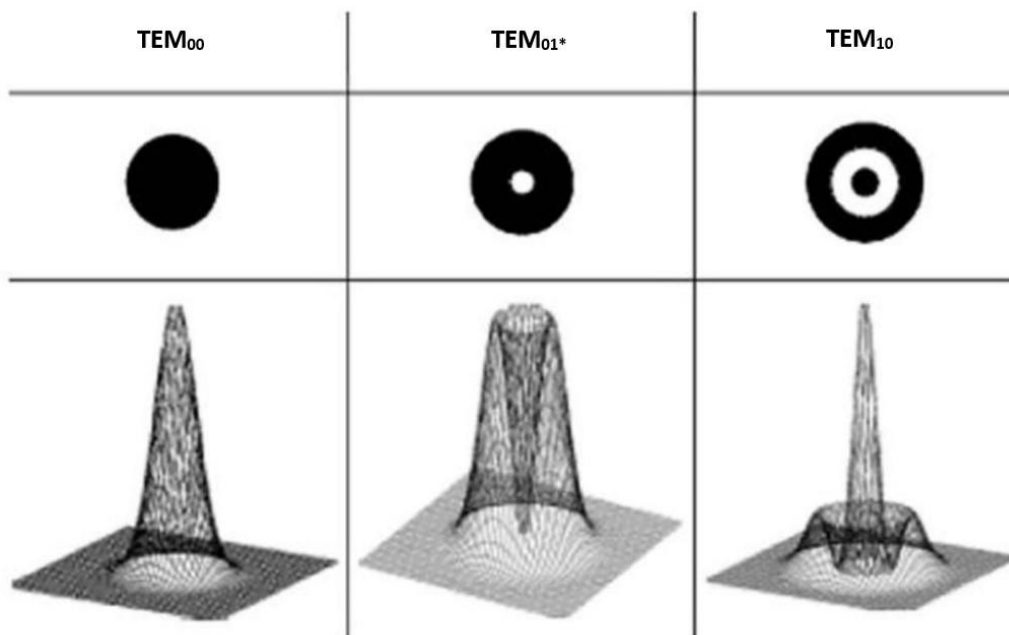


Figure 2.42: Illustrates different transverse electromagnetic modes (TEM) [111].

Beam quality can be characterised independently of laser wavelength via the M^2 factor, which is the BPP divided by λ / π and has a value of 1 for a perfect Gaussian laser beam [111]. Equation 2.8 gives the dimensions of the minimum diameter of the waist for a Gaussian beam, which illustrates that energy density can be

improved using a short focal length of the focusing lens or by increasing the diameter of the original beam.

$$W_0 = \frac{4M^2\lambda f}{\pi D_{in}} \quad (2.8)$$

2.5.4.3 Multimode print-head optical fibers as a potential solution

Although there is a preference for fibre-coupled diode lasers over high-power diode lasers, the former still lacks the necessary power for PBF processes. To address this issue, it is possible to leverage the flexibility of fibres by combining multiple fibres in a 1D or 2D array configuration within a laser head, as shown in Figure 2.43.

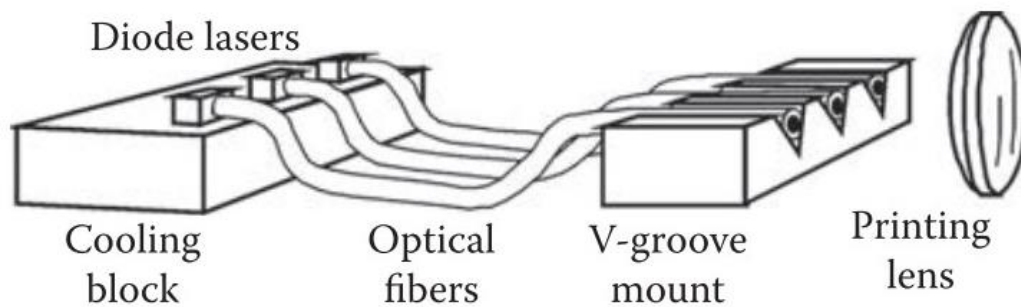


Figure 2.43: Illustration of 1D Array Configuration of Multi Fibre-Coupled Diode Lasers in a Laser Head [107].

Creating multimode print-head optical fibers involves gluing a multi-fibre coupled diode into a V-grooves substrate with specific spacing between centres in 1D or 2D, as shown in Figure 2.44. A printing lens is then attached to the end of the v-groove array, providing focused multi-laser spots at a particular focal length determined by the printing lenses used. This ensures a high and precise output by imaging the array of fibers over the processing area.

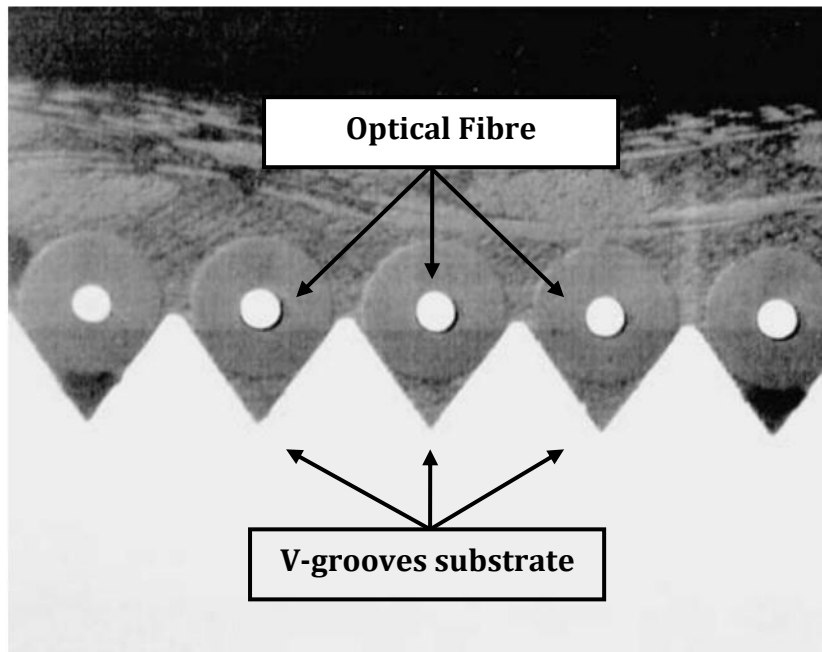


Figure 2.44: Front view of multi-fibre-coupled diode lasers attached to a V-groove substrate [107].

The application of addressed arrays of multi-laser sources was primarily confined to the printing industry, as these processes did not require a high energy output. This focused use stemmed from the fact that the intensity of energy required for printing applications is typically lower compared to other industries. The lack of necessity for extreme energy input made the utilization of these light source arrays particularly suitable for print media.

The KODAK APPROVAL Digital Colour Proofing System, developed by Eastman Kodak Company, features a unique print head that utilizes laser emitters directly onto the media. The print head is equipped with replaceable laser diodes, compactly arranged in contiguous V-grooves, each attached to single-mode optical fibers with a 5 μm core enabling high-precision image printing. The images are projected onto the media through a print lens, forming a series of print spots. The image quality is further improved by reducing the optical fibers' core diameter from 125 μm to 18 μm [107].

Despite its advanced technology, the optical setup faces some challenges. The poor connection point between fiber lasers and fiber laser head reduces beam efficiency to approximately 10% and causes irregularities in power output at each fiber end. The system is also sensitive to fiber noise from fiber movements during print-head movements, inconsistencies between fibers, crimps, and sharp bends, potentially dispersing energy into higher-order modes. Laser mode hopping, a type of lasing instability, may also cause similar disruptions.

To enhance coupling reliability and to reduce power loss, the core size of the fibre-coupled diode laser must be smaller than the fibre of the print head or similar, with zero gaps between the connection. Furthermore, to reduce fiber noise, it is recommended to use higher-order modes with high NA fiber optics. The large fiber NA (0.24) enables sustained light in these modes without automatic attenuation. In addition, optical lenses with high NA (0.48) can also be utilized to eliminate unstable higher-order modes, allowing for most of the higher-order-mode light and power to reach their intended destination.

The first use of this technology in PBF is presented by Karp et al. [110]. This paper present multiple edge-emitting lasers focused into a large core multimode fiber array. The system utilizes 16 fibre channels in a laser head with a total power of 690 W (60 W/diode laser) at 976 nm. The fibre's numerical aperture (NA) is 0.22, and the system uses a v-groove block to arrange the fibers in a linear pattern, as shown in Figure 2.45. The relay lens system is designed for a 0.15 NA direct diode laser and provides a close-packed, wide field of view. The downside of this work is that the power limitations at each spot and laser divergence limited linear print speeds to a few millimetres per second, and the technique has yet to realize build speed benefits.

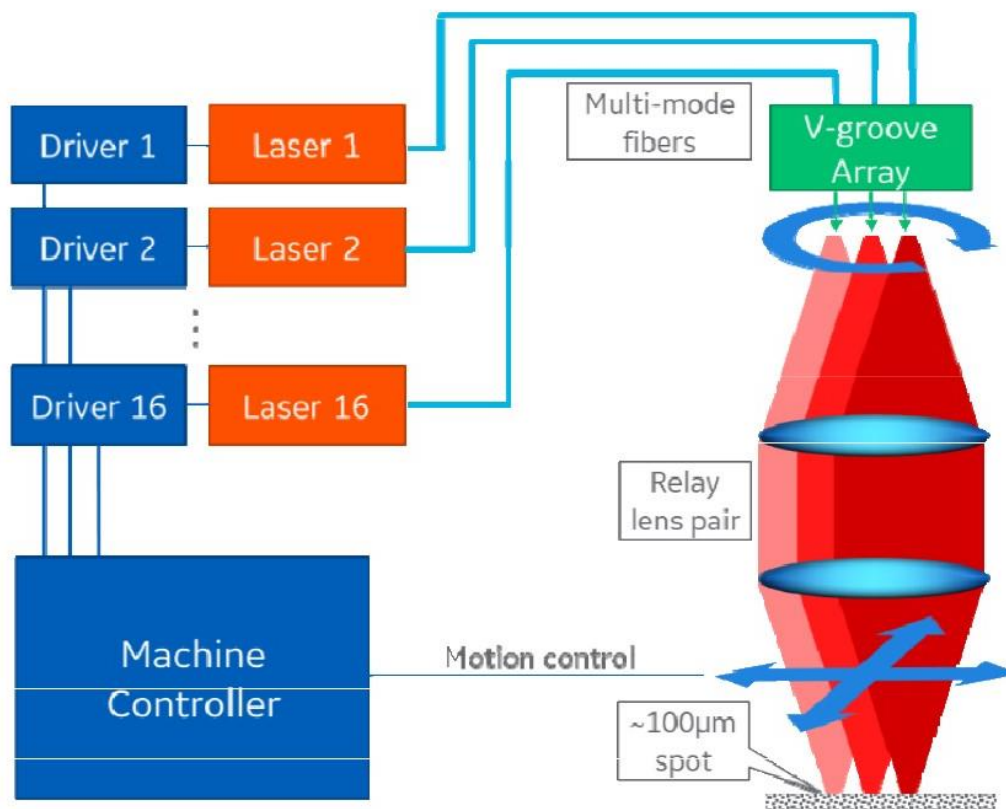


Figure 2.45 Schematic of multiple edge-emitting lasers coupled into V-groove fibers Array, developed by Karp et al. [110].

The study does not provide a comprehensive view of the beam profile of the optical system. The beam profile is crucial in understanding the interaction between the laser and the material being processed. Detailed beam profile characterisation is necessary to evaluate the system's performance and potential limitations. Furthermore, the work lacks in-depth information about the impact of using a multi-laser array head on the microstructure of the final parts. Understanding how the laser system affects the microstructure is vital for assessing the quality of the final product and determining whether the process can be optimised for better results. The work showed the use of this technology with low melting temperature material. While this may simplify the process, it raises questions about the technique's applicability to materials with higher melting points, a factor crucial in many real-world applications.

Moreover, a 980 nm wavelength laser presents absorption limitations, restricting the process's efficiency. To enhance the system's performance, a shift to a shorter wavelength, such as 808 nm or 450 nm, could significantly improve absorption, contributing to better process efficiency. Overall, while the study provides valuable insights, there is still room for improvement and further investigation in the field.

2.5.5 The State-of-the-Art use of Diode Lasers in traditional LPBF

High-power diode lasers (HPDL) are being explored as alternative laser sources for use within LPBF; they are more compact and energy-efficient than fibre lasers and have longer lifetimes [20]. The ability of HPDL to emit short wavelengths (450 nm- 3300 nm) with up to 60% wall-plug efficiency has promoted their use within material processing applications such as soldering, cutting, surface treatments, and welding [20]. Matthews et al. used addressable single-diode lasers as heat sources in an attempt to increase LPBF productivity. The researchers applied a diode-based additive manufacturing (DiAM) method to four 1.25 kW stacked diode arrays (comprising 60 individual laser bars) to provide a total of 5 kW optical power at a wavelength of 1007 nm [21]. The incoherent output beam was homogenized by a liquid crystal light valve along with a Q-switched Nd: YAG Laser Beam as a hybrid laser with a wavelength of 1064 nm. This was used to melt an area of 2-3 mm for each layer in a single exposure. However, the complexity of the optical system and the short laser pulse through the photomask restricted the processing field to $2 \times 2 \text{ mm}^2$.

Furthermore, the long wavelength of the lasers used in DiAM and the available output power of 20 J/cm^2 incident on the powder bed limited the process to low melting temperature metals (Sn powder). Studies of part density and processing efficiency have not yet been reported. Another multi-spot LPBF system has been developed by Fraunhofer ILT that does not require galvo-mirrors to direct the irradiated laser energy onto a powder bed. Instead, it uses a fixed array of multiple laser spots moving on a gantry system [22]. These multiple high power laser spots create a controllable intensity distribution to create 3D structures with high flexibility in terms of productivity and building space. However, to generate high-power multi-laser spots with a wavelength of 976 nm capable of melting the powdered feedstock, several laser diode modules need to be incorporated to form a single spot of 200 W [23]. A multi-diode laser approach named Diode Area Melting (DAM) was introduced by investigators at The University of Sheffield [24], designed to use low laser powers with more efficient absorption profiles for LPBF. An 808nm single diode module comprising 19 emitters was focused using cylindrical micro-lenses and used to cover a processing area $4.75 \text{ mm} \times 0.25 \text{ mm}$ as a linear stripe. Each emitter contributed an output power of 2.5 W, which supplied a total of 50 W (power density of $4.21 \times 10^3 \text{ W/cm}^2$), and a 99% dense component of 316L stainless steel powder was fabricated. This work was able to initially prove that utilisation of wavelength optimised lasers could efficiently melt powders with temperatures exceeding 1300°C using less than 2.6 W laser power per emitter and reduction in overall component residual stress [24-27]. However, high laser power is still being used, ranging from 200 W to 5 kW. In addition, the poor beam quality of the HPDL used limited the ability to generate a spot size comparable to the SLM systems ($60 \mu\text{m}$), limiting the processing

efficiency and scalability. Fibre-coupled diode lasers offer several advantages over HPDLs (i.e., beam quality, flexibility, lifetime, performance, and scalability). Using optical fibre to deliver the beam will improve the beam quality by delivering a uniform beam and consistent output. In addition, the optical fibre provides more freedom to the laser module by separating the laser module from the processing area, which enhances the cooling capability of the laser module, leading to better efficiency, longer lifetimes, and increased system reliability, which has been reported to be the most prominent challenge to adopt diode laser in PBF. Furthermore, the fibre-coupled diode laser allows combining multiple diode modules to increase power output, making it more convenient to scale up the processing area without significantly increasing size or complexity.

2.6 Process Parameters Associated with Energy Input

2.6.1 Laser power

Laser power is the primary energy source responsible for fusing the powder particles in powder bed fusion systems. In SLM, the processing parameters (such as scanning speed, layer thickness, and hatch spacing) are adjusted according to the laser power and beam characteristics. For instance, using a high-power laser increases the prospect process speed rate, which is limited when using a low-power laser [112]. The spot size controls the hatch spacing, which is suggested to be 70% of the spot size, to ensure overlapping between the scanned tracks [82]. In addition, the layer thickness is adjusted based on the laser intensity and its ability to penetrate through the material [112]. The intensity must exceed the energy threshold to reach a targeted material's required melting temperature. For materials with high reflectivity or high thermal conductivity, such as silver and aluminium, the intensity must be higher than the threshold to overcome the slow temperature gradient during the process.

Furthermore, increasing the laser power (intensity) influences the productivity and the relative density of the built parts in SLM [113]. However, it needs to be taken into consideration that increasing the build rate has limitations (laser power, scanning speed, and material properties), and exceeding these limitations to increase the build rate may cause undesirable properties (such as porosity, keyhole) in printed parts. Figure 2.46 depicts how the Selective Laser Melting (SLM) process is affected by laser power [114]. It shows that increasing the laser power from 100 W to 500 W raises the maximum temperature of the powder bed, resulting in changes in the tracks formed. When the laser power increased over 200 W, the Volumetric Energy Density (VED) goes beyond the typical threshold of 100 J/mm^3 , causing changes in the morphology of the tracks leads to defects in the final parts. This leads to a change from uniform continuous to irregular tracks, resulting in a phenomenon known as "balling".

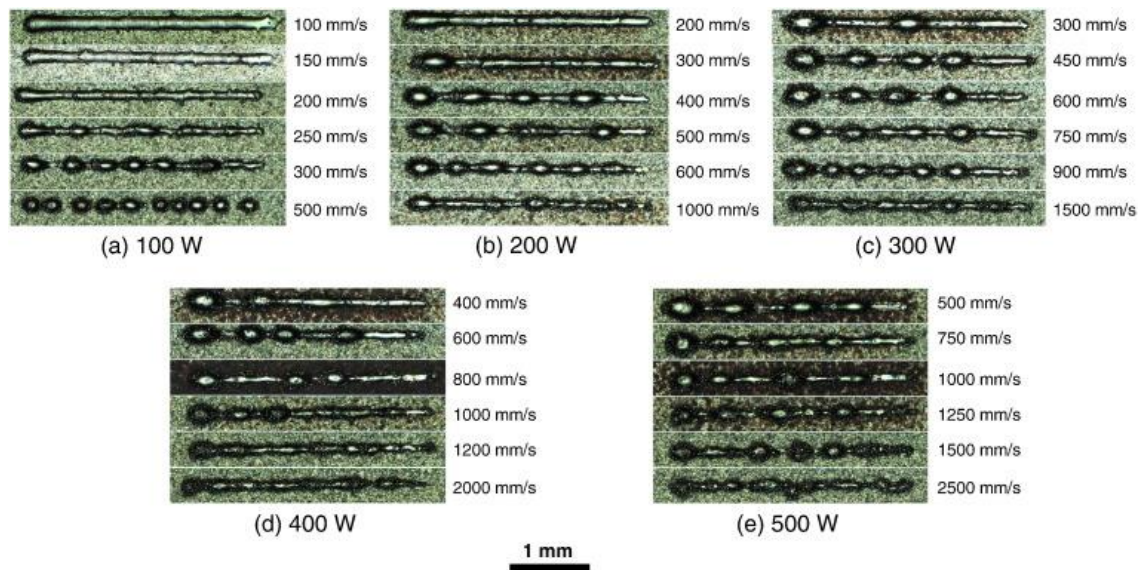


Figure 2.46: Demonstrate the effect of increasing the laser power under constant scanning speed within the range of (400 mm/s to 2000 mm/s) on the morphology of forming single tracks at different laser powers: (a) 100 W, (b) 200 W, (c) 300 W, (d) 400 W, and (e) 500 W, in order to investigate the limitations of using VED (Volumetric Energy Density) [114].

Therefore, the laser power should be carefully determined to reach the maximum build rate and, at the same time, the required part quality. Increasing the intensity is proportional to the laser power and spot size, (reducing the spot size will increase the intensity), which has a minimum size specified by the wavelength of the beam. For instance, using a CO₂ laser and Yb-fibre laser with equivalent power will generate a different intensity, which is a hundred times higher in Yb-fibre than CO₂, due to the ability to reduce the spot size. The shorter wavelength enables achieving a smaller spot size with the same beam quality, as shown in Equation 2.8. This, in turn, reduces the required laser power for material processing in SLM systems.

2.6.2 Scanning speed

Scanning speed is the second most important parameter controlling the energy input in selective laser melting. It directly impacts the morphology of the melt pool since it controls the time interaction between the laser and the materials. Several group projects studied the effect of the scanning speed over the quality of the tracks to optimise the processing parameters in SLM [112,115,116]. They concluded that reducing the scanning speed leads to an increase in the time interaction, and as a result, the temperature will grow to exceed the material's requirement, which leads to undesirable defects in fabricated parts.

In contrast, exceeding the optimal scanning speed reduces the interaction time between the laser and the material, leading to insufficient energy input for fusing the powder particles. Researchers used scanning speed to determine optimal energy input parameters for various laser types, considering each laser's power level and beam characteristics. For example, Sun et al. [113] investigated enhancing the productivity of 316L SS using different laser systems (100 W, 380 W) by adjusting the scanning speed to optimize energy input. They found that the scanning speed could be increased up to 3.8 times when using a 380 W laser. They concluded that increasing laser power necessitates a higher scanning speed, accelerating the SLM process and consequently boosting productivity. In separate studies, Yadroitsev [112] and Bertoli et al. [114] explored the limitations of processing parameters on energy density. They found that laser power and scanning speed are subject to limitations; these parameters cannot be increased indefinitely as they depend on other factors like material properties and wavelength.

2.6.3 Layer thickness

Layer thickness is a vertical direction (Z-axis) processing parameter that significantly influences the resolution, density, and mechanical features of manufactured components during the SLM process. The optimum layer thickness depends on the laser energy and the size and distribution of the powder particle. A thick layer may prevent the laser beam from penetrating through the layer, leading to defects (de-lamination, porosity, and reduced mechanical strength) due to a lack of fusion between layers. In contrast, using a thin layer may lead to reduced packing density quality, producing rough surfaces.

Sufiiarov et al. [117] investigated the impact of changing the layer thickness on the mechanical properties by varying the layer thickness from 30 μm to 50 μm on nickel superalloys. The author found that the 30 μm enhanced the mechanical strength of the fabricated parts, whereas 50 μm increased the elongation but reduced the mechanical strength due to porosity, which developed cracks in the fabricated parts. Similarly, Zhang et al. [118] studied the impact of the layer thickness on porosity and microstructure and, therefore, on mechanical properties. The layer thickness was changed from 20 μm to 80 μm while the other processing parameters remained constant. They found that increasing the layer thickness increased the porosity and cracks in fabricated parts.

Wang et al. [119] successfully fabricated 316L parts with a high density of 99.99%, using a 400 W laser with a layer thickness of 150 μm , improving productivity ten times compared to commercial SLM systems. This success is due to the use of fine particles, reported to be 18 μm , which helped improve the packing density quality.

Yadroitsev et al. [112] found 50 μm to be the optimal layer thickness for 904L powder with an average particle size of 20 μm . He reported that the value of the maximum layer thickness during the build of the first layers should not pass 120 μm . Therefore, as shown by the collected data in Table 2.6, most SLM investigators worked within the range of 20 - 70 μm to ensure sufficient bonding between layers, reduce porosity, and enhance the mechanical properties.

2.6.4 Hatch distance and scanning pattern

Previous studies have emphasised that hatch distance (HD) significantly influences the heat accumulation between the tracks, surface morphology, and overlap rate [120]. Furthermore, the hatch distance defines the relative density and building rate, as the part is a layer-manner constructed, and each layer is produced in a multi-track fashion. Therefore, optimising the HD is critical because a small HD may lead to accumulating temperature above the material threshold, which leads to evaporation, thermal distortions, or keyhole phenomena. Moreover, increasing the hatch distance above the laser interaction zone leads to insufficient melting between the tracks, as shown in Figure 2.47.

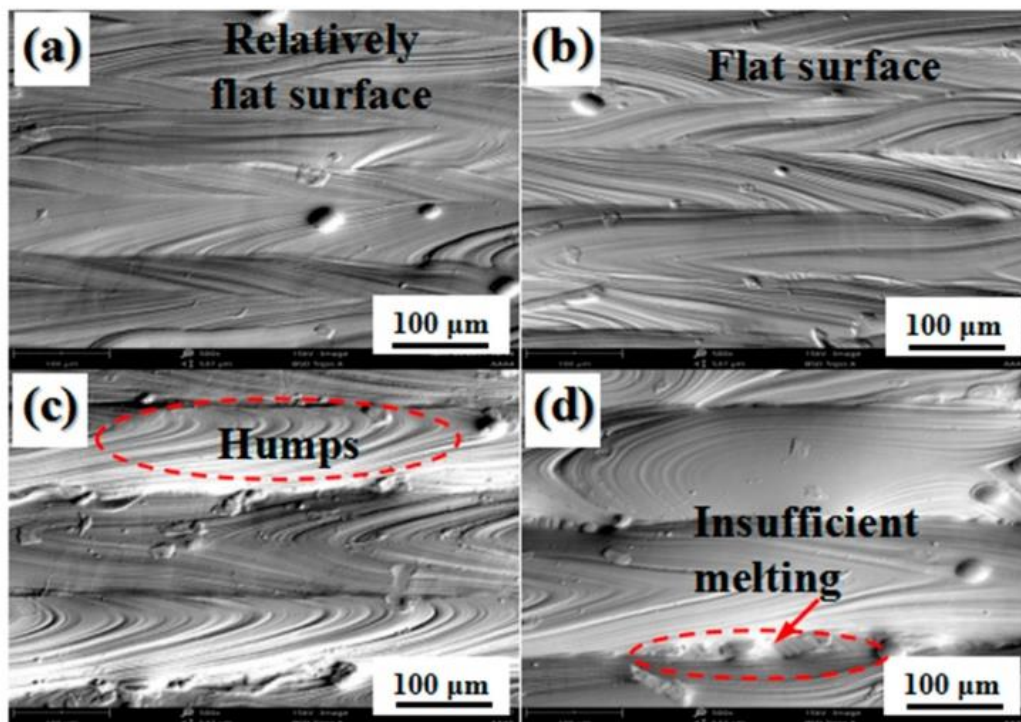


Figure 2.47 Surface morphology at different hatch distances (a) 75 μm (b) 100 μm (c) 150 μm (d) 200 μm .

One of the methods to increase the productivity of SLM systems is to increase the hatch distance by defocusing the laser beam. Metelkova et al. [121] increased the productivity of the SLM system to 18% by using an 800 W laser, and the spot size defocused to 242 μm . The previous studies had almost exclusively focused on the ability to increase productivity by changing the beam focal point; thus, the quality and the surface morphology have not been investigated, which is essential since part resolution decreases with increasing melt pool size.

Dong et al. [120] conducted a numerical modelling and experimental investigation on the effects of the hatch distance on heat transfer and the melt pool morphology of 316L SS parts using the SLM system. The processing parameters for this work were varied for 75, 100, 1500, and 200 μm , whereas other parameters kept a fixed laser power (200 W), layer thickness (50 μm), and spot size (75 μm). It was reported in the literature that increasing the hatch distance from 75 μm to 200 μm led to a reduction in the accumulated heat, decreasing the melt pool width and increasing the laser penetration. It was found that the surface roughness and part density were strongly affected by the value of the hatch distance, where 100 μm (54% overlap rate) was found to be an optimal value, which produced a high-quality surface finishing and 99.9% dense parts. In addition, using considerable hatch distance, coarse microstructures developed due to the reduction in the cooling rate.

Another study [43] investigated the influence of the processing parameters on the balling phenomenon. It was reported that HD had not shown a significant impact on the balling phenomenon once the key parameter had been optimised (laser power, scanning speed), especially with lengthy tracks, due to rapid solidification in the SLM process, emphasising the importance of scanning strategies during the SLM process.

The scanning strategy (ST) dictates how much energy each layer receives. Thus, the cooling rate and the heat gradient change by varying the length of the scanned vectors, the pattern and direction of each path, and the rotation of layers during the build process, which influences the microstructure formation and the properties of the part. The scanning strategies can be classified into three techniques as follows:

- The single-line scanning strategy, which can be either unidirectional or bi-directional, is seen as the most direct approach. This method establishes a continuous parallel line path, illustrated in Figure 2.48 (b). Thijs et al. [122] found that shifting from a unidirectional to a bi-directional strategy resulted in better part density.
- Spiral Strategy (in-out/out-in): where the laser moves in a loop direction from the edge to the centre or from the centre to the edge, as shown in Figure 2.48

(g/h). Nickel et al. [123] conducted a numerical modelling followed by an experimental investigation of the spiral scanning strategy. They concluded that the out-in spiral pattern had the lowest and most uniform stresses and assumed that the last scanned track generated the most significant stresses due to the short-scanned line at the end.

- Islands strategy: This approach involves the laser moving over a short distance in either a unidirectional or bi-directional manner, covering a target area in square blocks, as shown in Figure 2.48 (a). Lu et al. [58] comprehensively analysed the effect of varying the size of the island strategy on Inconel 718. It was reported that island sizes smaller than 3×3 mm tended to increase the formation of cracks in part due to increased junctions between the islands, which led to weak bonding.

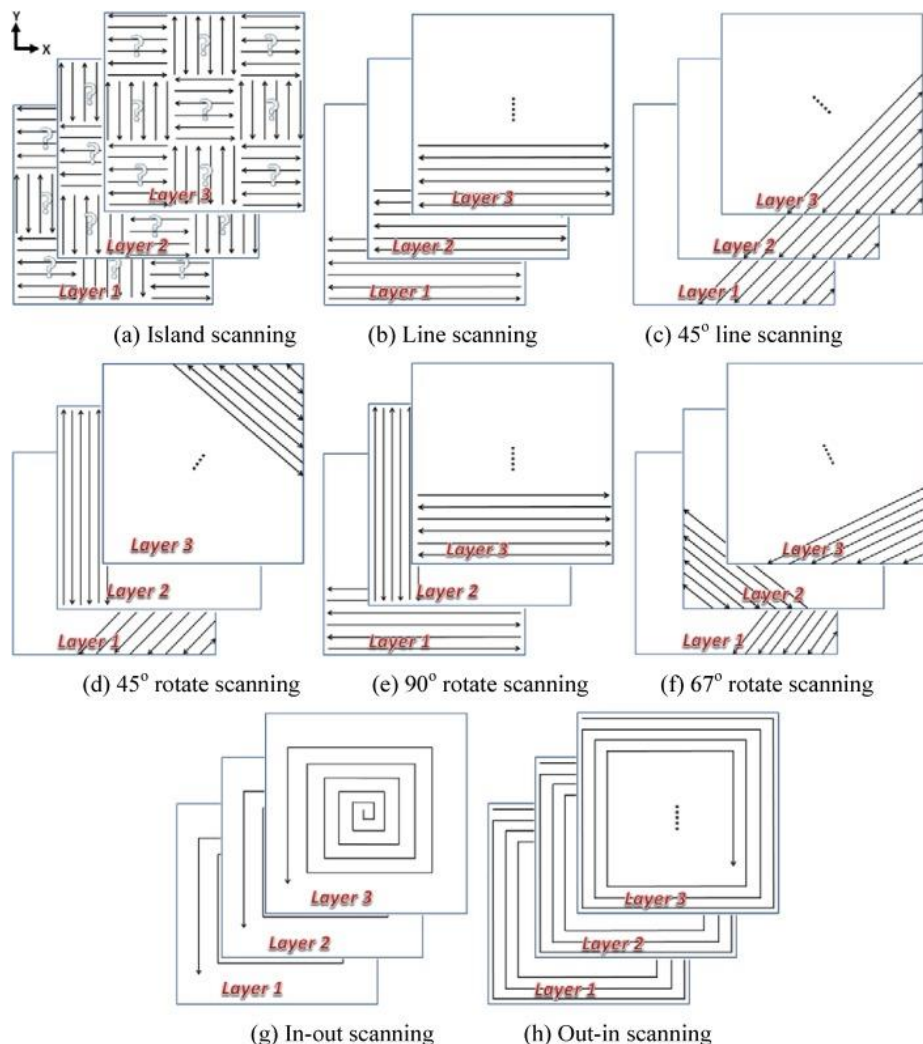


Figure 2.48: Different techniques of scanning strategies: (a) island (b) single line (g) spiral (in-out) (h) spiral (out-in).

Finally, it is important to rotate the scanning pattern to increase the bonding between the layers and reduce defects, stress, and distortion.

2.7 Productivity and Scalability

Compared with conventional production technologies, the different fundamental relation of cost, batch size, and product complexity distinguishes AM technology in general, particularly PBF systems. There is no additional cost for small batch sizes compared to mould technologies, and there are no design restrictions compared to subtractive techniques. Selective laser melting (SLM) and electron beam melting (EBM) are metal-based technologies that have witnessed a rapid rise in use by major industries such as aerospace, automotive, and medical. However, the problems presented in the above subsections (power consumption, thermal stress, scalability, and processing time) limit the potential of these technologies to be more widely adopted by other industry sectors, especially in a high production volume. Productivity is one of the problems associated with the economic aspect of SLM and plays a key role as a competitive manufacturing technology in future applications.

Most SLM devices are equipped with a 100-400 W laser beam source focused into 75 μm , which limits the processing time due to the small processing area of the laser (10^{-4} - 10^{-3} mm^2) with a relatively slow speed (few hundred to thousand mm/s) to ensure reliability and repeatability of produced parts. In addition, the optical scanning systems SLM uses for metal processing, the Galvo scanner, consisting of the double-axis mirror scanning system and a focal length f -theta, have limited the construction area to 250 x 250 x 300 mm^3 .

Three main processing parameters influencing the build rate in SLM are scanning speed, hatch distance and layer thickness, as presented in Equation 2.9.

$$\text{Building rate} = L_t S_v H_d \quad (2.9)$$

From the literature, the scanning speed and layer thickness depend on the laser power; however, hatch distance is limited by laser specification. Researchers have employed various methods to boost the productivity and scalability of SLM machines:

- Increasing the laser power can lead to a faster scanning speed [113]. Additionally, multi-beam techniques for thicker layer penetration [69] can expand the spot diameter, enlarging the scanning area and build rate [121]. However, there are constraints when increasing the laser power due to material characteristics [114], potentially resulting in thermal defects, as elaborated in section 2.6.1. Furthermore, higher laser power systems require significant electrical power and efficient cooling systems, which could escalate production costs.

- Using topology optimisation (TO) is key to enhancing the product's structure. This method aims to reduce the volume that needs melting, which in turn minimises both the processing time and material costs [124]. One of the primary benefits of additive manufacturing (AM) is the freedom it offers in design. Therefore, for TO to be effective, mechanical models and simulations are vital to ensure that the optimised product retains the mechanical properties of the original design. However, current topology optimisation software (e.g., ABAQUS [125], Magics [126], ANSYS Mechanical and Altair [127]) primarily focuses on static load scenarios and does not cater for applications that demand a dynamic (nonlinear) study. Moreover, specific orientations in additive processing can influence the quality of lattice structures, especially horizontal struts, and bridges. Some research suggests that lattice structures might not be ideal for specific metals, such as titanium. Furthermore, TO does not offer solutions to enhance the scalability of SLM systems.
- In parallelisation SLM systems, multiple scanning laser heads are incorporated within a single SLM system [128]. This approach helps reduce processing time, using several laser beams simultaneously or sequentially to melt and cover different sections while maintaining consistent parameters like scanning speed and layer thickness. However, the laser unit is known to be the most power-consuming, especially as most SLM systems equipped with lasers have electrical-optical efficiency of 45%. For instance, the laser unit in SLM needs 2-3 kW to generate 100 W output, which consumes 70% of the total power of the machine tool [14]. In addition, each laser source needs its Galvo scanning system, cooling systems, and power supplier, which increases the system cost and the energy consumption of the process. Besides, the further a laser spot has to move from the centre of the focusing lens, the greater the probability of beam profile deterioration and energy waste, thus, limiting the area that can be reliably melted by a single deflected laser source or repeatability of the system.
- Alternative methods have been explored, including defocusing the laser beam [123] and employing a preheated optical system to reduce the required energy input [68], aiming to improve productivity. However, these methods can result in higher production costs or a reduced quality of the manufactured parts.

By reviewing Additive Manufacturing technologies, High-Speed Sintering (HSS) was deemed the fastest and most scalable AM technology [129]. As a result of dispensing infrared absorbable ink onto the powder bed, the material can be selectively sintered when the infrared lamp moves across. HSS is not suitable for processing metallic powders, but the concept was found to be inspirational to

foster a novel AM process applicable to producing metallic parts. Using simultaneous multiple laser beams directly over the powder bed will help improve scalability, raise productivity, and overcome some inherent drawbacks of the SLM and BEM processes [21,24,56,119].

Efforts have been made to explore the challenges and potential of implementing this technique to process a metallic powder. Focusing a 19 emitter diode module to cover an area of $0.25 \times 4.75 \text{ mm}^2$, known as diode area melting (DAM) [27], or creating an optically addressable laser in a wide area using a 5 kW laser diode with a 1 MW Q-switch [21] are the two representable approaches. However, it appears that they were unable to control each beam source individually, which reduced the feature resolution of the produced parts. In addition, the influence of each laser array on the processing parameters has not been evaluated. Recently, using a fibre-coupled diode laser of 974 nm with a power of 42 W focused into $150 \mu\text{m}$ gives the ability to control the laser individually and improve the beam quality [130].

Nevertheless, the pitch between each laser was approximately $600 \mu\text{m}$. Therefore, the absence of overlapping between beam spots prevents direct interaction between the individual beams (remelting, uniform temperature gradient) and significantly negatively impacts the part quality and density, which has been reported to be a maximum of 61%. The inappropriate pitch distance leads to poor surface quality and increased porosity due to the formation of every single track, which pulls the surrounding powder and creates areas of denudation [130]. Furthermore, using a shorter wavelength can theoretically improve the energy efficiency and absorption of certain materials.

Overall, research work reported in the literature has confirmed the positive influence of using a laser array on the processing parameters and produced parts. The energy efficiency has been significantly improved by 80% [24]. The ease of adoption and the availability of better fibres facilitate the improvement of laser beam quality, making it easier to retrofit the laser into the system with a shorter wavelength. This allows for better energy absorptivity, expanding the availability of the range of processable materials [19][131]. Apart from the above, thermal stress can also be reduced by gradually elevating the temperature, melting the laser source, followed by annealing lasers, which can be done by controlling each laser individually with the help of scanning strategies. It was reported that using parallel lasers in the SLM system has increased productivity and reduced thermal stress [56]. Series laser array has significantly overcome the spatter effect, which is common in a single spot process due to increased recoil pressure and negatively influences mechanical properties such as ultimate tensile strength, strength and fatigue [132].

Up to now, using an addressable low-power laser to process metallic powders by additive means has not been achieved. This work lies in investigating a new laser head using a fibre-coupled diode laser to increase the beam quality and a microlens array to minimise the pitch distance between spots, by which both part quality and density can be significantly improved. This work will investigate the influence of the short wavelength (450 nm-808 nm) over processing parameters and processing new materials, such as copper and silver, which are difficult to process using commercial SLM systems. The range of processable PBF materials will increase by taking advantage of the short wavelength of the fibre-coupled diode laser, which significantly impacts the reflectivity of metallic materials. This will influence initial costs, lower energy consumption, increase processing speed, and lead to innovation in PBF.

2.8 Energy Density Overview

The energy density (ED) is a group of independent parameters (i.e., laser power, scan speed, layer thickness, hatch distance), which is applied as an energy metric to quantify the required energy input to melt metallic powder under different conditions in (SLM). Each parameter significantly affects the final quality of the produced parts and their mechanical properties. There are extensive correlated studies (simulation as well as experimental) among some of these parameters and the undesirable phenomena in SLM. Depending on the research study, whether it is optimising the processing parameters [116,133,134] or studying the effects of the parameters on specific phenomena such as microstructure, balling, and thermal behaviour) in SLM [43,71,135,136], a mathematical relationship between key parameters is formed to identify the amount of energy input. In general, laser power is tuned based on material properties and optical delivery; the layer thickness is adapted to ensure complete solidification of each layer, and hatch distance is determined to ensure overlapping between tracks and remelting, where the scanning speed is adjusted accordingly. The production of high-density metal parts with high-quality surfaces depends on the quality of every single track then each layer. Therefore, researchers quantify the energy density at various dimensions (linear energy density (J/mm), surface energy density (J/mm²) and volumetric energy density (J/mm³), as illustrated in Table 2.5.

Table 2.5: A different mathematical approach to identify the Energy Input.

Eq. number	Energy density	Equation	References
(2.10)	Linear energy density	$LED = \frac{P}{V}$	[116][112][115]
(2.11)	Surface energy density	$ED_{SH} = \frac{P}{V H_d}$	[137][138] [139]
(2.12)		$ED_{SD} = \frac{P}{V D}$	[140][141][142]
2.13)	Volumetric energy density	$VED = \frac{P}{V H_d L_t}$	[133][114][143] [144][145][122]
(2.14)		$VED = \frac{4 P}{V D^2}$	[71][59][27]
(2.15)	Normalised energy density	$E^* = \frac{P^*}{v^* l^*}$ $= \frac{AP}{2vlr \rho C_p (T_m - T_0)}$	[146]

2.8.1 Linear energy density

The most important parameters to quantify the amount of energy input when performing a single track are laser power (P) and scanning speed (V), as presented in Equation (2.10) and known as linear energy density (LED). Researchers have used (LED) to evaluate the combined effect of laser power and scan speed on the solidification behaviour and morphology of a single track. Previous studies have shown that increasing the laser power allows faster processing speeds and higher thermal penetration depths [112,115,116]. Furthermore, using a fast scan speed results in less heat being transferred and less time to diffuse the powder particles, which reduces the melting width and the heat-affected area. For instance, Wang et al. [116] used LED to study the influence of processing parameters on the morphology of single tracks. The experiment was conducted on Inconel 625 by varying the laser power (100 W-200 W) and the scanning speed (40 mm/s to 200 mm/s), providing LED between 0.5 J/mm and 5 J/mm; the layer thickness was set to 0.05 mm. The author observed three morphologies at different energy input

levels (lack of fusion, sufficient melt, excessive melting). The optimal LED, which provided constant melt, was reported to be between 1 and 1.5 J/mm. Furthermore, the author stated that the track width and height decreased as the LED ratio increased.

Similarly, Yadroitsev et al. [112] used linear energy density to predicate a processing map for depositing steel 904L and to study the stability of the melting pool by measuring the width and depth of single tracks, including penetration depth into the substrate. Single tracks were formed using a constant energy input $P/v = 227$ J/mm at two levels of power (25-50 W) and varying scanning speeds (0.06-0.22 and 0.03-0.11), respectively. It has been reported that providing the same energy density at a different power led to a different formation of single-track patterns, as shown in Figure 2.49.

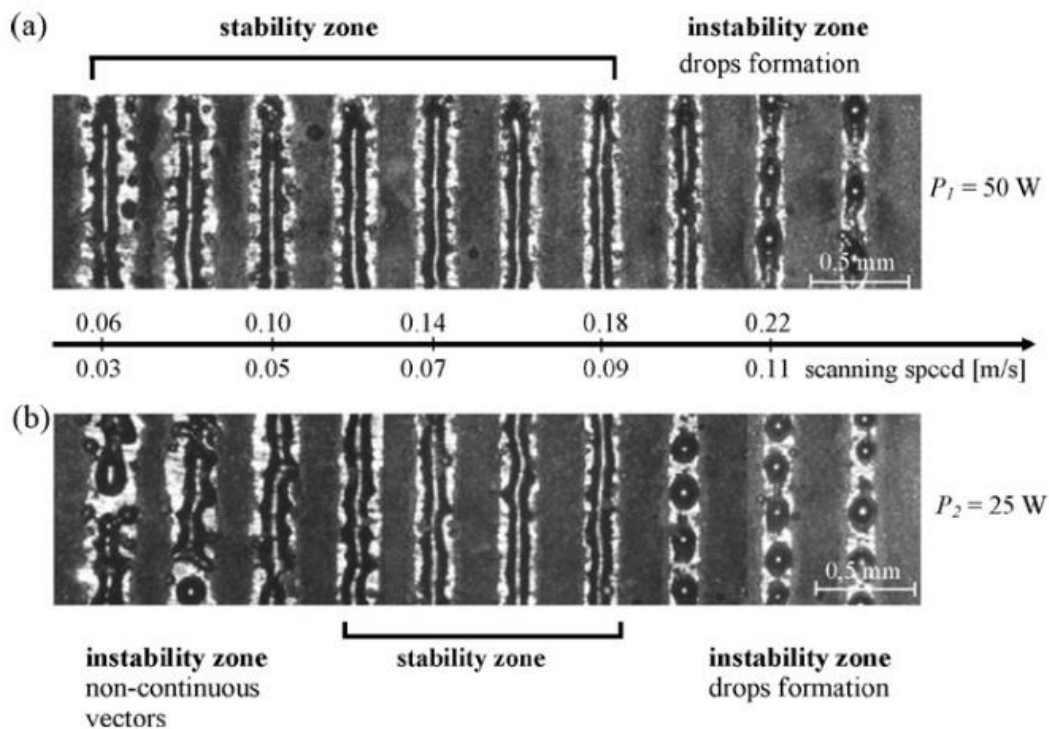


Figure 2.49: Shows the changes in the optimal processing window resulting in a consistent single track using two different laser powers: (a) 50 W and (b) 25 W [112].

The advantages of high laser power over low power were the increased stability zone and the penetration depth. The study of forming multilayers concluded that more energy is required to form stable tracks for the first layer due to the higher thermal conductivity of bulk material (substrate) compared to powder, thus requiring more energy to heat the substrate. Kusuma et al. [115] presumed a similar conclusion: "The threshold energy density for the powder case samples is much lower than that for non-powder case samples". Accordingly, the linear

energy density is more sensitive to laser power than scanning speed. The laser source is not correlated with the P/A ratio but rather with the square root velocity and wavelength absorption. Although LED cannot determine the specific melt pool geometry at different processing conditions, it can be useful when combined with other processing parameters.

2.8.2 Surface energy density

Surface energy density is an alternative approach used to calculate and investigate the effect of the energy input for fabricating multiple tracks or multiple layers which are defined in Equation 2.11 and Equation 2.12. Researchers use laser spot diameter instead of the hatch distance [38, 39] when the investigation is related to the effect of the beam characteristic, which is more connected to the heat flow of the beam power. In both equations, the fundamental concept is similar; the hatch distance should be controlled by the spot size of the laser to manage the same overlapping ratio. In their study, Liu et al. [141] used Equation 2.12, spot diameter, to investigate the impact of laser intensity by changing the spot size on a different range of particle sizes and measuring the ultimate tensile strength and surface finish. The author reported that increasing the spot size reduced the energy input, which reduced the relative density and surface finishing of fabricated parts. For instance, using laser power of 50 W at 100 mm/s at different focal lengths of 0.026 mm and 0.48 mm will reduce the energy density from 10 J/mm² to 5 J/mm². This variation in energy density due to the change in beam characterisation cannot be predicted using the linear energy density equation. Liu et al. concluded that the wider particle ranges decreased the required energy density and improved the mechanical properties of the part.

Similarly, Okunkova et al. [141] analysed the influence of different laser modes (Gaussian distribution, top hat, Donut (inverse-Gaussian)) on the melt pool formation on the spatters and the melt pool solidification. The researcher investigated the surface energy density threshold under different processing parameters in order to obtain a stable zone. Employed surface energy density helped the researcher predict changes in the morphology of the single track at different laser modes and comparable energy density.

On the other hand, using the hatch distance in Equation 2.12 assisted the researcher in studying the effect on the surface roughness and porosity. Hu et al. [137] reported that the hatch distance had not significantly impacted the porosity until the scanning speed exceeded 60 m/min due to rapid solidification between scans, similarly stated by Maeda et al. [138].

2.8.3 Volumetric energy density (VED)

Volumetric energy density is the most current energy input expression researchers use to study various phenomena in selective laser melting. VED employed the most effective independent parameters which are represented in Equation 2.13 as laser power, hatch distance, scanning speed, and layer thickness. Most prior research has concluded that VED has a specific range, which can reduce the impurities of the manufactured parts, control the microstructure, and improve the mechanical properties. Providing VED below the threshold of the processed material leads to increased porosity, reducing the tensile strength and fatigue resistance due to insufficient energy input. In contrast, increasing the VED causes the metallic powder to vaporise, warpage defects or balling phenomena due to excessive energy input. Ciurana et al. [30] used a customised powder bed to study the influence of VED on CoCrMo powder. The substrate was manufactured to provide a sloped surface at 40 μm to 500 μm . Laser power was varied from 25 W to 500 W, and the scanning speed from 33.3 mm/s to 83.3 mm/s, where the hatch distance remained equal to the spot size of the laser, which was 150 μm . The combination of laser power and scanning speed had a more significant effect than layer thickness on the shape of the tracks. VED of 151 J/mm^3 was optimal for producing a continuous track of CoCrMo. Yakout et al. [143] identified the optimal processing parameters to produce dense parts from Invar 36 using VED. The processing window to achieve 99% density was between 60-75 J/mm^3 , where high thermal stresses were observed when the VED was increased above 75 J/mm^3 . The author observed similar grain structure and density values when similar VED was provided by varying the combination of the process parameters. Thijs et al. (2010) [122] studied the influence of VED parameters on the microstructure of Ti-6Al-4V by varying only the scanning parameters (hatch distance, scanning speed) and scanning strategy. The scanning strategies showed a significant impact on the part's density. For instance, the combination of the processing parameters was used to provide a fixed VED of 93 J/mm^3 ; the relative density was improved from 99.35, 99.6 to 99.9% by employing different scanning strategies (unidirectional, zigzag and cross-hatching, respectively). This improvement in part density is related to the cooling rate, which differs between the strategies and cannot be indicated using VED. Another study by Gu et al. [144] concluded that VED has limitations for predicting the porosity and morphology of SLM parts, even when applying similar energy density. Gu et al. stated that the relative density improved by increasing the value of VED, but processing under a similar value of VED (61 J/mm^3) by varying the processing parameters (laser power, scanning speed) led to a drop in the relative density once the laser power dropped below 70 W or the scanning speed below 389 mm/s, as shown in Figure 2.50.

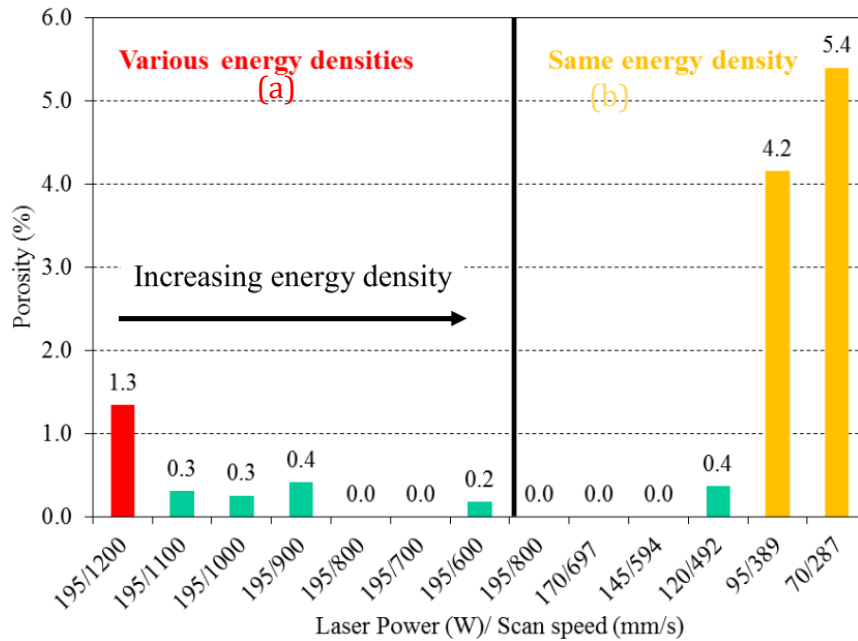


Figure 2.50: Relative density under (a) same laser power with different scanning speeds (b) Same VED by varying (power/speed) [114].

This led Bertoli et al. [114] to investigate the reliability and limitations of using the VED to predict the optimal processing parameters in SLM. Bertoli et al. varied the processing parameters (laser power and scanning speed) to produce single tracks at a similar VED 242 J/mm^3 value. As illustrated in Figure 2.51, the result varied from defective tracks to continuous smooth tracks. The author concluded that VED is typically a thermodynamic quantity, which means it cannot predict the complex physics involved, including the flow of Marangoni, hydrodynamic fluctuations, and recoil pressure, which drive heat and mass transfer in directions different from the molten bath, ultimately influencing the final morphology.

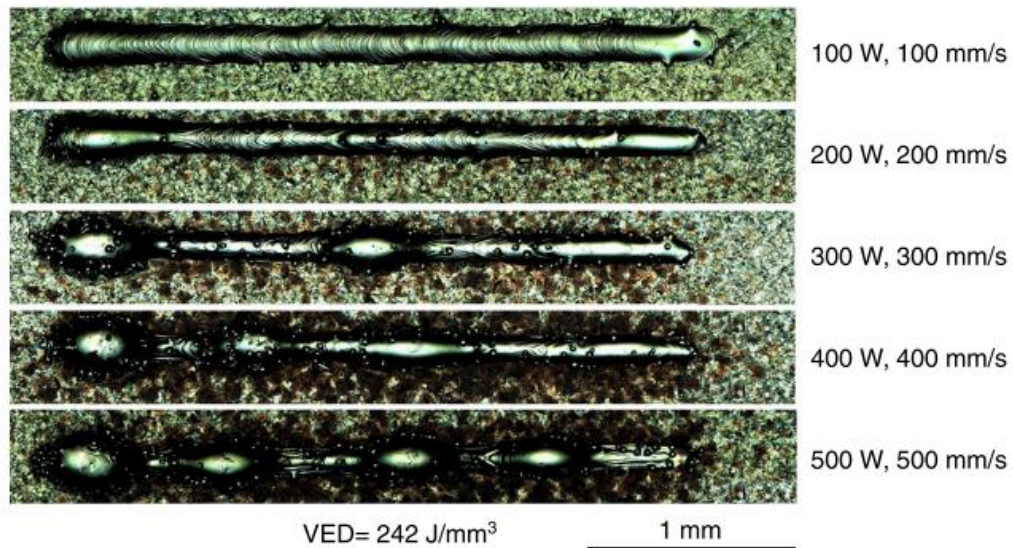


Figure 2.51: Single track morphology at the same VED (242 J/mm³) under different processing parameters.

In conclusion, energy density generally has an impact on thermal history, microstructure, and mechanical characteristics. The microstructure and mechanical properties can be optimised by controlling the significant processing parameters which impact the energy input on an optimised process window. The optimum energy density for different metals reported in the literature has been summarised in Table 2.6.

Table 2.6: Summarises the optimal processing parameters from previous work.

Eq.	Heat source		Material	Processing parameter				Optimal ED	Ref.
	Laser system (spot size- mm)	Wavelength (μm)		Power (W)	Velocity (mm/s)	Thickness (mm)	Hatch (mm)		
LED	SLM machine HRPM-II	N/A	IN625	100 – 200	40 – 200	0.05	-	1-1.5 (J/mm)	[116]
	PM 100	1.075	904L	25 - 50	60 -240	0.05	-	0.4– 1.1 (J/mm)	[112]
	House built- in (0.100)	1.064	CP-Ti	100-180	150 – 600	0.05	-	0.2-1.2 (J/mm)	[115]
ED _{SH}	House built- in	10.6	WC-CO	60-200	1.5-200	-	0.18	2-200 (J/mm ²)	[138]
	IPG YLR-200	1.07	17-4PH	200	0.16-1.6	0.02-0.04	0.09-0.13	Not specified	[137]
ED _{SD}	House built-in (0.048-0.28)	1.064	316L	50	200	0.05	0.08	62.5(J/mm ²)	[140]
	Nd: YAG (0.200)	1.064	18Ni300 steel	100	180-220	0.03	-	>2.00 (J/mm ²)	[142]
VED	Nd: YAG (0.15)	1.080	CoCrMo	25-500	33.3-83.3	0.04-0.5	0.150	151(J/mm ³)	[133]
	YB fibre laser (0.055)	1.07	316L	100-500	100-2500	0.075	0.055	242(J/mm ³)	[114]
	N/A	N/A	Invar36	285-300	880-960	0.04	0.10	60-75(J/mm ³)	[143]
VED _{Spot}	Diode bar (0.25*4.75)	0.808	316L	50W	1-5	-	(0.25*4.75)	42(J/mm ³)	[27]
	YB fibre laser (0.15)	1.070	316L	200	444	0.058	-	60.1-73.3(J/mm ³)	[147]
	House built-in (0.262)	1.08	316L	800	250	0.03	-	60.377 (J/mm ³)	[121]

2.8.4 Normalised energy density (NED)

The thermodynamic cycle in SLM contains a large number of parameters which were not employed in energy input equations. For that reason, optimising the processing parameters in SLM, which uses different laser systems, are not directly transferable. Once the laser beam penetrates the surface of the powder bed, it induces a thermodynamic cycle which depends mainly on laser characteristics: power (P), scanning speed (v) and spot size diameter (r); material properties: spectrum absorptivity (A), thermal conductivity (k), thermal diffusivity (D); different transformation phases in energy and temperature; as well as the geometry and size of the workpiece. The temperature level delivered to the material surface defines the processing characteristics (heating, melting or vaporisation). Several efforts have been made to develop mathematical models to predict the formation of impurities (porosity, keyholes, vaporisation, lack of fusion) during the SLM process. Although these numerical models offer a high precision standard, they are considered to be expensive and require lengthy experimental validation. Ion et al. [148] developed a practical alternative to numerical process modelling, which depends analytically on thermodynamic variables by simplifying them into dimensionless groups known as normalised energy density, Equation 2.15. The particular advantage of Ion et al. approach is that it can identify the processing maps for a specific material under different PBF systems by avoiding excessive experiments that inevitably lead to the identification of incomplete laser parameters. The normalised energy input defined in Equation 2.15 normalised the most effective processing parameters in SLM processes as follows:

- Normalised the beam power as follows:

$$P^* = \frac{AP}{rk(T_m - T_0)} \quad (2.16)$$

- Normalised scanning speed as follows:

$$v^* = \frac{vr}{D} \quad (2.17)$$

- Normalised layer thickness as follows:

$$l^* = \frac{2l}{r} \quad (2.18)$$

- Normalised hatch distance as follows:

$$h^* = \frac{h}{r} \quad (2.19)$$

Where P^* , v^* , l^* and h^* are the normalised primary SLM parameters. The normalisation approach is more comprehensive than VED as it is taking into account the material properties and processing parameters such as (A) Absorptivity, (ρ) material density, (C_p) specific heat, (D) thermal diffusivity, (k) thermal conductivity, (T_0) ambient temperature, (l) layer thickness, (h) hatch distance, (v) scanning speed, (r) Beam Radius and (T_m) powder bed temperature.

Thomas et al. [146] have developed the normalisation approach to generate a processing map for various metallic powders (Ti-6Al-4V, 316L, Inconel 625, Duplex SS, CM247, and FeCoCrNi), as shown in Figure 2.52.

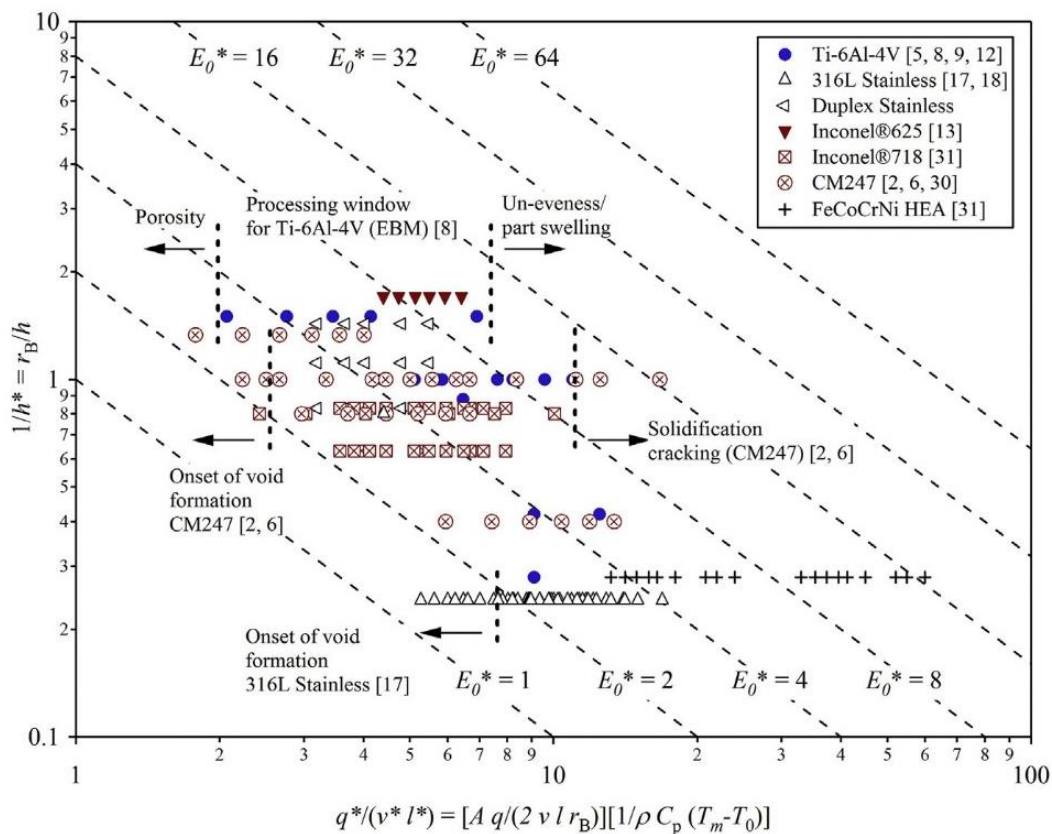


Figure 2.52 Normalised Energy Density for various EBM materials developed by Tomas et al. [146].

The ratio between E^* and $1/h^*$ presents the normalised heat input for every scanned vector, which is used to define the variation in energy efficiency during the processes. For instance, a high value of E_0^* means the combination of the processing parameters has exposed the system to high heat input; in contrast, the low values lead to insufficient heat to fuse the powder. In addition, the use of $1/h^*$ is related to the spot diameter of the laser, which is considered to be an important processing parameter that controls the overlap between two adjacent melting pools. The choice of a large hatch distance can be faster in the production of a part, but the overlap between adjacent scanning lines may result in less

melting if there is not enough laser power. In contrast, a narrow hatch distance value increases the entire production time of the part by introducing more remelting and, therefore, unnecessary heat input.

This study will use the normalised energy density approach to theoretically identify the processing region and practically validate the optimised processing using volumetric energy density, supported by previous literature data.

2.9 Literature Review Conclusions

The literature shows that Powder Bed Fusion (PBF) faces significant challenges, such as low processing efficiency, a restrictive scanning mechanism (galvo system), scalability issues, and low wall plug efficiency, particularly with highly reflective material. These challenges limit process efficiency, raising the need for a solution to enhance performance.

The existing galvo system exacerbates the challenges by constricting the processing area. Incorporating multiple galvo techniques to mitigate this problem increases the system's cost, which adds financial constraints to technical ones. In addition, increasing the scanning laser system or laser power can lead to cracks and internal stress due to high thermal gradients, adding additional costs by post-processing the final parts. Instead, we should focus on the wavelength, the key factor in boosting process efficiency.

Currently used lasers in SLM have limitations that diode lasers can overcome. Various research works have endeavoured to surpass the constraints of the SLM process, which are discussed in section 2.5.5 and summarized in Table 2.7. However, these attempts are restricted in their ability to incorporate short wavelengths, enhance beam quality, and consolidate multiple diode lasers as an individually controllable heat source. These improvements have the potential to enhance the PBF process. Moreover, none of the related works has investigated the ability to process high melting temperature materials such as Ti6Al4V, copper, or Aluminium, nor have they comprehensively characterised the final parts, such as microstructure and mechanical analysis, which are crucial to understanding the influence of employing multi-laser beams.

Therefore, high-power diode lasers that increase PBF process efficiency need better beam quality. Optical approaches for PBF also have room for improvement as they come with limitations, such as a short focal length and inability to individually control each beam, which can hinder the construction of finer features. A configuration of fibre-coupled diode lasers can enhance processing efficacy and scalability. Nevertheless, additional research is required to validate these findings and optimise such a system.

To evaluate the performance of the newly developed laser, the energy density for the process needs to be calculated and optimised. However, the current methods to calculate the energy density have limitations, as they do not include the material properties and the laser, which are part of the process and are not meant to be for multi-individual spots. A new method of calculating energy density for multi-spot processes is needed to address these challenges. In addition, this method can facilitate a deeper understanding of the processing parameters in relation to the morphology of the melt pool, microstructures, and the mechanical properties of the final parts.

In conclusion, while PBF presents promising possibilities in additive manufacturing, several crucial limitations must be addressed, including absorptivity and the laser system, to achieve its full potential. Therefore, a combination of novel approaches and technological advancements guided by rigorous scientific exploration is necessary to move forward.

Table 2.7 Summary of Systems and Limitations in the State-of-the-Art of Diode Lasers in Traditional Laser Powder Bed Fusion (LPBF).

References	Laser Power of system	Wavelength (nm)	processing area (mm)	Addressable individual spots	Material processed	Microstructure	Mechanical properties	Limitations of the work
[21]	4.8 kW (diode laser array) + 1 MW (Q-switched laser)	1007 nm (diode laser array) + 1064 nm (Q-switched laser)	2-3 mm Up to 18 x 18	No	Sn	No	No	<ul style="list-style-type: none"> The system requires a high-power laser system, which can be expensive. The system is limited to materials as the wavelength is similar to SLM systems. The system is limited in terms of improving the processing area. The microstructures and mechanical properties have not been characterized. The roughness evolution over multiple layers in a full print was not studied.
[22]	200 W	976 nm	Not reported	yes	Not reported	No	No	<ul style="list-style-type: none"> Poor beam quality Lack of information provided
[24]	50 W	808 nm	4.75 x 0.25 mm Or 6.5 x 0.3 mm	No	316L	No	No	<ul style="list-style-type: none"> Only single layers are processed, with manual powder spreading. No complex 3D geometries were printed. The scanning speed is limited to 1-5 mm/s due to the low laser power density. This restricts the build rate.
[110]	960 W	976 nm	2 mm width	Yes-but not Demonstrated	(CoCr) alloy	No	No	<ul style="list-style-type: none"> No microstructure or mechanical analysis reported Optical stability under high power conditions presents a challenge. A consolidated limitation lies in managing thermal aspects, scaling the concept to incorporate more lasers, and achieving kilowatt-level outputs. The system is limited to materials as the wavelength is not far from SLM systems.

Chapter 3: Experimental Methodology

Summary

This chapter provides a comprehensive account of the methodology and experimental setup utilized in the research study. First, it presents the need to develop a new approach in PBF to process metallic powder called Diode Area Melting (DAM). This method employs multiple fibre-coupled diode lasers customised with a short wavelength and low power for parallel processing metallic feedstock at high speed. Moreover, the chapter briefly describes the characterisation of laser systems, single diode modules (808 nm, 450 nm) and the multi-laser head (CTP). Then, it explains the special modifications to the system and the characteristics of the equipment needed for DAM processing. Finally, the chapter provides a brief overview of the characterization techniques used to analyse the mechanical and microstructural properties of the final parts.

3.1 Introduction

The need to enhance productivity and efficiency while reducing production costs in developing powder bed fusion (PBF) is evident. PBF system manufacturers and research institutions have been continuously improving the productivity and efficiency of PBF. Among the metal component fabrication techniques, Selective Laser Melting (SLM) is most commonly used in the aerospace, automotive, and medical sectors. It is classified as a Powder Bed Fusion Process (PBF) and can produce near-net-shape metal components by melting and depositing thin metal powder layers using a high-power, highly focused scanning laser.

However, SLM has been criticised for limitations on productivity, specifically, the rate at which material can be processed per second. As discussed in the literature section, to overcome this challenge, researchers have explored two methods: using high-power lasers to maintain higher energy densities while scanning the powder surface faster and integrating multiple laser sources within the build chamber to increase the surface area of the powder that can be processed simultaneously. Unfortunately, neither of these methods can increase productivity while maintaining part quality (density, surface quality, internal stress) without requiring a post-process, which adds extra cost and time to the overall processing time.

This research will focus on two key aspects: wavelength and the use of multiple addressable fibre-coupled diode lasers, which have yet to be widely investigated. The development of a novel approach will be considered in this research. In addition, investigate the effect of the new approach on the quality of the parts.

The experimental work developed in the present research is structured by two general stages; each focused on specific objectives as described below:

- First stage: An experimental investigation will be carried out to define the importance of the short wavelength in the PBF process. This investigation will study the effect of using low-power 450 nm and 808 nm diode lasers during the PBF of Ti6Al4V, one of the most widely/commonly used materials in SLM processing. A DAM methodology will be employed, with the diode laser physically traversing in the x/y plane to raster scan the surface of the powder bed. However, compared with the work of Zavala et al. [27], an optical fibre coupled diode laser will be used to deliver a flexible and improved beam quality within the PBF test rig, as explained in the previous section. The effect of laser wavelength on melt pool characteristics will be studied for comparable energy densities. Consequently, if the technique is effectively demonstrated in Ti6Al4V, then a wide range of materials can also be expected to be processed effectively.

- Second stage: Parametric investigation on the effect of using a multiple laser array head, which is called a coherent combination of multiple transverse paths (CTP), in PBF processes. In this study, up to ten low-power diode lasers (less than 5 W each) are used in a potentially scalable configuration to large write areas without speed/resolution/deformation penalty. A short laser wavelength of 808 nm is used to achieve high absorption and processing efficiency. Furthermore, individual control of each laser allows the management of intensity distributions across the linear array of laser beams, enabling complex custom parts to be built. The effect of laser power, scanning speed and beam profiles during DAM processing of Ti6Al4v has been investigated. A normalised energy density approach has been developed to identify the process conditions required to produce high density components. The microstructure and mechanical analysis have been conducted to understand the effect of the selected processing parameters on the final parts. The research aimed to develop a high-resolution, energy-efficient powder bed fusion system with enhanced process thermal control that can be scaled up for high production. The study employed diode area melting of Ti6Al4V utilizing 808 nm laser sources and variable multi-beam profiles.

3.2 Brief description of the Diode area melting system

At the beginning of the research project, it was found necessary to construct an integrated system to conduct the required experiments to complete the research. Therefore, the key components requirements for developing a system encompassing essential elements of the Powder Bed Fusion (PBF) process, including the control unit, cooling, movement stage, and enclosure chamber, were discussed. An overview of this system is provided to contextualize subsequent sections, each detailing individual components, and their functions. The system overview consists of two sections: one outlining the component and another providing a concise explanation of its operation. As shown in Figure 3.1 the Diode area melting system consists of the following components:

- (1) A personal computer (PC): To generates G-codes, control the laser Head's movement, record the process temperature, and monitor the temperature.
- (2) Laser power drive: To control the diode laser modules in line with the geometry of the final parts, a 10-laser power driver is used. The driver operates at a constant voltage of 3.5 V while the current is adjusted to ensure consistent optical power throughout the process for each laser. This technique ensures that the laser output power is stabilized and prevents any fluctuations in the output power due to changes in current.

- (3) Laser cooling system: To ensure optimal performance of diode lasers, it is critical to maintain a temperature below 25°C using a cooling unit specifically designed for this purpose. The output power, wavelength, and beam quality of the laser are all significantly impacted by changes in operating temperature, which can cause the laser to drift out of range and negatively affect its performance. Therefore, consistently maintaining the appropriate temperature is also essential for prolonging the lifespan of the laser.
- (4) A two-axis gantry movement system is used to move laser head modules over the powder bed in both X and Y directions. The laser head can either be a single emitter of 808 nm or 450 nm or a laser head array.
- (5) A customised powder-handling system with a 200 cm diameter building area.
- (6) The enclosed chamber is equipped with an oxygen sensor for monitoring the environment.
- (7) A CTLM-2H1SF300-C3 model pyrometer from MICRO-EPSILON UK Ltd was utilised inside the chamber to measure the surface temperature when the laser passes a specific processing area. The pyrometer can detect temperatures from 350°C to 2000°C. The field of view is adjustable to 500 μm . The transmission spectrum's central wavelength is 1.6 μm .

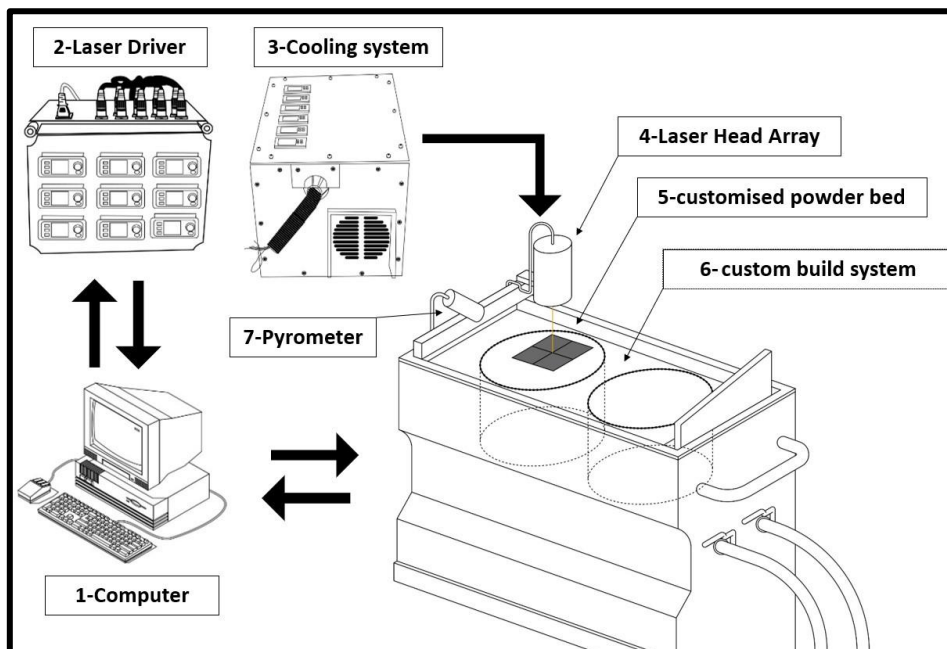


Figure 3.1 Schematic of the main component of the diode area melting (DAM) used in this research project.

3.3 Brief description of the Diode Area Melting process

The BPF process in the current research project is shown in Figure 3.2. In stage (1), the research focuses on designing key processing parameters for a given build structure, such as laser power, scanning speed, and hatch distance. This is done by applying the design of the experimental method and calculating the energy density using the normalized energy density in advance. Next, a CAD file of the 3D model is sliced into 2D images representing a single layer using an SLM system. Next, the Lightburn CNC program (Lightburn Software LLC., Version 1.0.04) generates a G-code to control the laser driver, cooling system, and gantry (X-Y) motion. This G-code is sent to the microcontroller unit in the machine, which sends positional commands to the two axes motors to prepare the system for creating the required structure.

In stage (2), the software sends a command to the laser driver unit, which flows electrical current to all ten diodes to be turned on or off based on the 2D geometry. It is important not to exceed the laser's maximum power of 4.8 A and 3 V. Each of the ten diodes can be activated individually or simultaneously. A thermistor individually measures the temperature of the ten diode lasers, controlled by the thermoelectric (TEC) cooler, as shown in stage (4). The temperature of the lasers should not exceed 25°C to maintain the output power of the lasers during the process. An air-cooling mechanism assists the TEC cooling process by using copper plates as heat dissipators. As the laser head traverses across the powder bed, the emitters of the laser head (CTP) are turned on and off as required to selectively melt particular areas of the powder bed. The pyrometer measures the temperature by pointing it at the middle of the processing area where the laser interacts with the powder.

In stage (4), a new layer of powder is applied to the top of the completed layer, and the process is repeated until the final part is manufactured.

In stage (5), the final parts are hot-mounted and characterized to investigate the effect of the processing parameters such as beam profiles, laser power, scanning speed, and hatch distance.

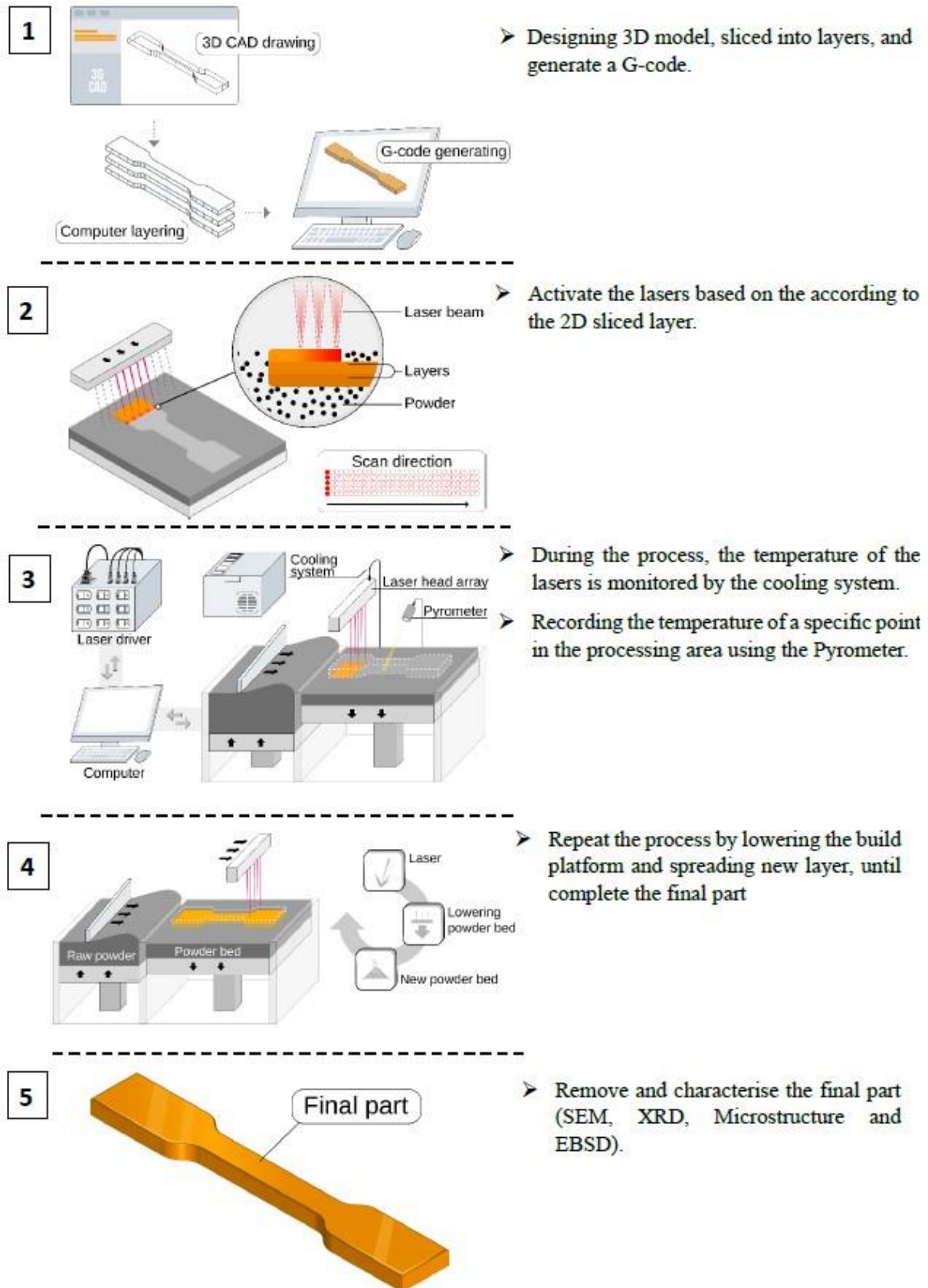


Figure 3.2: Step-by-Step Breakdown of the Diode Area Melting Process.

3.4 Diode Area Melting System Development

3.4.1 Movement stages

The system has been designed to provide an ideal PBF environment. Therefore, due to the high tendency to form an oxidation layer during the PBF process, the system is designed to be an enclosed chamber purged with inert gases. The processing area will be vacuumed and pumped with argon gas; The oxygen level is continuously measured to maintain the oxygen level down to 0.2% during the process. Two glove ports were constructed to give accessibility to tools inside the vacuumed chamber or to support any actions needed during the build process. One of the advantages of the new DAM system is the movement of the key components, which is controlled by a computer automatically. The gantry system has a movement range of 400 cm on the Y axis and 200 cm on the X axis. The optical system (single or multiple lasers) is mounted on the motorised stage for transverse movements in X-Y planes. In Addition, 4 Stepper motors automatically control most of the mechanical moving (wiper, powder bed, powder container and laser head), as shown in Figure 3.3. The new DAM system considered the uses of different laser heads (Fibre Laser, Edge Emitter, Galvano system) during the design stage to allow us to examine different laser scanning methods and wavelengths. A monitor board was created to regulate the environmental parameters in the chamber, such as the temperature of pistons, pressure, and oxygen level. This allowed for constant monitoring and control of the experimental environment, which was crucial during the PBF process.

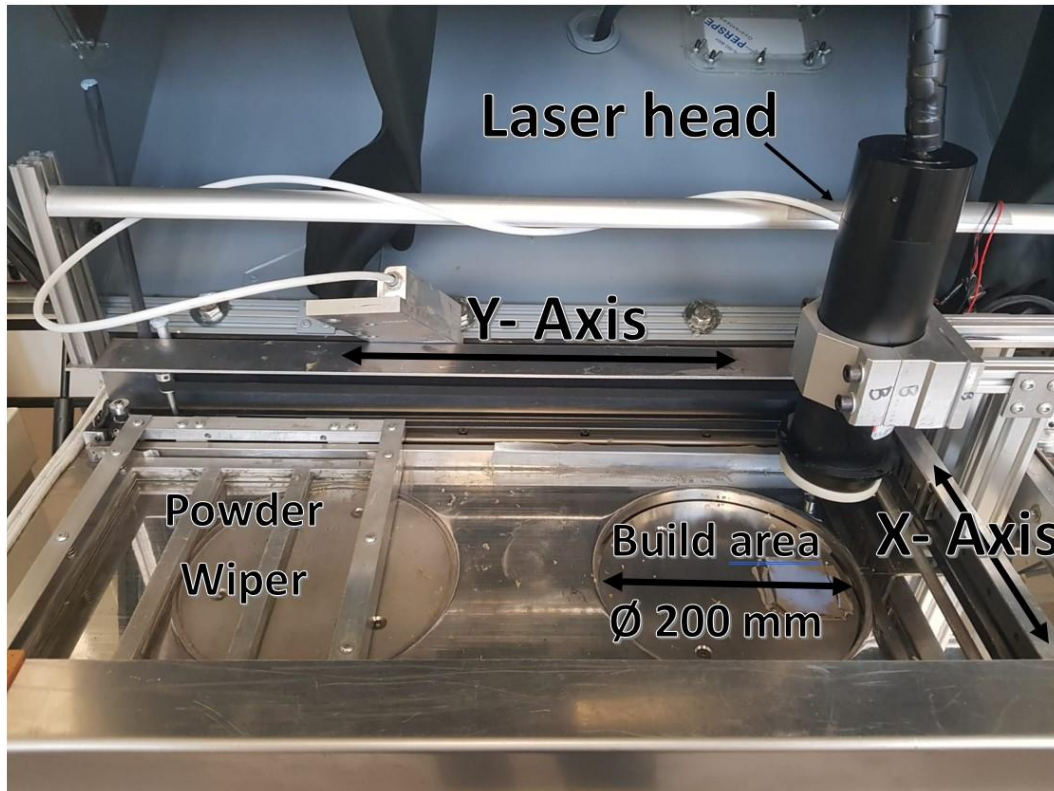


Figure 3.3: View of the Processing Area, Illustrating Integral Components within the Inert Chamber, including Laser Head, Build Area, Powder Wiper, Air Flow Gas, and X-Y Gantry.

3.4.2 Powder handling unit

For the purposes of this research, a custom-built powder-handling unit was built specifically to meet the needs of the study. The system employed a fully automated powder bed with a 200 mm diameter building area. The build piston was embedded with a conductive heater which can raise the temperature to 300°C. Powder layer as thin as 50 μm ($\pm 20 \mu\text{m}$) can be deposited by using a silicon wiper.

Our investigation revolves around applying a relatively low laser power of 4.5 W, which may be insufficient to melt metallic powder such as Ti6Al4V, as mentioned by Yadroitsev et al. [112]. This energy level may lead to the first layer failing to adhere appropriately to the substrate, instigating issues in subsequent printing layers. This adverse outcome can compromise the structural density, precision, and overall quality of the produced parts. Ensuring strong attachment of the initial layer is thus important to prevent any displacement or misalignment during the subsequent deposition process. Early trials conducted under varying processing parameters, as shown in Table 3.1, did not yield a successful bond

between the first layer and the substrate, complicating the PBF process, as shown in Figure 3.4.

Table 3.1 Impact of processing parameters (different scanning speeds) on the adhesion of the first layer in the PBF process.

Sample number	Power (W)	Scanning speed (mm/min)	Observed results
1	4.5	20	vaporisation
2	4.5	50	vaporisation
3	4.5	75	Balling
4	4.5	100	Balling
5	4.5	150	Balling
6	4.5	200	Balling
7	4.5	300	Unmelted
8	4.5	400	Unmelted

Figure 3.4 shows that the metallic powder vaporized at a maximum power of 4.5 W with a scanning speed range of 20 to 50 mm/min, indicating excessive energy. Meanwhile, a scanning speed increase from 75 mm/min to 200 mm/min balling phenomenon started to form due to insufficient power, as most energy dissipated through the substrate. Exceeding a 200 mm/min scanning speed resulted in low energy to melt the powder. This challenge requires rectification to improve the fabrication process. These observations highlight the necessity for devising a robust technique to progress the research and achieve optimal results.

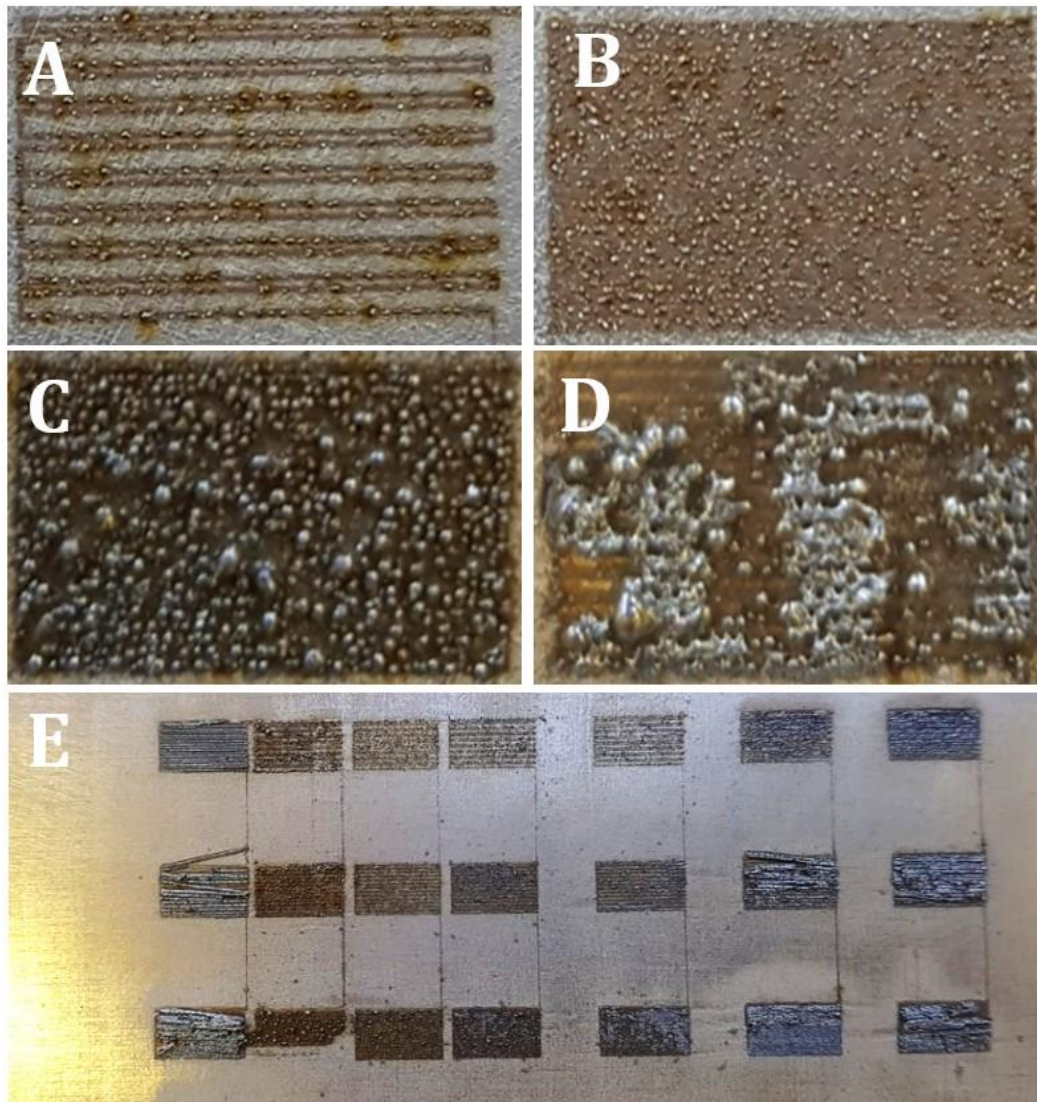


Figure 3.4 Lack of fusion (adherent) and balling phenomena under different scanning speeds (A) 25 mm/min (B) 50 mm/min (C) 75 mm/min (D) 150 mm/min (E) deposited second layer.

One of the methods we tested was a Ti6Al4V foil with a thickness of 100 μm as a substrate. A single layer of Titanium powder, 50 μm thick, was applied to the foil substrate and scanned using lasers. Nevertheless, this approach did not result in a successful fusion of Titanium powder with foil. Furthermore, the high thermal conductivity of the Ti6Al4V alloy caused rapid cooling and solidification, which made the 100 μm foil of Ti6Al4V crumble, complicating the fusion process even more.

Mushtaq Khan et al. [149] presented a method to build 3D parts made of gold successfully. This technique involved drilling holes with a diameter and depth of 1 mm and subsequently filling these holes with powder. The laser was then used to melt the powder. This melting formed a pillar structure, anchoring the subsequent layer. These structures formed the base layer, which acted as a

substrate. Adopting this approach demonstrated a strong bond in the areas covered by these holes, as shown in Figure 3.5 (c, e) shows that areas not covered by holes were subject to balling phenomena and warpage. This method ensures the stable and successful construction of 3D parts.

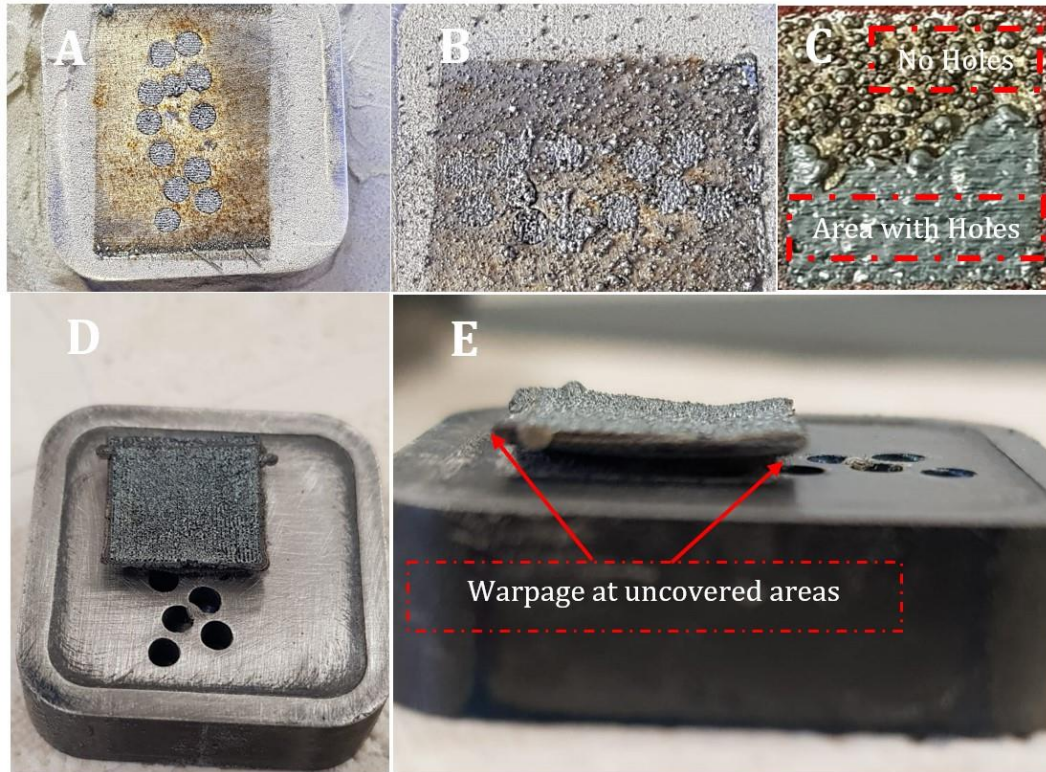


Figure 3.5: The images demonstrate the enhancements achieved when employing a substrate with holes: (A) stage one, where the material is melted inside the holes, (B) stage two, involving the deposition of a second layer, (C) after multiple layers, a smooth melt is observable on the area covered by holes while balling occurs on the flat surface, (D) a top view of the final multi-layer samples, and (E) a side view where warping is apparent on the area not covered by holes.

A steel substrate of 60 x 60 mm was manufactured. The substrate has a processing area of 40 x 40 mm, with a pattern of precisely drilled holes, as shown in Figure 3.6; each hole has a diameter of 1 mm and a depth of 0.5 mm. This uniquely designed substrate adopted played a critical role in successfully achieving the goal of this project of using the low-power diode laser as a PBF process.

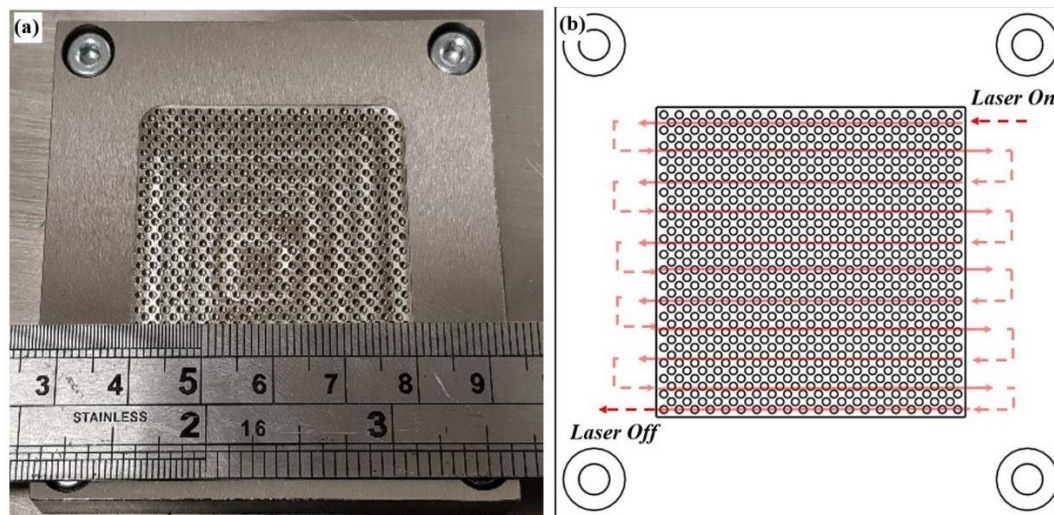


Figure 3.6: Substrate configuration employed in the current study.

3.4.3 cooling system

Diode lasers are sensitive to temperature changes; as a result, the output power and wavelength of the laser can change with temperature changes [108]. This can affect the overall performance of the PBF process, especially in this research, where multiple lasers will be used. To mitigate this, diode lasers often have temperature stabilization systems in place to keep the temperature of the laser constant during the process. One of the most straightforward techniques to control the temperature of a diode laser is to use a thermoelectric cooler (TEC). Other techniques, such as using liquid cooling, Micro-channel and spray cooling also useful to control the temperature of the diode laser, but TEC is more common due to its simplicity, reliability and low cost [150]. The TEC can be attached directly to the diode laser package, and the temperature can be controlled by adjusting the current passing through the TEC. This method is simple, effective, and widely used in diode laser systems. As a result, A thermoelectric cooler (TEC) is being considered due to its ability to control the temperature inside the laser module or the mounted. Figure 3.7 shows the necessary components of (TEC) which will be used in this project to control the temperature of 12 lasers.

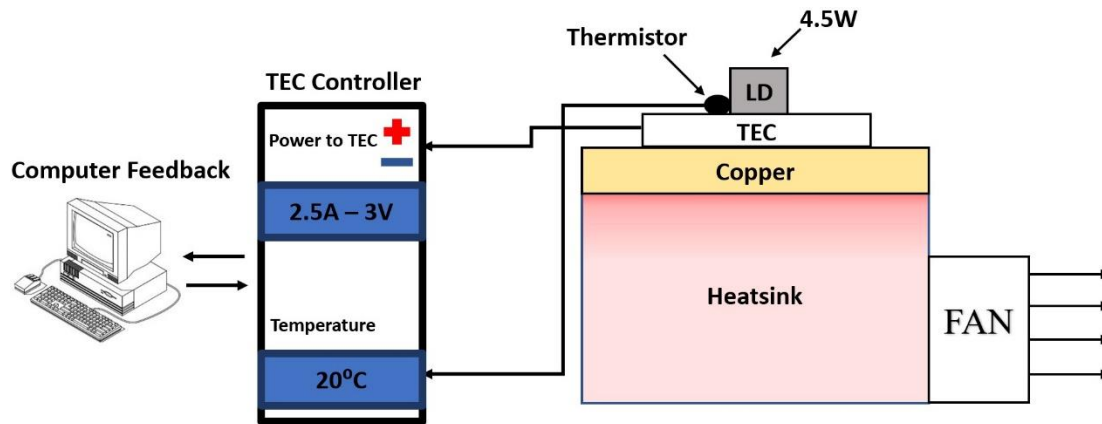


Figure 3.7 Schematic of the cooling system setup used for controlling the temperature of the diode laser shown (computer, TEC controller, TEC ,and fan heat seatsink).

A typical TEC cooling system comprises a thermoelectric cooler (TEC), a heat sink, a fan, thermistors, and a temperature controller. The TEC is made up of two dissimilar metals sandwiched between two ceramic plates. When an electric current passes through the TEC, one side absorbs heat while the other releases it, creating a temperature gradient. The heat sink is in direct contact with the hot side of the TEC and facilitates heat dissipation. Meanwhile, the temperature controller regulates the current delivered to the TEC, thereby controlling the temperature of the laser diode mounted onto the cold side of the TEC. The temperature controller monitors the temperature of the diode laser and adjusts the current applied to the thermoelectric cooler to maintain a constant temperature.

It is important to identify the Heat load (Q_c), the heat generated by the laser. The heat load must be lowered by 2.5 times TEC's Q_{max} (maximum cooling capacity) to ensure effective cooling under worst-case scenarios. The calculation of Q_c using Equation 3.1 considers the optical efficiency, which reflects the amount of electrical energy converted into light energy. This efficiency includes the electrical power used for the desired output and the wasted power not contributing to the output. As specified by the laser provider, the electrical power is 14.34 W (4.78 A x 3 V), and the optical output is 4.5 W; therefore, Q_c equals 9.84 W for each laser. Since we have 12 diode lasers, each of the two lasers is attached to a single TEC, where all the TECs share a single heat sink, as shown in Figure 3.8. Then, the total $Q_c = 19.68$ W.

$$Q_c = P_{in} - P_{out} \quad (3.1)$$

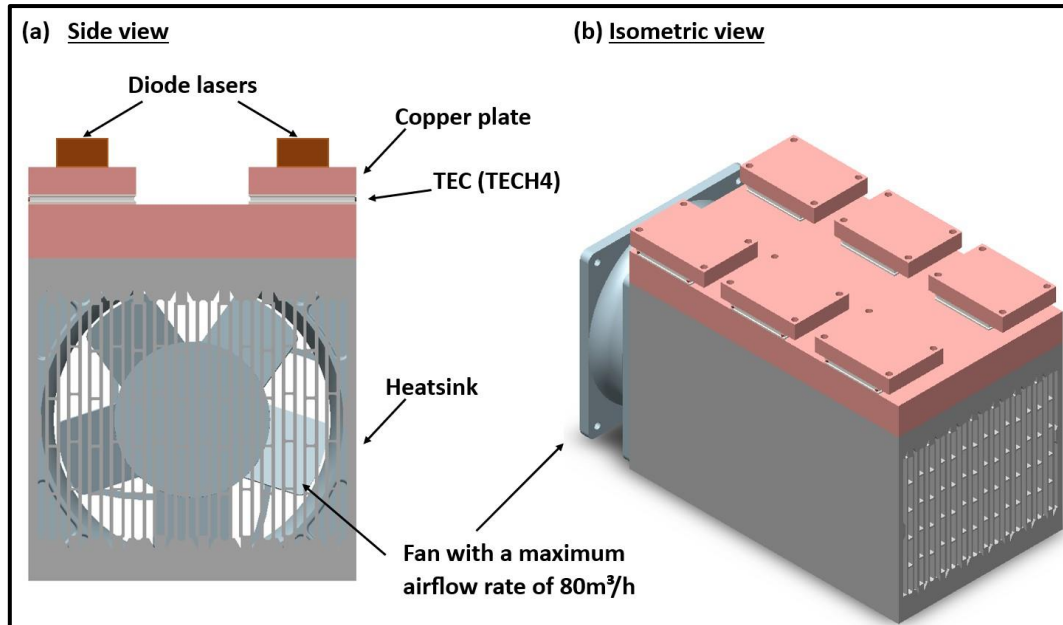


Figure 3.8: Final cooling system design to control up to 12 lasers.

When selecting a TEC module, it is important to consider its maximum cooling capacity (Q_{max}), the maximum temperature difference it can handle (ΔT_{max}), and the maximum current it can draw (I_{max}). After reviewing the specifications from the supplier (Thorlabs) in Table 3.2, the TECH4 module is the optimal choice for managing the heat load. The TECH4 module has a Q_{max} of 44.8 W, a ΔT_{max} of 66.3°C, and an I_{max} of 4.6 A at a V_{max} of 15 V.

Table 3.2 TEC data provided from supplied (Thorlabs).

Item #	I_{max}	$T_H = 27\text{ }^\circ\text{C}$			$T_H = 50\text{ }^\circ\text{C}$			AC Resistance @ 30 °C	Dimensions (See Above Diagram)					Performance Graphs
		Q_{max}	V_{max}	ΔT_{max}	Q_{max}	V_{max}	ΔT_{max}		A	B	C	D	E	
TECF1S	1.2 A	6.0 W	7.0 V	68.8 °C	6.7 W	7.9 V	77.9 °C	6.50 Ω	18.0 mm (0.71")	18.0 mm (0.71")	18.0 mm (0.71")	4.9 mm (0.19")	N/A	
TECF2S	1.9 A	9.7 W	8.2 V	66.4 °C	11.5 W	9.1 V	73.8 °C	3.30 Ω	18.0 mm (0.71")	18.0 mm (0.71")	18.0 mm (0.71")	3.4 mm (0.13")	N/A	
TECD2S	2.1 A	5.1 W	3.7 V	85.8 °C	5.7 W	4.2 V	74.7 °C	1.50 Ω	12.0 mm (0.47")	12.0 mm (0.47")	12.0 mm (0.47")	3.4 mm (0.13")	N/A	
TEC3-2.5	2.5 A	6 W	3.6 V	65 °C	6 W	4.1 V	73 °C	1.2 Ω @ 27 °C	20.5 mm (0.807")	16.0 mm (0.630")	16.0 mm (0.630")	4.0 mm (0.159")	N/A	
TECH3S	3.7 A	35.3 W	14.3 V	64.8 °C	36.2 W	15.3 V	74.0 °C	3.80 Ω	30.0 mm (1.18")	30.0 mm (1.18")	30.0 mm (1.18")	3.2 mm (0.13")	N/A	
TECL4	3.8 A	77.1 W	32.3 V	68.5 °C	85.6 W	35.6 V	76.4 °C	6.00 Ω	50.0 mm (1.97")	50.0 mm (1.97")	50.0 mm (1.97")	5.3 mm (0.21")	N/A	
TECH4	4.6 A	44.8 W	15.2 V	66.3 °C	48.2 W	16.6 V	75.7 °C	2.50 Ω	40.0 mm (1.57")	40.0 mm (1.57")	40.0 mm (1.57")	3.8 mm (0.15")	N/A	
TEC3-6	5.6 A	13 W	3.6 V	65 °C	14 W	4.1 V	73 °C	0.5 Ω @ 27 °C	24.6 mm (0.969")	20.1 mm (0.791")	20.1 mm (0.791")	4.0 mm (0.159")	N/A	
TECJ6	5.9 A	87.9 W	23.5 V	67.7 °C	103.5 W	26.2 V	76.1 °C	3.25 Ω	40.0 mm (1.57")	40.0 mm (1.57")	40.0 mm (1.57")	4.1 mm (0.16")	N/A	
TECD6	6.0 A	14.1 W	3.6 V	66.0 °C	15.1 W	3.9 V	74.5 °C	0.45 Ω	20.0 mm (0.79")	20.0 mm (0.79")	20.0 mm (0.79")	3.8 mm (0.15")	N/A	
TEC1.4-6	6.0 A	6 W ^b	1.7 V ^b	67 °C ^b	6.6 W	1.9 V	75 °C	0.27 Ω @ 25 °C	14.2 mm (0.560")	14.2 mm (0.560")	14.2 mm (0.560")	3.8 mm (0.150")	Ø5.0 mm (Ø0.20")	
TECJ8	7.8 A	123.2 W	23.6 V	66.6 °C	145.8 W	27.8 V	74.5 °C	2.40 Ω	40.0 mm (1.57")	40.0 mm (1.57")	40.0 mm (1.57")	3.7 mm (0.15")	N/A	
TECH8	8.5 A	75.6 W	14.2 V	66.2 °C	84.2 W	15.7 V	75.0 °C	1.50 Ω	40.0 mm (1.57")	40.0 mm (1.57")	40.0 mm (1.57")	3.5 mm (0.14")	N/A	
TECH11	11.7 A	101.0 W	13.5 V	66.4 °C	110.0 W	15.0 V	75.5 °C	1.05 Ω	40.0 mm (1.57")	40.0 mm (1.57")	40.0 mm (1.57")	3.2 mm (0.13")	N/A	
TECD14	13.2 A	31.8 W	3.8 V	72.0 °C	34.0 W	4.2 V	75.0 °C	0.23 Ω	30.0 mm (1.18")	30.0 mm (1.18")	30.0 mm (1.18")	3.9 mm (0.15")	N/A	

a. Performance graphs can be found on the spec sheet for this item. Click on the blue icon to view the TEC dimensions and specsheet.
 b. These values for the TEC1.4-6 are given at 25 °C.
 I_{max} = Maximum Current
 T_H = Temperature of Hot Surface
 Q_{max} = Maximum TEC Heat Load
 V_{max} = Maximum Voltage
 ΔT_{max} = Maximum Temperature Differential

In order to maintain the necessary cooling capacity for the diode, the required TEC operating current and voltage must be calculated using Equation 3.2 and Equation 3.3. The Lasers need to be cooled by 0°C degrees, and the ambient temperature is assumed to be 30°C, then the target temperature difference (ΔT) will be 30°C. This indicates that the TEC must create a temperature difference of at least 30°C between its two sides (the hot side and the cold side). Hence, the target $I = 2.09$ A, $V = 6.91$ V, and the total heat load for all 6 TECs is 204.72 W.

$$I = (Q_c/Q_{\max}) \times I_{\max} \quad (3.2)$$

$$V = (I/I_{\max}) \times V_{\max} \quad (3.3)$$

In order to select a suitable heatsink that can effectively maintain the temperature of all electronics, including lasers and TECs, it is important to ensure that the calculated thermal resistance R_{thHS} is lower than the thermal resistance of the heatsink. The supplier of the heatsink has provided a thermal resistance value of 0.1°C/W. By assuming an ambient temperature of 30°C, the resulting temperature of the heatsink would be 50.472°C, indicating a temperature increase of 20.472°C above the ambient temperature. According to Equation 3.4, if Q_h is 318 W and ΔT is 20°C, the calculated thermal resistance of the heatsink is 0.06°C/W.

$$R_{\text{thHS}} = \Delta T/Q_h \quad (3.4)$$

This value is lower than the manufacturer's specified thermal resistance of 0.1°C/W, suggesting that the heatsink should be able to handle this heat load effectively under these conditions. In addition, having an air fan heatsink will increase the cooling efficiency of the system. Figure 3.9 (a) shows the final assembly of the cooling system used in this research project. The setup comprises a copper platform, a Peltier component, and a heatsink that has a fan. The diode laser is positioned on top of the copper platform. Heat is transferred from the laser to the copper platform, Peltier component, heatsink, and finally to the surrounding air, as shown in Figure 3.9 (b). Therefore, it is crucial to monitor the ambient temperature to ensure stable operation of the system over extended periods as it will be situated in an enclosed chamber.

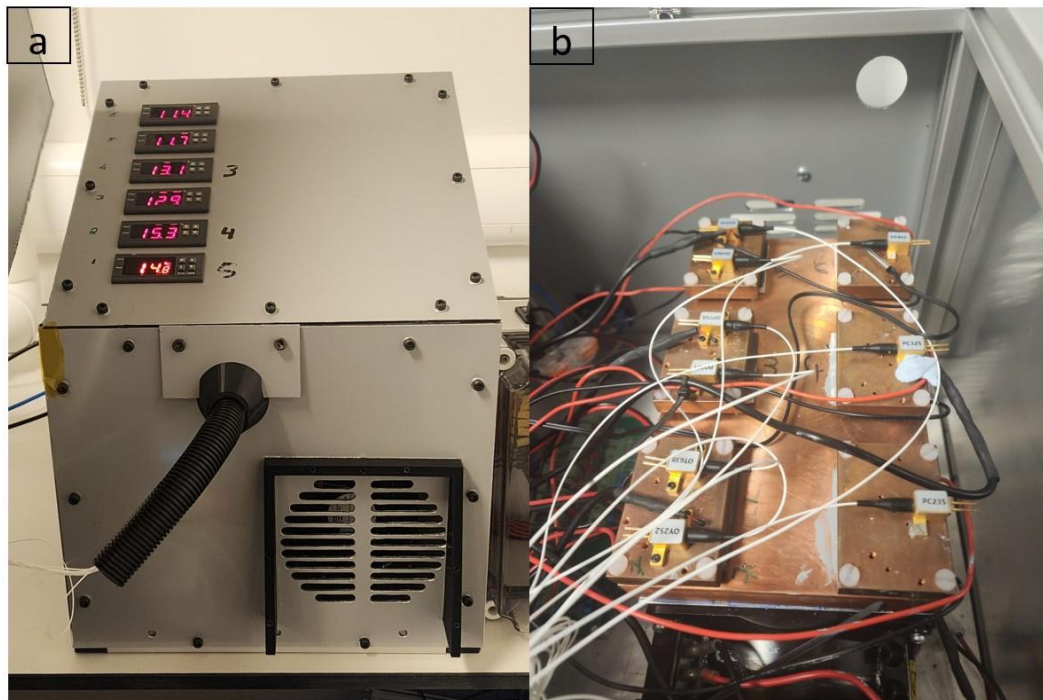


Figure 3.9: The Cooling System: (a) The exterior view of the cooling system shows the temperature control unit, (b) The internal assembly of all cooling components.

3.4.3.1 Test the Stability of the cooling system.

In this research project, a comprehensive experiment was conducted to evaluate the stability of the cooling system employed. The experiment setup, illustrated in Figure 3.10, includes ten diode lasers, a power meter, a thermometer, a power supply, and a PC. The experiment aimed to test the cooling system's efficiency and the effects of temperature on the laser's output power, current, and efficiency. To measure the laser temperature and provide the necessary data to adjust the temperature of the Peltier component, a TH10K thermistor was connected to the laser case. A power meter and Beam Profiler were placed in the laser beam path to detect the optical power and measure the threshold current, intensity, and operational voltage. The DC-power supply was used to power the fibre laser at maximum operational power, generating an equivalent optical power of 4.5 W, as shown in Figure 3.10. All data was recorded and analysed using Thorlabs' software. Additionally, the effect of temperature was investigated at 15, 20, 25, and 30°C, and the cooling system's performance was closely monitored to ensure the accuracy of the results.

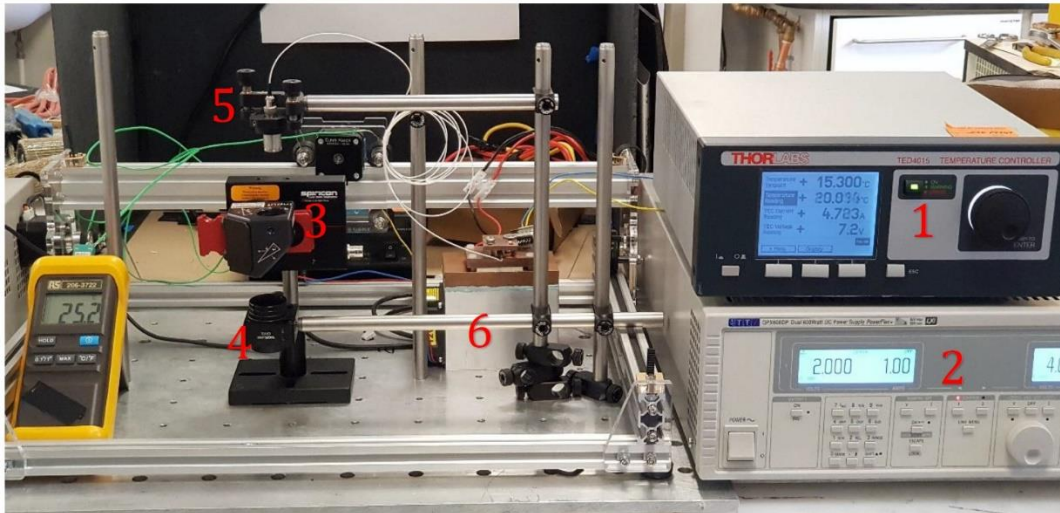


Figure 3.10: Setup Employed for Testing the Stability of the Laser Temperature and the Cooling System: (1) Laser Temperature Controller, (2) Laser Power Supply, (3) Beam Profile, (4) Laser Power Meter, (5) Laser Module, (6) Cooling Unit.

The performance of the cooling systems was evaluated in terms of their ability to maintain laser temperature stability under different operational conditions, such as high/low laser output and varying room temperatures (18-26°C). The experiment was carried out continuously for up to 6 hours at maximum power, with the temperature behaviour of 6 lasers monitored, illustrated in Figure 3.11, which presents the performance for 1 minute to make it a clear chart. When the laser is turned on, the temperature of the laser rises within 10 seconds before reaching the limit point (16°C) that activates the TEC. In 5 seconds, the TEC cools down the laser to the set temperature. Nevertheless, no noteworthy laser temperature or output power changes were observed for long periods of operation. Thermal imaging of the laser after 5 hours of continuous use, as shown in Figure 3.12, confirmed the laser temperature stability at around 5-15 degrees.

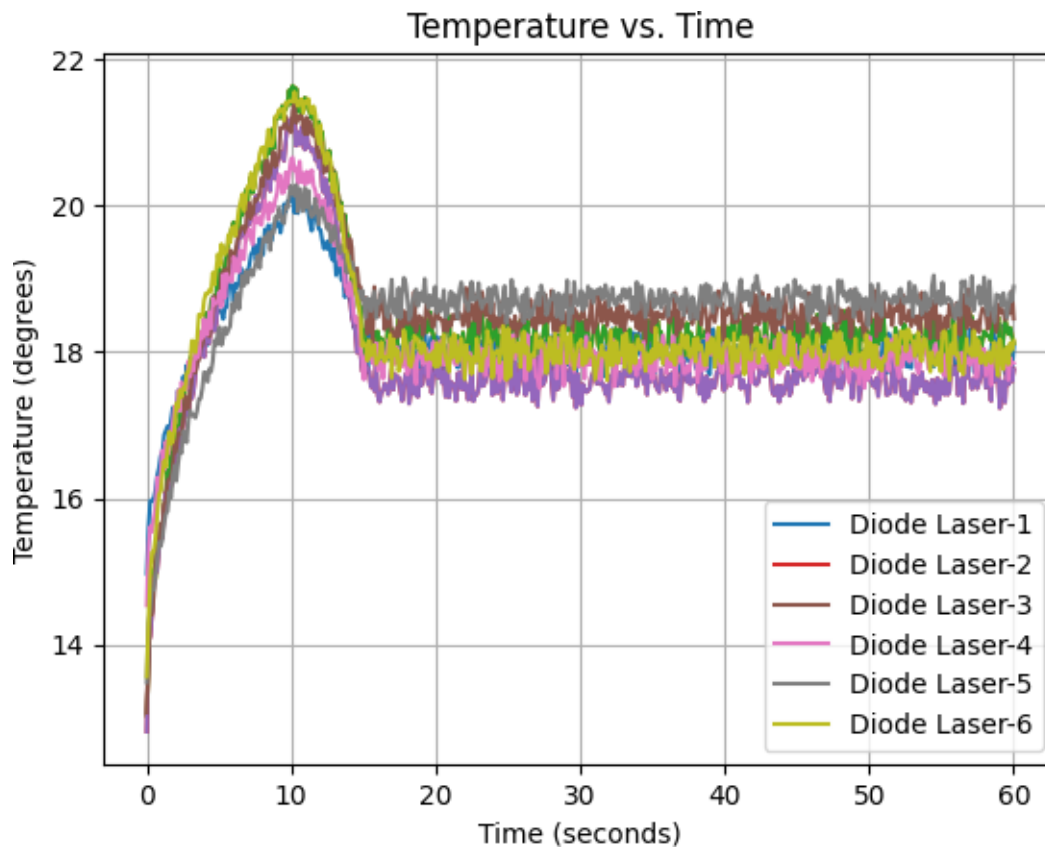


Figure 3.11: The temperature measurement of six diode lasers operating at maximum power for 1 minute, demonstrating stable temperature at 18°C when integrated into the cooling system.

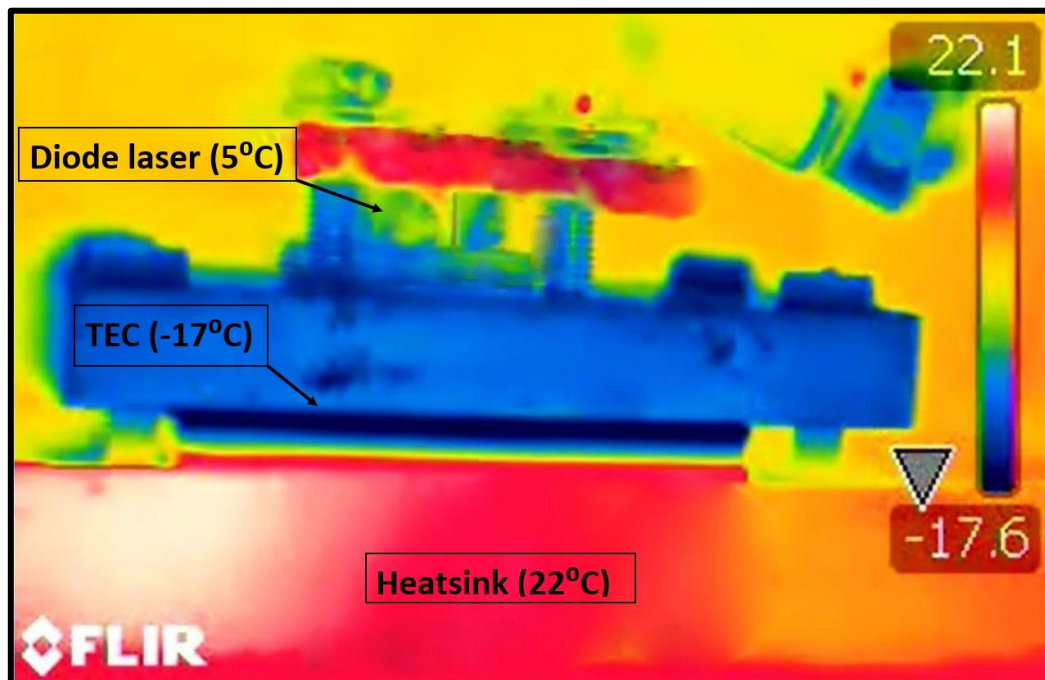


Figure 3.12: Thermal Image of Single Diode Laser assessing temperature stability after 5 Hours of Maximum Power Operation.

3.4.3.2 Effect of heat on the optical output

The optical power of the experiment is found to be highly dependent on temperature, as shown in Figure 3.13. The Power-Current curve displayed a consistent, non-linear decrease in output power as the temperature increased between 15°C to 30°C. The optical power decreased by approximately 0.1% between 15°C and 20°C, whereas it decreased by approximately 5 % at 30°C. This is due to a decrease in photon density resulting from radiative recombination, where electrons and holes combine and emit photons. As the temperature increases, the rate of this process also increases, leading to a reduction in the number of photons and, ultimately, the optical power of the laser. The temperature dependence of optical power is particularly crucial in the PBF process, where light intensity must be maintained by controlling the temperature; for that reason, the maximum temperature was set to 16°C to prevent any unwanted outcomes.

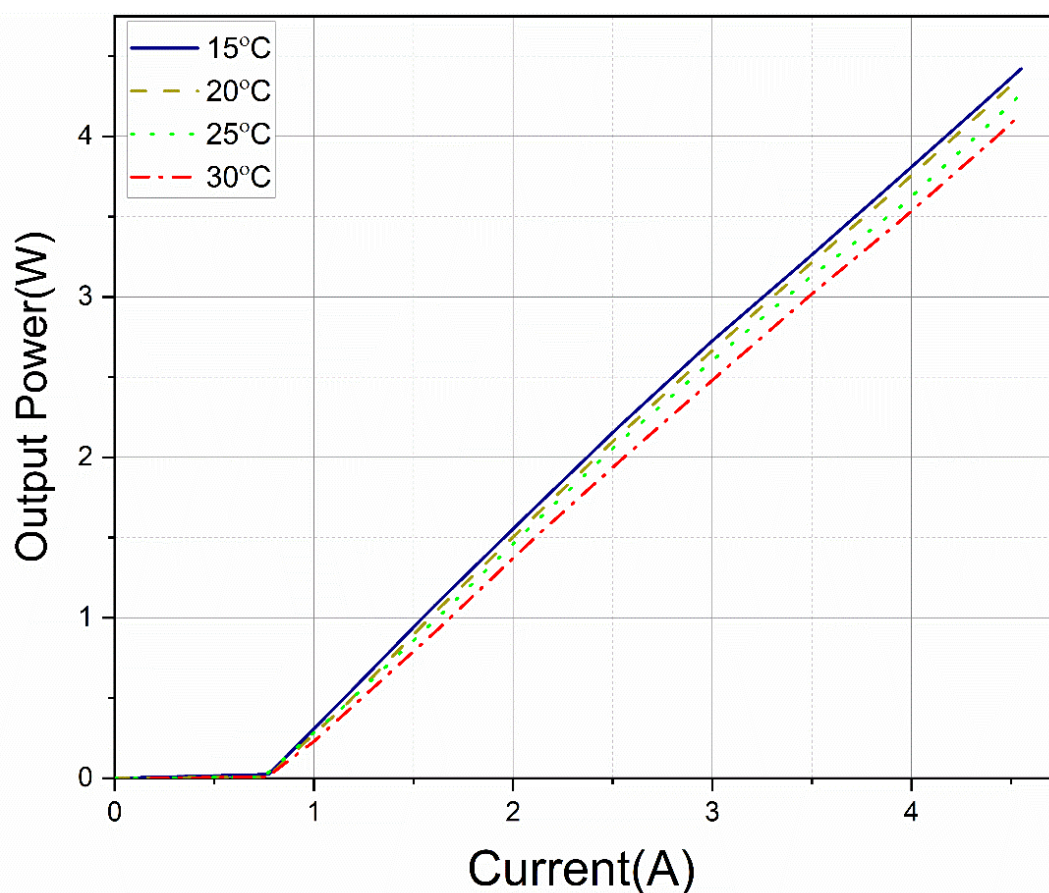


Figure 3.13: Demonstrate the effect of temperature on the output laser power (Power-Current curve, P-I) at four temperature levels (15°C, 20°C, 25°C ,and 30°C), where the laser power decreases as the temperature increases.

3.4.3.3 Effect of heat on Conversion Efficiency

Another important factor is the conversion efficiency (η_c). The impact of heat on conversion efficiency is a critical consideration for Laser systems, especially Diode lasers in the PBF process. Conversion efficiency measures how effectively a system can convert input electrical energy into optical energy power, which is obtained by calculating the ratio of the output power with the input electrical power, given by Equation 3.5. The ability of a system to convert one form of energy to another is closely tied to its conversion efficiency, which is significantly influenced by the presence of heat.

$$\eta_c = \frac{P_{opt}}{V_{op} \times I_{op}} \quad (3.5)$$

Figure 3.14 shows that the efficiency of the conversion process is affected by temperature, which is an inverse relationship between temperature and efficiency. As the temperature increases from 15 to 30°C, the conversion efficiency drops by 7%. This is consistent with the laws of thermodynamics, which predict that efficiency decreases as temperature rises. The reason for this is that the system experiences greater resistance and energy losses and thermally induced material deformations, all of which hinder the energy conversion process. Therefore, to maintain efficiency, it is essential to control the temperature carefully and prevent thermal degradation.

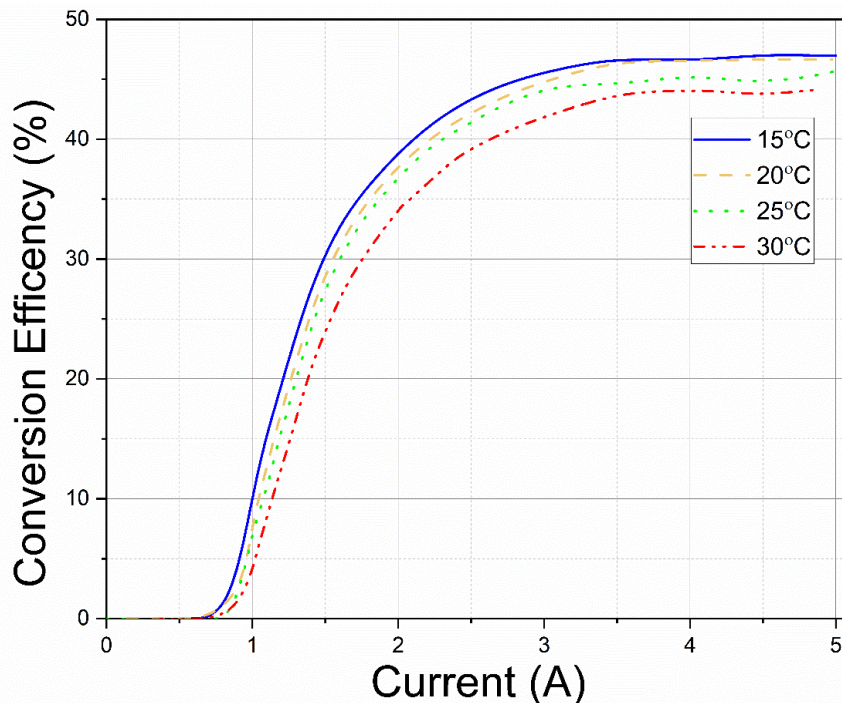


Figure 3.14: Shows the conversion efficiency of the laser (electrical to optical power), which is significantly influenced by the laser's operating temperature within the range of 15°C to 30°C.

3.4.4 Laser driver unit

The laser beam characteristics, including output power, wavelength, and heat generated by the laser module, are significantly impacted by the electrical power delivered to the laser. Laser diodes are current-driven and current-sensitive, which means that any change in the drive current will lead to a variation in the output power and wavelength. Therefore, any instability in the drive current, such as noise or drift, will directly impact the performance of the laser diode and its lifetime. Additionally, the current directly affects the temperature of the diode junction. Hence, any instability in the current source will result in junction temperature jumping, ultimately changing the laser's output characteristics. Therefore, to ensure the stability of the laser diode, a constant current source is required as the load characteristic of the diode is not static. The voltage and resistance of the diode vary with current and temperature, making it necessary to maintain a constant current regardless of the load connected to its output.

In this research project, a DPS3005 constant voltage current step-down power supply was used to deliver a constant current to diode lasers. Nine laser drivers (DPS3005 model) were assembled in a single compact box, as shown in Figure 3.15. Each is initially set to a parameter of 2 A and 3 V. Once the process starts, we manually or remotely increase the current to 4.8 A via a Bluetooth communication port, targeting an output power of 4.5 W during operation.



Figure 3.15: The laser power supply used to control each laser module individually.

In order to verify the stability of the laser output in the system we designed, the power-voltage-current characteristics were tested after a continuous lasers run for 5 hours within the operation range (voltage from 0 to 3 V) and (the current from (0 to 6 A). During the experiment, the power was measured using a laser power meter. The Light-Current-Voltage (LIV) Figure 3.16 shows a consistent alignment between the output power and the required voltage and current, as provided by the supplier. This underlines the system's ability to maintain a steady power output from the laser even after extensive use.

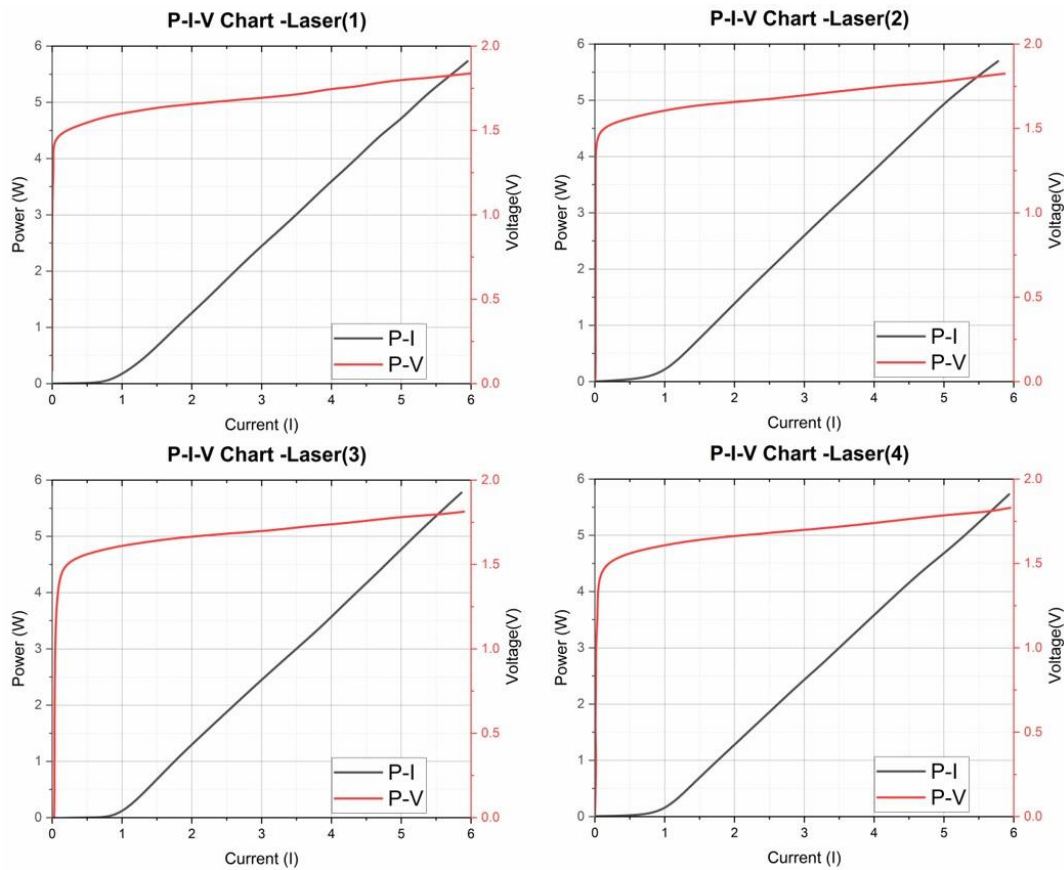


Figure 3.16: P-I-V chart for 4 different lasers shows the stability of the output power.

Monitoring the electrical performance of lasers during operation is critical. Any deviation from the manufacturer's specified voltage indicates laser damage, which requires immediate replacement and ending the process. This is because any abnormality can lead to inconsistent output power in the laser array, which impacts the energy density and can cause instability in (PBF) process. However, it is worth noting that such occurrences are rare in the experiments conducted in this project.

3.5 Laser characterisation

This section of the study aimed to analyse the characteristics of the laser beam to determine the beam profile and spot size, and to understand the impact of these characteristics on the PBF process. In order to investigate the capability to create a 3D net shape using 808 nm and 450 nm as single fibre laser sources or multiple addressable sources, the appropriate operating environment must be provided, including factors such as spot size, beam quality, and beam distribution. Power density and distribution at the focal plane are the critical key factors responsible for the efficiency and reliability of processing materials. This can be accomplished by characterizing and optimizing the laser beam using an optical system, which will be discussed in more detail below.

3.5.1 Single laser

In this research work, two multimode single fibre-coupled diode lasers (808 nm, 450 nm) were used to compare the processing of titanium feedstock. The optical ratio method (focusing lens to collimation lens) was adopted to reduce the spot size with a focal. The optical ratio method depends on using two lenses: a collimation lens and a focusing lens collimation lens, as illustrated in Figure 3.17.

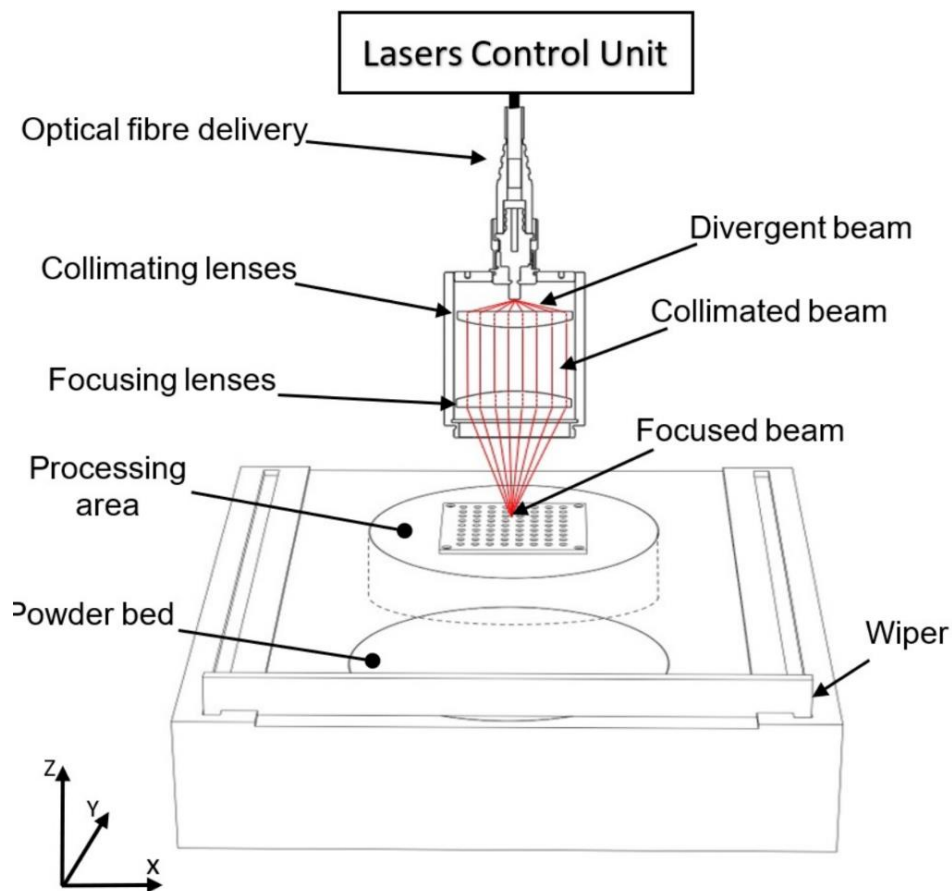


Figure 3.17: Schematic illustration of the optical system for the single diode laser [25].

As shown in the figure, the laser beam diverges and spreads out over longer distances, resulting in a more prominent spot size and lower power density at the workpiece. Therefore, the collimation lens is used to make the laser beam parallel, while the focusing lens is used to focus the laser beam onto a small spot. By adjusting the distance between the two lenses, the spot size can be reduced to a size comparable to the feature size of the PBF process. The ratio between the focal lengths of the two lenses determines the optical ratio. The smaller the ratio, the smaller the spot size that can be achieved.

The 808 nm laser has a maximum power of 3.5 W, delivered using an optical fibre with a numerical aperture (N.A.) of 0.22 and a core diameter of 105 μm . The output beam was collimated to a diameter of 8 mm, with full angle beam divergence of 0.001° using a fixed optical collimator (Thorlabs F810FC-850) with a focal length of 36.20 μm . Finally, the beam was focused using an achromatic doublet lens (Thorlabs - AC254-060) with a focal length of 33 to a spot size of 175 μm ($1/e^2$) at a focal distance of 60 mm.

The 450 nm module has a maximum laser power of 3.5 W, delivered using a fibre optic with N.A. of 0.22 and a core diameter of 200 μm . First, the beam was collimated to a diameter of 6.7 mm with a full angle beam divergence of 0.001° using a fixed collimator (Thorlabs F810SMA-405). Then an achromatic lens (Thorlabs - AC254-030) focused the beam to a spot size of 175 μm ($1/e^2$) and a focal distance of 30mm. Both lasers were characterised using a scanning slit (NanoScan2sPryo/9/5), As shown in Figure 3.18 (a).

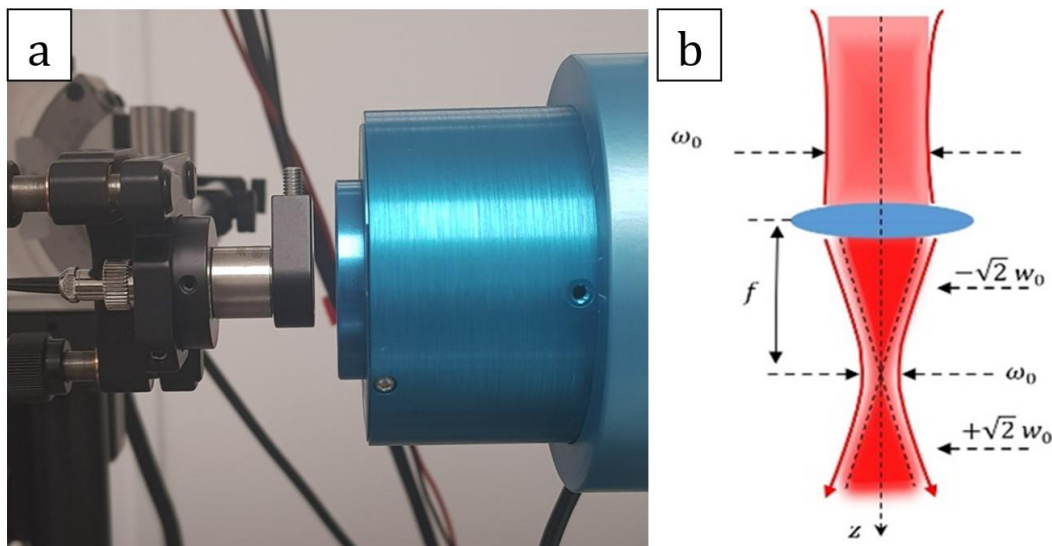


Figure 3.18: The setup of the beam profiler to characterise the laser beam using different optical setups.

The beam parameters were calculated by measuring the beam profile at several axial positions Z , calculating beam width value $w(z)$, and then minimum square

fitting was used to obtain w_0 , z_0 , and M^2 . The beam radius was measured as a function of Z position by measuring the laser diameter along the Z-axis with an incremental increase of 10 μm until the ISO standard (11146-1) distance was reached, as shown in Figure 3.18 (b).

$$M^2 = \frac{\pi \times w_0^2}{2\lambda \times 2Z_r}$$

Where: w_0 is the beam diameter at the beam waist (mm), λ is the wavelength (nm), Z_r is the Rayleigh length (mm), and M^2 is the beam quality. The beam profile of the 808nm (Figure 3.19-a) and 450 nm (Figure 3.19-b) lasers have a Gaussian distribution profile, demonstrated in Figure 3.19 by superimposing a Gaussian fit over the measured profile in red.

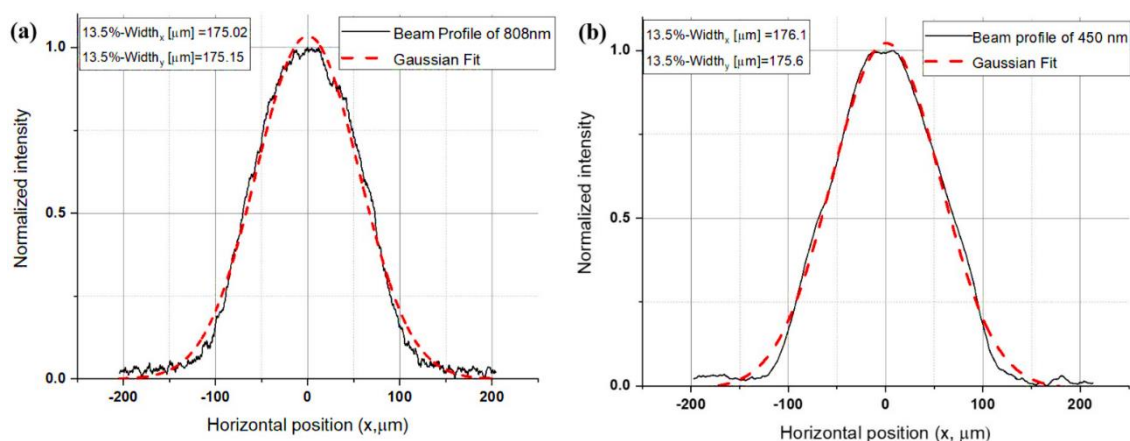


Figure 3.19: Beam profiles and Gaussian fit of (a) 808 nm and (b) 450 nm.

Therefore, both lasers have a spot size of 175 μm , which gives an intensity of 145 W/mm^2 when 3.5 W is used, as presented in Table 3.3.

Table 3.3: Specifications of Diode lasers used in this research investigation [25].

Parameters	(NIR) 808nm	(Blue)450nm
Laser Specifications		
Laser Power	3.5 W	3.5 W
Wavelength	808 nm	450 nm
Core size	105 μm	200 μm
Numerical Aperture (N.A)	0.22	0.22
Characterised Laser Beam for Processing		
Collimating	8 mm	6.7 mm
Focusing	175 μm	175 μm
Intensity	145 W/mm^2	145 W/mm^2

3.5.2 Multiple individually addressable laser sources (CTP)

Multiple individually addressable lasers have evolved from previous single laser source work. Fibre-coupled diode sources are coupled into a bespoke laser head rather than a single fibre-coupled diode laser or emitter bar. Multiple individually addressable laser sources traverse the powder bed in a parallel, illustrated in Figure 3.20 (a). Short wavelength (808 nm) 5 W fibre lasers are used. The short wavelength ensures strong absorptivity, whilst the fibre delivery ensures good beam quality and allows the laser diodes to be located away from the processing environment. Figure 3.20 (b) indicates that the fibre-coupled laser diode modules are connected to a customized 2-D fibre array head (2D-FAH). The 2D-FAH consists of a 2D array of v-groove lines. Each linear array has 50 multimode fibre channels with a 105 μm core and a numerical aperture of 0.22 NA. The overlap of adjacent melt pools is essential for high part density, as shown in Figure 3.20 (c). As such, the fibres were positioned at 127 μm centre-to-centre spacing, giving a total width of 6.35 mm. An imaging lens was used to relay emitted light from the v-groove array and focus onto the powder bed. The relay optics collimate and focus each beam from the 2D FAH at a magnification of 0.6. The laser head assembly was designed to allow for in-situ pre/post-heating or re-melting during the process. A post-heating scanning strategy was used to homogenize the

temperature field and reduce the cooling rate by using the second linear array as heat input after the first array (melting lasers) passed by.

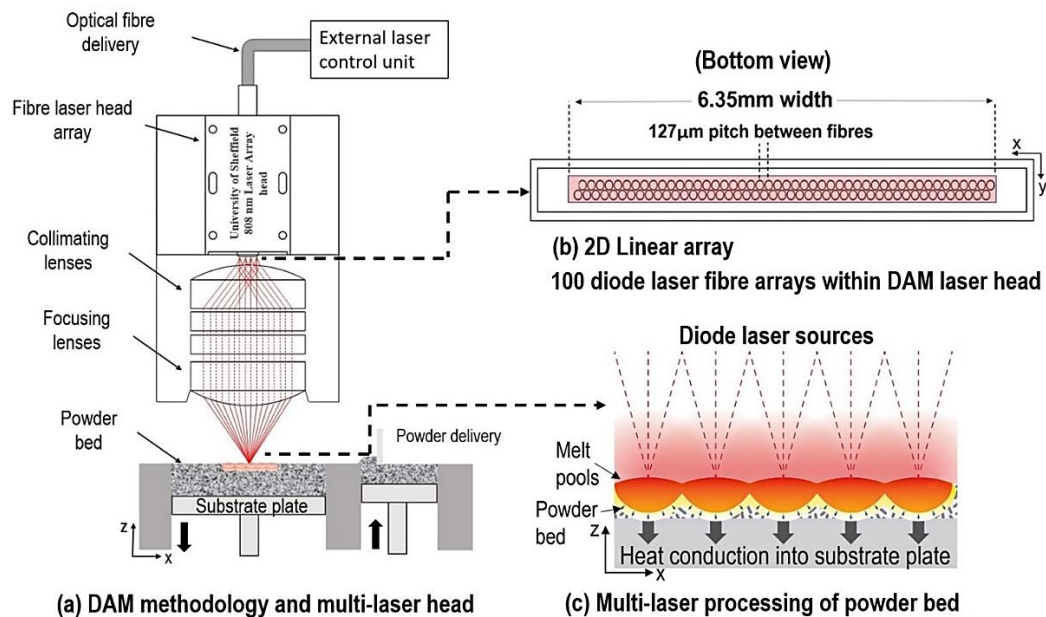


Figure 3.20: (a) Schematic of DAM (b) configuration of laser head beam profile (c) schematic of melt pool [151].

Though the developed laser head has the potential to use up to x100 laser sources simultaneously during DAM processing, only x10 lasers will be utilised for this study in order to better understand on a small-scale multi-laser interaction and effect on melt pool formation.

As shown in Figure 3.21, the laser head is mounted within a bracket and installed in the optical system. Precise alignment is important to ensure consistent positioning and alignment of the beams. Two lasers (numbers 1 and 50) located on opposite ends of the array are activated to verify the alignment. The laser head is mounted on a micro-alignment stage for accurate adjustment and characterization, as shown in Figure 3.21. A beam profiler is fixed in front of the laser head to capture and analyse the laser head array beams. The alignment process continues until the spot sizes of lasers number 1 and 50 match, indicating that the entire laser array is appropriately aligned and consistently positioned.

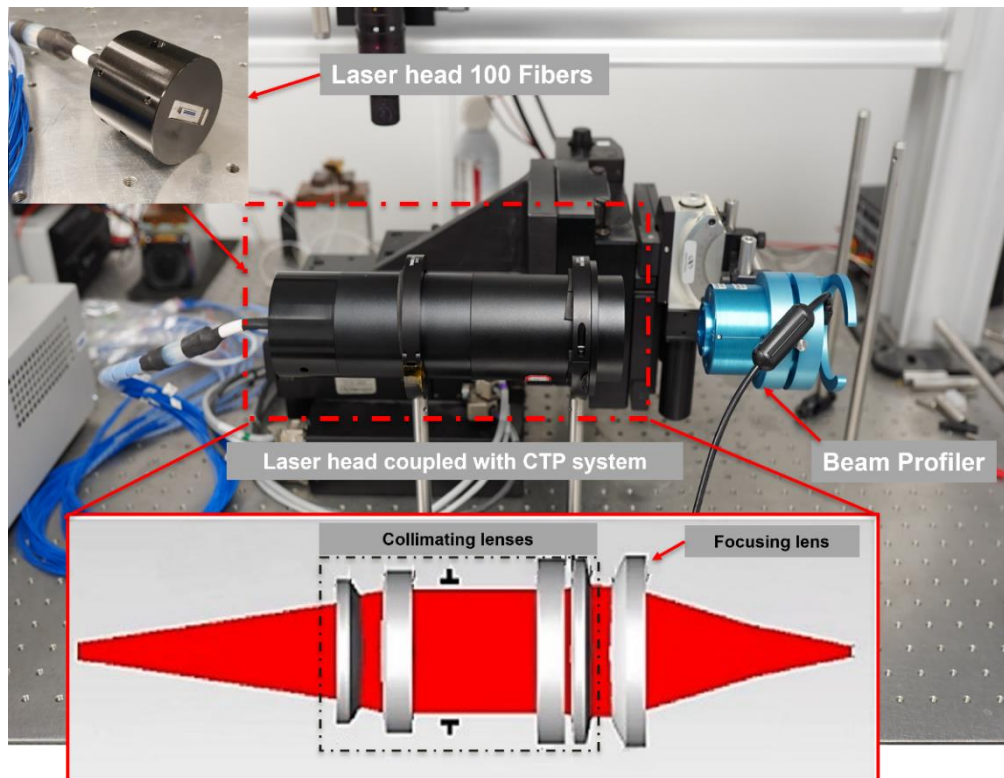


Figure 3.21: The setup of the beam profiler used to characterise the 2D array laser head.

Based on the beam profile data, each beam is focused on an individual Gaussian profile with a spot size of $65 \mu\text{m}$ to give a total width of 3.5 mm at a focal length of 63.5 mm. In this study, three laser beam profiles were activated within the laser head laser profile-1 (LP1), profile-2 (LP2) and profile-3 (LP3).

Activating x10 lasers within an x2 array with a spacing of $38.1\ \mu\text{m}$ between the beam (centre to centre) will lead to a rectangle processing area of ($0.381\ \text{mm} \times 0.13\ \text{mm}$), as shown in Figure 3.22. This should enable either a pre/post-heating effect or re-melt of the melt pool during scanning and perhaps reduce the melt pool cooling rate, as second array beams will follow the melting beams.

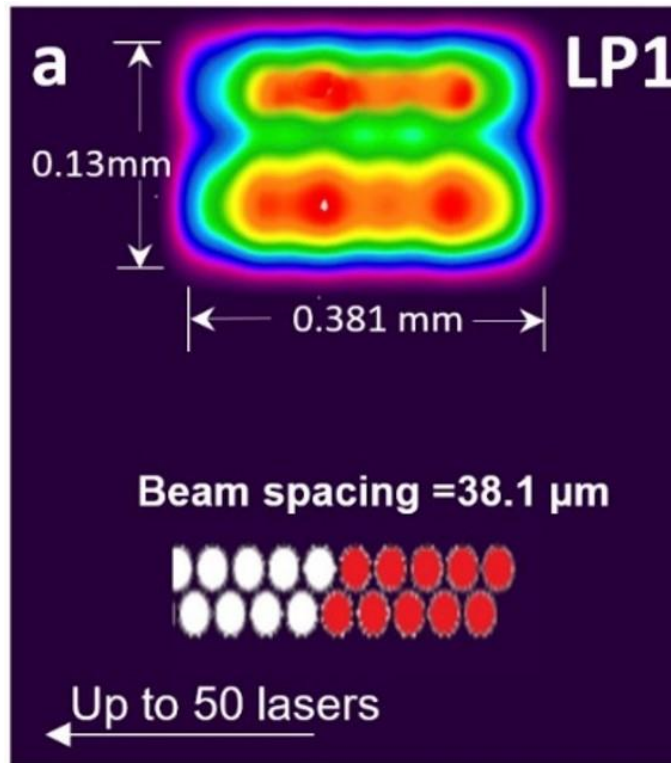


Figure 3.22: shows the measured beam profiles for ten activated laser fibers within the 2D laser head array (LP1), illustrating their shape and beam specifications [151].

The second profile LP2 uses a present single line array of x10 lasers, with a spacing of 1.72 mm, creating a stripe line with a width of 1.72 mm, as shown in Figure 3.23. This should increase write width compared to LP1 but increase the cooling rate.

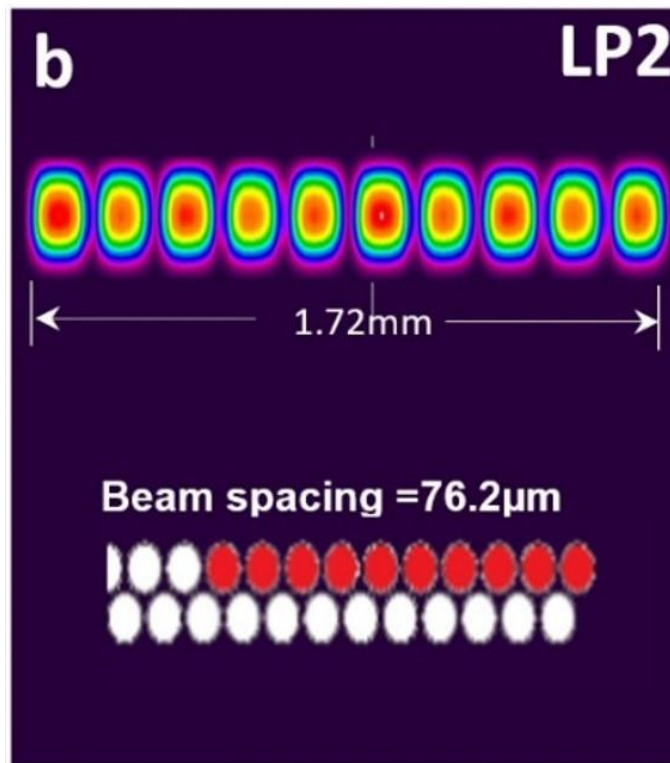


Figure 3.23: Shows the measured beam profiles for ten activated laser fibers within the 1D laser head array configuration (beam spacing 76.2 μm), which propagate a single stripe beam called (LP2) [151].

LP3 uses a single line array with a gap between each laser (254 μm centre-to-centre) to create the largest write-width of 2.5 mm with a pitch distance of 152.5 μm (when using x10 lasers), as shown in Figure 3.24.

As described in previous sections, a constant current laser driver was used to control each laser source and vary power as the laser assembly traverses the powder bed to create the component using a two-axis gantry system.

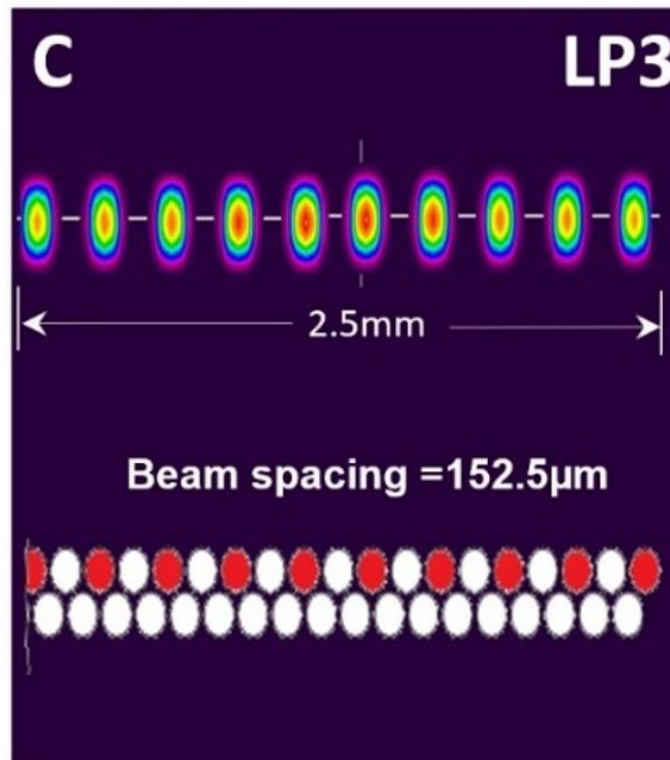


Figure 3.24: shows the measured beam profiles for ten activated laser fibers within the 1D laser head array configuration, with a single fiber spacing (one on/one off- beam spacing $152.5 \mu\text{m}$), propagating individual single beam spots called (LP2) [151].

3.6 Material

Gas-atomised Ti6Al4V powder (supplied by LPW Ltd, UK) with a particle size of 15–50 μm was used in this work. The chemical composition corresponds to the ASTM standard F13608, and Physical properties were considered at 1604 $^{\circ}\text{C}$, as presented in Table 3.4. In this research, the alloy's average thermal properties at the approximate powder bed operating temperature are used at 1604 $^{\circ}\text{C}$ (1877K), which is our temperature of interest. This method follows the same practice carried out by Wang et al. [152] and Thomas et al. [146]. However, in this study, it will also be assumed that the thermo-physical properties are unchanged by melting.

Table 3.4: The chemical composition and properties of Ti-4Al-4V.

Chemical composition								
Element	Al	V	Fe	O	C	N	H	Ti
wt.%	5.8	3.8	0.3	0.15	0.02	0.05	0.03	Balance
Physical Properties at 1604 $^{\circ}\text{C}$								
Specific heat capacity (C_p)						526 ($\text{K Jg}^{-1}\text{K}^{-1}$)		
Melting Temperature (T_m)						1604 ($^{\circ}\text{C}$)		
Material density (ρ)						4430 (Kg/m^3)		
Thermal diffusivity (D)						6×10^{-6} (m^2/s)		

SEM images demonstrating the shape and size distribution of powder particles are presented in Figure 3.25 (a). Most particles are spherical. Their size distribution was measured using a laser particle distribution analyser (Malvern Mastersizer 3000 PSA). The result was (d_{10} : 23.5 μm ; d_{50} : 33.3 μm ; d_{90} : 47.3 μm) as presented in Figure 3.25 (b).

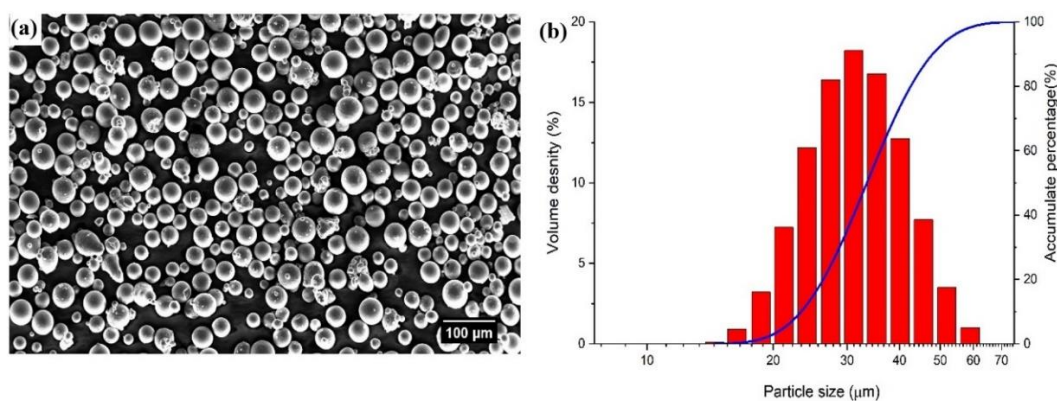


Figure 3.25: (a) Ti-6Al-4V powder morphology; (b) particle size distribution.

3.7 Characterisation

3.7.1 Archimedes Density Test

The density was measured using a Mettler Toledo density metre to characterise the manufactured samples based on the Archimedes principle, as suggested by Spierings et al. [153]. Each sample was weighed individually in the air and then in the water. Then, percentage densities were calculated by comparing the samples' densities to commercial Ti6Al4V, which has a 4.43 g/cm^3 density. All manufactured samples were measured five times independently, and the results were averaged. Samples exhibiting densities $> 90\%$ were hot mounted, polished, and cross-sectioned to be examined visually for porosity, Microstructure morphology, XRD and mechanical properties.

3.7.2 Optical 3D Microscope (Surface Roughness)

The surface roughness of Ti6Al4V samples with densities exceeding 90% was quantified using an optical 3D microscope (Alicona infinite focus). The test area measured $10 \text{ mm} \times 10 \text{ mm}$ and was examined using a x10 magnification lens. Three measurements were taken at intervals of 4 mm on the top surface, and the average roughness (Ra) was calculated for each location. The resulting Ra values were then correlated with the relevant processing parameters.

3.7.3 Samples Preparation

The following methodology was employed to prepare the selective laser melted (SLM) Ti6Al4V samples for microstructure analysis without etching. The preparation involves many steps, including (a) sectioning, (b) hot-mounting, (c) grinding, (d) polishing, and (e) cleaning and storage. The sectioning process was performed using a diamond saw machine [Sectom - 50, Struers UK Ltd] at a speed of 3000 RPM with a feed rate of 0.02 mm/s, followed by the hot mounting method. In the hot mounting process, the sample was immersed in a conductive thermoset polymer using SimpliMet Machine [Buehler UK Ltd, London, UK] at 600°C and 7 bar pressure. Next, the samples were ground and polished using a Buehler Automet Grinder-Polisher with P600, P1200, and P2500 grit papers. During the grinding process, a force of 27 N was applied for 1 minute with a plate speed of 150 rpm and a head speed of 60 rpm in a complimentary head rotation direction and then polished with diamond suspensions using $6 \mu\text{m}$, $3 \mu\text{m}$, and $1 \mu\text{m}$ diamond grits until a mirror-like finish was obtained. To relieve the microstructure of Ti6Al4V, a mixture of colloidal silica (OP-S) and hydrogen peroxide (30%) was used for 10 Minutes at a force of 15 N with a plate speed of

150 rpm and a head speed of 60 rpm. Lastly, the samples were cleaned with ChemoMet polishing cloth with water for 10 minutes. The prepared samples were then stored in a desiccator with the surface protected using a metallographic cap.

3.7.4 Scanning Electron Microscopy (SEM) and Energy Dispersive X-ray Analysis (EDX)

Surface morphology, surface roughness, and Microstructural analyses were conducted using a scanning electron microscope SEM (Tescan VEGA3) equipped with backscattered electron diffraction (EBSD) detector. The surface morphology and surface roughness images were taken at a beam intensity of 15 kV to obtain high-resolution images at a distance of 15 mm under different magnifications (x100, x200, X500 and X1000). The EBSD technique was used in this study to analyse the crystallographic orientation of samples with an area of 809 $\mu\text{m} \times 606 \mu\text{m}$ and a step size of 0.5 μm . The diffraction patterns obtained from the backscattered electrons were collected and processed using EBSD software to determine the crystallographic orientation of the material.

3.7.5 X-Ray Diffraction Analysis

X-ray diffraction (XRD) analysis using Cu K α radiation was conducted with the (D2 Phaser -Bruker) instrument. The Cu tube was set to 40 kV and 45 mA. An incoming X-ray was filtered with a 1 mm X-ray mask, which was then emitted outward with a 2 mm divergent slit. The analysis was performed over a scanning range of 2 θ angles, typically between 20 $^\circ$ and 100 $^\circ$, with a step size of 0.02 $^\circ$.

3.7.6 Nanoindentation Test

The hardness and elastic modulus of fabricated samples were measured using the nanoindentation technique suggested by Fischer-Cripps [154]. Nanoindentation tests were performed using a Triboindenter with a Berkovich tip of 100 nm radius and at an angle of 142.3 $^\circ$. The test was performed with a 4 \times 4 matrix using an open-loop trapezoidal method of loading and unloading, with 5s hold per stage at 13000 μN maximum loads. With load and depth plots obtained from the experiments, the sample elastic modulus was calculated using:

$$\frac{1}{E_r} = \frac{1 - \nu_i^2}{E_i} + \frac{1 - \nu_s^2}{E_s}$$

Where Poisson's ratio of indenter $\nu_i=0.07$; Elastic modulus of indent $E_s=1140$ GPa; Poisson's ratio of Ti- 6Al-4V $\nu_s = 0.342$. The hardness is calculated by the following:

$$H = \frac{P_{max}}{A}$$

Chapter 4: The impact of wavelength on Absorbance

Summary

This chapter discusses several important factors related to metallic powder, such as (type of material, particle size, and powder quality) to expand the knowledge and find the optimal powder characteristic, improving the process efficiency.

The absorptivity measurements are conducted on three materials (copper, Ti6Al4V, and AlSi12) with different particle sizes and qualities. These measurements are essential for improving process efficiency and a better understanding of the interaction between radiation and powdered materials, as they provide more accurate data than relying on absorption data for bulk materials found in the existing literature. This chapter also includes findings that will be used to calculate the normalized required energy density.

4.1 Introduction

The interaction between a laser and powder materials involves multiple physical phenomena, such as absorption, reflection, scattering, melting solidification, phase transformation, evaporation, and thermal conductivity. The process is affected by various factors, including the material properties of the powder (e.g., the size, shape, and quality of the particles) and the laser characteristics (e.g., wavelength, spot size, and power). Numerous studies have highlighted the significance of wavelength when considering laser radiation-material interaction [155][156]. When the laser beam hits the powder surface, the laser radiation (I_0) directly impacts the surface particles. Each particle surface interaction results in radiation absorption (A) and reflection (R). The material properties quantify the extent of reflection occurring on the surface. The energy of the reflected beam (I_r) decreases due to Fresnel absorption, while the rest travels through the powder's pores and reaches the inner particles, as shown in Figure 4.1. The reflected beam from particles located at deeper levels within the powder intensely absorbs the radiation, functioning as pore-sinks.

Furthermore, this absorption process is heavily dependent on the wavelength of the laser beam, as certain wavelengths are absorbed more efficiently than others. As a result, surface particles experience heating due to laser radiation, and subsequent heat propagation is conducted through normal means (Q_c). While some heat is dissipated into the environment, it is crucial to consider the wavelength to optimize the process and comprehend the complex interaction between radiation and the powder material.

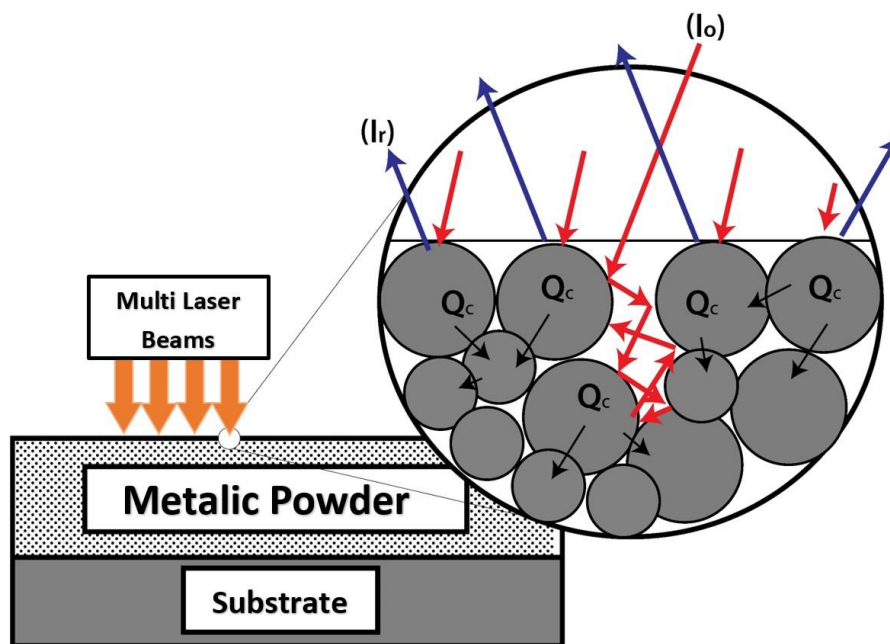


Figure 4.1: Absorption and Reflection of laser beam from a Powder Bed.

In previous studies, various methods were conducted to enhance process efficiency. By focusing on material modification (such as adding nanoparticles [157] or ageing the powders [158]) and/or optimizing the processing parameters of PBF (such as defocusing the laser beam to scan a larger area [159][121], optimizing scanning strategies [160]). Only a few studies focus on the wavelength to improve processing efficiency. Furthermore, previous studies have depended on the absorptivity of bulk materials for modelling or numerically calculating to identify the processing region, like the normalization method. As a result, it is necessary to investigate the influence of wavelength on the absorptivity of PBF materials under various conditions (new or aged powder, particle size, and different wavelengths) to utilize the best findings for improving process efficiency. Also, measuring the actual absorptivity of the powder is crucial rather than relying on absorption data for bulk materials found in the existing literature. In this chapter, the absorptivity measurement has been conducted on three different materials: copper, Ti6Al4V, and AlSi12. Copper has two different particle sizes, 15-75 μm and +212 μm , while AlSi12 was studied with a 15-45 μm . Ti6Al4V has two different particle sizes, 15-45 μm and 90-120 μm . The absorptivity value found in this study of Ti6Al4V under the spectrum of 808 nm and 450 nm will be used to calculate the normalized required energy density.

4.2 Experimental procedure

The metallic powders were compressed into a small cup with a diameter of 10 mm and a depth of 5mm. The surface was then levelled using a glass microscope slide to ensure a flat top. The absorptivity of Ti6Al4V powder was measured and compared with copper and AlSi12 powders. A spectrophotometer (Ocean HDX Vis NIR) utilises spectralon as a 100% reflective reference material. The measurement was performed at room temperature within the 380–1100 nm wavelength range. To calculate absorptivity as a function of wavelength, Equation 4.1 was used, assuming no transmission and taking the average of 10 reflective measurements in this study.

$$A(\%) = 100 - \text{measured reflectivity} (\%) \quad (4.1)$$

4.3 Results and Discussions

4.3.1 Effect of the Wavelength on the Materials

Figure 4.2 shows the optical absorption coefficients for common/challenging SLM materials, such as Ti6Al4V, copper, and AlSi12, within the 400 to 1100 nm wavelength range. Figure 4.2 shows an increased absorptivity for all materials at a shorter wavelength. The powder absorption varies significantly with the laser wavelength. For example, the absorptivity of Ti6Al4V increases by 14% when using a 450 nm laser source compared to a 1064 nm fibre laser.

Absorption increases substantially more for highly reflective and conductive materials like copper and AlSi12. The absorption for copper increases from 9% at 1060 nm to 26% at 808 nm, an increase of approximately 189%. Moreover, the absorption at 450 nm is 88%, a remarkable 78% increase compared to the 1064 nm fibre laser. Similarly, the absorption of AlSi12 also increases at shorter wavelengths, with 19% absorption at 1060 nm, 26% at 808 nm, and 48% at 450 nm. The increase in absorption from 1060 nm to 450 nm for AlSi12 is approximately 153%.

The improved absorption at lower wavelengths, such as 450 nm, can be attributed to the fact that shorter wavelengths have higher photon energies. As a result, these higher-energy photons are more effective at interacting with the material, leading to greater absorption of the laser energy. This enhanced absorption is particularly noticeable in highly reflective and conductive materials, such as copper, due to their strong interaction with light at shorter wavelengths. Additionally, shorter wavelengths may enable more efficient energy transfer to the material, facilitating better overall performance in SLM processes [21,24,155,156].

In this study, which focuses on Ti6Al4V, the absorptivity at 808 nm and 450 nm will be utilized to calculate the normalized energy density.

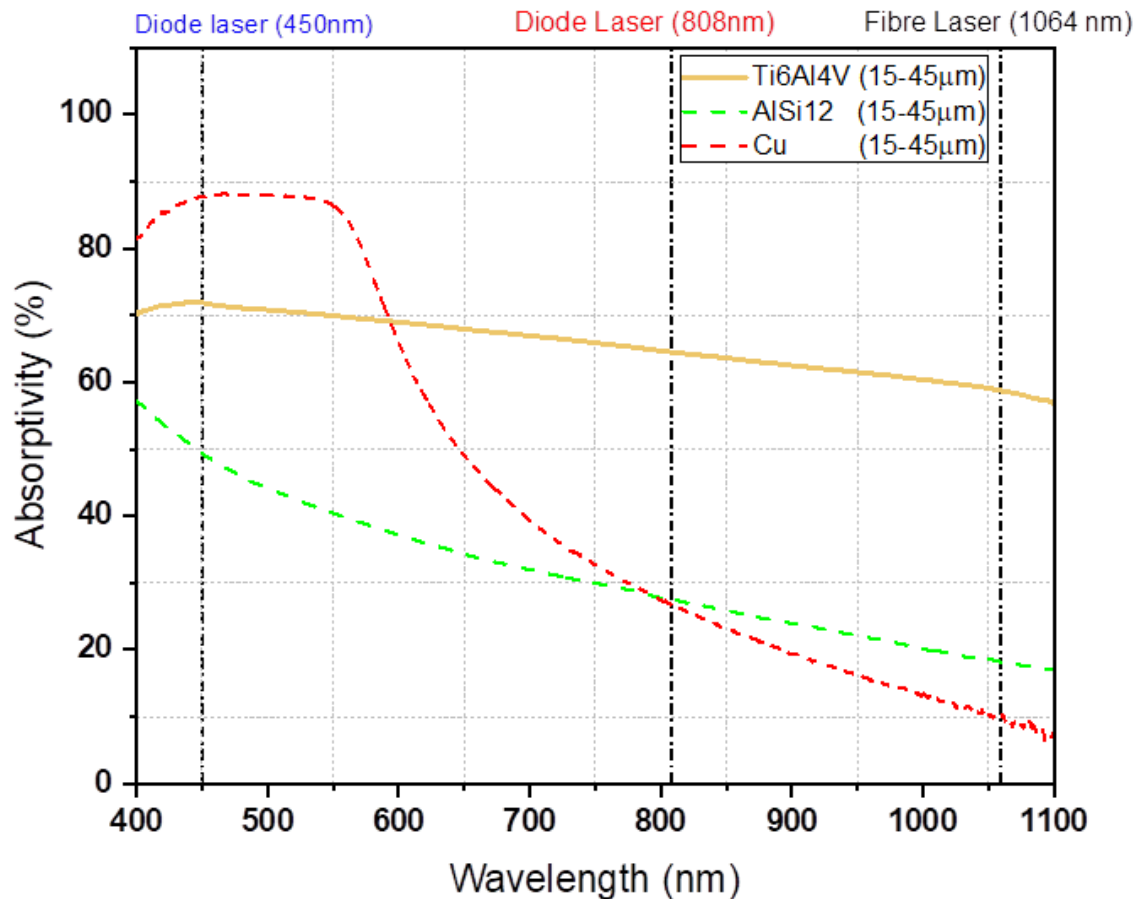


Figure 4.2 The optical absorption of Ti6Al4V, AlSi12 and Cu within the 400 to 1100 nm wavelength range.

4.3.2 Comparative Analysis of Laser Absorption in Copper and Ti6Al4V Powders with Different Particle Sizes

The influence of average particle sizes and distributions on absorptivity was investigated using pure copper and Ti6Al4V powders. The average particle size distribution significantly impacts the packing density, which in turn influences the laser absorption of the material. By measuring the packing density of the materials, it has been noticed that the powder with fine average particle size distribution led to high-density packing compared to large average particle powder distribution, which has been reported in previous research [161][162]. The packing density for particles between 15-45 μm sizes is 8.87 g/cm^3 for copper and 4.34 g/cm^3 for Ti6Al4V. In contrast, larger particles exhibit a packing density of 8.51 g/cm^3 for copper and 4.01 g/cm^3 for Ti6Al4V.

As a result, a noticeable decrease in absorptivity is observed for larger particle size distributions compared to finer particle distributions for copper and Ti6Al4V, As shown in Figure 4.3. In the case of copper, the absorptivity decreases from 11%

to 9% at 1054 nm, 27% to 12.7% at 808 nm, and 89% to 77% at 450 nm when using a large particle size distribution compared to a fine size. Similarly, Ti6Al4V demonstrated a decrease in absorptivity from 65% to 49% at 1054 nm, 69% to 52% at 808 nm, and 70% to 62% at 450 nm. The differences in absorptivity between copper and Ti6Al4V can be explained by their distinct material properties, such as thermal and electrical conductivities, which influence the interaction of radiation with the material.

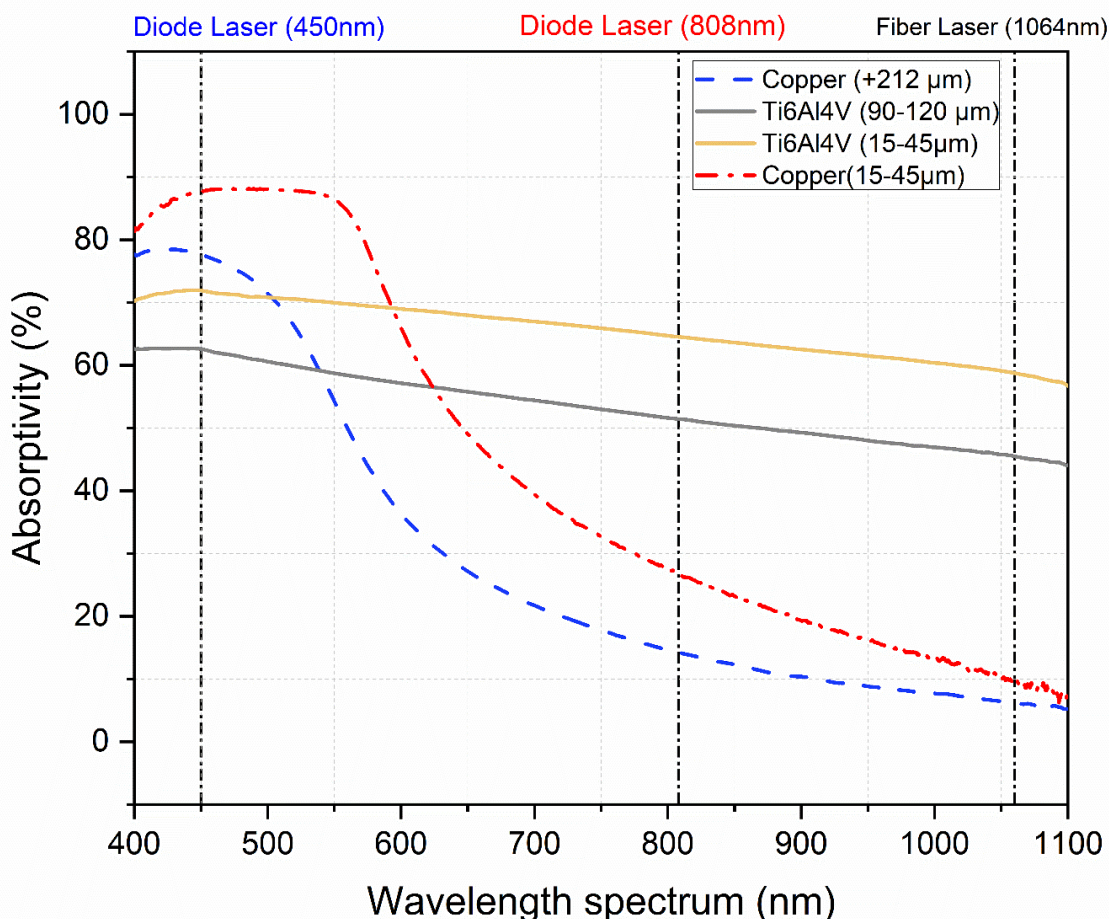


Figure 4.3: The optical absorption of Ti6Al4V and copper using different average particle sizes and distributions within the 400 to 1100 nm wavelength range.

The increased absorption in smaller particles can be attributed to their higher surface area to volume ratio and the presence of numerous tiny gaps between them. These small gaps function as black bodies, allowing radiation to be absorbed through multiple absorption and reflections, as shown in Figure 4.4. In contrast, larger particle sizes exhibit more reflection away from the powder (scattering), leading to a power loss. This is because the incident light on larger particles is more likely to be reflected rather than absorbed. As a result, the energy from the incident light is not efficiently utilized, and the overall absorption

decreases. In conclusion, using small particles in PBF leads to higher absorption, higher conductivity, improved thermal efficiency, and improved processing efficiency, which has been reported [27][163].

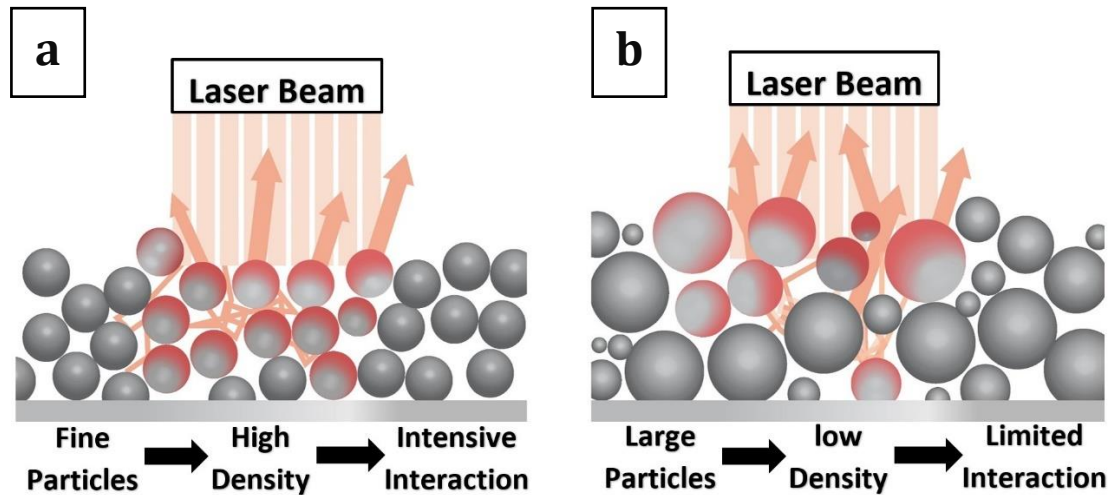


Figure 4.4: Illustration of the laser beam interaction with powder (a) fine particles and (b) large particles.

4.3.3 Comparative Analysis of Laser Absorption in Copper and Ti6Al4V Powders with Different Particle Sizes

The virgin metal powder was subjected to an ageing process for 48 hours to investigate the impact of oxidation on radiation absorption. Cu and Ti6Al4V powders were placed in a furnace at a temperature ranging from 200-500°C, and a low argon flow rate (10 bar) was employed to encourage oxidation without inducing melting or sintering. The 48-hour ageing duration facilitated the formation of a thin oxide layer on the surface of the particles. Following this treatment, the powder was allowed to cool to room temperature before being collected for subsequent analysis or processing.

At a wavelength of 1060 nm, the absorptivity factor increases by 1.89; at 808 nm, the factor rises by 1.44; and at 450 nm, the factor experiences an increase of 1.09. Due to a higher absorption coefficient of copper oxide (CuO or Cu₂O) than pure copper, copper oxide can absorb laser light more efficiently. This enhanced absorptivity is attributed to the amplified interaction between laser light and the copper oxide layer. The oxide copper layer formations create a gradient in refractive index that bounces back and forth between the oxide layer and the metal surface, as shown in Figure 4.5 (beam 1). This effect leads to an increase in the material's light absorption, compared to pure copper in Figure 4.5 (beam 5), which increases by using a shorter wavelength, as reported by Jadhav et al. [158].

On the contrary, the aged Ti6Al4V powder showed a noticeable reduction in radiation absorption across the entire wavelength range. The absorptivity factor decreased by approximately 0.86 at 1060 nm, 0.88 at 808 nm, and 0.97 at 450 nm. This decrease is due to the oxide layer on the surfaces of the powder particles, which likely consists of titanium dioxide (TiO₂) and other oxides of Aluminium and Vanadium, covering the particle surfaces, and the laser beam needs to penetrate. The individual oxidized layers of the different elements cause more light scattering due to the varying refractive index at the surface Figure 4.5 (beam 2 & beam 3). Also, forming pores between these oxide layers, which have different refractive indices, leads to additional scattering effects Figure 4.5 (beam 4). This effect becomes even more pronounced at the powder surface. Multiple reflections between individual oxidized particles cause increased scattering in the upper layers, preventing the laser radiation from penetrating deeper into the powder bed. A similar effect has been observed with polycrystalline alumina, which has been reported [164][165]. This leads to higher reflectance of the powder and, therefore, lower absorbance. Moreover, the presence of an oxide layer on the Ti6Al4V powder particles can lead to issues in the final product, such as reduced density and mechanical properties, as reported by Velasco-Castro et al. [166].

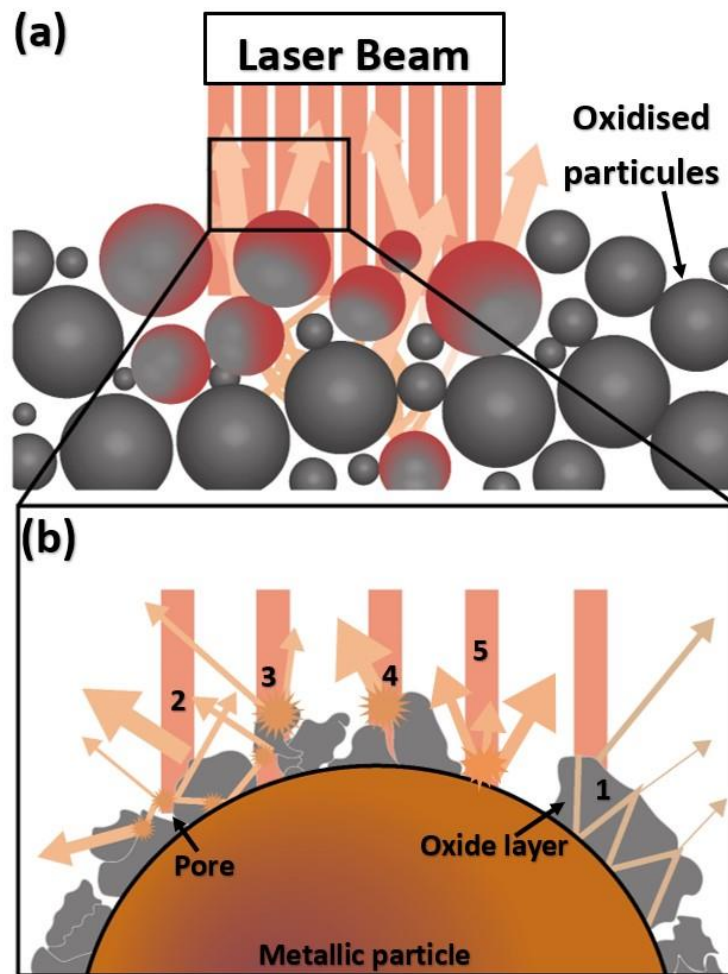


Figure 4.5: Illustration of the interaction between the laser and oxidised surface particle.

It is important to note that copper, being a pure element, forms a single type of oxide material, which makes it easier to increase its absorptivity. In contrast, Ti6Al4V is an alloy consisting of multiple elements, forming various oxides. This complexity may contribute to the reduced improvement in laser absorptivity observed in aged Ti6Al4V powder compared to aged copper powder.

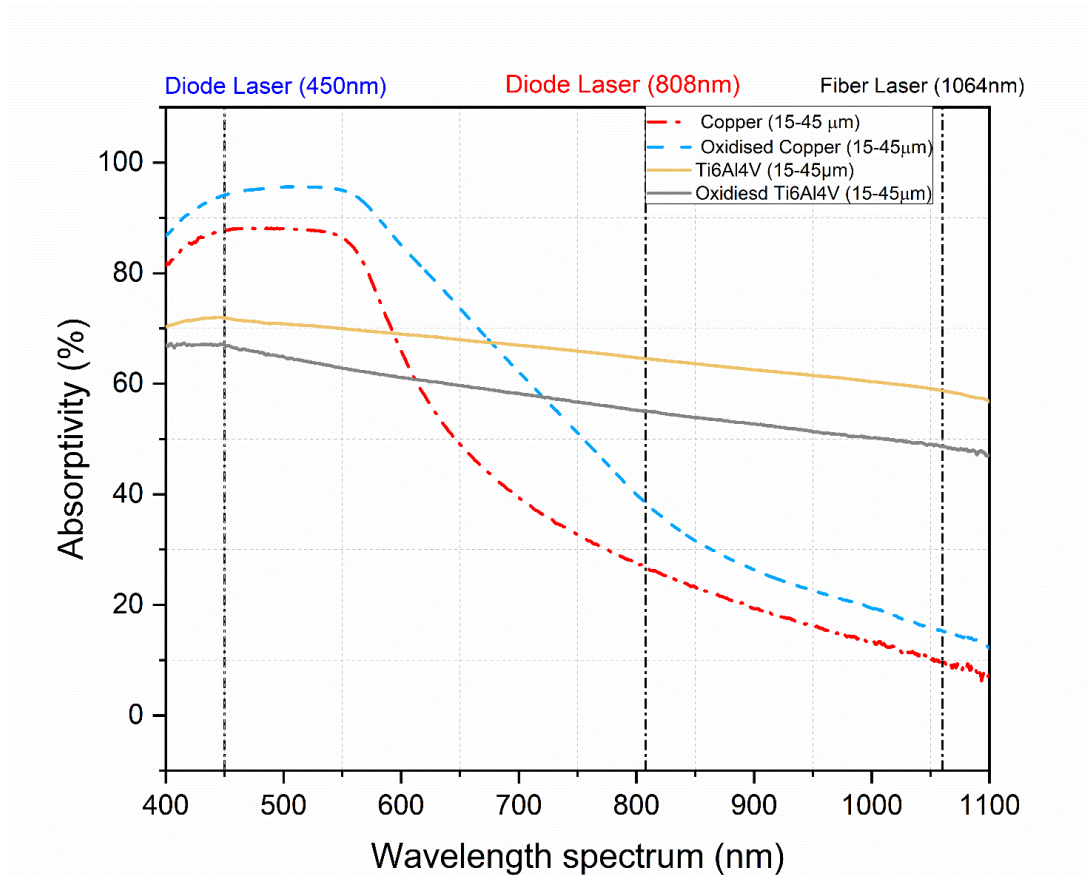


Figure 4.6: The optical absorption of (oxidised /new) Ti6Al4V, Cu within the 400 to 1100 nm wavelength range.

4.4 Conclusions

In this chapter, we investigated the effects of different conditions, including wavelength, particle size, and powder quality, on the absorptivity of Ti6Al4V, copper, and AlSi12 powders. The analysis was conducted across the 380–1100 nm wavelength range.

In terms of the effect of the wavelength on the materials, our findings revealed that absorptivity generally increased for all materials at shorter wavelengths. For example, Ti6Al4V demonstrated a 14% increase in absorptivity when a 450 nm laser source was used instead of a 1064 nm fibre laser. Absorption increased significantly more for highly reflective and conductive materials like copper and AlSi12, with copper experiencing an increase in absorption from 9% at 1060 nm to 26% at 808 nm and a 78% increase to 88% at 450 nm. AlSi12 followed a similar practice, an absorption increases of approximately 153% from 1060 nm to 450 nm. This improved absorption at lower wavelengths can be attributed to the higher photon energies at these wavelengths, leading to a more efficient interaction with the material and, therefore, better absorption of the laser energy.

The particle size also exhibited an impact on absorptivity. A decrease in absorptivity was observed for larger particle size distributions compared to finer particle distributions for copper and Ti6Al4V. For example, the absorptivity of copper dropped with large particle size distribution. Ti6Al4V showed a similar trend, with absorptivity reduction. This observation can be explained by the higher surface area to volume ratio and the presence of numerous tiny gaps in smaller particles, which function as black bodies, allowing radiation to be absorbed through multiple reflections.

Finally, we also explored the impact of oxidation on radiation absorption. The oxidization process involved exposing the virgin metal powder to heat for 48 hours, forming an oxide layer on the particle surfaces. This led to increased radiation absorption of the aged copper powder across all measured wavelengths, with the absorptivity factor rising by 1.89, 1.44, and 1.09 at 1060 nm, 808 nm, and 450 nm, respectively. This result was attributed to the stronger interaction between laser light and the copper oxide layer. Conversely, the absorptivity of aged Ti6Al4V powder reduced across all wavelengths, which could be attributed to the varying refractive index at the surface and the presence of multiple oxide layers, causing more light scattering and, thus, lower absorbance.

In conclusion, our findings indicate that improving the process efficiency can be achieved by using short wavelengths (808, 450 nm) with the help of the correct powder particles.

Chapter 5: Efficient Energy Absorption with 450-808 nm DL in Ti6Al4V

Summary:

This chapter focuses on investigating the use of low-power, short-wavelength fiber-coupled diode laser sources and the influence of shorter laser wavelengths (450-808 nm) on material absorption and processing efficiency in a Diode Area Melting (DAM) approach, specifically for Ti6Al4V. The chapter begins by emphasizing the importance of wavelength on absorptivity and processing efficiency, highlighting the higher absorption rates achieved with shorter laser wavelengths.

The experimental procedure is conducted in two stages. The first stage involves evaluating the process efficiency of short-wavelength diode lasers (450 nm and 808 nm) in melting Ti6Al4V at different laser powers and scanning speeds. The surface temperature and single-track morphology, including melt pool depth, width, and density, are measured and analysed.

The second stage focuses on determining the optimal processing parameters for building 3D high-density parts. A normalisation energy density is used to calculate the effective parameters for creating sufficient melt pool width and depth.

Overall, the chapter demonstrates the feasibility of using low-power, highly scalable fiber-coupled diode laser sources with shorter wavelengths for improved material absorption and processing efficiency in PBF.

5.1 Introduction

The previous chapter proved the importance of wavelength on the absorptivity of the energy of different metallic powders, Therefore, the processing efficiency. It was found that when processing Ti6Al4V, absorption was 11% higher using 450 nm lasers when compared to using 808 nm lasers and 14% higher than 1064 nm lasers. This chapter investigates the use of low-power, highly scalable fibre coupled diode laser sources and the influence of shorter laser wavelengths (450-808 nm) on material absorption and processing efficiency using a Diode Area Melting (DAM) approach. The effect of laser wavelength on melt pool characteristics Ti6Al4V will be studied for comparable energy densities. The investigation was carried out in two stages. The first stage was to assess the ability of lasers to melt the Ti6Al4V using different laser powers and scan speeds whilst measuring the surface temperature and analysing the single-track morphology (melt pool depth, width, and density). The second stage was to determine processing parameters for three-dimensional manufacturing using a process energy normalisation approach developed by Thomas et al. [146].

5.2 Experimental procedure

The research was conducted in two stages. The first stage involved evaluating the process efficiency of short wavelengths diode laser (450nm and 808nm) in melting Ti6Al4V at the maximum laser power and different scanning speeds. This stage also involved measuring surface temperature and analysing single-track morphology, including melt pool depth, width, and density. The second stage focused on determining the optimal processing parameters to build 3D high-dens parts successfully. To achieve this, the normalised energy density was developed by Thomas et al. [146].

5.2.1 Stage-1: Single-track laser processing and characterisation

To study the influence of energy density at different wavelengths, a series of single tracks was produced by varying the scanning speed (V) and maintaining laser power at 3.5 W. The process parameters used are listed in Table 5.1. Seven single tracks were produced with a length of 15 mm for each laser wavelength (with x3 repeats). The selected scanning speed ranges were chosen to provide sufficient energy input. This was based on the linear energy density (LED) calculation, using the most effective processing parameters as shown in Equation 2.10 P is the laser power in Watts, and V is the scanning speed in mm/min.

$$LED = \frac{P}{V}$$

This approach was adapted from work undertaken by Wang et al. [152] on Ti6Al4V, where the energy density falls within the range of $0.2 < \text{LED} < 0.5$, which can be achieved in this study for a given laser power by varying the scanning speed between 10 mm/min to 500 mm/min. In this research, the layer thickness was kept constant at 1 mm, and the substrate was preheated to 200°C before laser irradiation. During the processing, the surface temperature was measured using the pyrometer to measure the temperature profiles of the process and correlate them to the wavelength of laser absorption. The top surface morphology of the melt pool was characterized using SEM (Tescan Vega3 LMU) with 15 keV beam intensity. The tracks were then hot-mounted, polished, and cross-sectioned to examine the melt pool morphology in terms of the width and depth of each track. Geometric shapes of each cross-section were analysed using SEM and quantified using ImageJ (NIH, Bethesda, MD, USA). The measurement was conducted for three different cross-sections for each track, and their results were averaged.

Table 5.1 SLM processing parameters for single-track formation.

Laser power (W)	Wavelength (nm)	Scanning speed (mm/min)	LED (J/mm)
3.5 (W)	808 and 450	500	0.42
		400	0.53
		300	0.7
		200	1.05
		100	2.1
		50	4.2
		10	21

5.2.2 Stage-2: Normalisation:

Conventional SLM processing contains a large number of parameters that influence the thermodynamic cycle during the process. Most SLM users define the energy input density using four factors: laser power (P), Scanning speed (V), layer thickness (l_t); and hatch distance (h). However, these factors alone are not sufficient to predict the real energy input since we must also include the effect of the material properties such as Absorptivity, A , and thermal diffusivity, D . Therefore, SLM processing parameters are not directly comparable between different systems and materials by using the volumetric energy density VED method. Bertoli et al. investigation on the reliability of volumetric energy density showed that VED is insufficient to define the process parameters as it does not take into account the complex physics such as hydrodynamic instabilities, recoil pressure, and Marangoni flow [114]. By summarising the processing parameters and the optimal energy density from the literature in Table 5.2, it was found that

each work has different processing values and optimal energy densities. For this reason, a normalisation approach has been adopted in this research. This normalisation approach enables the transfer of known process parameters from one study to another. Additionally, it includes the influence of the wavelength on energy input, which is a key parameter of this study. The normalised processing diagram takes into account the properties of the material (i.e., absorptivity, thermal conductivity, etc.) as described by the following equations:

$$E^* = \frac{P^*}{v^* l^*} = \frac{AP}{2vlr \rho c_p (T_m - T_0)} \quad (2.15)$$

Where E^* represents the normalised volumetric energy density (VED) required to melt the material. P^* , v^* , h^* and l^* are the normalised primary SLM parameters which has been discussed in detail in section 2.8.4 in Chapter 2.

Table 5.2: Summary of processing parameters for SLM of Ti6Al4V from literature.

Laser system		Processing parameter				Optimal ED (J/mm ³)	Ref.
Spot size (μm)	Wavelength (nm)	Power (W)	Velocity (mm/s)	Thickness (μm)	Hatch (mm)		
70-120	1060	375	686 – 1029	60-90	0.12-0.18	33.74-68.47	[167]
50-68	1070	100-400	200-2000	30-50	-	-	[152]
50-200	1070	400	25-150	200	0.35-0.140	38-95	[168]
100	1060	150-195	500-1200	30	0.100	50-69	[135]
20	1060	82.5	500	40	0.05	82.5	[69]
75	1070	150-200	800-1500	20	0.075	66-166	[169]

To compare and summarise the processing parameters of Ti6Al4V as used in the various references from the literature (Table 5.2), the normalised processing data was calculated and is presented in Figure 5.1. In the figure, $1/h^*$ is plotted as a function of $\frac{q^*}{v^* l^*}$ to assist in plotting E_0^* as the diagonal dash lines on the graph. E_0^* represents the energy density required to melt the material. In this way, it is possible to compare the processing parameters from different studies to define the broad range of the E_0^* for this study. Thus, enabling this study to define a processing window for the material. From this plot, it can be seen that the energy density required to ensure > 99.0% density is in the range $2 < E_0^* < 8$. When

$E_0^* > 8$ the material will be exposed to excessive energy, leading to over-melting, whilst $E_0^* < 2$ leads to insufficient melting, as demonstrated by Thomas et al. [146]. In this study, the processing parameters were tuned to obtain E_0^* within these limits.

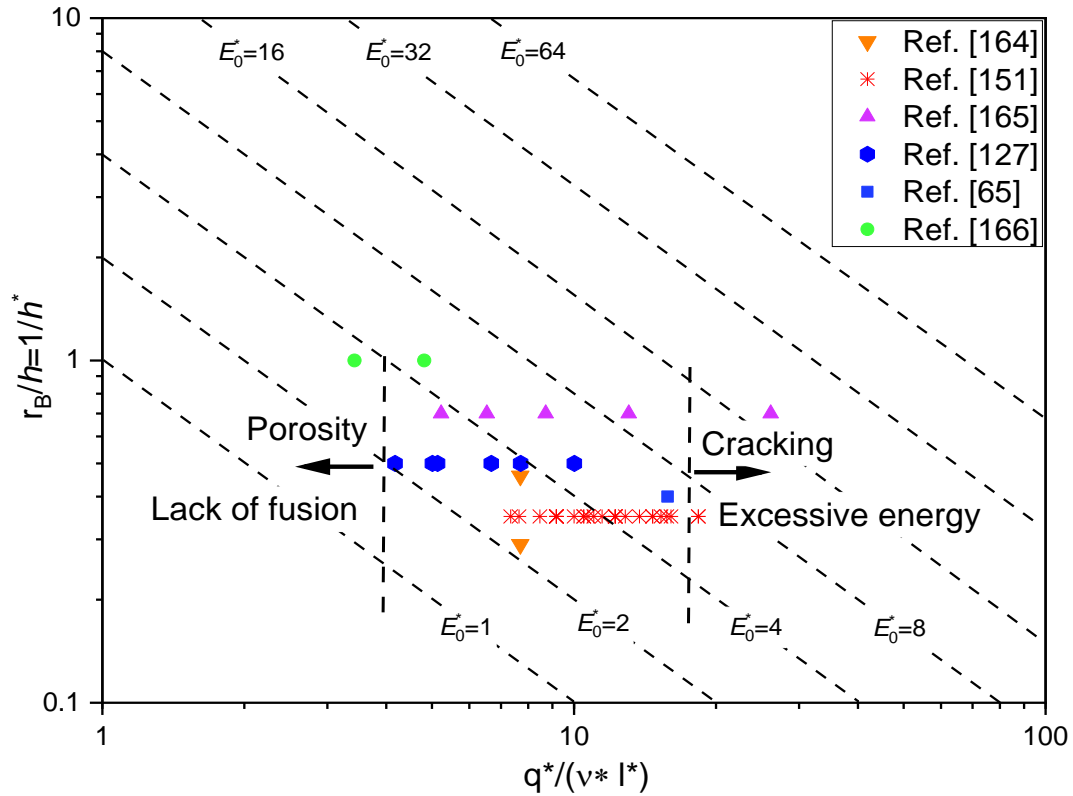


Figure 5.1: Normalised energy density of Ti6Al4V from literature.

5.3 Results and discussions

5.3.1 Influence of wavelength on surface temperature

As the first stage of this study, the surface temperature of Ti6Al4V powder was measured to determine the maximum achievable temperature and to monitor the thermal cycle. The surface temperature increases as the laser beam enters the measurement spot, rapidly reaching peak temperature before slowly receding to room temperature after the laser spot has passed. Three temperature transients were recorded and averaged for a range of scan speeds (10 mm/min to 500 mm/min). The maximum temperature attained is plotted in Figure 5.2 for laser irradiation at both 808nm and 450nm. Higher temperatures were recorded at slower scanning speeds for both wavelengths due to the higher energy input generated. The maximum temperature reached at each scanning speed is noticeably different for the two wavelengths, with the maximum surface temperature reached at 450 nm higher by approximately 12% compared to that at 808 nm. At 10 mm/min, the maximum temperature for 450 nm was 1920°C, and for 808 nm was 1760°C. This 12% higher average temperature correlates well with the measured 11% higher absorption for the shorter wavelength light.

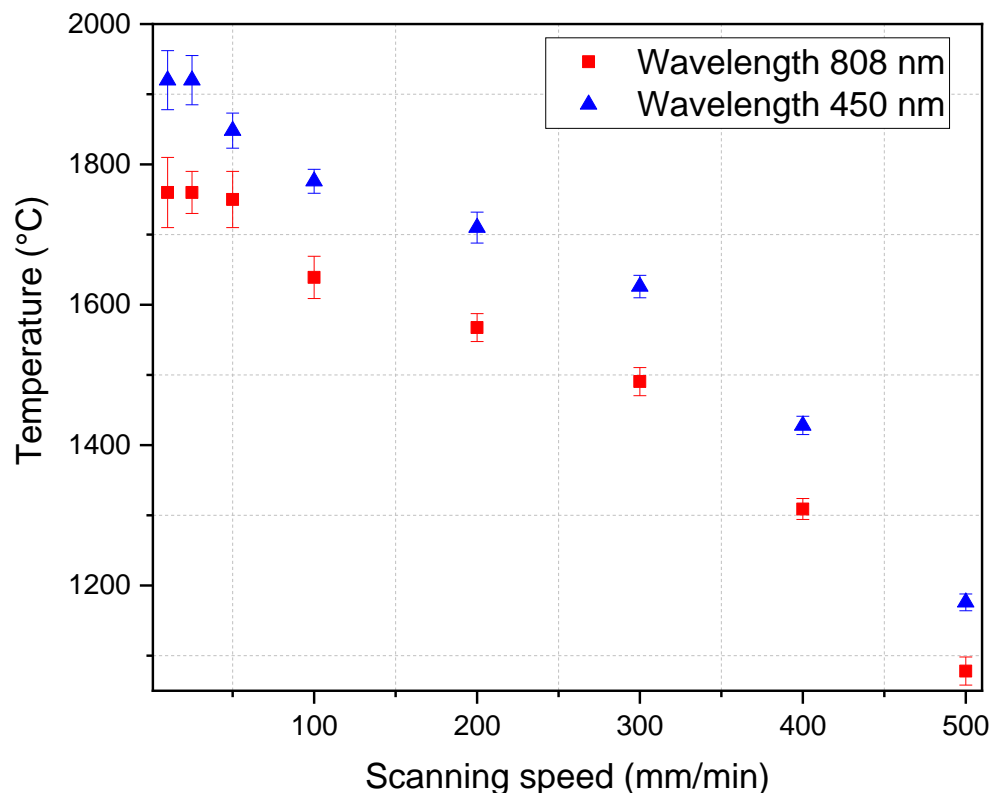


Figure 5.2: The maximum temperature measured during laser processing at various scanning speeds for 808 nm and 450 nm wavelengths.

Temperature transients are plotted in Figure 5.3 for 808 nm and 450 nm laser irradiation at a speed of 50 mm/min, showing the temperature within the measurement spot as the laser beam passes through. The 450nm laser achieved a maximum temperature within 260 ms, whereas the 808 nm laser achieved this after 530 ms. This phenomenon can be related to the absorption spectrum of Ti6Al4V powder, where more energy is absorbed and converted to heat at a shorter wavelength, allowing the shorter wavelength laser source to achieve a maximum temperature faster. However, at speeds of 50 mm/min or below, a large fluctuation in temperature of approximately $\pm 100^{\circ}\text{C}$ was observed, as can be seen in Figure 5.3. This is possibly due to keyhole formation caused by the increase in interaction time, similar to the effect reported by Matthews et al. [170].

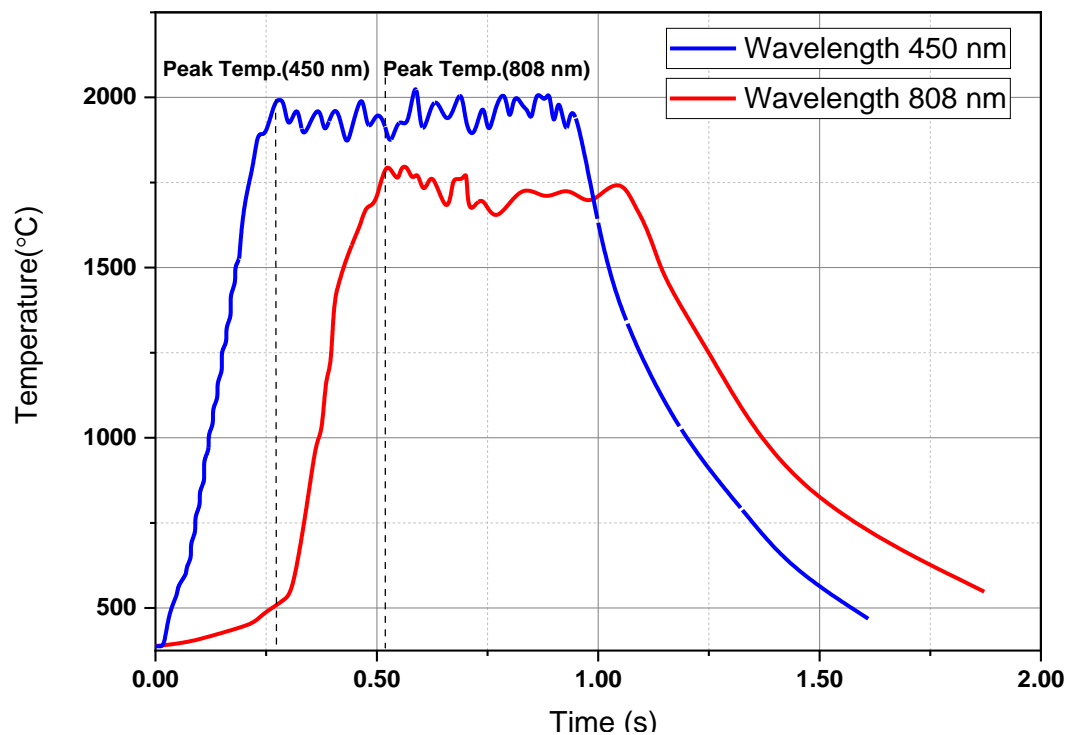


Figure 5.3: Temperature measurement at a speed of 50 mm/min.

5.3.2 Influence of the wavelength on the morphology of single laser tracks

Single tracks were processed using 450 nm and 808 nm wavelength lasers in order to determine the influence of wavelength, and therefore absorptivity, on single-track geometric features. Surface morphology and cross-sectional geometric characteristics of single tracks were investigated using SEM. Table 5.3 documents the melt-pool depth and width for 14 sets of laser parameters that produced reportable results, i.e., some amount of melting was observed. The table represents the melt pool depth, width and the feature produced for different parameters.

Table 5.3 A summary of single-track processing parameters and resultant melt pool characteristics.

wavelength (nm)	Laser Power (W)	Scanning speed (mm/min)	Top Surface width (μm)	Morphology of cross-sectioned		Observation
				melt pool Depth (μm)	melt pool width (μm)	
808	3.5	10	225	408	395	Keyhole formation
		50	192	374	386	continuous melt pool
		100	183	165	339	continuous melt pool
		200	176	135	311	discontinuous melt pool
		300	154	126	282	balling
		400	insufficient	insufficient	insufficient	Insufficient
		500	insufficient	insufficient	insufficient	Insufficient
450	3.5	10	228	518	433	Keyhole formation
		50	217	429	417	Keyhole formation
		100	208	414	394	continuous melt pool
		200	199	240	379	continuous melt pool
		300	182	229	309	discontinuous melt pool
		400	170	211	165	balling
		500	insufficient	insufficient	insufficient	insufficient

Both the 450 nm and 808 nm lasers were tested for their ability to melt Ti6Al4V. It was determined that both lasers were capable of melting the material. However, the difference in absorptivity between the two wavelengths can also

result in different processing windows, even when both laser parameters are kept constant. The 450 nm laser was found to have a wider processing window than the 808 nm laser, with a range of 2.1 J/mm to 1.05 J/mm for speeds ranging from 100 mm/min up to 200 mm/min. In comparison, the processing window for the 808 nm laser was found to be from 4.2 J/mm to 2.1 J/mm for speeds ranging from 50 mm/min up to 100 mm/min. The processing efficiency of the 450 nm laser is significantly higher than that of the 808 nm laser, with the processing window for the former being 50% more efficient than the latter. This is primarily due to the higher absorptivity of the Ti6Al4V material at the 450 nm wavelength, which allows for a wider range of processing speeds and more efficient use of the laser energy. In other words, the 450 nm laser requires less energy to achieve the same melting effect as the 808 nm laser, making it a more efficient option for processing Ti6Al4V.

5.3.3 Melt pool top surface morphology.

Figure 5.4 shows the top surface morphology of single tracks produced by the two different wavelength lasers for a range of scan speeds at fixed power (3.5 W). This determines whether the surface will exhibit a continuous smooth morphology, a coarse, irregular morphology, or contain a number of keyholes. Increasing the scanning speed results in a narrower track width for both 450 nm and 808 nm. Further reduction of the scanning speed results in keyhole formation due to excessive energy input.

Morphology varied significantly with scan speed for both laser wavelengths. At high speeds above 300 mm/s, both lasers had insufficient energy to form a melt pool, and solid structures were not possible. This was a result of the lower peak temperature reached due to the rapidly moving laser source. The powder was sintered to some extent, but the resultant samples had little or no mechanical strength and easily crumbled when physically handled. Similar behaviour was observed at very low scan speeds of 10 mm/min or slower, in this case producing non-periodic keyholes. The keyholes can be attributed to the higher incident energies, where a high melt pool temperature is attained at slow scanning speeds.

The process window for the 450 nm laser is much wider than that at 808 nm. This is due to higher absorptivity at the shorter wavelength. At 450 nm, a continuous and smooth top surface was formed at scanning speeds ranging from 50 to 200 mm/min (Figure 5.4). However, at scanning speeds above 200 mm/min, the balling phenomena start to appear until the energy input is insufficient to melt powder at speeds above 400 mm/min. This phenomenon is commonly observed for metals processed with lower energy densities, as reported by Yadroitsev et al. [112], where energy density was insufficient to melt powder at high scanning

speeds resulting in severe balling. On the contrary, a stable process window for 808 nm is observed from 50 to 100 mm/min, with keyholes forming at 50 mm/min or below. Discontinuous melt pools with balling were observed between 100 and 300 mm/min. Above 300 mm/min, the energy was found to be insufficient to form melt pools.

The width of the track generally increased with energy density; for the 450 nm laser the track was generally wider than at 808 nm due to higher absorption. This is illustrated by Figure 5.5, which plots the average width of the melt pool track measured at the top surface as a function of scanning speed. For example, at 100 mm/min the width of the track was 208.2 μm when the 450 nm laser was used, compared to 182.8 μm for the 808 nm laser. The width of tracks processed using the 450 nm laser remained above 200 μm for speeds below 200 mm/min, whereas for 808 nm the track width narrowed below 200 μm at speeds above 50 mm/min.

450 nm lasers produced better track surface quality at a scan speed of 100 mm/min at 3.5 W compared to 808 nm lasers, as observed in Figure 5.4. This power is substantially lower than used in commercial SLM systems (typically 100 to 900 W) and anything reported in the literature. The 808 nm laser produced satisfactory results in terms of morphology but at a slower speed of 50 mm/min due to its lower absorption than 450 nm. This has been achieved whilst exhibiting a high wall plug efficiency of 70% compared to the typical 20% of fibre lasers.

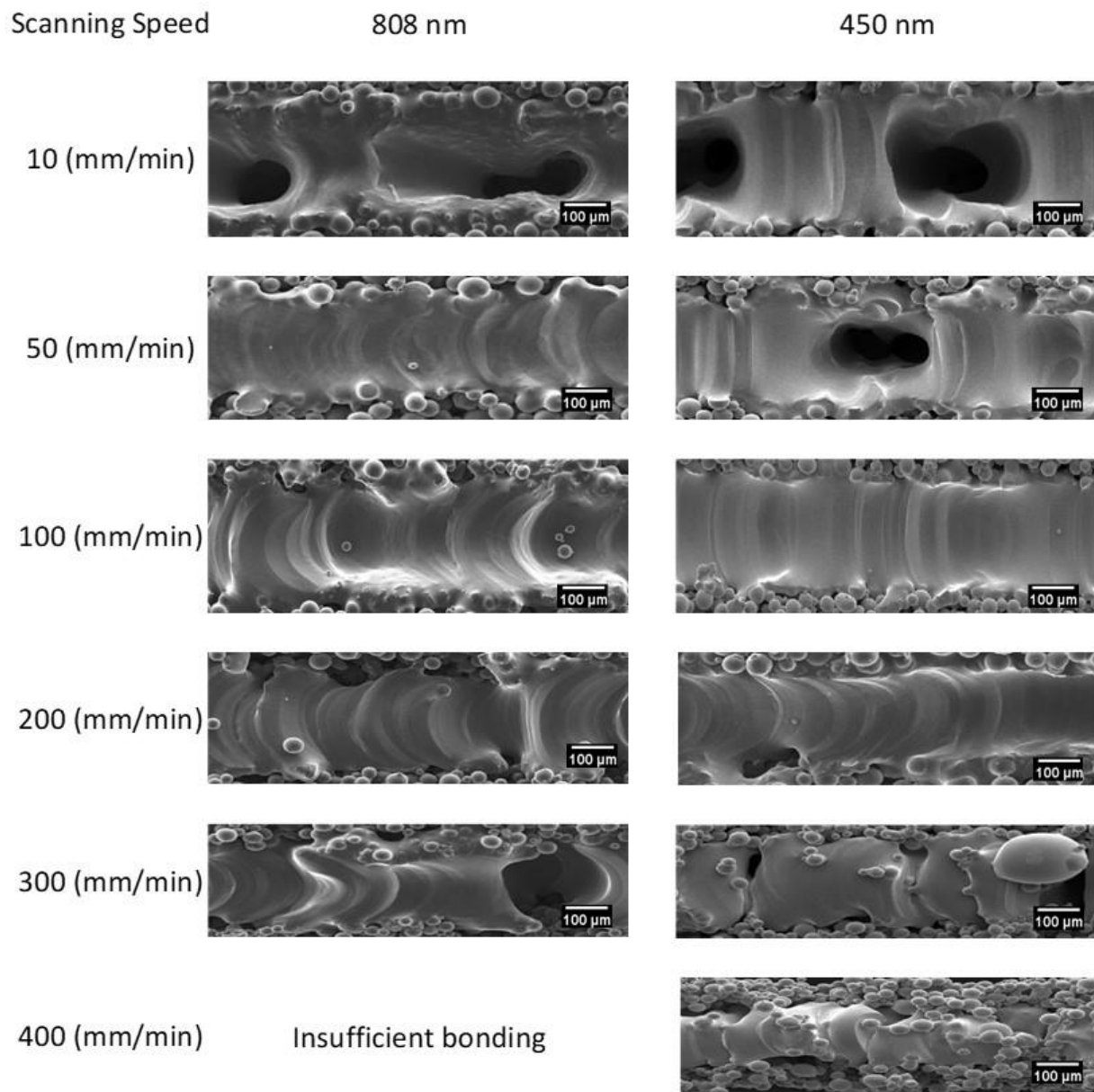


Figure 5.4: Top surface morphology under different scanning speeds for 808 nm and 450 nm wavelength laser processing.

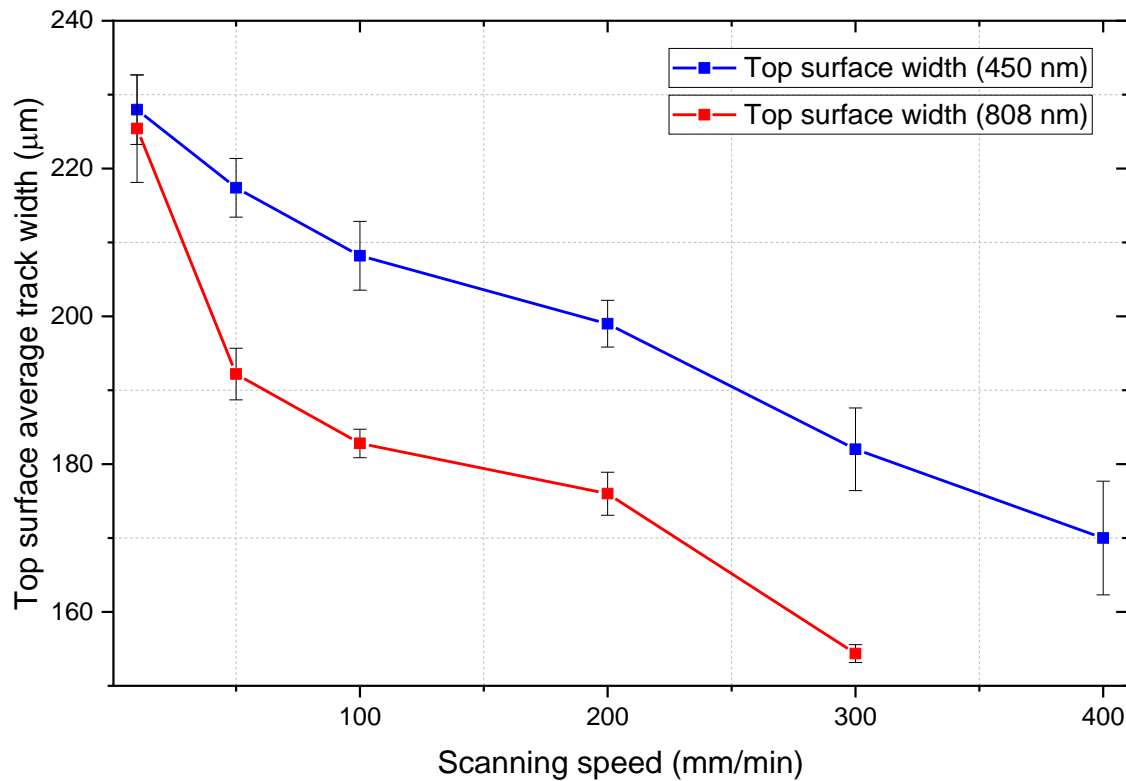


Figure 5.5: Effect of scanning speed on melt pool width for both lasers (808 nm, 450 nm).

5.3.4 Morphology of cross-sectioned tracks

Scanning speed affects energy density and is, therefore a dominant parameter in influencing the shape and morphology of a single track. When the scanning speed was below 50 mm/min, the energy input was high enough for lasers at both wavelengths to penetrate deeply and create keyholes. Figure 5.6 shows the cross-section of tracks processed with the 450 nm and 808 nm lasers at different scanning speeds, allowing a comparison of the depth and width characteristics of the tracks. The depth and width of tracks reduce with increasing scan speed for both wavelengths. Furthermore, it can be noted that the penetration depth is 20-40% deeper for the 450 nm laser compared to 808 nm. Figure 5.7 shows the relation between the geometric features of single tracks and scanning speed, plotting the reduction in melt pool depth (a) and width (b) as scanning speed increases from 10 to 400 mm/min. For the same scanning speed, tracks produced using 450 nm light are generally wider than those using 808 nm (Figure 5.7 b). The track narrows from 416 to 165 µm with increasing scanning speed up to 400 mm/min for 450 nm, whereas for 808 nm, the track width narrows from 395 to 281 µm for a maximum 300 mm/min speed.

Wavelength also has a significant influence on the melt pool depth. This can be described using (Figure 5.7 (a)), which plots the melt pool depth as a function of scan speed. At the same scan speed, keyhole formation occurred with a deeper penetration depth when processed with 450 nm compared with 808nm. In addition, keyhole formation for 450 nm was more prominent at speeds below 50 mm/min, whereas for 808 nm keyholes were observed at speeds below 10 mm/min. 450 nm also exhibited deeper penetration than 808 nm. Generally, there is a wider processing window for 450 nm compared to 808 nm. This provides flexibility in terms of process adaptability and capacity to improve the SLM process. It also allows lower powers and makes it possible to scan at faster speeds.

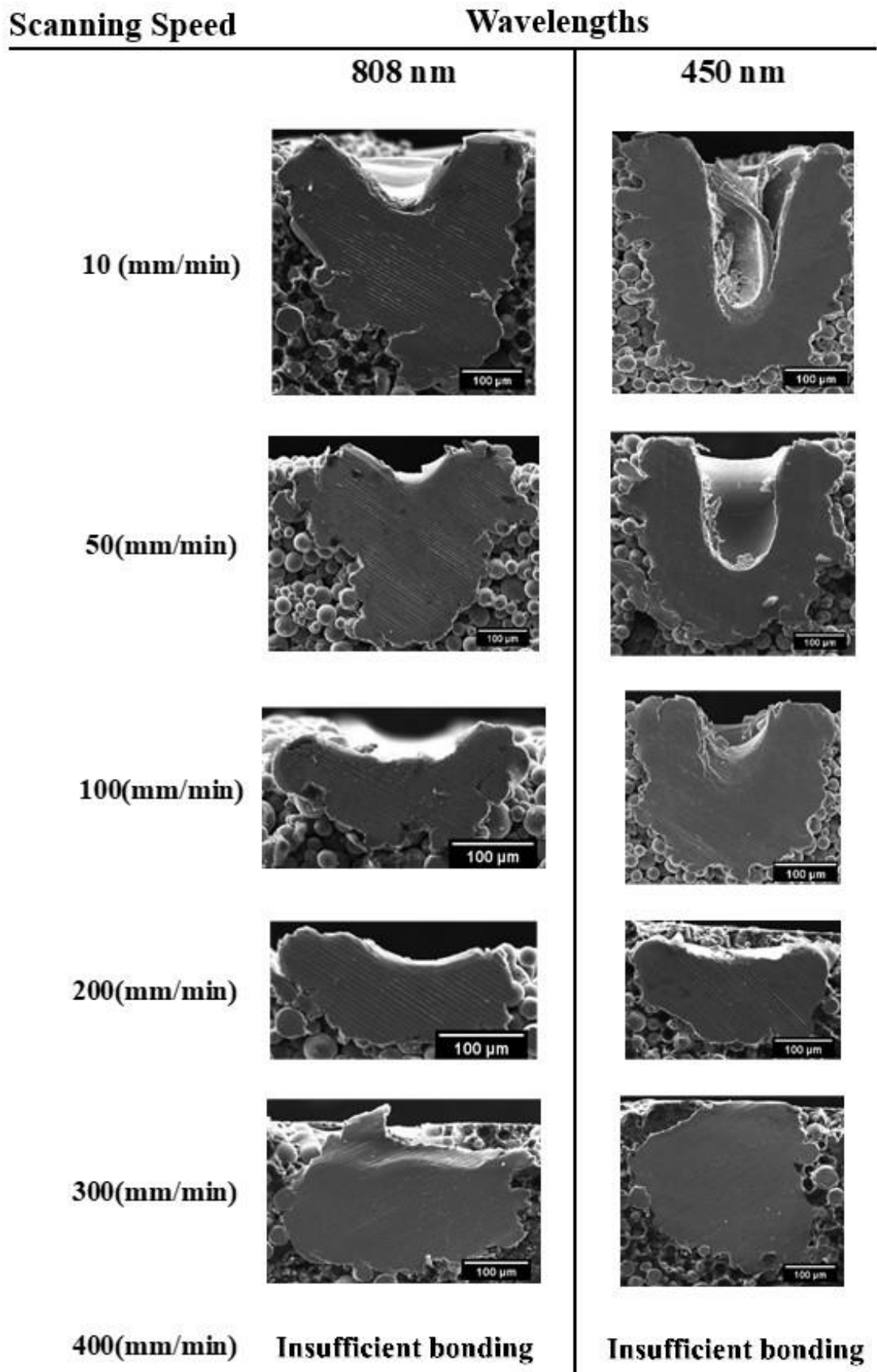


Figure 5.6: Cross-section morphology of melt pool at different scanning speeds.

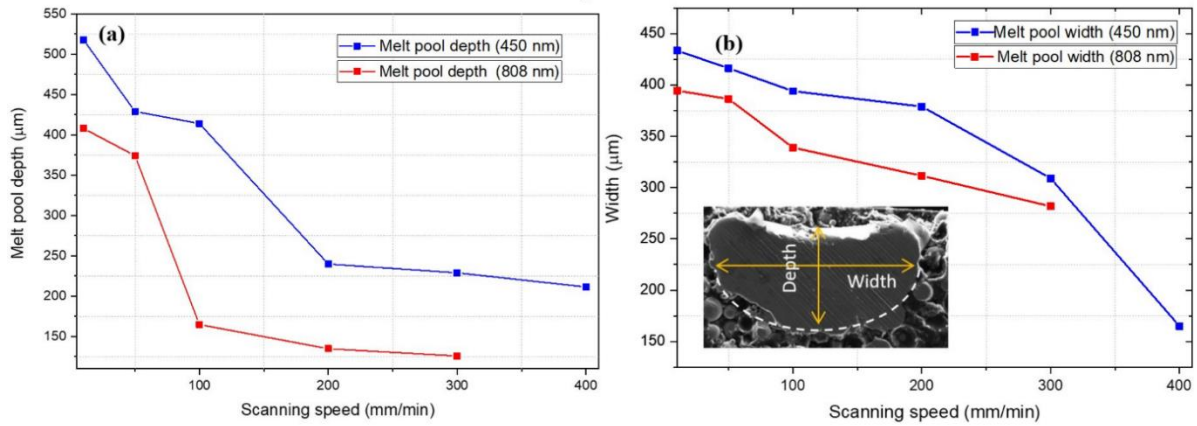


Figure 5.7 Variation of melt pool (a) depth and (b) width with scan speed for 450 and 808nm lasers.

5.3.5 Multilayer Fabrication

5.3.5.1 Processing regions for 450-808nm powder bed fusion of Ti6Al4V

Several variables need to be considered in order to achieve high part density in SLM, such as scan speed, layer thickness, power, and hatch distance. The combination of these variables needs to be carefully explored for any given laser power to avoid the introduction of defects related to insufficient wettability or poor overlapping. Results from the single-track experiments can provide an estimate of the melt pool morphology under different processing parameters, allowing a selection of suitable process parameters for the fabrication of multilayer samples. This section investigates the effect of wavelength on microstructure, part density and processing parameters.

According to our analysis of the dimensionless processing data (normalisation) discussed in chapter 2 and Section 5.2.2, the key SLM parameters and their interaction with each other were considered to determine the minimum energy required to melt Ti6Al4V. Laser power q^* (3.5 Watt), scanning speed v^* (25-400 mm/min) hatch spacing h^* (100- 200 μm) and layer thickness l^* (50-100 μm) were selected and normalised as summarised in Table 5.4. Multilayer samples were processed to a size of 7 mm × 7 mm × 2 mm. Figure 5.8 shows the normalised processing diagram, which represents the required energy input, E_0^* , to be absorbed by a material for specific volume $2r_B l^*$ as isopleth dashed lines. The y-axis $\frac{1}{h^*}$, where E_0^* on x-axis as log10 scale.

Table 5.4: Experimental parameters investigated for Ti6Al4V.

$q(q^*)$	$v(v^*)$	$h(h^*)$	$l(l^*)$
3.5 W (57) *	25 mm/min (0.006)	200 μ m (2.30)	50 μ m (1.15)
	50 mm/min (0.012)		
	75 mm/min (0.018)		
	100 mm/min (0.024)		
3.5 W (51) **	200 mm/min (0.048)	157 μ m (1.80)	100 μ m (2.29)
	300 mm/min (0.072)	100 μ m (1.15)	
	400 mm/min (0.096)		

(*Normalised power for 450 nm laser **Normalised power for 808 nm laser)

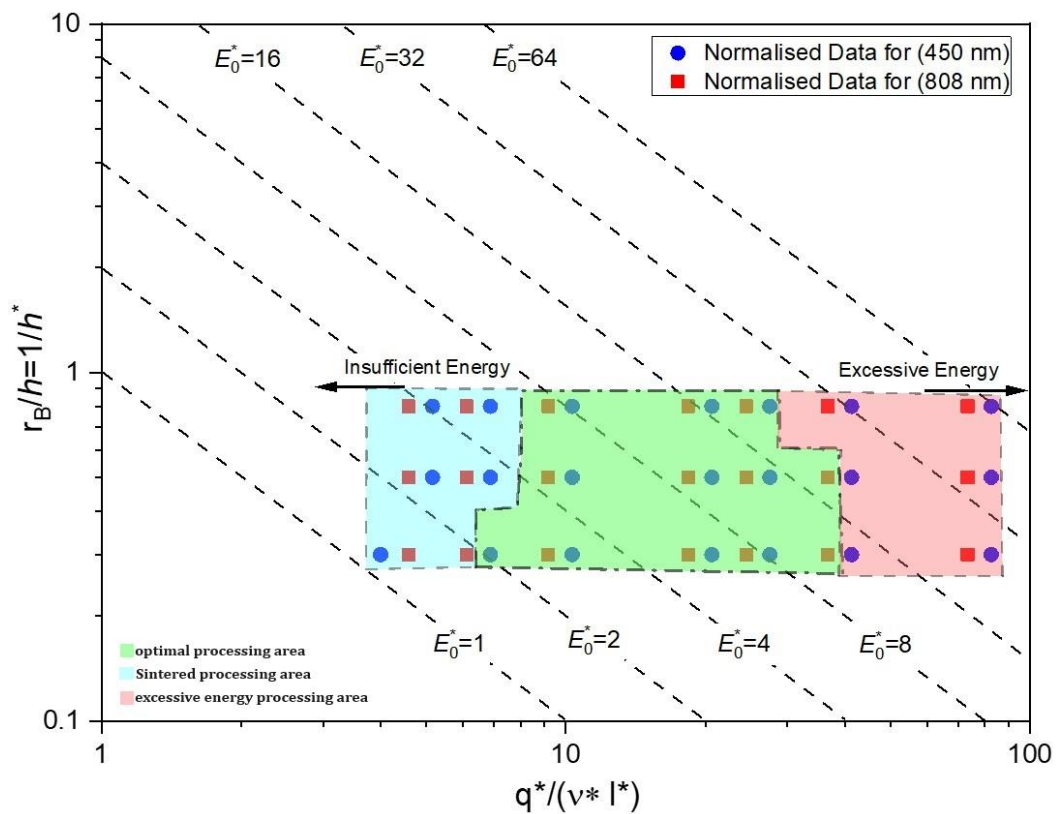


Figure 5.8: Normalised diagram showing the location of the experimental parameters and the visible region for given laser power.

Accordingly, it was evident that a high value of ($E_0^* > 8$) would lead to excessive energy input, resulting in voids and keyholes forming. In contrast, low-energy input ($E_0^* < 2$) will be insufficient to fuse the material or generate sufficient wettability, leading to imperfect parts. The highest density samples of density greater than 90% were produced in a region between $2 < E_0^* < 8$ for selected laser power and wavelengths.

The effect of v^* was more pronounced than h^* on the density of the parts. For instance, increasing the v^* will provide E_0^* values below the threshold of the material. Adjustment of hatch distance to maintain the optimal E_0^* within the range of ($2 < E_0^* < 8$) was not sufficient to improve the density of parts. As the scanning speed increased above $v^* = 0.072$ (equivalent to 300 mm/min) an inconsistent melt pool was formed, as shown in Figure 5.9. The optimal results were achieved at scanning speeds below $v^* < 0.048$ (equivalent to 200 mm/min), while spattering was observed at $v^* < 0.012$ (equivalent to 50 mm/min) as a result of excessive energy input. The maximum processing range was generally higher for 450 nm than 808 nm.

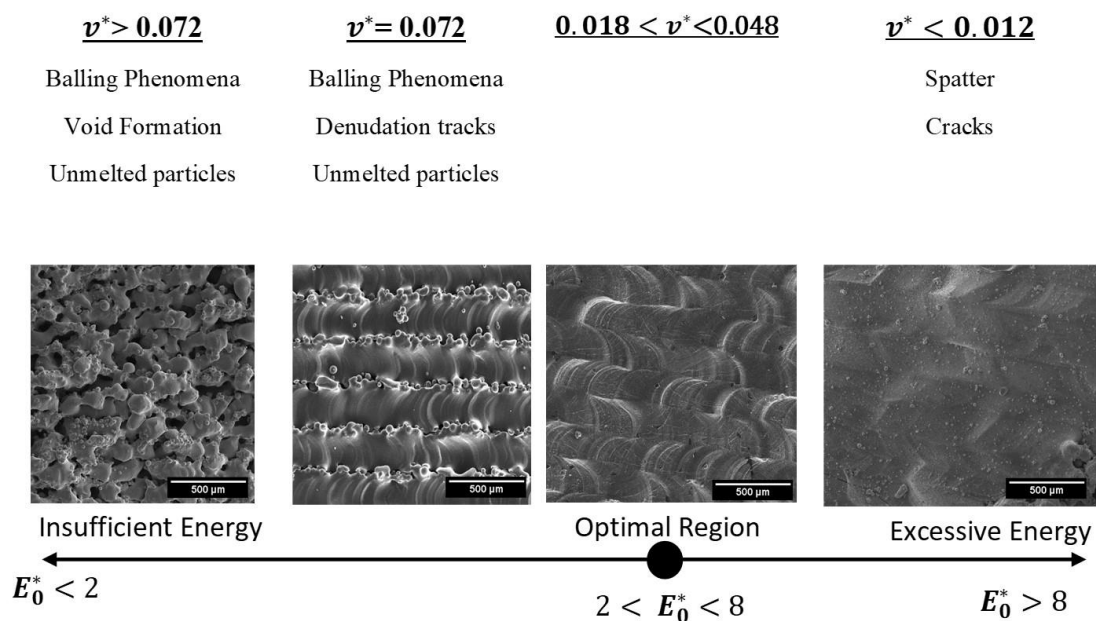


Figure 5.9: The effect of the scanning speed on the specimen's top surface.

The effect of the normalised h^* was noticeable when the v^* was within the effective range from 0.012 to 0.048 (equivalent to 50 to 200 mm/min). In general, the hatch distance affects the thermal history of the process, and therefore influences the microstructure, density and process efficiency [146]. As can be seen in Figure 5.10, decreasing the overlap of laser paths by selecting a normalised overlap $1/h^* > 0.5$ leads to excessive energy being delivered into the powder. This high energy causes vaporisation spatter and the formation of keyholes, which reduces part density, as shown in Figure 5.10 (c). Reducing the $1/h^*$ to < 0.3 leads to poor weldability between the tracks resulting in sintered powder between tracks that deteriorates density and mechanical properties (Figure 5.10 (a)).

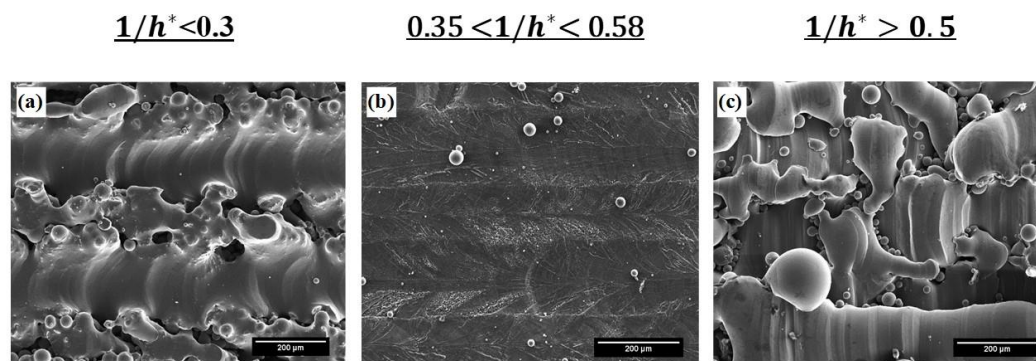


Figure 5.10 The effect of hatch distance on the top surface of the specimens (a) Hatch distance of 200 μm increases the separation between the tracks. (b) 157 μm is the optimal value to provide a better joint. (c) 100 μm reduces the processing efficiency and excessive energy.

The normalised overlapping $1/h^*$ within the range of 0.3 - 0.5 was found to be optimal for increased part density, which also showed a smoother surface finish as can be seen in Figure 5.10 (b).

The layer thickness significantly affected the required energy to melt the material E_0^* . The excessive E_0^* points on the normalised diagram were shifted from the “optimal” region to “insufficient” region when a layer thickness of 100 μm was applied. Correspondingly, the experimental results at a layer thickness of 100 μm showed insufficient bonding between layers. In contrast, the use of 50 μm layer thickness showed solid bonding and higher-density parts. Therefore, a wider range of feasible processing parameters is permitted for layer thicknesses of 50 μm and below.

5.3.5.2 Part density

By selecting the appropriate processing parameters associated with the SLM process, high density parts (> 90%) can be achieved. Figure 5.11 (a) represents the density values of parts fabricated utilising 808 nm laser within the normalised range of $2 < E_0^* < 8$. The density varies from 79.15% to 93.42% of the theoretical value implying the presence of deficiencies. The highest density of 93.42% was achieved at a scanning speed of 75 mm/s, hatch distance of 157 μm , and 50 μm layer thickness, as shown in Figure 5.12 (a). For a thick layer of 100 μm , higher energy input is needed to achieve sufficient bonding between layers. Such input cannot be achieved using this level of laser power even when scanning speeds are reduced. The density of specimens reduced due to excessive energy when a scanning speed of 50 mm/min was used or 100 μm hatch distance was applied.

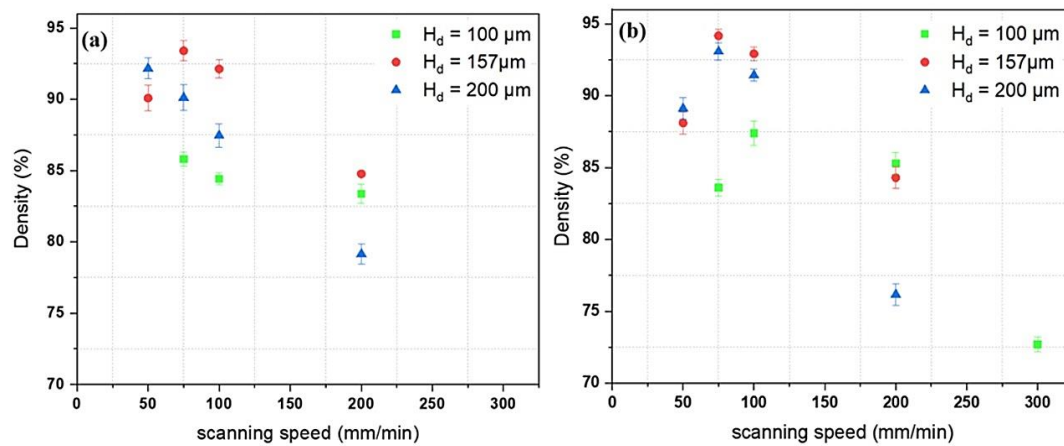


Figure 5.11: Density of parts fabricated using (a) 808 nm and (b) 450 nm.

The density of specimens fabricated using the 450 nm laser was similar to that of specimens fabricated with the 808 nm laser. Over the range of scanning speeds from 50 to 200 mm/min, the density of samples processed using 450 nm varied between 83.31% to 94.16% of that of bulk material, as shown in Figure 5.11 (b). For 450 nm, at a scanning speed of 25 mm/min, large holes and over-melting were evident in the specimen, resulting from excessive energy input. The maximum density of 94.16% was achieved at a scanning speed of 75 mm/min, as shown in the top surface microscope image in Figure 5.12 (b). A maximum density of 93% is observed in specimens fabricated using 808 nm. This density can be achieved at 450 nm at a scanning speed of 100 mm/min. The slower scanning speeds can be expected to allow the melt pool to settle for longer in its molten state, resulting in a wider melt pool, with lower cooling rates potentially reducing stresses and resulting in an overall improved surface. By using a 3.5 W laser of 450 nm wavelength, this study was able to manufacture parts of density above 94%, with further improvement, approaching comparable densities of >99% manufactured by conventional 200 – 1000 W lasers. Therefore, as an alternative to ever-increasing laser powers in order to improve processing speed and part

density (particularly for reflective materials), laser wavelength offers a further variable enabling low-power diode lasers to process materials effectively. In general, defects in the sample which lower the density of fabricated parts in this study can be related to several “real world” uncertainties, such as instability in the laser focal length as the laser traverses the powder bed and the inaccuracy of the deposition system.

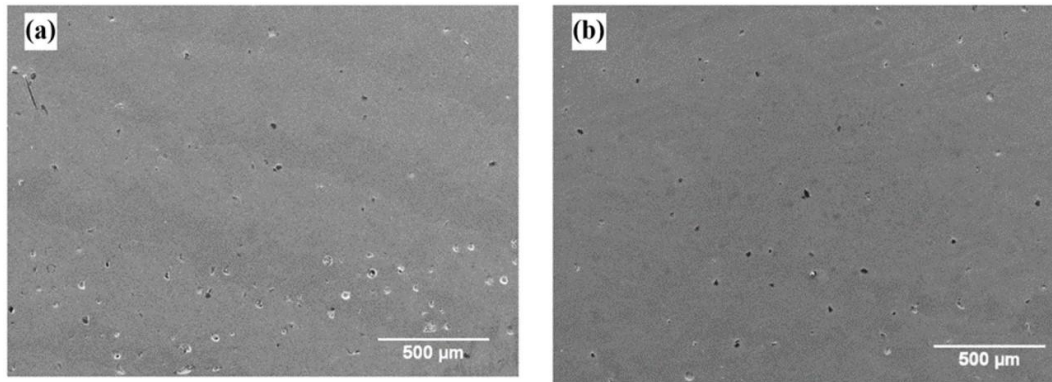


Figure 5.12: Top surface porosity of specimen fabricated using (a) 808 nm and (b) 450 nm.

5.3.5.3 Microstructure (XRD)

The microstructure of Ti6Al4V is characterised by a combination of α phases and β phases at room temperature. These phases are related to the thermal gradient and the solidification of the melt pool in the SLM process [171]. Generally, parts produced by SLM predominantly show the α martensite microstructures only, as a result of the fast cooling rate associated with the process [122]. In comparison to SLM, for Ti6Al4V by EBM, the temperature of the powder bed is normally held at 600 °C, which is above the temperature of martensitic transformation (575°C). This leads to lamellar ($\alpha+\beta$) microstructure in the as-manufactured microstructure. The cooling rate is the influential factor that controls the transformation of α martensite to ($\alpha+\beta$) during the process. As reported by Ahmed et al. [89], the α phase forms at rapid cooling rates higher than 410°C/s, which is exceeded in the SLM process. However, a cooling rate between 20 and 410°C/s would give time for the β phase to form, which can either be achieved by maintaining the powder bed temperature above 575°C or slow processing speed in order to reduce the cooling rate.

In this study, the relatively slow scanning speed of the diode laser maintains the temperature above β transus for a longer period of time compared to SLM, thereby reducing the cooling rate, and promoting the development of the β phase. As a result, the XRD pattern in Figure 5.13 shows a presence of two types of microstructures: α phase and β phase with both laser wavelengths (450 and 808 nm).

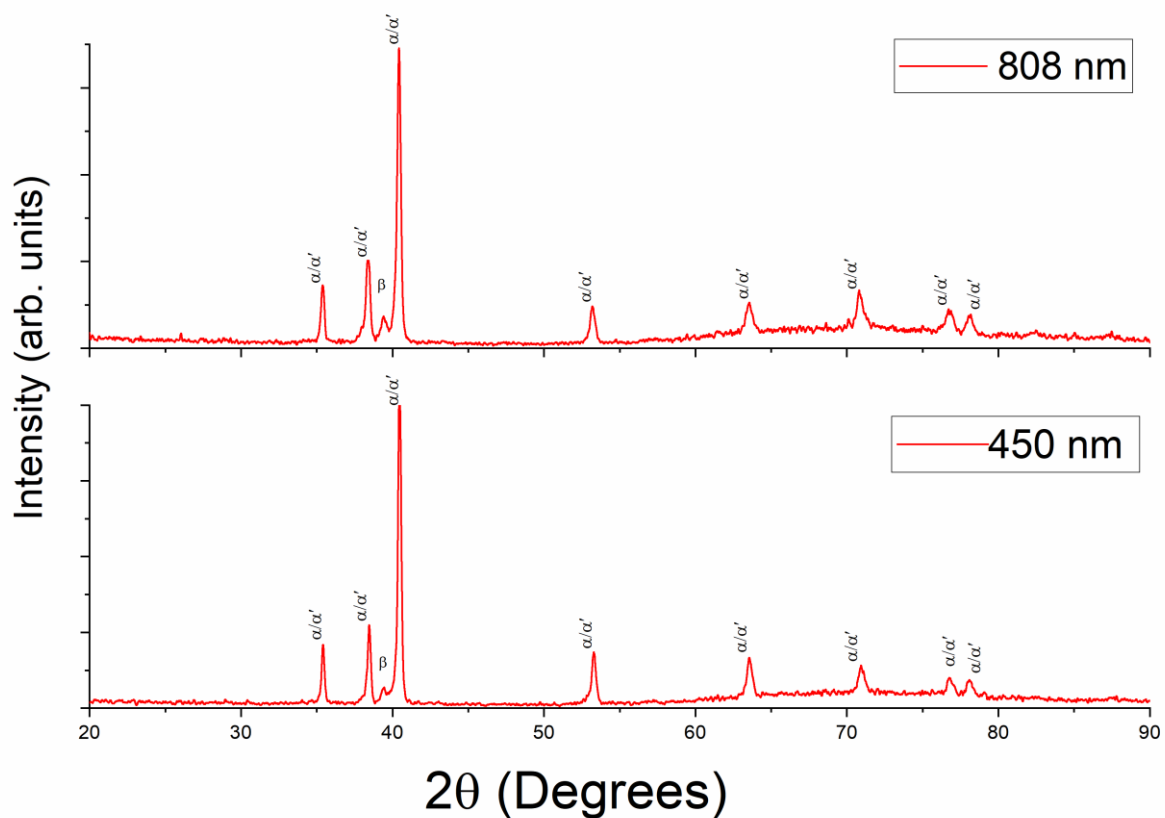


Figure 5.13: XRD profile for 808 nm and 450 nm, showing the presence of β phase.

The cooling rate in this study was calculated using Equation 5.1. The pyrometer was used to measure the temperature with respect to time as detailed earlier the cooling rate was calculated by the time taken for the temperature to drop from β transus temperature ($T_{\beta \text{ transus}} = 994^{\circ}\text{C}$) to the end of martensitic transformation temperature ($T_{\text{ms}} = 575^{\circ}\text{C}$) for Ti6Al4V [89]. In this study, the range of parameters developed a cooling rate in the range of 750°C/S to 1400°C/S . Even though the cooling rate of the DAM process exceeded the critical cooling rate of 410°C/s , it is still comparatively slower than SLM and EBM. Table 5.5 summarises the different processes and associated cooling rate and microstructure associated at different parameters. The high absorptivity of 450 nm and 808 nm lasers allow the use of low powers at low scanning speeds ranging from 75 to 100 mm/min. This maintains the temperature above the β transus for a longer period of time, thus reducing the cooling rate and developing the β phase in as-built samples, similar to results achieved by Simonelli et al. [172]. The author successfully obtained $\alpha + \beta$ microstructure in the SLM process by reducing laser power and scanning speed, which as a result increased the diffusion time and reduced the cooling rate.

$$\text{Cooling rate} = \frac{\Delta T}{\Delta t} = \left| \frac{T_{\beta \text{ transus}} - T_{ms}}{t_{\beta \text{ transus}} - t_{ms}} \right| \quad (5.1)$$

Table 5.5 A comparison of cooling rate and corresponding microstructures of Ti6Al4V processed using SLM, EBM and DAM.

Process	Cooling Rate °C/S	Microstructure	remarks	Ref.
SLM	$10^5 - 10^6$	(martensite) α	Power is 400 W and Speed is 1500 mm/s	[152]
	Not specified	(Widmanstätten) $\alpha + \beta$	Power is 42 W and scanning speed is 58 mm/s.	[172]
EBM	$10^3 - 10^5$	(Widmanstätten) $\alpha + \beta$	Speed is 800 mm/s, 700°C chamber temperature	[173]
DAM	750-1400	(Widmanstätten) $\alpha + \beta$	Speed is 75-100 mm/min, 200°C preheat	This study

The polarised light micrograph was used to identify the top surface microstructure of specimens, as shown in Figure 5.14. The microstructure was dominated by a mixture of Widmanstätten and Martensite. Figure 5.14 (b) shows that α has decomposed into equilibrium ($\alpha + \beta$) basketweave microstructure with different sizes and orientations, using the 450 nm laser. Similar results obtained with a slightly higher amount of martensite α microstructure compared with 450 nm, as shown in Figure 5.14 (a). This can be related to the high absorption of 450 nm which is prolonging the time above the transus temperature and decreasing the cooling rate.

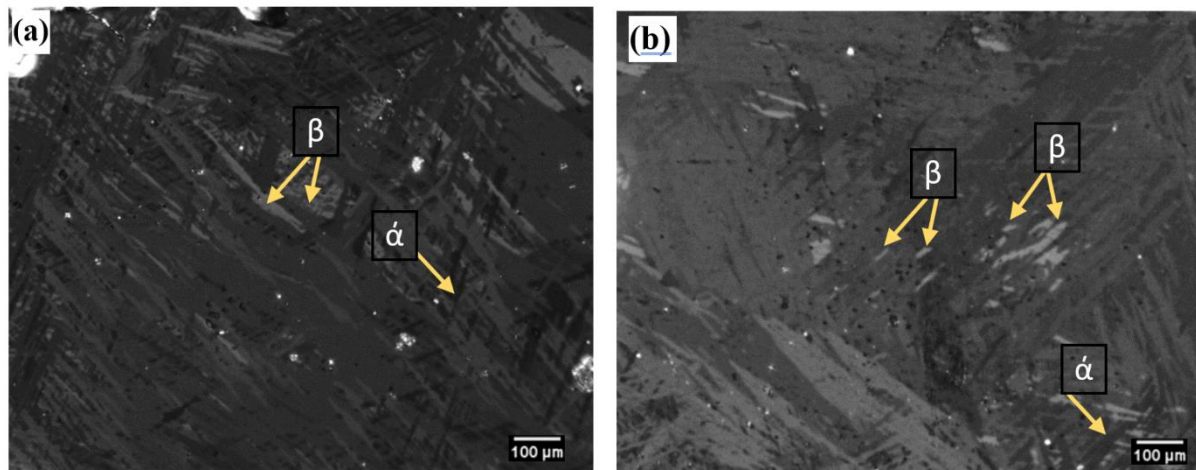


Figure 5.14: Ti6Al4V microstructure at the top surface of the samples shown β when processed using diode lasers (a)808 nm, and (b)450 nm.

5.3.5.4 Nanoindentations (hardness & elastic modulus)

In this section, the top surface of the highest density parts are further investigated for their hardness and elastic properties using the nanoindentation technique suggested by Fischer-Cripps [154]. In general, the formation of the microstructure (Widmanstätten and Martensite) in final parts significantly influences mechanical properties. According to He et al., the presence of Martensite (α) microstructure increases parts' hardness and decreases elasticity [95]. The microhardness of SLM parts measured by Thijs et al. has a Vickers hardness within the range of 381-479 (3.70-4.69 GPa) [122]. He et al. also reported the microhardness to be 395 Hv (3.7 GPa), and the elastic modulus was 107 GPa [95]. On the other hand, the microhardness of EBM parts was around 3.2-3.5 GPa, and the elastic modulus was 118 GPa, as reported by Facchini et al. [174]. In this study, the nanoindentation hardness of parts processed using the 450 nm laser and 808 nm was found to be 4.59 GPa and 4.7 GPa, respectively. The elastic modulus for 450 and 808 nm was measured to be 114 GPa and 111 GPa, respectively. Figure 5.15 plots the average hardness and elastic modulus measured in the current study.

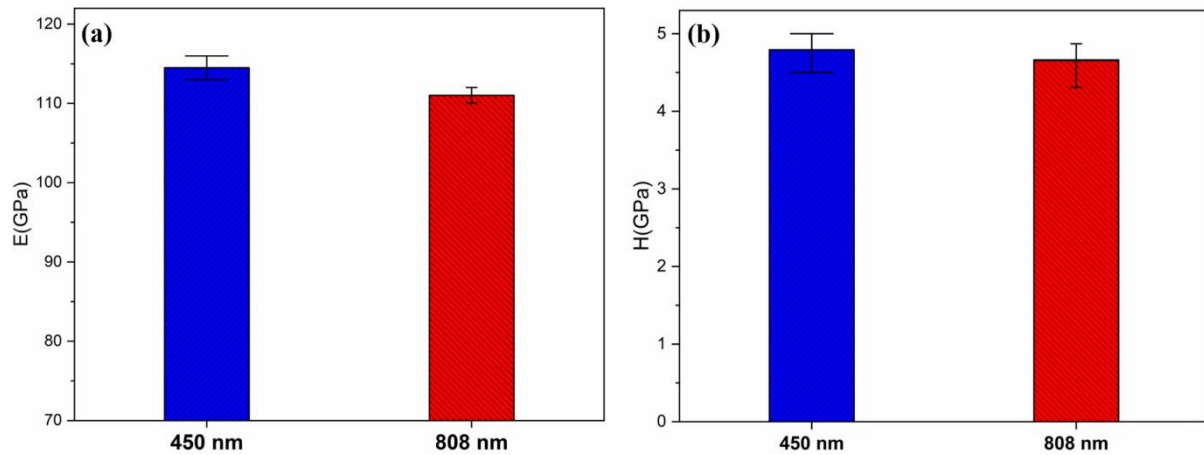


Figure 5.15: Ti6Al4V mechanical properties (a) Elastic modulus (b) Hardness

5.4 Conclusions

Ti6Al4V powdered feedstock was processed using a diode area melting approach with both 808 nm and 450 nm wavelength lasers. It was found that low laser powers diode lasers of 3.5W generate temperatures capable of creating melt pools with energy densities similar to traditional selective laser melting. This is due to the relatively higher absorptivity at short wavelengths (808 and 450nm) compared to SLM's laser (1060 nm). The absorption of Ti6Al4V powder was found to be 11% higher using 450 nm laser sources compared to 808 nm, resulting in an average of 12% higher temperatures with a maximum surface temperature of 1920°C.

Parametric studies and normalization models were used to identify the effective parameters to produce a sufficient melt pool width and depth that can successfully produce dense parts for future analysis. Parts with a density greater than 90% were produced within the range of $2 < E_0^* < 8$ by tuning the scanning speed within the normalised speed of $0.018 < v^* < 0.048$, which corresponds to conventional SLM processing windows for Ti6Al4V. The width and depth of the melt pool tracks varied between 150 to 520 μm and were generally 5-10% wider and 20-40% deeper using 450 nm laser sources compared to 808 nm laser.

Keyhole formation was observed for both lasers at low scan speeds, with the 450 nm laser forming keyholes at speeds below 50 mm/min and the 808 nm laser forming keyholes below 10 mm/min. These keyholes were generally formed for high energy densities $E_0^* > 8$ and insufficient fusing of material at energy density values $E_0^* < 2$. A consistent, smooth melt pool formed at scanning speeds of 100 mm/min up to 300 mm/min. However, insufficient melting was observed for both lasers above a scanning speed of 300 mm/min. Normalized overlapping within the range of 0.3-0.5 was found to be optimal for increased part density with a hatch distance of 0.157 μm .

Microstructure analysis revealed the presence of two types of microstructures, α phase and β phases, formed during DAM processing compared to only the α prime formed in commercial SLM systems. This is due to the relatively low scanning speed (mm/min), which generates cooling rates ($\sim 750\text{-}1400^\circ\text{C/S}$) compared to SLM, allowing β phases to form.

The mechanical properties of parts manufactured by 450 nm and 808 nm lasers were found to be comparable to SLM parts manufactured with 100–1000 Watt systems, significantly when improving the density values to be above 99% (through further system development), which may do not need post-process, therefore, improve the process efficiency.

This chapter investigated using 450 nm and 808 nm lasers to enhance absorptivity with low-power lasers and provided promising results. As this project progresses, the next phase will be dedicated to applying an 808 nm diode laser within a 2D array setup. The aim is to enhance the efficiency of the Powder Bed Fusion (PBF) process while ensuring the production of high-quality parts. This goal is envisaged to be further advanced through a thorough investigation and understanding of the capabilities of employing 808 nm lasers within a 2D laser head array. Such an arrangement aims to boost output power, which in turn will enhance process efficiency. Moreover, the influence of a multi-laser spot process on the high melting temperature material Ti6Al4V will also be scrutinised, further contributing to the project's ongoing development.

Chapter 6: Multi-beam 808nm Laser

Melting of Ti6Al4V

Summary:

This chapter is about using multiple addressable diode lasers to enhance the efficiency and scalability of the Powder Bed Fusion (PBF) process. The main aim is to create a PBF system that is high-resolution, energy-efficient, and scalable for production. This will enable the production of accurate and repeatable parts with desired mechanical properties. Additionally, the chapter explores the use of a 2D laser head array and evaluates the impact of different beam profiles on process efficiency, scalability, microstructure, and mechanical properties.

The research is conducted in multiple stages, starting with evaluating the optimal beam profile configurations (activating two lasers) for a solid merging of melt pools. Then, Single-layer samples are processed using x5 activated lasers with three different beam profiles, and the effects on density, surface roughness, and morphology are analysed.

The next stage involves developing a normalised energy density approach for the multi-laser process (x10 lasers activated). X-ray diffraction, nano-hardness measurements, and scanning electron microscopy (SEM) are used for microstructure and mechanical properties analysis.

The chapter highlights the potential of employing low-power, high-efficiency 808 nm diode lasers in the developed multi-laser fiber-coupled DAM approach. This advancement contributes to large-scale manufacturing applications in the PBF process.

6.1 Introduction

This chapter focuses on exploring the use of multiple addressable diode lasers to improve the efficiency and scalability of the PBF process. The system uses up to 10 low-power diode lasers, each with a power output of 4.5W, to achieve high absorption and processing efficiency. The ability to individually control each laser allows for the management of intensity distributions across the 2x linear array of laser beams, enabling the construction of complex custom parts and improved thermal control during the process. The study evaluates the impact of three different beam profiles on process efficiency and scalability, including microstructure and mechanical properties. The investigation involved analysing single-line scanning, the effect of laser beam profiles, the effect of laser power and scanning speed. The normalised processing windows for Ti6Al4V were determined for multilayer parts using x10 simultaneous laser sources. The primary objective is to develop a high-resolution and high-energy efficiency PBF system that is scalable for production, allowing for the production of accurate and repeatable parts with the desired mechanical properties for their intended application. Ultimately, this chapter aims to enhance the understanding and capabilities of Diode Area Melting (DAM) for large-scale manufacturing applications.

6.2 Experimental procedure

A multilaser array was used to process Ti6Al4V alloy powder inside the custom-built chamber to maintain the processing environment. Argon was purged into the chamber, and an argon air knife with filtered gas re-circulation was used to reduce the spatter from reaching the laser head and settling onto the powder bed. The laser head traversed over the powder bed in the x-y axis with speeds ranging from 10 mm/min to 1000 mm/min. An IR-Pyrometer was also incorporated into the system at an angle of 60° to measure the surface temperature during the process, as explained in Chapter 3.

The research was conducted in multiple stages. The first stage was performed by activating two lasers within the 2D head array at different pitch distances to establish the optimal beam profile configuration required to ensure a solid merge between melt pools created by each laser, as shown in Figure 6.1. This will enable the selection of a suitable laser beam profile arrangement for single-layer samples. Following this, x5 lasers were activated using three different beam profiles, which were identified from the previous stage, to process single layers from 1 mm thick powder. At this stage, the sample was characterised to understand the effect of the beam profile, power, scanning speed, and hatch distance on the samples (i.e., density, surface roughness and surface morphology).

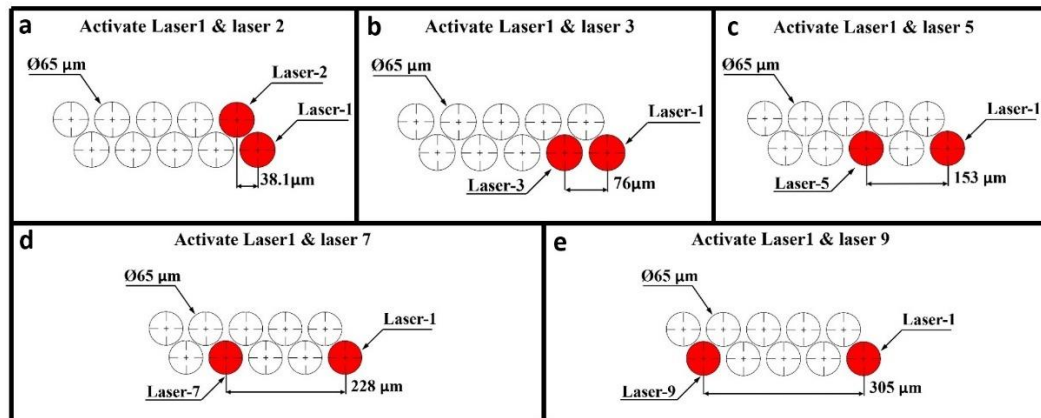


Figure 6.1: Illustration of the dual laser configurations employed for single track.

The next stage was to develop the normalised energy density approach for the multi-laser process, following the work undertaken by Thomas et al. [146], to determine the process parameters for multi-layer parts using x10 simultaneous laser sources. The microstructure and mechanical properties of manufactured parts were analysed and compared with components produced using a commercial LPBF system. The Archimedes principle was used to measure the density, as proposed by Spierings et al. [30]. Samples showing densities >95% were selected and then used to measure the surface roughness. These were then hot-mounted and polished to be examined for microstructure and mechanical properties. X-Ray diffraction was used to conduct phase and microstructure analysis, while nano-hardness was utilized to measure the microhardness. The average surface roughness was measured using an optical 3D microscope. Microstructural analyses were conducted using a scanning electron microscope (SEM) equipped with an electron back-scattered diffraction (EBSD) detector.

6.3 Results and discussion

6.3.1 Single line scanning

The melt pools generated by adjacent laser spots are expected to overlap and create a single wide track due to the arrangement of laser channels in a close-packed array. According to our previous investigation in Chapter 5, the melt width of a single laser source was approximately 10% larger than the laser beam size (Full Width at Half Maximum-FWHM), which can be expected due to the relatively slow scanning speed (50 mm/min to 100 mm/min). To evaluate the effect of pitch distance (d_p) on melt pool resolution, two lasers were activated at a laser power of 4.5 W and a scanning speed of 100 mm/min. The d_p was varied by activating the two lasers in different configurations by omitting channels within the array and spacing out the lasers used by one period at a time, as shown in Figure 6.1.

The channel configurations and profile used in this investigation and the resulting surface morphology of fabricated tracks in Ti6Al4V powder are shown in Figures (6.3, 6.4, 6.5, 6.6, and 6.7) (with the dashed yellow circles indicating laser spot position relative to each other).

When Lasers 1 and 2, with a pitch distance of $38.1\mu\text{m}$, were activated, they functioned as a single unified beam, as shown in Figure 6.2 (a), resulting in the creation of a single solid uniform melt pool (Figure 6.2 (a)).

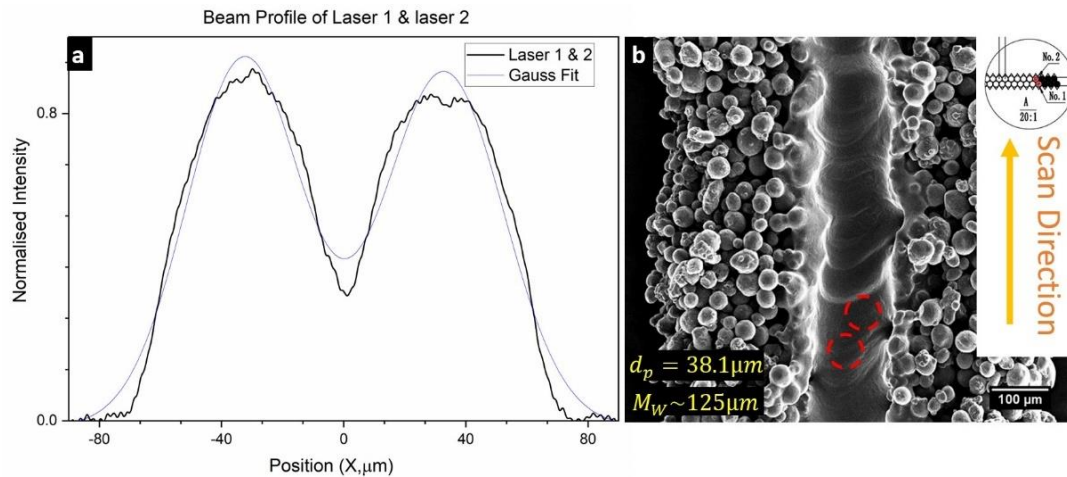


Figure 6.2: (a) Beam profile of Channels 1&2 ($d_p = 38.1\mu\text{m}$), (b) Morphology of single tracks.

Activating Lasers 1 & 3 with a d_p of $76\mu\text{m}$ led to a gap between the lasers of $11\mu\text{m}$, as shown in Figure 6.3 (a). Even though there was a space between the lasers, the melt pool combined to form one single track, as shown in Figure 6.3 (b).

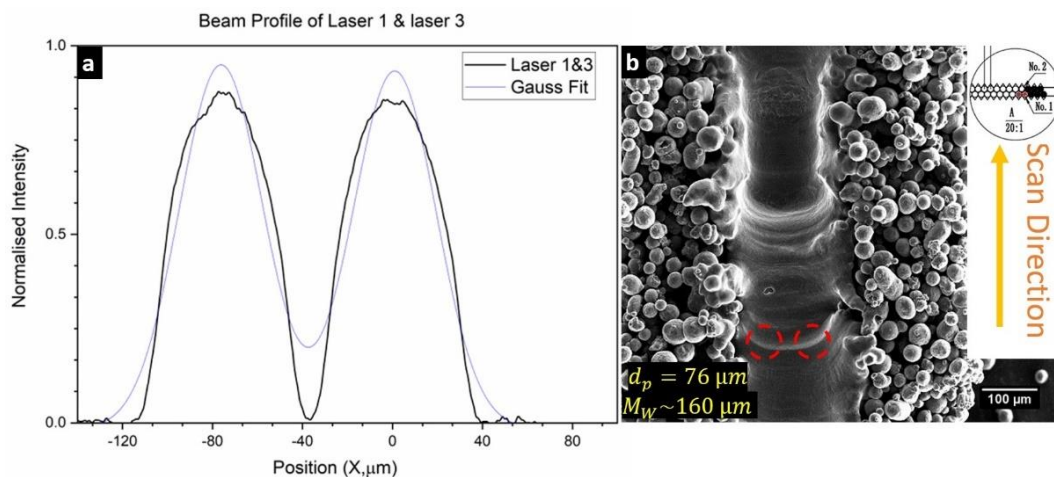


Figure 6.3 (a) Beam profile of Channels 1&3 ($d_p = 76\mu\text{m}$), (b) Morphology of single tracks.

Lasers 1 and 5, with a d_p of $153\mu\text{m}$, generated individual beams with a gap of $87\mu\text{m}$, Figure 6.4 (a). The powder was processed by two individual beams with a spot size of $65\mu\text{m}$ each resulting in a relatively wider melt pool (Figure 6.4 (b)) compared with the previous configuration.

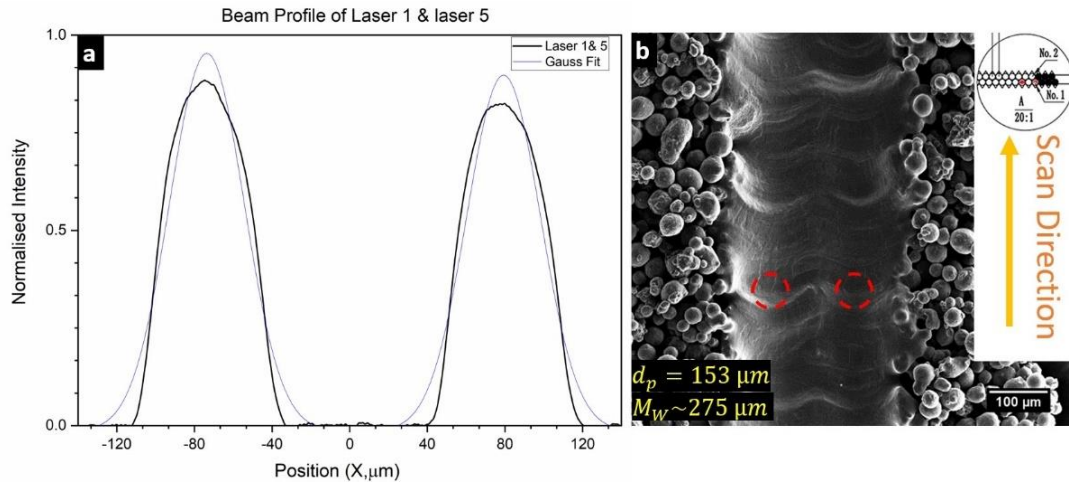


Figure 6.4 (a) Beam profile of Channels 1&5 ($d_p = 153\mu\text{m}$), (b) Morphology of single tracks.

Increasing the pitch distance to $228\mu\text{m}$ by activating Lasers 1 and 7, resulting in an unprocessed area of $163\mu\text{m}$, as shown in Figure 6.5.

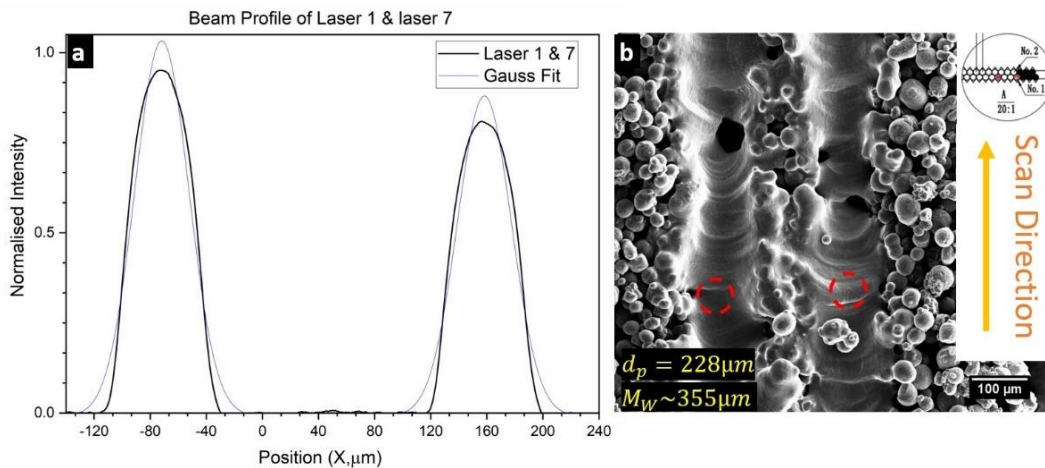


Figure 6.5 (a) Beam profile of Channels 1&7 ($d_p = 228\mu\text{m}$), (b) Morphology of single tracks.

Lastly, with lasers 1 and 9, the maximum pitch distance is $305\mu\text{m}$. Both lasers act as separate sources without overlapping (Figure 6.6).

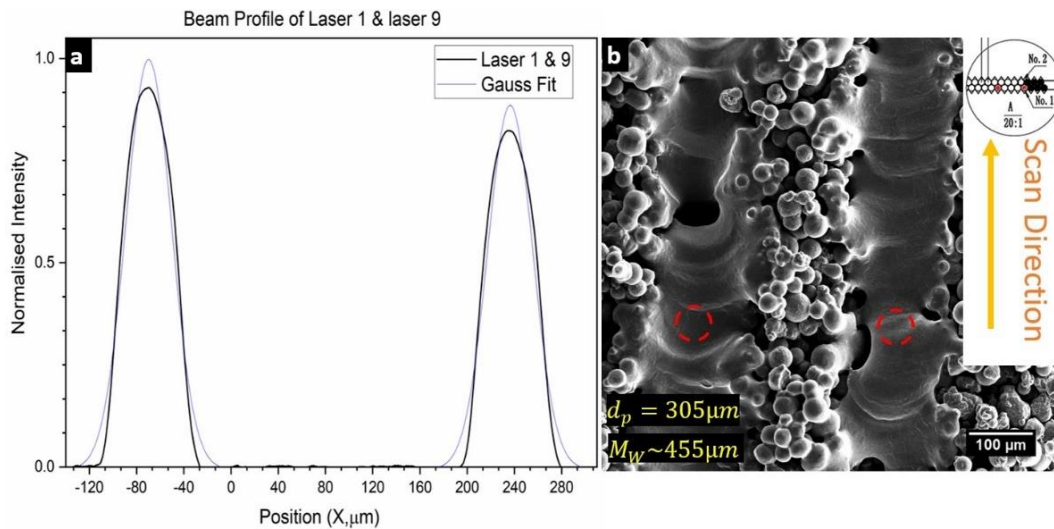


Figure 6.6 (a) Beam profile of Channels 1&9 ($d_p = 305 \mu m$), (b) Morphology of single tracks.

In general, when the d_p of channels increases, the two molten tracks change from being entirely merged to being completely separate. For values of d_p less than the melt pool width ($< 160 \mu m$), formed by activating channels (1&2, 1&3, and 1&5) the melt pools merge together and form a single wide track, with the track width increasing from $125 \mu m$ in Figure 6.2 (b) to $275 \mu m$ in Figure 6.4 (b). A partial separation between the two molten tracks is observed when d_p is increased to $228 \mu m$ by activating channels 1&7, as shown in Figure 6.5 (b). We also note that decreasing the laser pitch increases the surface energy density and therefore influences the melt pool morphology. With an even higher pitch distance ($d_p = 305 \mu m$), the two melt pools become completely separated with an unprocessed area of powder $\sim 140 \mu m$ wide visible between the tracks as shown in Figure 6.6 (b). The morphology of tracks also changes, from a uniform continuous track when using channels 1&2 to a discontinuous track with defects (unmelted powders, porosity within the single track) when 1&9 were used. The configuration of channels 1&2 results in a preceding laser spot, which indicates that the intensity increases and the time to conduct energy away from the melt pool decreases. The melt pool (that subsequently solidifies to form the track) is strongly influenced by this overlapping effect, with deeper melt pools created as a result of the higher energy densities. The opposite is also true, offsetting the parallel beams so that they are spaced out from each other results in a reduction in the surface energy input (E_s). However, the track width increases because the energy is distributed over a wider area. Zhang et al. [175] studied the effect of increasing the offset between 2 lasers in the lateral direction under different laser power and found that surface energy density is mainly influenced by laser power and hatch spacing. For instance, increasing the laser power from 60W to 100W increases the maximum hatch spacing from $140 \mu m$ up to $200 \mu m$ with a wider merged melt pool. Similarly, a computational study of synchronized multibeam

strategies by Heeling et al. [176] found that the melt pool width increased considerably when using a hatch spacing larger than 0.75 times the beam diameter. In this work, it was observed that the width of the melt pool increased significantly for offsets similar to or larger than the diameter of the beam. Therefore, to ensure complete merged melting, from this point forward the investigation is limited to pitch distances less than $153\mu\text{m}$ i.e., LP1, LP2 and LP3.

6.3.2 Single layer scanning

6.3.2.1 Effect of laser beam profiles

The key processing parameters in LPBF that affect the temporal and spatial energy distribution throughout the process are laser power, scanning speed, hatch distance and layer thickness. Therefore, researchers have combined these parameters into different metrics energy density (linear energy density, surface energy density, and volumetric energy density) to evaluate the effectiveness of parameter-set on the morphology of the samples [114]. This study uses the surface energy density to investigate the effect of laser power, scanning speed and pitch distance (laser profiles) on the melt pool morphology. It is important to gain an understanding of the dimensions of tracks created using an array of lasers, complete layers will be formed by overlap of consecutive scans, this overlap must be optimized in order to prevent defects related to excessive or insufficient surface energy input. In contrast to a traditional LPBF system where the track is formed using a single heat source (single laser), the current laser system uses multiple lasers that together create a single wide track for each scan. Figure 6.7, 6.9, and 6.10 show the surface morphology using SEM, for a single layer created using x5 simultaneous lasers under three different beam profile configurations (LP1, LP2, LP3 respectively). A single layer of 10×10 mm scanning area was fabricated using laser powers of 3.5 W and 4.5 W at varying scanning speeds (75 mm/min - 300 mm/min), where the hatch distance H_d was fixed at 10% of the beam profile. The effect of the laser profile and the associated surface energy input (E_s), is noticeable on the results. Thus, E_s influences the morphology of the layer and the processing range (laser power and scanning speed). Figure 6.7 shows the results for LP1, where the melt pool width of each track created with x5 lasers is approximately $286\mu\text{m}$. The surface is uniform, and the tracks are consistent and closely merged with each other. The beams within each track form a smooth surface, however between adjacent tracks there is a slight protrusion. The boundary between the tracks is well fused, creating a continuous layer; this is further investigated in the cross-section examination. An average surface roughness (R_a) of $2.02 \mu\text{m}$ was achieved at 4.5 W and scanning speed of 75mm/min. This is attributed to the 2D array configuration of LP1, where the second, interleaved row of lasers increases both the surface energy input (E_s) and

the interaction time with the melt pool, which reduces the R_a . The results for LP2 are shown in Figure 6.8, showing wider continuous tracks ($\sim 405 \mu\text{m}$ wide) with a smooth top surface similar to LP1. However, the boundary between adjacent scans is more pronounced, indicating a higher surface roughness ($R_a = 4.6 \mu\text{m}$) compared with LP1. This can be attributed to a reduction in both the surface energy input (E_s) and the interaction time compared with LP1, since for this configuration there is no second row of lasers following the first. The results for LP3 are shown in Figure 6.9. Although the use of the LP3 configuration produced continuous single tracks for each scan, the surface energy input (E_s) of LP3 was insufficient to merge adjacent tracks and smooth single layers could not be produced. This resulted in incomplete overlap and defects (un-melted particles), which affect the morphology resulting in a high surface roughness, $R_a = 20.5 \mu\text{m}$. Therefore, LP3 cannot successfully form single layers and is deemed unsuitable for multilayer parts.

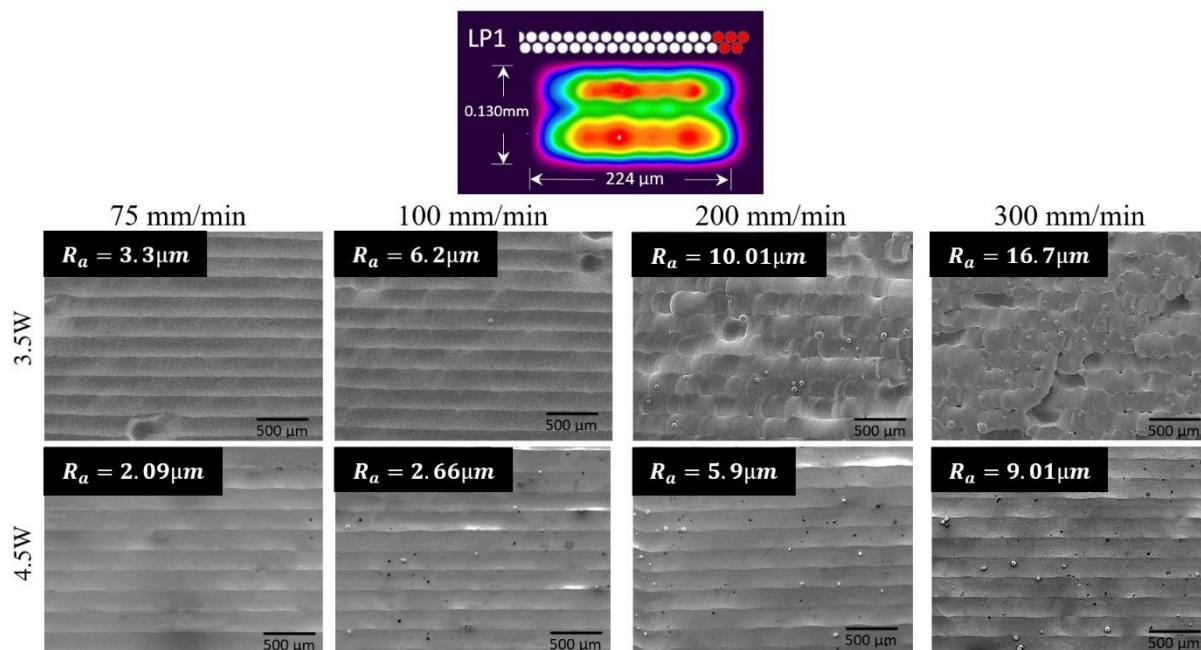


Figure 6.7: Surface morphologies of Ti6Al4V under different processing parameters using LP1 configuration (each track was formed using x5 lasers)

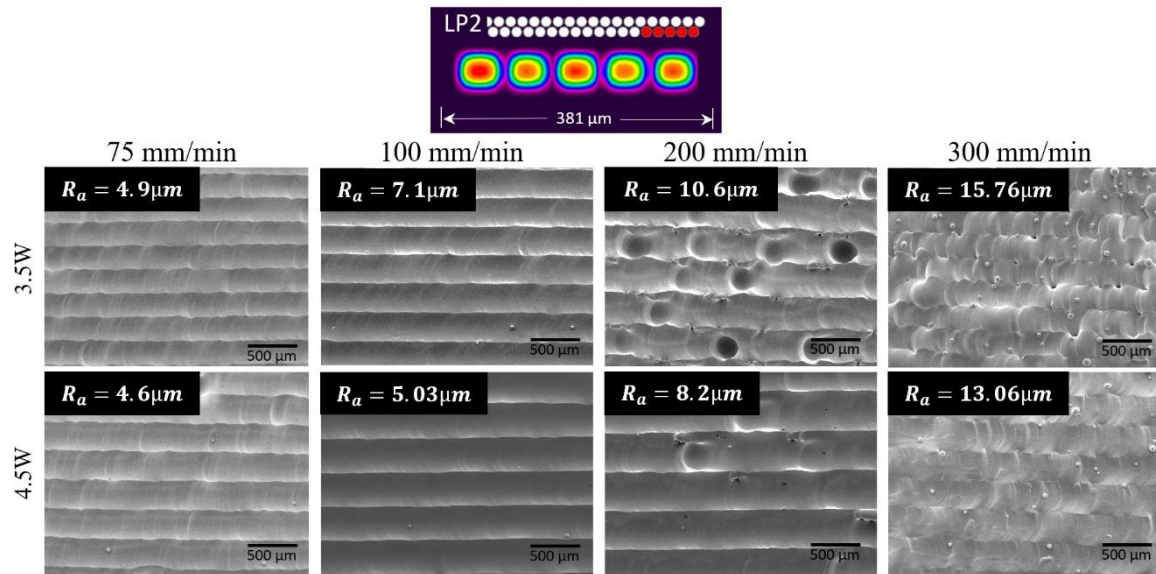


Figure 6.8: Surface morphologies of Ti6Al4V under different processing parameters using LP2 configuration (each track was formed using x5 lasers).

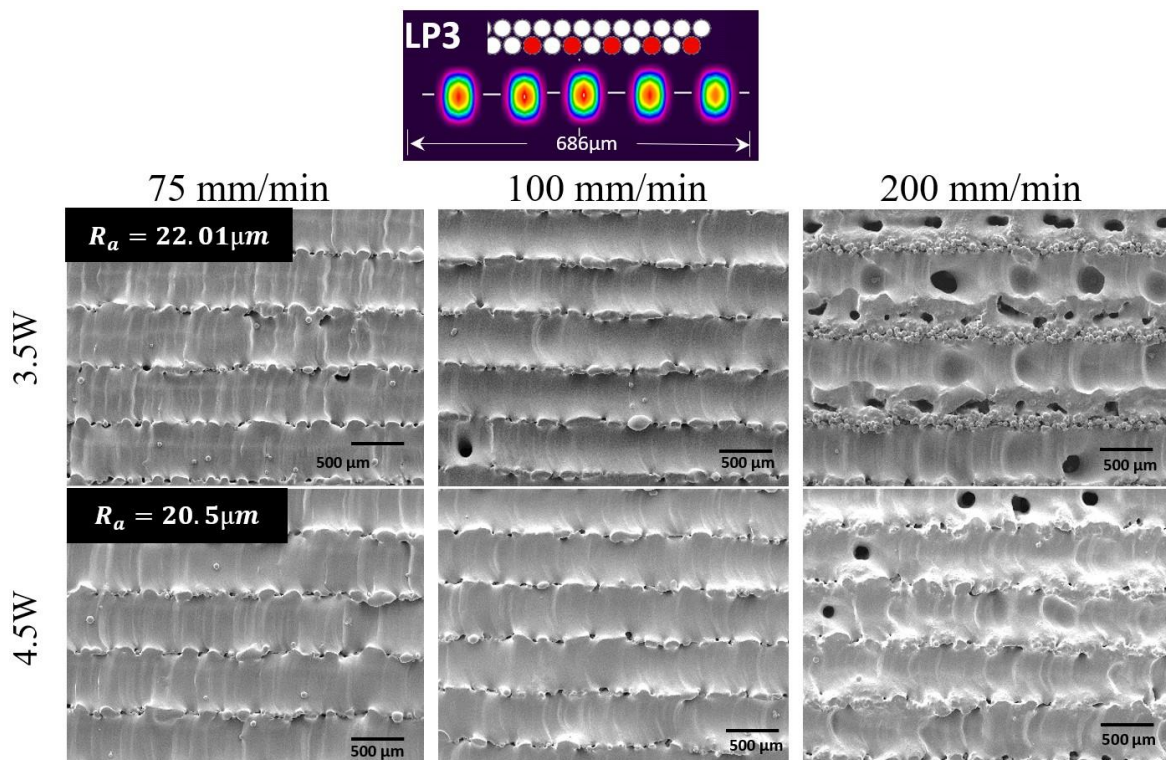


Figure 6.9: Surface morphologies of Ti6Al4V under different processing parameters using LP3 configuration (each track was formed using x5 lasers).

Figure 6.10 shows the cross-section, observed by SEM, of single layers generated in Ti6Al4V using LP1, LP2, LP3 scanning strategies. The scanning speed was fixed at 100mm/min with varying overlap distance between the scans at 10%, 20% and 30% of the melt pool size in order to evaluate the influence of overlap distance on melt pool morphology. LP1 produced a melt pool depth d_m of 180 μm for $H_d=250 \mu\text{m}$, with a high-density smooth surface. As the H_d was increased the depth increased slightly to 194 μm and 188 μm for $H_d=200 \mu\text{m}$ and $H_d=150 \mu\text{m}$, respectively. The cross-section for LP2 shows a wave-like surface structure for 10% overlap. The track depth decreased to 168 μm for $H_d=350 \mu\text{m}$ compared to LP1. However, as the H_d was reduced the surface roughness reduced whilst the melt pool depth increased to 174 μm and 179 μm for $H_d=300 \mu\text{m}$ and $H_d=280 \mu\text{m}$, respectively. These results indicate that the layer depths and the average R_a improve by reducing the H_d . For LP3, the melt pool depth was less than 100 μm for all conditions. Weak bonding and inconsistent tracks were observed. This is due to the distribution of energy over a wider range perpendicular to the scanning direction, forming a wider track with incomplete overlap, as already described. The maximum melt pool depth is strongly affected by this phenomenon since the recoil pressure increases with increasing intensities [176] [177]. Yadroitsev et al. claim that the reduction in track height observed in their work was due to denudation phenomena [178]. The first scan pulls powder towards the melt pool from neighbouring regions, thereby leaving insufficient powder for the following scan, and consequently creating a defective layer. Similar results have been reported by Tsai et al. [179]. These observations inform us that it is not preferable to employ pitch distances corresponding to double the beam diameter or overlap distance more than 10% of the melt pool width to ensure satisfactory surface quality with high throughput performance.

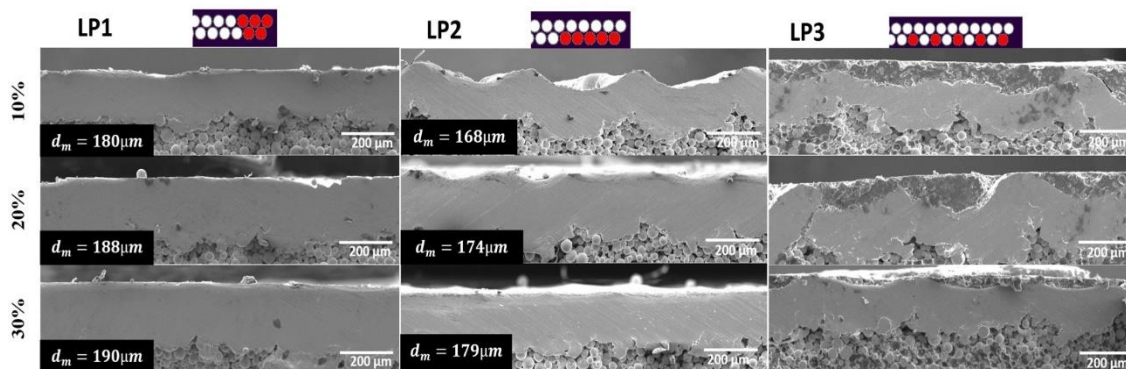


Figure 6.10: Cross-section morphology for a single layer produced using LP1, LP2, and LP3 at different overlap distances.

Table 6.1 compares processing performance efficiency between a single beam and various multi-laser array configurations. The experiment was designed to calculate the processing time of single $10 \times 10 \text{ mm}^2$ area layers at 4.5 W, 100 mm/min (optimal parameter for all profiles). Scanning times using LP1, LP2, and LP3 are 5, 9 and 15 times faster than for the single-diode laser.

The single beam, with a spot diameter of $65 \mu\text{m}$ and hatch distance of $40 \mu\text{m}$, will cover a scanning length of 2500 mm, which requires 1500 seconds to complete a single layer. In comparison, the LP1 with $\times 5$ laser has a scanning width of $224 \mu\text{m}$, which reduces the scanning length to 500 mm for a hatch distance of $200 \mu\text{m}$. This configuration effectively reduced the scanning time to 300 seconds, making the process five times faster than the single laser.

LP2 configuration of five 1D lasers has broadened the scanning width to $300 \mu\text{m}$ to reduce the scanning length and time to 285 mm in just 171 seconds, which is nine times faster than the single laser. The LP3 array improved the scanning width to $400 \mu\text{m}$ and hatch distance to $400 \mu\text{m}$, thereby scanning a length of 98 mm in simply in 98 seconds, fifteen times faster than the single laser.

Upon future upscaling of the LP1 array to $\times 50$ lasers, the scanning time is predicted to be $\times 88$ faster than for a single traversing diode laser. These results demonstrate that LP1 and LP2 scanning configurations could be used to enhance processing quality and throughput with the option of scaling to large arrays.

Table 6.1 : Comparison between a single laser and multi-laser array 4.5 watts, $\times 5$ lasers approach for a single layer ($10 \times 10 \text{ mm}^2$)

Scanning Profiles	scanning width (μm)	Hatch Distance (μm)	Scanning length (mm)	time (sec)@100 mm/min	Faster
x1 single laser	65	40	2500	1500	-
LP1 x5 laser arrays (2D)	224	200	500	300	x5
LP2 x5 laser arrays (1D)	300	300	285	171	x9
LP3 x5 lasers arrays (1D)	400	400	98	98	x15
x50 laser arrays (1D)	3800	3400	17	17	x88

6.3.3 Effect of laser power and scanning speed

Whilst laser power and scanning speed are explicitly linked to energy density, the effect of laser power is more evident on surface morphology (porosity/surface roughness) and the processing window, whereas the scanning speed significantly influences melt depth (as shown in Figure 6.11). For all configurations, increasing laser power from 3.5 W to 4.5 W is observed to improve the processing performance, whilst the effect of scanning speed is more dominant on the depth. For instance, when a laser power of 3.5 W was used, a low surface roughness appeared at a 200 mm/min scanning speed for all laser profiles, as was shown in (Figures 6.8 - 6.10). However, increasing the laser power to 4.5 W improved the processing window to allow for scanning speeds in excess of 300 mm/min for LP1 and 200 mm/min for LP2. In general, the results show that increasing the laser power and/or reducing the scanning speed will increase the surface energy input (E_s), and therefore the melt pool depth (and hence thickness) of the fabricated layer. For LP1, the optimal surface energy density results in high density at scanning speeds ranging from 75 mm/min up to 200 mm/min and 75 mm/min up to 300 mm/min for 3.5 W and 4.5 W, respectively (as can be determined from Figure 6.7). At a 75 mm/min scanning speed, a maximum melted layer thickness close to 220 μm was achieved using laser power of 4.5 W. In comparison, LP2 formed a fully dense layer at a scanning speed up to 100 mm/min and 200 mm/min for 3.5 W and 4.5 W laser powers, respectively (Figure 6.8). LP2 produced a maximum thickness of about 190 μm under similar processing conditions to LP1. LP3 did not show a significant improvement when increasing the laser power from 3.5 W to 4.5 W, as evidenced in (Figure 6.9). For LP3, smooth continuous single tracks are formed when traversing the multi-laser beams at speeds slower than 100 mm/min, whereas bonding defects appear between the tracks at faster speeds. However, it should be noted that the reduction in surface energy density (when using LP3) is due to the wide pitch distance. Scanning speed not only dictates the melt pool depth but also influences the surface finish. Fast scanning speeds above 200 mm/min produce spatter on the surface, which causes uneven powder spreading in subsequent layers thus effecting multi-layer parts. This phenomenon is more common when two adjacent lasers are used in the LPBF process [16,179]. Since 4.5 W provides excellent surface properties, high density and higher productivity compared to 3.5 W, 4.5 W was selected to produce the multi-layer parts for the remainder of this study.

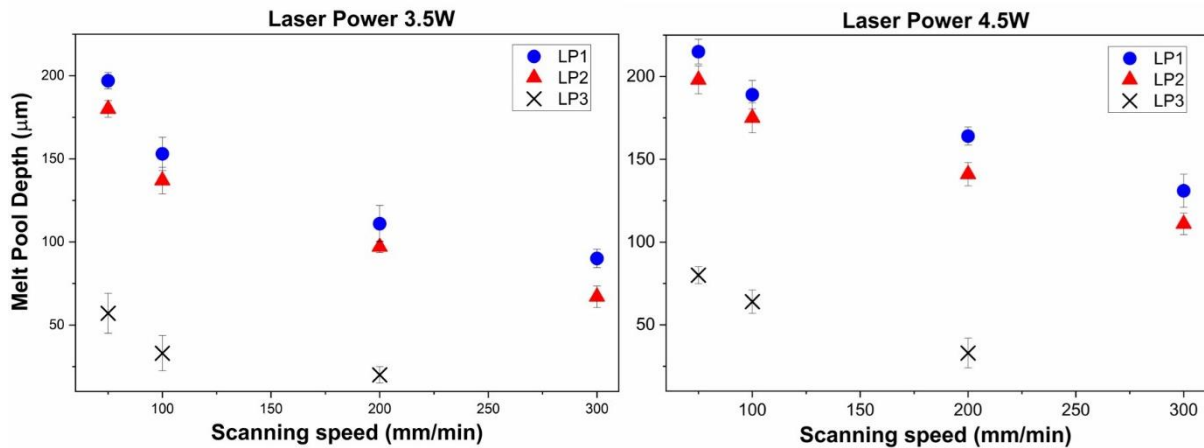


Figure 6.11: Effect of laser power and scanning speed on melt pool depth for 3.5W and 4.5W laser powers.

6.3.4 Normalized processing windows for Ti6Al4V (multilayer)

A total of 15 experiments were performed using x10 lasers in LP1 and LP2 configurations. These experiments cover the range of process parameters within the limits given in Table 6.2 to identify the optimal processing window for Ti6Al4V by evaluating the density of the specimens. It is known from previous studies conducted by Thomas et al. [146] and Jiang et al. [180] that laser power and scanning speed are the key determinants of part density in SLM. For this reason, a maximum laser power of 4.5 W was used, while the energy input was controlled by varying the scanning speed only. Furthermore, the effect of overlapping of adjacent beams/melt pools influences process efficiency; increasing the hatch distance improves the production rate. Therefore, based on our single-layer study (6.3.2), the investigators opted to fix the overlap distance at 10% of laser width, which is sufficient to obtain a good overlap.

Table 6.2: Processing parameters using x10 diode lasers of Ti6Al4V to normalize energy density.

Processing Parameters	Units	LP1	LP2
Laser power (P)	W	4.5	
Scanning speed (v)	mm/min	75-600	
Scanning width (r)	μm	762	414
Hatch distance (H_d)	μm	685	372
Layer Thickness (l)	μm	70	

LPBF of Ti6Al4V has been extensively investigated using 1070 nm lasers with one study using 808 nm [25]. However this prior work has primarily used single beam sources [152] or a maximum of x2 beams (preceding or beside each other) [181]. The current research study is aiming to uses multiple laser beams. A sufficiently detailed explanation of the processing was provided, which we were able to adapt in our previous research for normalization of laser parameters for a single-source laser in chapter 5. The fundamental concept of normalization is to compare the actual energy over the minimum energy input for complete melting, keeping the material properties in mind.

The normalized volumetric energy density E^* obtained by calculating the normalized primary parameters P^* , v^* , h^* and l^* for single laser source. However, since this research uses a unique multi-beam configuration during the process, modification of the equation is required in order to calculate the normalized energy input for the overlapping multi-laser beams compared to a single laser. In Equation 2.15, Thomas et al. [146] considered the length of the beam, represented by $2r$, which defines both the width of the scan and the scan area. This is not applicable for multiple beams, in which the entire beam length delivers the energy, and thus r is replaced by the length of the beam as described by Equation 6.1.

$$r = (n 2r_b) + (n - 1) d_g \quad (6.1)$$

Where n is the number of lasers, r_b is the radius of a single laser, and d_g is the separation distance between lasers. This expression covers the LP1 and LP2 laser arrays used in this study. Thus, the diameter has been redefined by the length and the irradiated area is composed of the sum of all active beams and does not depend solely on the radius of a single beam. Similarly, the total energy input is the sum of the energy input from all active beams. This modified equation caters for the multi-beams, the effect of pitch distance, the effect of the number of the active beams and is directly applicable to scaled up models. Figure 6.12 shows the normalized processing diagram representing normalized energy density E^* (on the x-axis) and normalized hatch h^* (y-axis) on a log10 scale. The isopleth dashed lines represent the minimum energy input E_0^* required to melt the material at a specific volume $2rl^*$. In general, the green area within the range of $4.5 \leq E^* \leq 14.8$ represents the normalized processing parameter that results in high-density parts (>95% density). The use of processing parameters that give an energy density within the red zone defined by $E^* > 14.8$ leads to excessive energy, causing material vaporisation. In contrast, a lack of fusion occurs when employing a combination of processing parameters that provide $E_0^* < 4.5$ (i.e., within the blue region). Here the energy is insufficient to melt the powder between layers causing the density to drop below 90%.

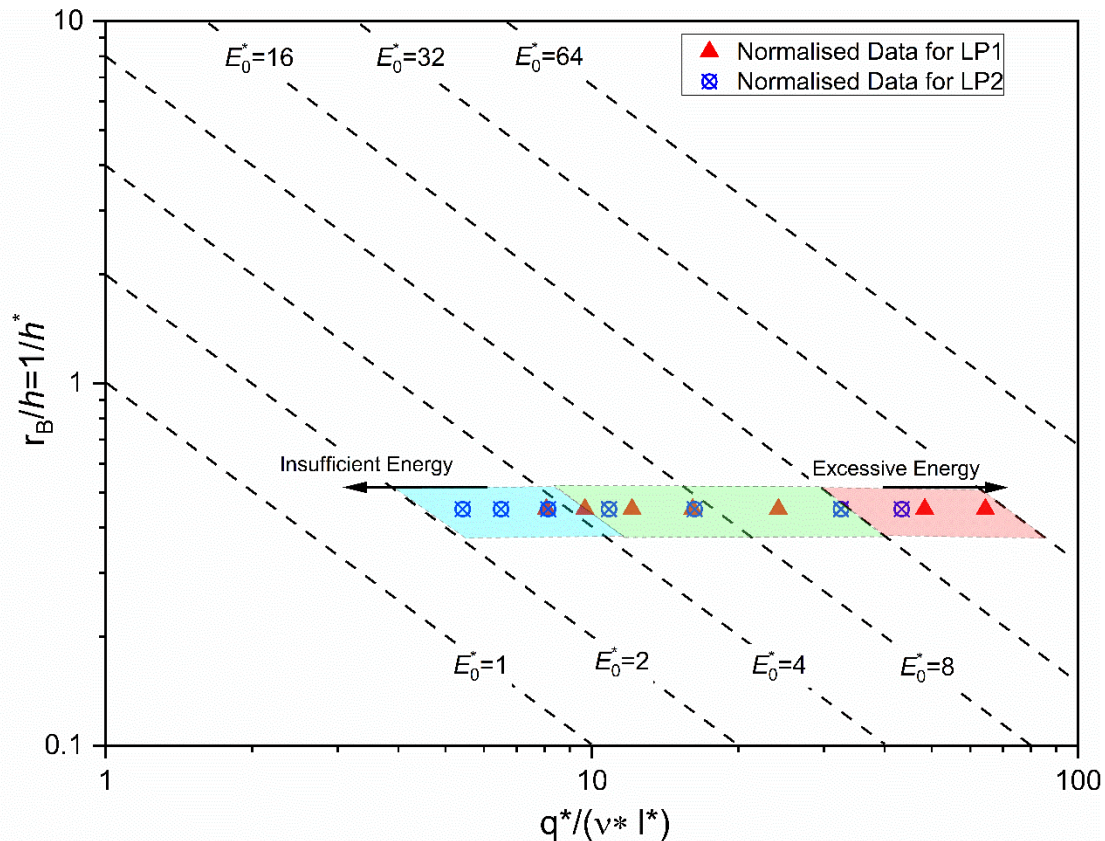


Figure 6.12: Normalized energy input showing the location of the experimental parameters and the optimal region for LP1 and LP2.

6.3.5 Density evaluation

In this study, the parameters that hold the main influence on part density are the pitch and the scanning speed. Figure 6.13 illustrates the variation in density according to E_0^* and the corresponding scanning speed for LP1 and LP2. At E_0^* of 7.3, both profiles provide a maximum density of 97.8% for LP1 (at a speed of 300 mm/min) and 96.7% (at a speed of 200 mm/min). LP1 produces higher density (>95%) at higher speeds within the range of 150 mm/min to 500 mm/min compared to LP2, for which high density parts are only possible in the range between 100mm/min to 300 mm/min. This is due to the smaller pitch in LP1, which significantly increases energy input, thereby improving the density of the part while improving the process efficiency. Figure 6.14 and Figure 6.15 show the cross-sections of multi-layer parts for LP1 and LP2, respectively and the variation of density with E_0^* and corresponding scanning speed. For both configurations, part density increases initially with increasing E_0^* by reducing the scanning speed. However, the density begins to decrease when $E_0^* > 14.8$ due to excessive energy input, which causes the samples to warp and distort making the parts unacceptable. In contrast, increasing the scanning speed moves E_0^* into the

“insufficient” region ($E_0^* < 4.5$) where the density falls sharply to less than 90% due to improper melting, lack of fusion and weak bonding between layers. It is important to note that using a combination of processing parameters to give a similar E_0^* for LP1 and LP2 does not guarantee the same sample density, as each sample has a different thermal history [152] as influenced by the laser configuration (pitch distance) used. A similar conclusion has been reported in [180].

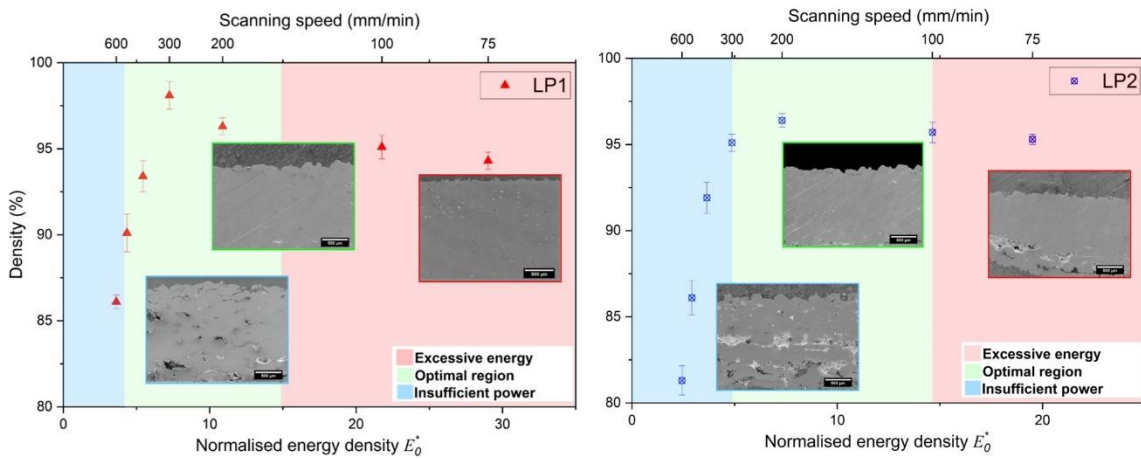


Figure 6.13: Variation of density with speed and normalised energy density for LP1 and LP2.

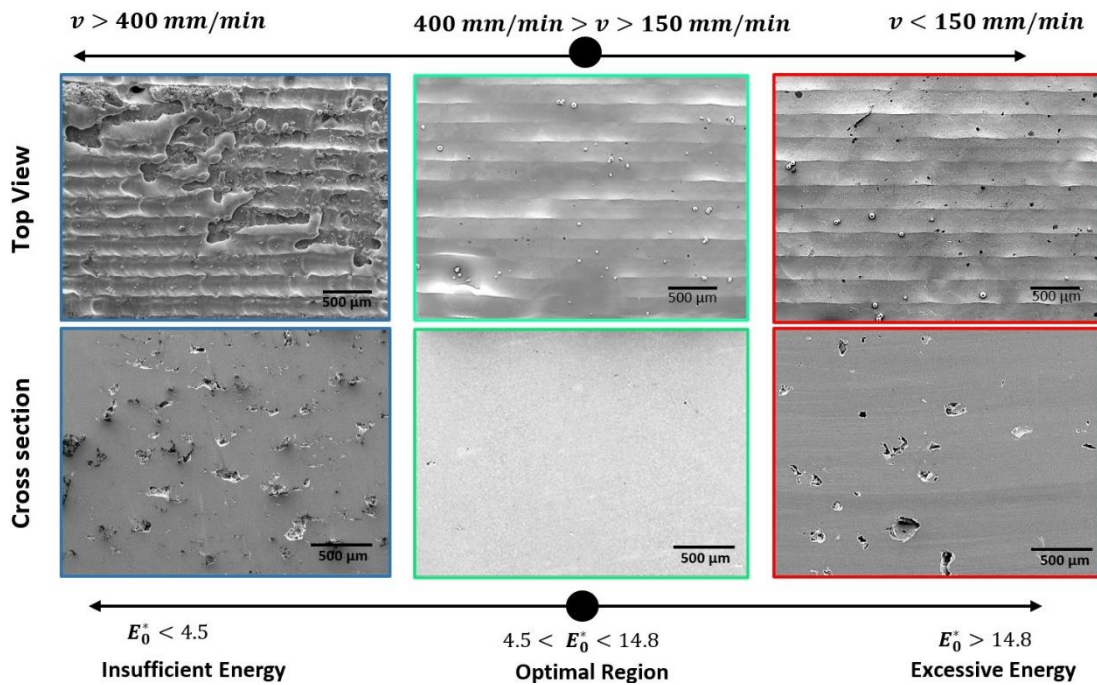


Figure 6.14: The effect of scanning speed on the top surface and cross-section for LP1.

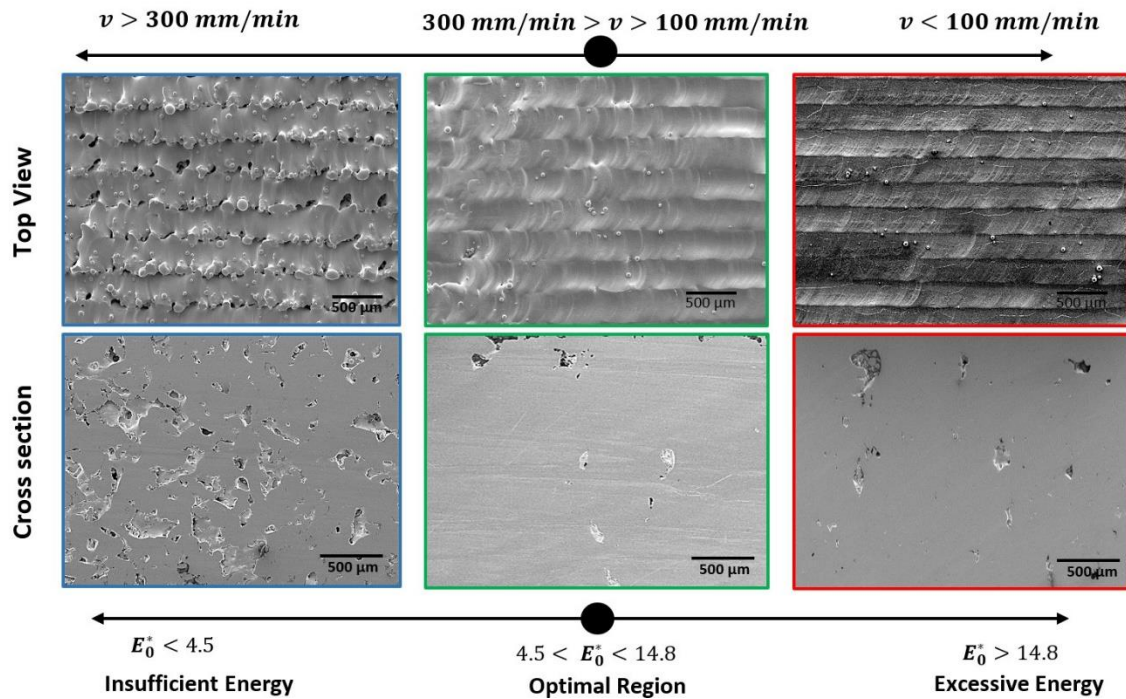


Figure 6.15: The effect of scanning speed on the top surface and cross-section for LP2.

6.3.6 Surface Roughness

Figure 6.16 shows 3D optical microscope images for multi-layer parts processed at different speeds using LP1 and LP2 configurations at a power of 4.5 W, for which variation of the top surface roughness can be observed and root mean squared surface roughness, R_a extracted. The laser power, scanning speed, and hatch distance are known to affect the surface roughness, with laser power and hatch distance reportedly having the greatest influence [180]. In our case, the pitch (similar to hatch distance in the single beam LPBF process) for LP1 and LP2 is different and dictates the power density. We have seen already that LP1 has a higher energy density compared to LP2. For both LP1 and LP2 configurations, R_a is observed to increase with an increase in speed. For 75 mm/min, R_a is minimal for both LP1 and LP2 at 7.1 μm and 8.6 μm , respectively. The surfaces are smooth and there are no visible striations or protrusions. However, the roughness for LP2 is generally higher than that of LP1 and even though R_a increases with speed at 300 mm/min, LP1 has 21% lower roughness than LP2, perhaps as a result of a re-melting effect that may be generated as a result of activation of the second linear array within the laser head. All parameters that produced densities greater than 95% were analysed for R_a , and generally LP1 has approximately 17-21% smoother surface than LP2. Energy density varies as a function of both speed and beam profile, consequently affecting the melt pool dynamics and resulting in a variation in surface R_a . Both LP1 and LP2 have different power densities due to their

particular beam configurations. In general, slow scanning speeds (less than 100 mm/min) reveal that higher energy densities produce more consistent melt pools (e.g., fully formed, consistent overlap) under multi-laser irradiation. In contrast, the lower energy input at higher speeds leads to spatter and particles that cause higher R_a . Similar findings have been reported in the literature, where low energies tend to lead towards the balling of melted powder and porosity [180].

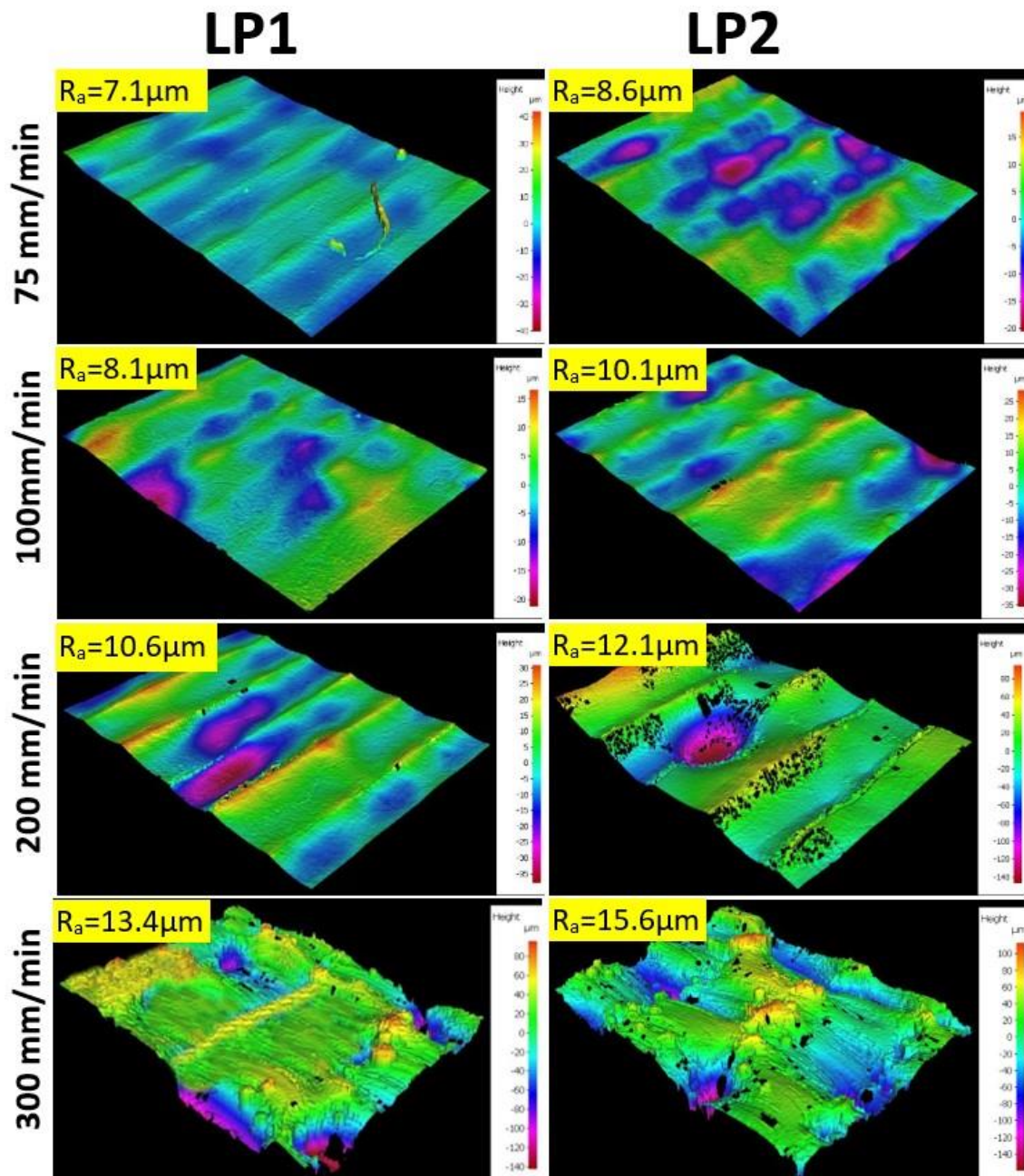


Figure 6.16 Surface roughness for different speeds and profiles, with corresponding r.m.s roughness R_a .

6.3.7 Microstructure

Only specimens with a density of $> 95\%$ were analysed, confined to processing speeds between 75 mm/min and 300 mm/min. The cooling rate is known to be a key factor in influencing the microstructure of Ti6Al4V in the LPBF process. The continuous cooling transformation has shown that microstructure formation can be controlled by controlling the cooling rate above the β transus (994°C), explained in detail by Ahmad and Rack [89]. The cooling rate during the process can be controlled by heating the chamber/powder bed or by adjusting processing parameters such as the hatch distance and/or processing speed. Our previous study in chapter 5 demonstrated that slow scanning speed combined with low laser power can help to reduce the cooling rate, providing the ability to develop a β phase. This capability is not a common capability of traditional LPBF processes. Figure 6.17 illustrates the effect of beam configuration (LP1 and LP2) and scanning speed on the microstructure with SEM images of the top surface of samples produced at various speeds using LP1 and LP2 at a fixed laser power. It can be seen that both profiles produce samples with dominant (α/β) microstructure. However, the effect of the beam profile on the coarseness of the α/β transformation is more pronounced than that of scanning speed. Above 100mm/min, both profiles produce a fine (α/β) Widmanstätten, composed of α lamellas and a small amount of β phase due to the relatively rapid cooling rate. In contrast, samples produced at scanning speeds below 100 mm/min are composed of coarse (α/β) Widmanstätten. Due to the second laser array in LP1, which maintains the temperature above the β transus for a longer period of time than LP2, the cooling rate is reduced, and a coarser microstructure is observed. Figure 6.18 shows the temperature transient measured using a pyrometer for LP1 and LP2. The temperature rise is similar for both configurations; however, differences can be observed in their cooling rates. It takes 0.67 s for LP1 to maintain the temperature between the $T_{\beta \text{ transus}} = 994^{\circ}\text{C}$ and the martensite temperature $T_{\text{ms}} = 575^{\circ}\text{C}$ compared to 0.37 ms for LP2. Therefore, the average cooling rate for LP1 was 600°C/s compared with 1086°C/s for LP2. This is consistent with the results of the microstructure reported in the literature.

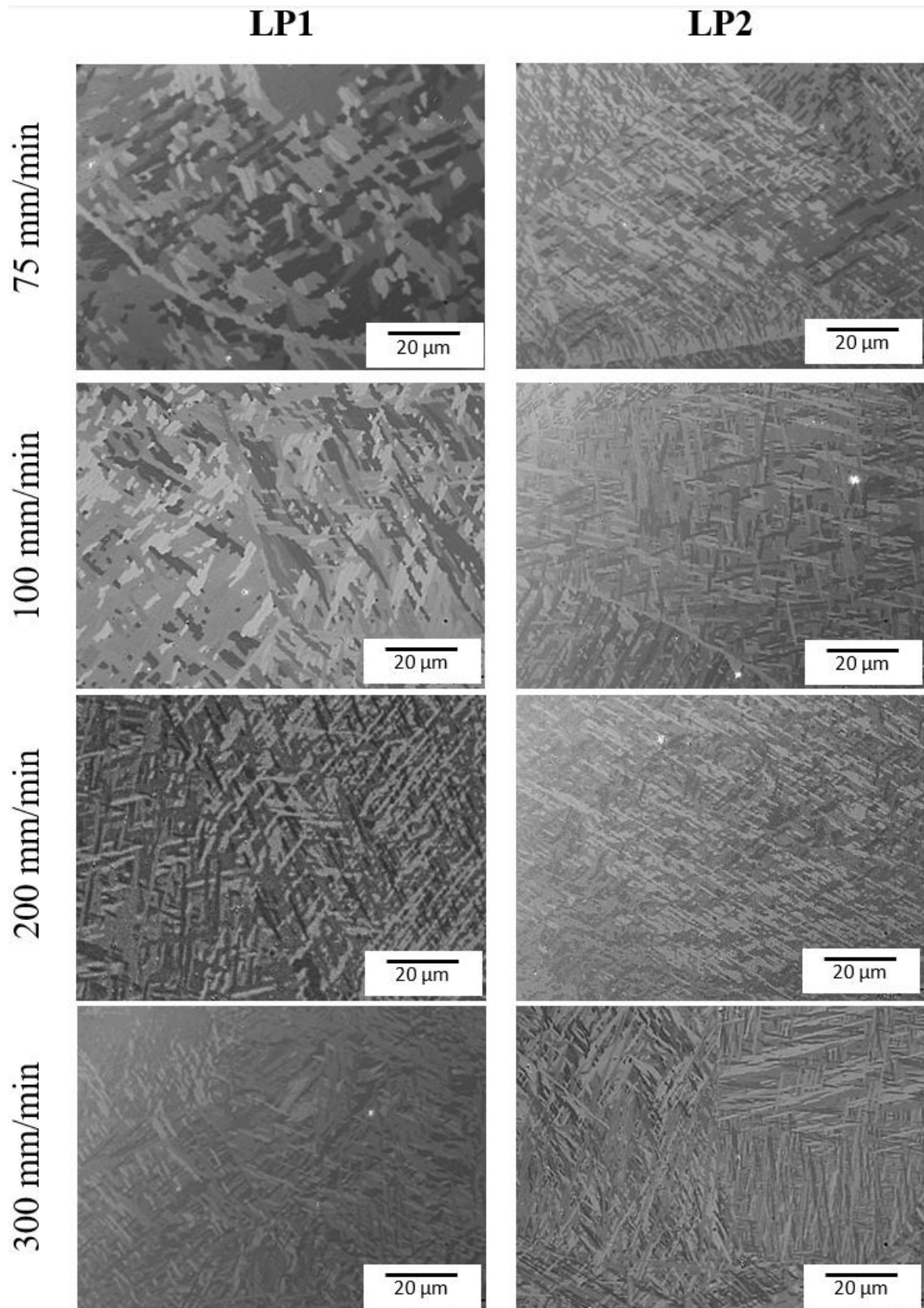


Figure 6.17: Ti6Al4V microstructural variation with speed and laser beam profile.

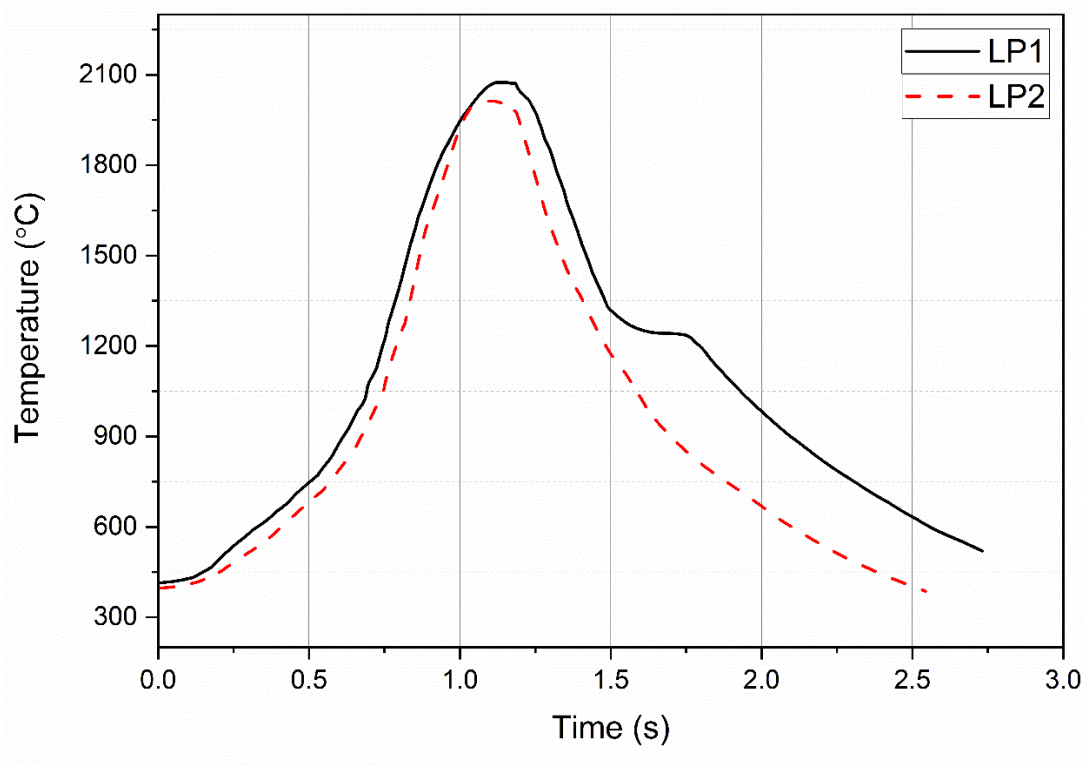


Figure 6.18: Temperature comparison at scanning speed of 75 mm/min for LP1 and LP2.

Further investigation has been conducted to evaluate the texture of the top surface of the samples (xy) to understand the effect of the beam profiles and the scanning speed during the process using electron backscatter diffraction (EBSD). EBSD has been carried out on an area of $809 \mu\text{m} \times 606 \mu\text{m}$ with a step size of $0.5 \mu\text{m}$. Figure 6.19 shows the colour inverse pole figure (IPF), which confirm a basketweave-like α - β microstructure observed inside the prior- β grains under all processing condition. The scanning speed has more influence on the crystallographic texture than the laser profiles. As shown in Figure 6.19, at a scanning speed of 75 mm/min, columnar β -grains are observed, whereas, at 200 mm/min, the material exhibits fine equiaxed β grains. However, the average grain size was larger using LP1 ($4.3 \mu\text{m}$) than LP2 ($3.7 \mu\text{m}$) at low speed, as shown in Figure 6.20. When the Ti alloy is heated for a significant time above the β grains, the grains tend to increase in size, whereas processing below the β grains will not change the grains as the α impedes the movement of β grain [182]. This is true when using LP1, which provides a significant surface energy density than LP2, as discussed previously. From the pole figures (Figure 6.21), α texture is weaker than the texture of the high temperature β phase. There is an apparent preference for the α phase, exhibiting a clear crystallographic orientation with a strong preferred direction along $\langle 0001 \rangle$ under all processing parameters. The samples produced using LP1 have a stronger α phase texture (about 26 times of random) compared with LP2. As the scanning speed was increased, the texture of the α phase got weaker and more random. For LP1 and LP2, the maximum intensity of the texture

reduced to 21.28 and 7.59, respectively. In case of β phase, it was found at low scanning speed tend to form a strong crystallographic orientation on $\langle 100 \rangle$ and minor on $\langle 111 \rangle$. LP1 shows stronger β phase texture than LP2 (about 38.40 compared to 26.26). Increasing the scanning speed weaker the β phase texture and changing the orientation to $\langle 111 \rangle$. This is owing to the greater proportion of α phase at high scanning speed, which has a more random crystallographic orientation due to the relatively large number of α variations included inside each β grain [183][184].

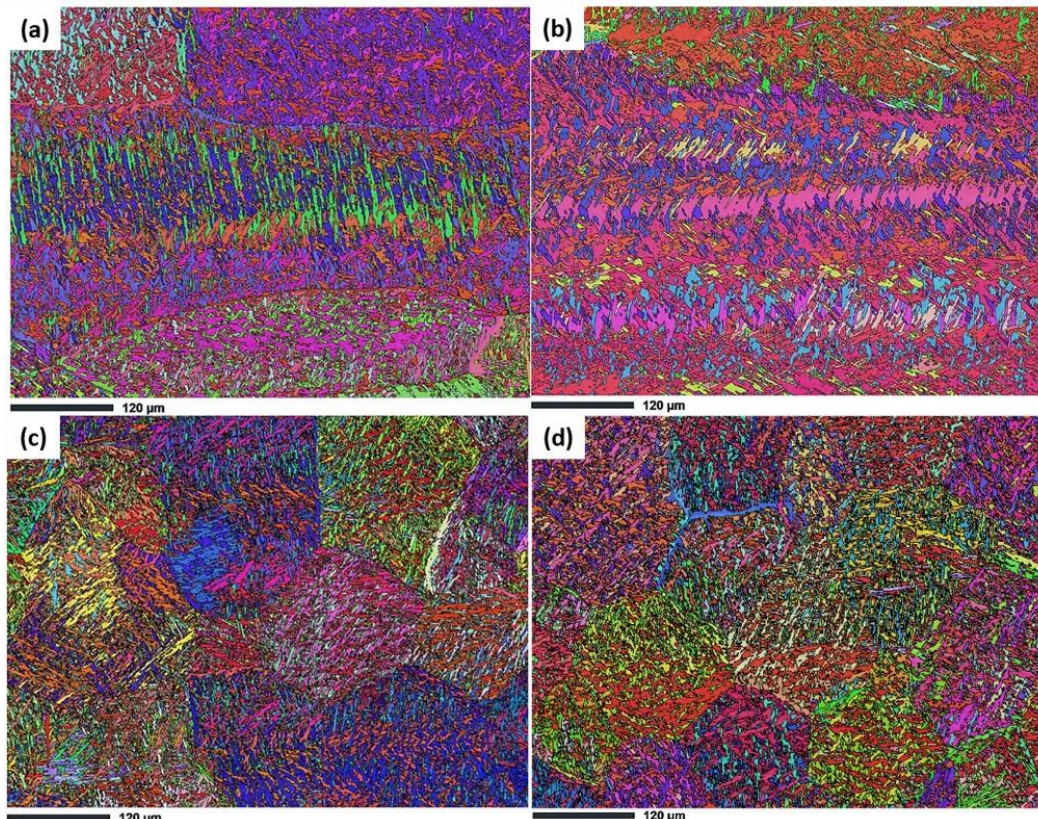


Figure 6.19: EBSD analysis of XY-plane (top surface) from the samples at processing parameters (a) IPF for LP1 at 75 mm/min (b) IPF for LP2 at 75 mm/min (c) IPF for LP1 at 200 mm/min (d) IPF for LP2 at 200 mm/min.

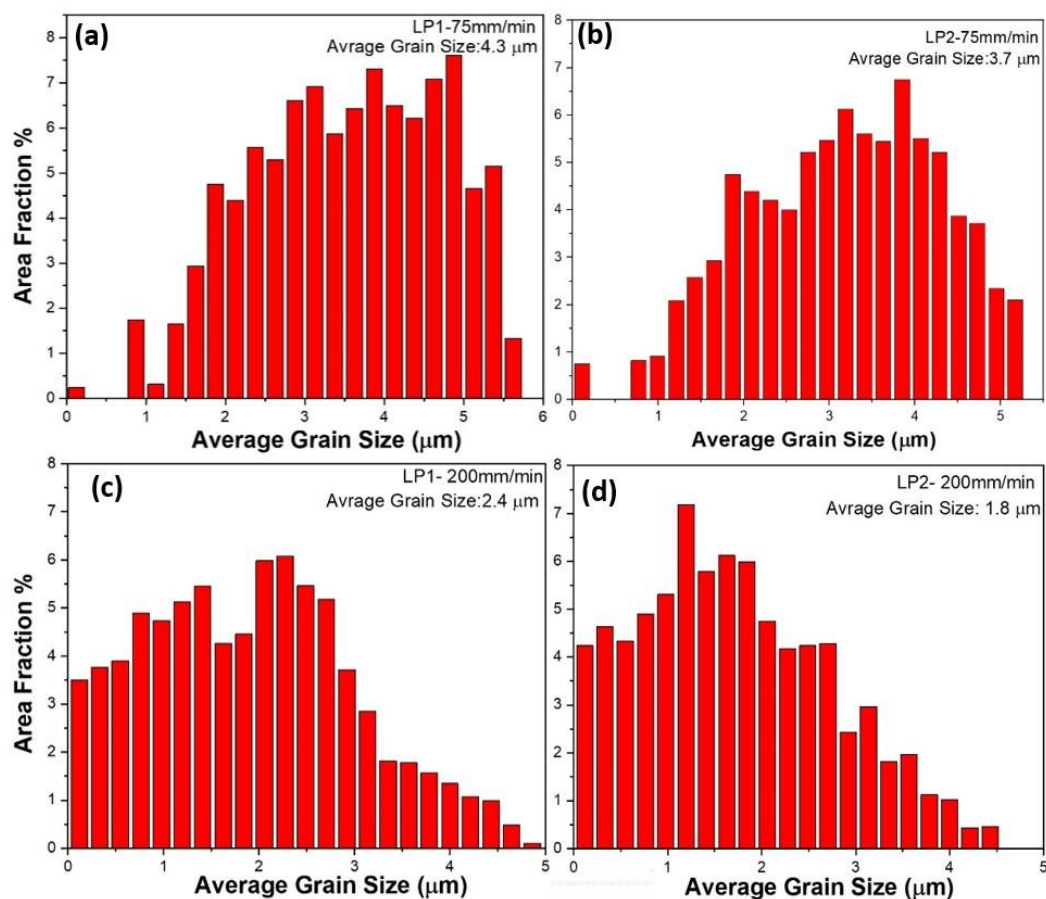


Figure 6.20: Average grain size (a) for LP1-75 mm/min (b) for LP2-75 mm/min (c) for LP1-200 mm/min (d) for LP2-200 mm/min.

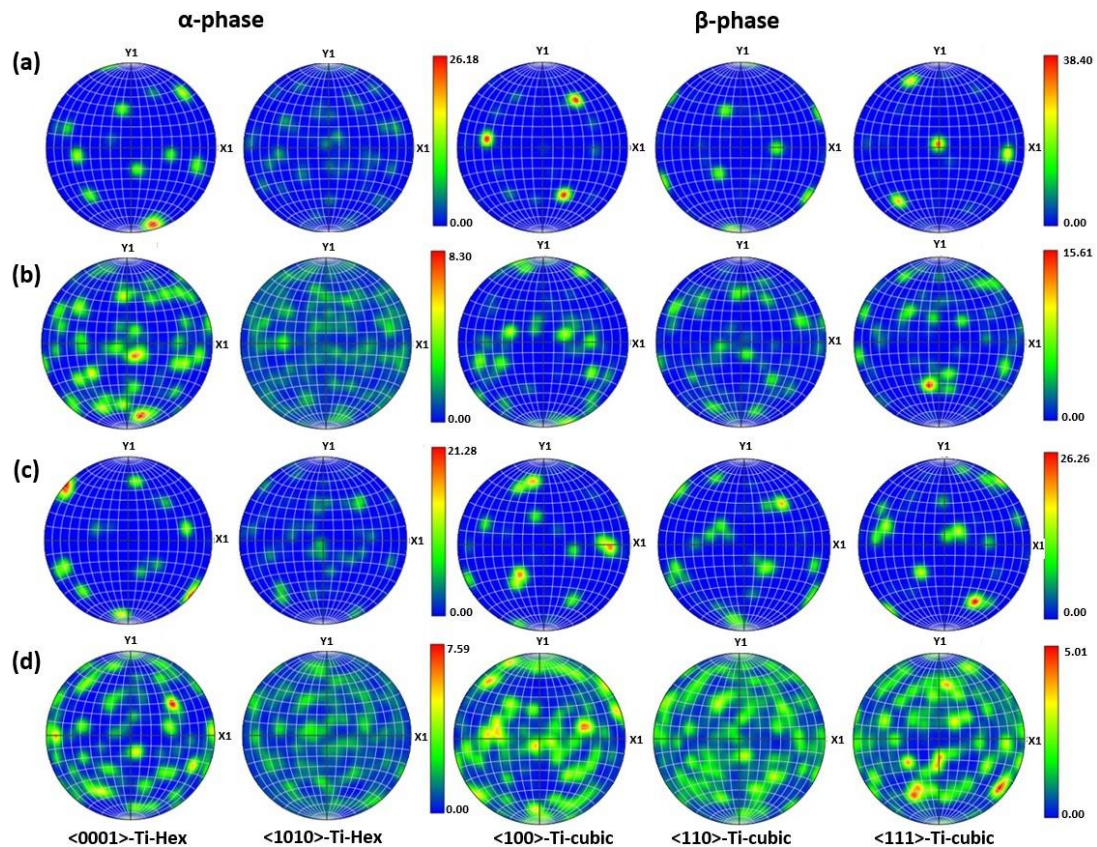


Figure 6.21: Corresponding pole figure (a) (PF) for LP1 at 75 mm/min (b) (PF)for LP1 at 200 mm/min (c) (PF)for LP2 at 75 mm/min (d) (PF) for LP2 at 200 mm/min

6.3.8 XRD

X-ray diffraction (XRD) can be used to confirm the existence of α/β in the samples produced by LP1 and LP2. Figure 6.22 plots the XRD response for LP1 and LP2 at different speeds for 4.5 W lasers. All peaks in the graph have been identified as ($\alpha/\acute{\alpha}$); this is because ($\acute{\alpha}$) and (α) share the same hexagonal closed pack crystal structure, making it difficult to differentiate between the peaks. At $2\theta = 35-39^\circ$, a diffraction peak can be observed, corresponding to the β (110) phase. This is true under all scanning speeds for LP1 and LP2. However, the peak intensity changes when the scanning speed and laser profiles are varied. For LP1, the β peak shifts to lower 2θ angles at scanning speed less than 200 mm/min. The β phase (200) at $2\theta=57^\circ$ was only observed at 75 mm/min, which is not common for LPBF processes. This is due to the second array, which has higher energy input and allows more time for $\acute{\alpha}$ to dissolve and form the β phase with coarser microstructure, consistent with the microstructure observed using the optical microscope. In general, the peak intensities of LP1 are higher than LP2, which correlates with a finer microstructure observed in LP2. For LP2 at scanning speed above (200 mm/min), the XRD patterns do not change significantly. At scanning

speeds below 100 mm/min a slight shift is observed in both the α and β peaks to lower 2θ angles, indicating a transformation from α' to β . Slow scanning speeds lead to a relatively reduced cooling rate, which gives time for α' to transform into the α/β phase. In addition, the slight reduction in the ratio of α'/α peaks indicates a higher volume fraction of β phase in the samples, as suggested by Qiu et al. [185].

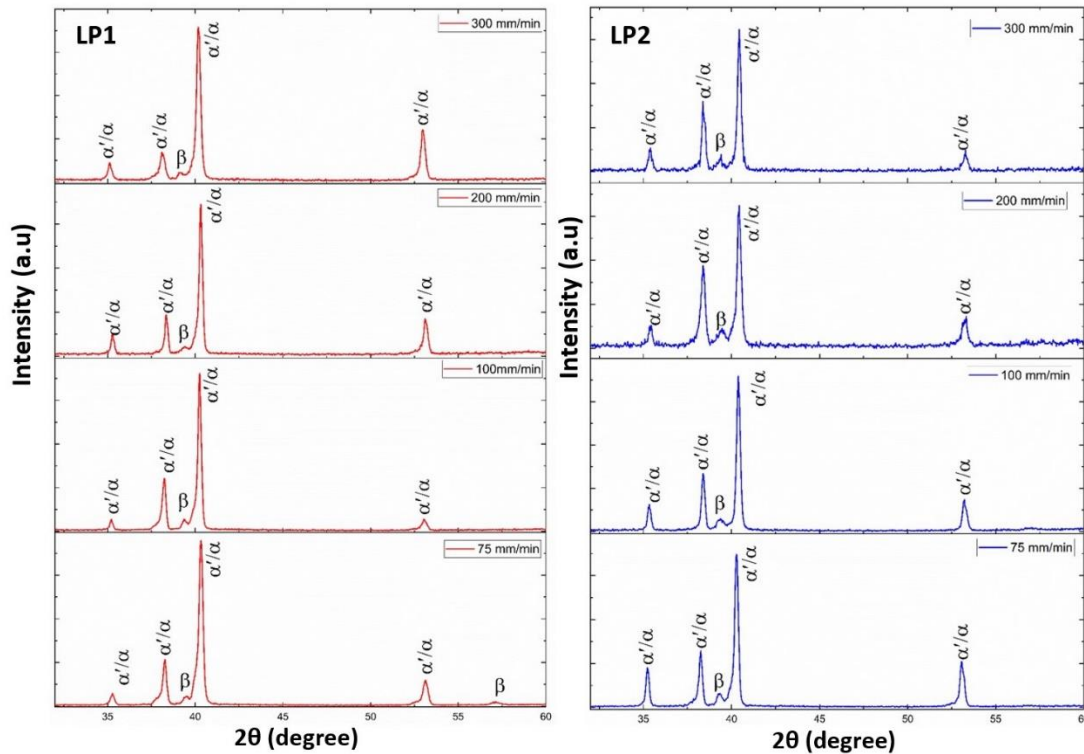


Figure 6.22: XRD graphs for LP1 and LP2 at different speeds using 4.5 W [151].

6.3.9 Nanoindentation

This section investigates the hardness and elastic modulus of fabricated samples using the nanoindentation technique suggested by Fischer-Cripps [35]. Hardness is mainly affected by the solidification process, i.e., the cooling rate affecting the microstructure. A reduction in hardness is associated with a coarser microstructure, which is significantly influenced by the processing parameters (pitch distance and scanning speed) used [146]. When the number of structural boundaries per unit volume of material is reduced (i.e., when the grain size is large), the distance over which dislocations can glide before hitting a grain boundary increases. Consequently, there is a reduction in material hardness. The results from nanoindentation measurements conducted on samples produced using LP1 and LP2 are shown in Figure 6.23 and Figure 6.24. These results show hardness to range between 4 GPa and 5 GPa over the range of scanning speeds

studied, whereas the elastic modulus is in the range of 110 GPa and 120 GPa. This is similar to the findings of Thijs et al. [122], who report the hardness of Ti6Al4V to be between 3.70 to 4.69 GPa with an elastic modulus of 107 GPa for parts manufactured using LPBF. Facchini et al. demonstrated a relative hardness of EBM samples around 3.2 to 3.5 GPa with an elastic modulus of 118 GPa [174]. Furthermore, Cai et al. [186] reported hardness varying from 4.0 to 5.5 GPa, depending on the indentation depth. For LP1 the average nano hardness at a scanning speed of 75mm/min and 100mm/min was 4.1 GPa and 4.5 GPa, respectively, and the corresponding elastic modulus was measured to be 119 GPa and 118 GPa. LP2 produced a sample with an average nano hardness of 4.5 GPa and 4.8 GPa at a similar scanning speed to LP1. The elastic modulus was 112 GPa and 110 GPa, which is comparatively less than for LP1. At scanning speeds above 100 mm/min, the change in average nano hardness and elastic modulus was negligible as there was no significant change for both profiles. The effect of the beam profiles on the hardness is more pronounced than the scanning speed, with a modest overall reduction. The hardness of samples produced at a scanning speed of 75 mm/min for LP1 is less than of LP2, correlating to the coarser microstructure, as discussed previously. This is consistent with the work reported by Thomas et al. [146], which concluded that pitch distance is the principal factor in controlling the hardness of the alloy. This is the case in our study, particularly for LP1 in which the overlap between adjacent spots is 50%.

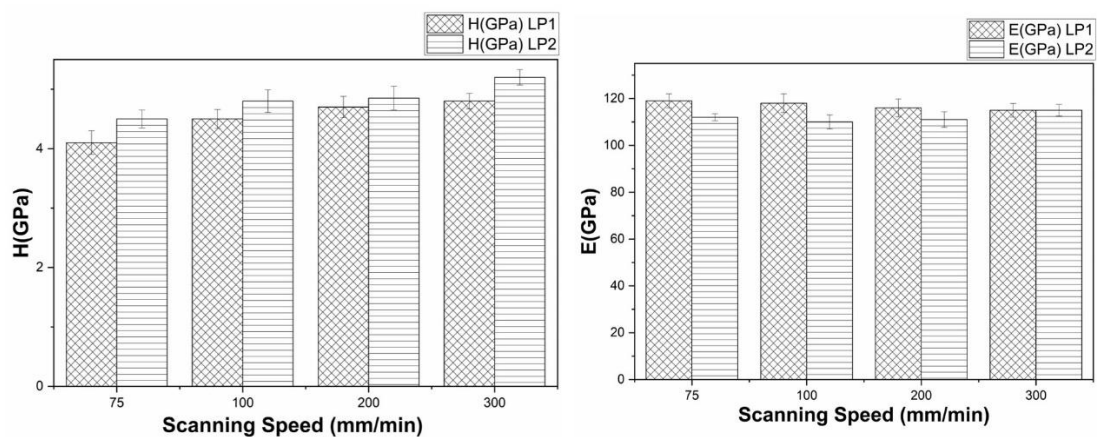


Figure 6.23: Nano hardness and elastic modulus comparison for LP1 and LP2 at different scanning speed.

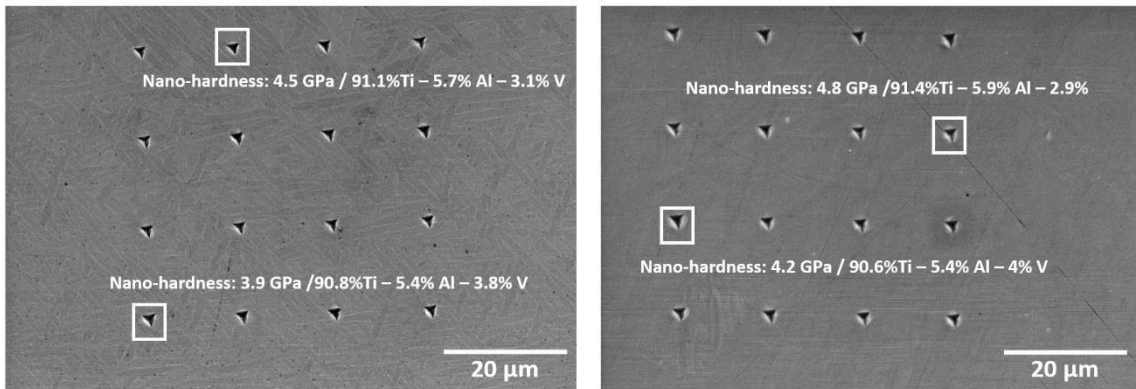


Figure 6.24: Nanoindentation and material composition for LP1 and LP2 at 75 mm/min.

Figure 6.25 plots the load, P as a function of displacement, h (the P - h curve) for indentations performed on samples produced using LP1 and LP2 at 75 mm/min. The curves show a more significant penetration depth in LP1 (coarser microstructure) compared to LP2. The penetration depth varies between 230-265nm for samples made using LP1 compared to the average penetration depth of 235nm for samples made using LP2. This could be attributed to indentation made at different phases, as shown in Figure 6.24. When the indenter is interacting with the LP1 sample, the P - h curve shows a higher depth value than LP2 (Figure 6.25), indicating that the microstructure of the LP1 sample is softer than LP2. The indentation that occurred over α/β lamellas has a higher depth compared with the α -phase region, as it is well known that α -phase is harder than the α/β phase. A similar conclusion has been reported in the literature [187]. The results confirm that the second laser array and the pitch distance significantly influence the microstructure and the mechanical properties of Ti6Al4V.

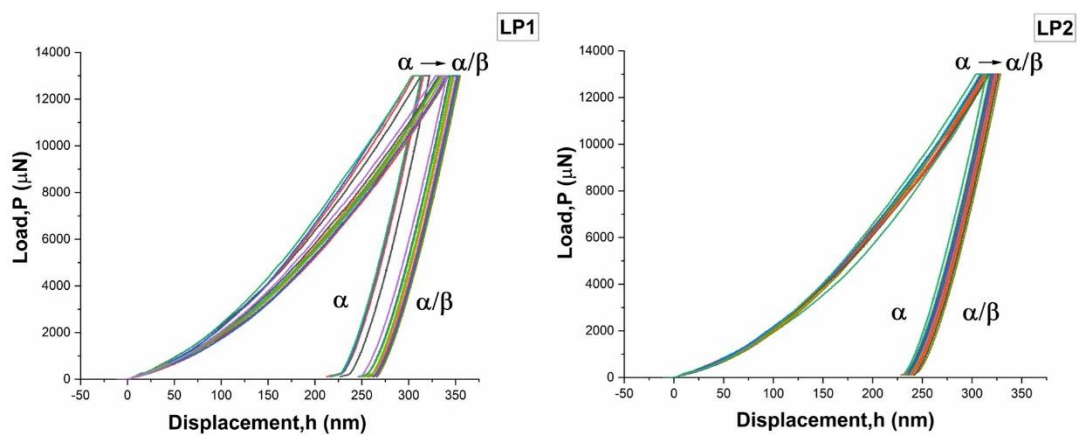


Figure 6.25: P-h Curves for samples produced at 75 mm/min for LP1 and LP2.

Further investigation of the composition was carried out using EDS to determine the specific concentrations of aluminium and vanadium in the alloy, since the concentrations of these elements is known to play a significant role in phase transformation. Vanadium is widely known to stabilize the β -phase, whereas Al is associated with the α -phase. Figure 6.24 does not show any evidence of significant variation in aluminium and vanadium elements for either sample set. This indicates that the transformation of phases is not influenced by a variation in alloying elemental composition but, significantly for this study, it is determined by the cooling cycle.

6.4 Conclusions

This chapter has demonstrated the feasibility, efficiency, and scalability of a fibre-coupled, multi-laser (DAM) methodology as a promising alternative to conventional Laser Powder Bed Fusion (LPBF) approaches. By utilizing low-power 4.5 W diode lasers operating at an efficient wavelength of 808 nm, the DAM approach achieved high powder bed temperatures, enabling the successful melting of Ti6Al4V powder. Compared to standard LPBF, the DAM approach improved laser absorption for Ti6Al4V powder by 15%.

A normalization model was developed for the multi-laser system, establishing that parts with a maximum density of 99% could be produced within a range of E_0^* values from 4.5 to 14.8. Below an E_0^* of 4.5, no melting occurred, while values exceeding 14.8 resulted in excessive melting. The surface roughness was found to vary depending on the selected beam profile and laser parameters. The implementation of two activated linear scanning arrays within the laser head demonstrated the lowest surface roughness, possibly due to a melt-pool re-melting effect.

Microstructure and mechanical property analyses were performed, revealing the presence of both alpha and beta grains in the XRD analysis, in contrast to commercial LPBF systems that typically produce only alpha grains. The DAM process induced much lower cooling rates compared to Selective Laser Melting (SLM), resulting in cooling rates of 600°C/s compared to 107°C/s. This slower cooling rate facilitated the formation of beta grains. Notably, a laser beam profile utilizing two linear arrays of lasers exhibited the slowest cooling rate. Samples produced using the DAM approach achieved densities exceeding 95%, hardness between 4 and 5 GPa, and elastic moduli up to 120 MPa.

This research highlights the potential of employing low-power, high-efficiency 808nm diode lasers in the evolved multi-laser fibre-coupled DAM approach. The ability to simultaneously scan large areas with enhanced thermal process control promises to improve productivity and efficiency in traditional LPBF.

Chapter 7: Conclusions & Future Work

7.1 Conclusions:

The research has revealed that utilizing a shorter wavelength leads to more considerable optical energy absorption by the metallic powder, thus reducing the overall power requirement. This allows for broader material processing. This discovery introduced a new method and system equipped with a fiber-coupled diode laser arranged in a 2D array laser head. This array features multiple, individually addressable, low-power and short-wavelength (either 808 nm in this research investigation or 450 nm for future work for better process efficiency) lasers that supersede the traditional galvo scanning mechanism in PBF systems. The new laser head, inherent to the Direct Additive Manufacturing (DAM) methodology, has demonstrated the capability to create 3D structures and process materials with high melting points, such as Ti6Al4V, exceeding peak temperatures of 1900°C. This has been done thru several stages, as follows:

Chapter 4 of this thesis highlights the critical role of various conditions, such as wavelength, particle size, and powder quality, on the absorptivity of different metallic powders. The study found that shorter wavelengths lead to increased absorptivity across all materials studied, with Ti6Al4V exhibiting a significant 14% increase in absorptivity when exposed to a 450 nm laser source compared to a 1064 nm fibre laser. Highly reflective and conductive materials like copper and AlSi12 also experienced significant increases in absorption with shorter wavelengths. Furthermore, larger particle sizes demonstrated reduced absorptivity compared to finer particle distributions for both copper and Ti6Al4V.

The impact of oxidation on radiation absorption was also studied, with aged copper powder displaying increased radiation absorption across all measured wavelengths, while the absorptivity of aged Ti6Al4V powder diminished across all wavelengths. These findings provide a foundation for advancements in process efficiency in metal additive manufacturing and related applications. By recognizing the crucial role of wavelength and particle size in material absorptivity, the development of a single fiber coupled diode laser with a spot

size comparable to the SLM laser system was made to optimize the efficiency and effectiveness of laser processing for Ti6Al4V and other alloys, which led us to in the next **chapter 5** to experimentally investigation of the process performance by using single low power- short wavelength fibre coupled diode laser (450-808 nm).

Chapter 5 culminated in significant findings, demonstrating that low-power diode lasers of 3.5W can generate temperatures adequate for creating melt pools with energy densities comparable to those observed in traditional SLM. This efficiency can be attributed to the enhanced absorptivity at shorter wavelengths (808 and 450nm), which outperforms the 1060 nm laser typically used in standard Selective Laser Melting (SLM). The absorptivity of Ti6Al4V powder was notably 11% higher with 450 nm laser sources than with 808 nm sources, resulting in an average temperature rise of 12%, and peak surface temperatures reaching up to 1920°C.

When the scanning speed was optimised within the normalized speed range of $0.018 < v^* < 0.048$, it was found that the densities of parts produced exceeded 90%. The dimensions of the melt pool track, specifically their width and depth, varied between 150 to 520 μm and were generally 5-10% wider and 20-40% deeper when processed with 450 nm laser sources compared to those processed with 808 nm lasers. Keyhole formation occurred at low scan speeds for both lasers. The 450 nm laser initiated keyholes at speeds below 50 mm/min, and the 808 nm laser at speeds below 10 mm/min. These keyholes were typically formed at high energy densities ($E_0^* > 8$), while inadequate material fusion was seen at energy density values $E_0^* < 2$. Normalized overlapping within the range of 0.3-0.5, with a hatch distance of 0.157 μm , proved optimal for enhancing part density. This has been taken into consideration during the development of a new laser head featuring a multiple-diode laser arranged in a 2D array, as it is paramount to consider optimal pitch spacing distance closely. The research findings underscore the influence of this factor, indicating that maintaining a pitch distance of less than 150 μm promotes optimal part density enhancement. This is particularly critical as excessive overlap can lead to an unnecessary increase in energy density, generating higher power than required. Conversely, a hatch distance that is too large can result in gaps between the single tracks and lead to regions of unmelted powder, compromising the overall quality and, process efficiency and scalability.

A further critical discovery from this chapter is the improvement in the microstructure. The Diode Area Melting (DAM) process, which has a slower scanning speed in comparison to commercial Selective Laser Melting (SLM) systems, has been found to produce both α and β phases in the fabricated components. In contrast, commercial SLM systems typically result in the production of a singular α' phase. The slower scanning speed of the DAM process results in slower cooling rates in the range of about 750-1400 $^\circ\text{C/s}$, which is significantly slower than the cooling rates seen in SLM. This slower cooling rate

leads to the formation of β phases. These findings have significant implications for the mechanical properties of the fabricated parts.

These findings emphasize the promising potential of employing multiple low-power, short-wavelength lasers in the DAM process. These findings led to a novel approach using a 2D array of fibre-coupled diode laser packed in an optical head, demonstrated in **chapter 6**.

Chapter 6 introduced the development and investigation of a novel 2D array fibre-coupled laser head comprising up to 10 addressable low-power diode lasers (808 nm), each with an output under 4.5 W. The development and assembly of a laser head are detailed with a remarkable array of individually addressable lasers. The unique assembly comprises 100 channels organized in a two-dimensional array, with a fiber core of 105 μm and a centre-to-centre spacing of 127 μm . Through the strategic utilization of microscopic optics with a magnification factor of 0.7, the lasers' array is impeccably projected onto the top of the powder bed. This results in an individual laser spot size of 65 μm and a total area writing width of 3.81 mm. The results overall showed an enhancement of the efficiency, scalability, and precision of the new DAM methodology. The unique aspect of this system is the ability to control each laser individually, enabling a nuanced control of intensity distributions across the linear array of beams.

The arrangement (1D or 2D) and pitch distance between adjacent laser channels significantly impact the formation and characteristics of melt pools in a laser melting process. To achieve complete merged melting, it is crucial to maintain a pitch distance not exceeding 153 μm (such as in Chanel 1&2, 1&3, and 1&5 configurations). When the pitch distance is smaller than the melt pool width (<160 μm), adjacent lasers generate melt pools that merge together, forming a single wide track. This configuration results in deeper melt pools and higher surface energy input. However, increasing the pitch distance beyond 153 μm (e.g., Chanel 1&5, 1&7, and 1&9) causes the molten tracks to separate entirely, resulting in wider tracks with unprocessed powder visible between them. Furthermore, larger pitch distances lead to reduced surface energy input and wider tracks.

Five lasers with three different beam profiles, LP1, LP2, and LP3, were utilized to expand the investigation. These particular laser profiles were chosen because they have the capability to produce single consolidated tracks during the laser melting process. However, the findings revealed that LP3 does not generate sufficient power to produce dense 3D components. Despite LP3 offering wider processing capabilities and higher efficiency than LP1 and LP2, the laser power level of 4.5 W proved insufficient for the desired process. The results consistently indicated a melt pool depth of less than 100 μm , weak bonding, and inconsistent tracks. Furthermore, the LP3 configuration failed to effectively merge adjacent

tracks, resulting in incomplete overlap and defects, which caused a high surface roughness of $R_a = 20.5 \mu\text{m}$.

As the development of the Multi Laser Head Array system is explored, addressing current limitations and identifying areas for improvement is essential. The diode area melting technique has shown promising results, enhancing scalability, microstructure, and mechanical properties of produced samples. Nevertheless, it's crucial to recognize that the system is still in its early stages, and further improvements are needed in laser control, integration with the gantry system, and powder bed feedstock as flowing, which is detailed as follows:

7.1.1 system control development

The current system configuration for controlling the laser head 2D fibre-coupled diode array is limited and does not allow for precise control based on 3D geometry, which is a major obstacle in achieving optimal process efficiency. Individual activation of each diode laser, gantry movement system, measurement system (such as pyrometer), and feedstock at each layer processing is required to improve the control. In this study, the Laser driver DPS3005 was employed for additive manufacturing. However, it has a delay of 10 seconds after sending the signal, which can limit the building of small feature sizes. A scanning strategy was developed using a G-code that scanned several areas as sections to overcome this issue. This approach optimizes timing and ensures a more synchronized response from the laser driver but does not overcome the ability to print small feature sizes. Moreover, Further investigation into the characterization of the intersections of the scanned sections is necessary to analyse the quality and integrity of the build.

The current individual activation of each system leads to additional process time, which compromises process efficiency. There is a 1 to 2 minute delay between each layer before initiating the subsequent layer. This delay allows the sample to cool down to room temperature, which disrupts the heating and cooling phenomena that occur during the laser melting process of metallic materials. Thermal gradients and temperature differentials created during the cooling and heating phenomena in metallic materials cause internal stresses and deformation within the part, leading to warpage or distortion. This negatively affects the fabricated components' dimensional accuracy and structural integrity, making them unsuitable for their intended applications.

Future work should focus on developing an integrated control system that can coordinate the laser head, gantry movement, measurement system, and powder bed feedstock to enhance DAM's process efficiency and quality. This integrated system would enable real-time control and synchronization of the various

components, eliminating the delays between process steps and ensuring efficient utilization of process time. Advanced process monitoring and control techniques should be implemented to mitigate the cooling and heating phenomena-induced warpage. This can be achieved by integrating in-situ temperature monitoring (High-speed thermal camera) and feedback systems, enabling dynamic adjustments to the process parameters such as laser power and scanning speed. Exploring novel strategies for heat management, such as localized pre-heating or controlled cooling techniques, could help regulate temperature differentials and minimize the impact of thermal gradients on the final part. These approaches would improve dimensional accuracy, reduce warpage, and enhance overall part quality.

7.1.2 Enhancing Efficiency and Material Processing with Shorter Wavelengths (450nm)

The results of the current work have shown that using 808nm wavelength diode lasers has significantly improved processing efficiencies and thermal control for engineering alloys using DAM methodology. However, to further improve absorption and enable low-power processing of high-reflective metals such as copper and aluminium, shorter wavelengths (450 nm) need to be integrated into the optical system. The development of a multi-laser head with individually addressable 2D linear arrays using 450 nm wavelength diodes is suggested for this purpose.

Scaled-up systems with more lasers at higher laser power would be beneficial to test, alongside optimizing pre- and post-heating strategies for superior microstructural control. Expanding the materials processed to include high-temperature and reflective alloys would also be advantageous. To support development, advanced modelling of the multi-laser process is recommended, along with implementing in-situ monitoring and feedback control. Longer-term goals should focus on robust system engineering for commercialisation, demonstrating complex 3D parts, and validating mechanical performance. Incorporating 450 nm multiple linear arrays as the new generation would contribute to controlling and reducing thermally induced residual stress while enabling additional microstructure control. Using a second array has shown promise in developing microstructure and mechanical properties. Using multiple arrays instead of a 2D array as shown in (Figure 7.1) can provide an interesting chance to integrate pre- and post-heating within the process. This, in turn, can regulate the cooling rate and enable control over the microstructure.

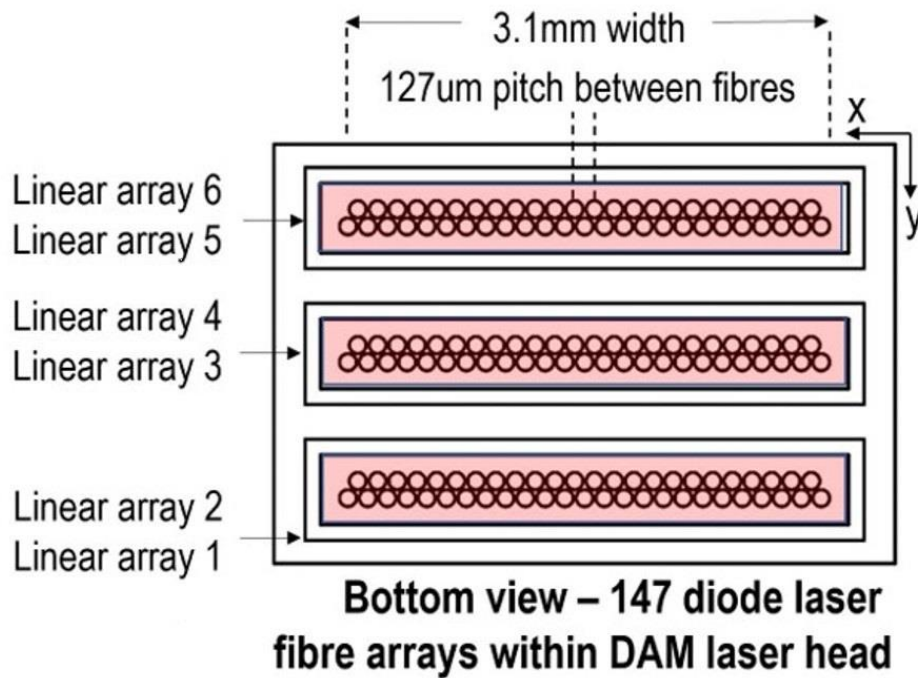


Figure 7.1: Development of Multiple 2array for better processing efficiency and microstructure control.

7.1.3 New Multi-laser Integrated System for the 3D Printing Process

This research explored using multi-diode laser arrays to achieve higher productivity by melting wider areas in parallel. However, challenges were encountered due to the slow movement of the laser source across the powder bed, resulting in an expanded heat-affected zone around the melt pool, leading to reduced geometric resolution and surface roughness on the component sides compared to traditional LPBF processes, as shown in Figure 7.2.

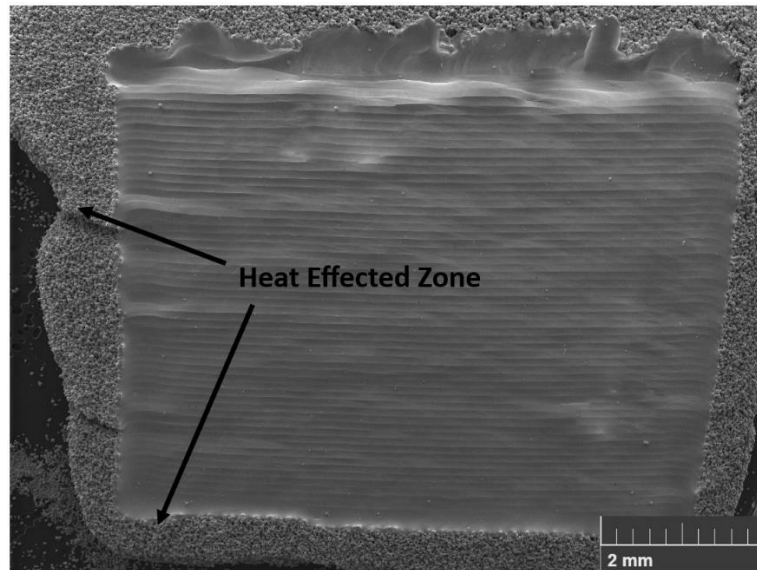


Figure 7.2: Heat effect zone as a result of the slow processing speed.

Therefore, implementing hybrid laser configurations offers advantages. Galvo lasers can maintain sharp contours and surface quality by rapidly scanning the outer edges of each layer. Meanwhile, the diode arrays process the inner regions much faster than a single spot. This combines flexible scanning patterns, established process control, and high build rates, as shown in Figure 7.3.

Furthermore, multiple lasers facilitate thermal management, allowing the galvo to pre-heat before the diodes melt. Having both laser types in one system makes the research more relevant to commercial needs. Overall, hybrid diode array and galvo configurations provide a pathway to balance productivity, quality, flexibility, and commercial viability. The galvo scanning helps mitigate limitations of large-area diode melting, while the diodes enhance build speed. This dual approach warrants further research to fully deliver the combined benefits of each laser technology in metal additive manufacturing.

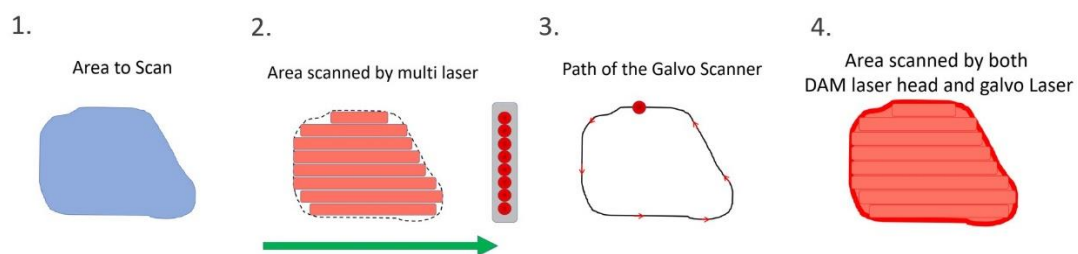


Figure 7.3: Integration of high-power fiber galvo scanning fiber laser (Contour Scan) with multi-laser DAM head for component infill.

7.1.4 Modelling and process monitoring

The DAM process is currently in its developmental stages, presenting numerous opportunities for further research. Like other L-PBF processes, DAM involves complex physical phenomena that occur during laser interaction with powder materials. In DAM, multiple laser beams work closely together to heat, melt, and solidify materials rapidly, adding to the intricacy of the process. Mathematical modelling and simulation techniques have been extensively employed in additive manufacturing (AM) to study these processes (references). It is highly recommended to utilize simulation techniques to deepen the understanding of this innovative process and explore its potential for optimizing the processing of different materials.

In DAM processing of Ti6Al4V, the cooling rates are significantly lower compared to SLM, resulting in samples containing β -grains, which can be attributed to the number of lasers and scanning speed used. Therefore, a comprehensive understanding of cooling and solidification rates is crucial for advancing the development of the DAM process. During the experiments, the temperature evolution on the surface was assessed using an IR-Pyrometer (CTLM-2H, Micro-Epsilon UK). However, it is advisable to conduct further experiments using more advanced thermal monitoring systems, such as a high-speed thermal camera, to validate the thermal gradients and cooling rates during the process.

7.2 Final recommendations

In conclusion, this research project offers suggestions to enhance the processing speed of DAM considering the existing 4.5 W laser power limitation, as follows:

1. Use shorter wavelength lasers like 450nm instead of 808nm. This increases absorptivity, allowing lower powers to melt the powder.
2. Optimize beam focusing optics and powder layer thickness to maximize energy density.
3. Arrange lasers with small spot spacing ($<150 \mu\text{m}$) LP1 for continuous melt tracks instead of spaced spots LP2. This improves overlap and scanning efficiency.
4. Use multiple diode arrays oriented perpendicular to the scan direction. This allows faster scanning of each layer in a single pass.
5. Pre-heat the powder bed before melting to reduce the laser power required. This could be done optically or with a heated build plate.

6. Scan bi-directionally instead of unidirectional. Eliminates time wasted returning after each pass.
7. Scale up to larger diode arrays with more lasers at higher total power. This is the ultimate solution but requires hardware development.
8. Explore hybrid scanning approaches, using galvo lasers for contours and diode arrays for internal regions.

References

- [1] Herzog D, Seyda V, Wycisk E, Emmelmann C. Additive manufacturing of metals. *Acta Mater* 2016;117:371–92. <https://doi.org/10.1016/j.actamat.2016.07.019>.
- [2] Dutta B, Babu S, Jared B. Comparison of various additive manufacturing technologies. In: Dutta B, Babu S, Jared Technology and Applications of Metals in Additive Manufacturing BBT-S, editors. *Sci. Technol. Appl. Met. Addit. Manuf.*, Elsevier; 2019, p. 55–76. <https://doi.org/10.1016/B978-0-12-816634-5.00003-0>.
- [3] Nandy J, Sarangi H, Sahoo S. A Review on Direct Metal Laser Sintering: Process Features and Microstructure Modeling. vol. 6. *Lasers in Manufacturing and Materials Processing*; 2019. <https://doi.org/10.1007/s40516-019-00094-y>.
- [4] DebRoy T, Wei HL, Zuback JS, Mukherjee T, Elmer JW, Milewski JO, et al. Additive manufacturing of metallic components – Process, structure and properties. *Prog Mater Sci* 2018;92:112–224. <https://doi.org/10.1016/j.pmatsci.2017.10.001>.
- [5] Mishra P, Ilar T, Brueckner F, Kaplan A. Energy efficiency contributions and losses during selective laser melting. *J Laser Appl* 2018;30:032304. <https://doi.org/10.2351/1.5040603>.
- [6] Tran TQ, Chinnappan A, Lee JKY, Loc NH, Tran LT, Wang G, et al. 3D Printing of Highly Pure Copper. *Metals (Basel)* 2019;9:756. <https://doi.org/10.3390/met9070756>.
- [7] Poprawe R, Hinke C, Meiners W, Schrage J, Bremen S, Merkt S. SLM Production Systems: Recent Developments in Process Development, Machine Concepts and Component Design, 2015, p. 49–65. https://doi.org/10.1007/978-3-319-12304-2_5.
- [8] Brandt M. The role of lasers in additive manufacturing. *Laser Addit. Manuf.*,

- Elsevier; 2017, p. 1–18. <https://doi.org/10.1016/B978-0-08-100433-3.02001-7>.
- [9] Tan C, Wang D, Ma W, Zhou K. Ultra-strong bond interface in additively manufactured iron-based multi-materials. *Mater Sci Eng A* 2021;802:140642. <https://doi.org/10.1016/j.msea.2020.140642>.
- [10] Tan C, Zhou K, Kuang M, Ma W, Kuang T. Microstructural characterization and properties of selective laser melted maraging steel with different build directions. *Sci Technol Adv Mater* 2018;19:746–58. <https://doi.org/10.1080/14686996.2018.1527645>.
- [11] Martin JH, Yahata BD, Hundley JM, Mayer JA, Schaedler TA, Pollock TM. 3D printing of high-strength aluminium alloys. *Nature* 2017;549:365–9. <https://doi.org/10.1038/nature23894>.
- [12] Zhang X, Mao B, Mushongera L, Kundin J, Liao Y. Laser powder bed fusion of titanium aluminides: An investigation on site-specific microstructure evolution mechanism. *Mater Des* 2021;201:109501. <https://doi.org/10.1016/j.matdes.2021.109501>.
- [13] Sanchez S, Smith P, Xu Z, Gaspard G, Hyde CJ, Wits WW, et al. Powder Bed Fusion of nickel-based superalloys: A review. *Int J Mach Tools Manuf* 2021;165. <https://doi.org/10.1016/j.ijmactools.2021.103729>.
- [14] Kellens K, Yasa E, Dewulf W, Duflou JR. Environmental Assessment of Selective Laser Melting and Selective Laser Sintering. *Going Green - Care Innov From Leg Compliance to Energy-Efficient Prod Serv* 2010;4:5.
- [15] Wohlers T. Wohlers T. (2020) Wohlers Report: 3D printing and Additive Manufacturing State of the Industry, ISBN 978-0-9913332-6-4. 2020.
- [16] Heeling T, Wegener K. The effect of multi-beam strategies on selective laser melting of stainless steel 316L. *Addit Manuf* 2018;22:334–42.

- <https://doi.org/10.1016/j.addma.2018.05.026>.
- [17] Kopf R, Gottwald J, Jacob A, Brandt M, Lanza G. Cost-oriented planning of equipment for selective laser melting (SLM) in production lines. *CIRP Ann* 2018;67:471–4. <https://doi.org/10.1016/j.cirp.2018.04.032>.
- [18] Dutta Majumdar J, Manna I. Laser processing of materials. *Sadhana* 2003;28:495–562. <https://doi.org/10.1007/BF02706446>.
- [19] Lee H, Lim CH, Low MJ, Tham N, Murukeshan VM, Kim Y-J. Lasers in additive manufacturing: A review. *Int J Precis Eng Manuf Technol* 2017;4:307–22. <https://doi.org/10.1007/s40684-017-0037-7>.
- [20] Kennedy E, Byrne G, Collins DN. A review of the use of high power diode lasers in surface hardening. *J Mater Process Technol* 2004;155156:1855–60. <https://doi.org/10.1016/j.jmatprotec.2004.04.276>.
- [21] Matthews MJ, Guss G, Drachenberg DR, Demuth JA, Heebner JE, Duoss EB, et al. Diode-based additive manufacturing of metals using an optically-addressable light valve. *Opt Express* 2017;25:11788–800. <https://doi.org/10.1364/OE.25.011788>.
- [22] Hinke C, Merkt S, Eibl F, Schrage J, Bremen S. Additive manufacturing: perspectives for diode lasers. 2015 IEEE High Power Diode Lasers Syst. Conf., IEEE; 2015, p. 39–40. <https://doi.org/10.1109/HPD.2015.7439684>.
- [23] Hengesbach S, Poprawe R, Hoffmann D, Traub M, Schwarz T, Holly C, et al. Brightness and average power as driver for advancements in diode lasers and their applications. In: Zediker MS, editor. *High-Power Diode Laser Technol. Appl. XIII*, vol. 9348, International Society for Optics and Photonics; 2015, p. 93480B. <https://doi.org/10.1117/12.2085068>.
- [24] Zavala-Arredondo M, Boone N, Willmott J, Childs DTD, Ivanov P, Groom KM, et al. Laser diode area melting for high speed additive manufacturing of metallic

- components. *Mater Des* 2017;117:305–15.
<https://doi.org/10.1016/j.matdes.2016.12.095>.
- [25] Alsaddah M, Khan A, Groom K, Mumtaz K. Use of 450-808 nm diode lasers for efficient energy absorption during powder bed fusion of Ti6Al4V. *Int J Adv Manuf Technol* 2021;2461–80. <https://doi.org/10.1007/s00170-021-06774-4>.
- [26] Zavala-Arredondo M, Ali H, Groom KM, Mumtaz K. Investigating the melt pool properties and thermal effects of multi-laser diode area melting. *Int J Adv Manuf Technol* 2018;97:1383–96. <https://doi.org/10.1007/s00170-018-2038-2>.
- [27] Zavala-Arredondo M, Groom KM, Mumtaz K. Diode area melting single-layer parametric analysis of 316L stainless steel powder. *Int J Adv Manuf Technol* 2018;94:2563–76. <https://doi.org/10.1007/s00170-017-1040-4>.
- [28] ASTM International. F2792-12a - Standard Terminology for Additive Manufacturing Technologies. 2013. <https://doi.org/10.1520/F2792-12A.2>.
- [29] Wong K V., Hernandez A. A Review of Additive Manufacturing. *ISRN Mech Eng* 2012;2012:1–10. <https://doi.org/10.5402/2012/208760>.
- [30] Gao W, Zhang Y, Ramanujan D, Ramani K, Chen Y, Williams CB, et al. The status, challenges, and future of additive manufacturing in engineering. *Comput Des* 2015;69:65–89. <https://doi.org/10.1016/j.cad.2015.04.001>.
- [31] Gibson I, Rosen D, Stucker B. Development of Additive Manufacturing Technology. *Addit. Manuf. Technol. 3D Printing, Rapid Prototyping, Direct Digit. Manuf.*, New York, NY: Springer New York; 2015, p. 19–42. https://doi.org/10.1007/978-1-4939-2113-3_2.
- [32] Bhavar V, Forge B, Kattire P. A review on powder bed fusion technology of metal additive manufacturing Business development of Additive Manufacturing View project 2014.

- [33] Huang Y, Leu MC, Mazumder J, Donmez A. Additive Manufacturing: Current State, Future Potential, Gaps and Needs, and Recommendations. *J Manuf Sci Eng* 2015;137:014001. <https://doi.org/10.1115/1.4028725>.
- [34] Gokuldoss PK, Kolla S, Eckert J. Additive manufacturing processes: Selective laser melting, electron beam melting and binder jetting-selection guidelines. *Materials (Basel)* 2017;10. <https://doi.org/10.3390/ma10060672>.
- [35] Gu, Dongdong, W. Meiners, K. Wissenbach RP. Laser additive manufacturing of metallic components: materials, processes, and mechanisms. *Int Mater Rev* 2012;657:163–80. <https://doi.org/10.1179/1743280411Y.0000000014>.
- [36] Yasa E, Kruth JP. Microstructural investigation of selective laser melting 316L stainless steel parts exposed to laser re-melting. *Procedia Eng* 2011;19:389–95. <https://doi.org/10.1016/j.proeng.2011.11.130>.
- [37] Zaeh MF, Branner G. Investigations on residual stresses and deformations in selective laser melting 2009. <https://doi.org/10.1007/s11740-009-0192-y>.
- [38] Zhang B, Li Y, Bai Q. Defect Formation Mechanisms in Selective Laser Melting: A Review. *Chinese J Mech Eng (English Ed)* 2017;30:515–27. <https://doi.org/10.1007/s10033-017-0121-5>.
- [39] Galarraga H, Lados DA, Dehoff RR, Kirka MM, Nandwana P. Effects of the microstructure and porosity on properties of Ti-6Al-4V ELI alloy fabricated by electron beam melting (EBM). *Addit Manuf* 2016;10:47–57. <https://doi.org/10.1016/j.addma.2016.02.003>.
- [40] Kasperovich G, Haubrich J, Gussone J, Requena G. Correlation between porosity and processing parameters in TiAl6V4 produced by selective laser melting. *Mater Des* 2016;105:160–70. <https://doi.org/10.1016/j.matdes.2016.05.070>.
- [41] Mumtaz KA, Erasenthiran P, Hopkinson N. High density selective laser melting of

- Waspaloy®. *J Mater Process Technol* 2008;195:77–87.
<https://doi.org/10.1016/j.jmatprotec.2007.04.117>.
- [42] Yap CY, Chua CK, Dong ZL, Liu ZH, Zhang DQ, Loh LE, et al. Review of selective laser melting: Materials and applications. *Appl Phys Rev* 2015;2.
<https://doi.org/10.1063/1.4935926>.
- [43] Li R, Liu J, Shi Y, Wang L, Jiang W. Balling behavior of stainless steel and nickel powder during selective laser melting process. *Int J Adv Manuf Technol* 2012;59:1025–35. <https://doi.org/10.1007/s00170-011-3566-1>.
- [44] Singla AK, Banerjee M, Sharma A, Singh J, Bansal A, Gupta MK, et al. Selective laser melting of Ti6Al4V alloy: Process parameters, defects and post-treatments. *J Manuf Process* 2021;64:161–87. <https://doi.org/10.1016/j.jmapro.2021.01.009>.
- [45] Kruth JP, Froyen L, Van Vaerenbergh J, Mercelis P, Rombouts M, Lauwers B. Selective laser melting of iron-based powder. *J Mater Process Technol* 2004;149:616–22. <https://doi.org/10.1016/j.jmatprotec.2003.11.051>.
- [46] Rombouts M, Kruth JP, Froyen L, Mercelis P. Fundamentals of selective laser melting of alloyed steel powders. *CIRP Ann - Manuf Technol* 2006;55:187–92.
[https://doi.org/10.1016/S0007-8506\(07\)60395-3](https://doi.org/10.1016/S0007-8506(07)60395-3).
- [47] Mills KC, Keene BJ, Brooks RF, Shirali A. Marangoni effects in welding. *Philos Trans R Soc London A Math Phys Eng Sci* 1998;356.
- [48] Zhang S, Wang Y, Xiong Z, Zhu M, Zhang Z, Li Z. Mechanism and optimization of activating fluxes for process stability and weldability of hybrid laser-arc welded HSLA steel. *Weld World* 2021;65:753–66. <https://doi.org/10.1007/s40194-020-01038-3>.
- [49] Niu HJ, Chang ITH. Instability of scan tracks of selective laser sintering of high speed steel powder. *Scr Mater* 1999;41:1229–34. <https://doi.org/10.1016/S1359->

- 6462(99)00276-6.
- [50] Mercelis P, Kruth J, Kruth J-P. Residual stresses in selective laser sintering and selective laser melting. *Rapid Prototyp J R* 2006;12:254–65.
- [51] Parry L, Ashcroft IA, Wildman RD. Understanding the effect of laser scan strategy on residual stress in selective laser melting through thermo-mechanical simulation. *Addit Manuf* 2016;12:1–15. <https://doi.org/10.1016/j.addma.2016.05.014>.
- [52] Li C, Liu ZY, Fang XY, Guo YB. Residual Stress in Metal Additive Manufacturing. *Procedia CIRP* 2018;71:348–53. <https://doi.org/10.1016/j.procir.2018.05.039>.
- [53] Liu S, Shin YC. Additive manufacturing of Ti6Al4V alloy: A review. *Mater Des* 2019;164:107552. <https://doi.org/10.1016/j.matdes.2018.107552>.
- [54] Buchbinder D, Meiners W, Pirch N, Wissenbach K, Schrage J. Investigation on reducing distortion by preheating during manufacture of aluminum components using selective laser melting. *J Laser Appl* 2014;26:012004. <https://doi.org/10.2351/1.4828755>.
- [55] Roehling JD, Smith WL, Roehling TT, Vrancken B, Guss GM, McKeown JT, et al. Reducing residual stress by selective large-area diode surface heating during laser powder bed fusion additive manufacturing. *Addit Manuf* 2019;28:228–35. <https://doi.org/10.1016/j.addma.2019.05.009>.
- [56] Wegener K, Heeling T, Zimmermann L. Multi-Beam Strategies for the Optimization of the Selective Laser Melting Process. *Solid Free Fabr 2016 Proc 27th Annu Int Solid Free Fabr Symp* 2016:1428–38. <https://doi.org/10.3929/ETHZ-A-010803938>.
- [57] Ali H, Ghadbeigi H, Mumtaz K. Effect of scanning strategies on residual stress and mechanical properties of Selective Laser Melted Ti6Al4V. *Mater Sci Eng A*

- 2018;712:175–87. <https://doi.org/10.1016/j.msea.2017.11.103>.
- [58] Lu Y, Wu S, Gan Y, Huang T, Yang C, Junjie L, et al. Study on the microstructure, mechanical property and residual stress of SLM Inconel-718 alloy manufactured by differing island scanning strategy. *Opt Laser Technol* 2015;75:197–206. <https://doi.org/10.1016/j.optlastec.2015.07.009>.
- [59] Wang D, Yang Y, Su X, Chen Y. Study on energy input and its influences on single-track, multi-track, and multi-layer in SLM. *Int J Adv Manuf Technol* 2012;58:1189–99. <https://doi.org/10.1007/s00170-011-3443-y>.
- [60] Liu ZH, Chua CK, Leong KF, Kempen K, Thijs L, Yasa E, et al. A preliminary investigation on Selective Laser Melting of M2 High Speed Steel. *Innov Dev Virtual Phys Prototyp - Proc 5th Int Conf Adv Res Rapid Prototyp* 2012:339–46. <https://doi.org/10.1201/b11341-54>.
- [61] Osakada K, Shiomi M. Flexible manufacturing of metallic products by selective laser melting of powder. *Int J Mach Tools Manuf* 2006;46:1188–93. <https://doi.org/10.1016/j.ijmactools.2006.01.024>.
- [62] Ji W, Liu C, Dai S, Deng R. Microstructure, Properties and Crack Suppression Mechanism of High-speed Steel Fabricated by Selective Laser Melting at Different Process Parameters. *Chinese J Mech Eng (English Ed)* 2023;36. <https://doi.org/10.1186/s10033-023-00877-7>.
- [63] Taheri Andani M, Dehghani R, Karamooz-Ravari MR, Mirzaeifar R, Ni J. Spatter formation in selective laser melting process using multi-laser technology. *Mater Des* 2017;131:460–9. <https://doi.org/10.1016/j.matdes.2017.06.040>.
- [64] Khairallah SA, Anderson AT, Rubenchik A, King WE. Laser powder-bed fusion additive manufacturing: Physics of complex melt flow and formation mechanisms of pores, spatter, and denudation zones. *Acta Mater* 2016;108:36–45.

- <https://doi.org/10.1016/j.actamat.2016.02.014>.
- [65] Bidare P, Bitharas I, Ward RM, Attallah MM, Moore AJ. Fluid and particle dynamics in laser powder bed fusion. *Acta Mater* 2018;142:107–20. <https://doi.org/10.1016/j.actamat.2017.09.051>.
- [66] Matthews MJ, Guss G, Khairallah SA, Rubenchik AM, Depond PJ, King WE. Denudation of metal powder layers in laser powder bed fusion processes. *Acta Mater* 2016;114:33–42. <https://doi.org/10.1016/j.actamat.2016.05.017>.
- [67] Ly S, Rubenchik AM, Khairallah SA, Guss G, Matthews MJ. Metal vapor micro-jet controls material redistribution in laser powder bed fusion additive manufacturing. *Sci Rep* 2017;7:1–12. <https://doi.org/10.1038/s41598-017-04237-z>.
- [68] Young ZA, Guo Q, Parab ND, Zhao C, Qu M, Escano LI, et al. Types of spatter and their features and formation mechanisms in laser powder bed fusion additive manufacturing process. *Addit Manuf* 2020;36:101438. <https://doi.org/10.1016/j.addma.2020.101438>.
- [69] Simonelli M, Tuck C, Aboulkhair NT, Maskery I, Ashcroft I, Wildman RD, et al. A Study on the Laser Spatter and the Oxidation Reactions During Selective Laser Melting of 316L Stainless Steel, Al-Si10-Mg, and Ti-6Al-4V. *Metall Mater Trans A* 2015;46:3842–51. <https://doi.org/10.1007/s11661-015-2882-8>.
- [70] Liu Y, Yang Y, Mai S, Wang D, Song C. Investigation into spatter behavior during selective laser melting of AISI 316L stainless steel powder. *Mater Des* 2015;87:797–806. <https://doi.org/10.1016/j.matdes.2015.08.086>.
- [71] Gunenthiram V, Peyre P, Schneider M, Dal M, Coste F, Koutiri I, et al. Experimental analysis of spatter generation and melt-pool behavior during the powder bed laser beam melting process. *J Mater Process Technol* 2018;251:376–86.

- <https://doi.org/10.1016/j.jmatprotec.2017.08.012>.
- [72] Trapp J, Rubenchik AM, Guss G, Matthews MJ. In situ absorptivity measurements of metallic powders during laser powder-bed fusion additive manufacturing. *Appl Mater Today* 2017;9:341–9. <https://doi.org/10.1016/j.apmt.2017.08.006>.
- [73] Lazov L, Angelov N. Physical Model About Laser Impact on Metals and Alloys. *Contemp Mater* 2010;1:124–8. <https://doi.org/10.5767/anurs.cmat.100102.en.124l>.
- [74] Rubenchik A, Wu S, Mitchell S, Golosker I, LeBlanc M, Peterson N. Direct measurements of temperature-dependent laser absorptivity of metal powders. *Appl Opt* 2015;54:7230. <https://doi.org/10.1364/ao.54.007230>.
- [75] Bajaj P, Wright J, Todd I, Jägle EA. Predictive process parameter selection for Selective Laser Melting Manufacturing: Applications to high thermal conductivity alloys. *Addit Manuf* 2019;27:246–58. <https://doi.org/10.1016/j.addma.2018.12.003>.
- [76] Hauser C, Childs T, Dalgarno KW, Eane RB. Atmospheric Control during Direct Selective Laser Sintering of Stainless Steel 314S Powder. *10th Solid Free Fabr Symp* 1999:265–72.
- [77] Ruiz JE, Cortina M, Arrizubieta JI, Lamikiz A. Study of the influence of shielding gases on Laser Metal Deposition of Inconel 718 superalloy. *Materials (Basel)* 2018;11. <https://doi.org/10.3390/ma11081388>.
- [78] Frazier WE. Metal Additive Manufacturing: A Review. *J Mater Eng Perform* 2014;23:1917–28. <https://doi.org/10.1007/s11665-014-0958-z>.
- [79] Niu HJ, Chang ITH. Selective laser sintering of gas atomized M2 high speed steel powder. *J Mater Sci* 2000;35:31–8. <https://doi.org/10.1023/A:1004720011671>.
- [80] Balbaa MA, Ghasemi A, Fereiduni E, Elbestawi MA, Jadhav SD, Kruth JP. Role of

- powder particle size on laser powder bed fusion processability of AlSi10Mg alloy. *Addit Manuf* 2021;37:101630. <https://doi.org/10.1016/j.addma.2020.101630>.
- [81] Spurek MA, Haferkamp L, Weiss C, Spierings AB, Schleifenbaum JH, Wegener K. Influence of the particle size distribution of monomodal 316L powder on its flowability and processability in powder bed fusion. *Prog Addit Manuf* 2022;7:533–42. <https://doi.org/10.1007/s40964-021-00240-z>.
- [82] Sun S, Brandt M, Easton M. 2 - Powder bed fusion processes: An overview. In: Brandt MBT-LAM, editor. *Woodhead Publ. Ser. Electron. Opt. Mater.*, Woodhead Publishing; 2017, p. 55–77. <https://doi.org/https://doi.org/10.1016/B978-0-08-100433-3.00002-6>.
- [83] Niendorf T, Richard HA, Leuders S, Riemer A, Tröster T, Thöne M. On the fatigue crack growth behavior in 316L stainless steel manufactured by selective laser melting. *Eng Fract Mech* 2014;120:15–25. <https://doi.org/10.1016/j.engfracmech.2014.03.008>.
- [84] Niendorf T, Leuders S, Riemer A, Richard HA, Tröster T, Schwarze D. Highly anisotropic steel processed by selective laser melting. *Metall Mater Trans B Process Metall Mater Process Sci* 2013;44:794–6. <https://doi.org/10.1007/s11663-013-9875-z>.
- [85] Cloots M, Kunze K, Uggowitzer PJ, Wegener K. Microstructural characteristics of the nickel-based alloy IN738LC and the cobalt-based alloy Mar-M509 produced by selective laser melting. *Mater Sci Eng A* 2016;658:68–76. <https://doi.org/10.1016/j.msea.2016.01.058>.
- [86] Thijs L, Kempen K, Kruth JP, Van Humbeeck J. Fine-structured aluminium products with controllable texture by selective laser melting of pre-alloyed AlSi10Mg powder. *Acta Mater* 2013;61:1809–19.

- <https://doi.org/10.1016/j.actamat.2012.11.052>.
- [87] Banerjee D, Williams JC. Perspectives on titanium science and technology. *Acta Mater* 2013;61:844–79. <https://doi.org/10.1016/j.actamat.2012.10.043>.
- [88] Hancock E, Smith W, Wilson R, Bors A. Lecture Notes in Computer Science (including subseries Lecture Notes in Artificial Intelligence and Lecture Notes in Bioinformatics): Preface. *Lect Notes Comput Sci (Including Subser Lect Notes Artif Intell Lect Notes Bioinformatics)* 2013;8048 LNCS. <https://doi.org/10.1007/978-3-642-40246-3>.
- [89] Ahmed T, Rack HJ. Phase transformations during cooling in $\alpha+\beta$ titanium alloys. *Mater Sci Eng A* 1998;243:206–11. [https://doi.org/10.1016/S0921-5093\(97\)00802-2](https://doi.org/10.1016/S0921-5093(97)00802-2).
- [90] Hancock E, Smith W, Wilson R, Bors A. *Computer Analysis of Images and Patterns*. vol. 8048. Berlin, Heidelberg: Springer Berlin Heidelberg; 2013. <https://doi.org/10.1007/978-3-642-40246-3>.
- [91] Rafi HK, Karthik N V., Gong H, Starr TL, Stucker BE. Microstructures and Mechanical Properties of Ti6Al4V Parts Fabricated by Selective Laser Melting and Electron Beam Melting. *J Mater Eng Perform* 2013;22:3872–83. <https://doi.org/10.1007/s11665-013-0658-0>.
- [92] Han J, Yang J, Yu H, Yin J, Gao M, Wang Z, et al. Microstructure and mechanical property of selective laser melted Ti6Al4V dependence on 2017;2:217–26. <https://doi.org/10.1108/RPJ-12-2015-0193>.
- [93] Roudnicka M, Misurak M, Vojtech D. Differences in the response of additively manufactured titanium alloy to heat treatment-Comparison between SLM and EBM. *Manuf Technol* 2019;19:668–73. <https://doi.org/10.21062/ujep/353.2019/a/1213-2489/MT/19/4/668>.

- [94] Zhao X, Li S, Zhang M, Liu Y, Sercombe TB, Wang S, et al. Comparison of the microstructures and mechanical properties of Ti-6Al-4V fabricated by selective laser melting and electron beam melting. *Mater Des* 2016;95:21-31. <https://doi.org/10.1016/j.matdes.2015.12.135>.
- [95] He J, Li D, Jiang W, Ke L, Qin G, Ye Y, et al. The Martensitic Transformation and Mechanical Properties of Ti6Al4V Prepared via Selective Laser Melting. *Materials (Basel)* 2019;12:321. <https://doi.org/10.3390/ma12020321>.
- [96] Ali H, Ghadbeigi H, Hosseinzadeh F, Oliveira J, Mumtaz K. Effect of pre-emptive in situ parameter modification on residual stress distributions within selective laser-melted Ti6Al4V components 2019:4467-79.
- [97] Caprio L, Demir AG, Previtali B. Comparative study between CW and PW emissions in selective laser melting. *J Laser Appl* 2018;30:032305. <https://doi.org/10.2351/1.5040631>.
- [98] Steen WM, Mazumder J, Steen WM, Mazumder J. Basic Laser Optics. *Laser Mater Process* 2010:79-130. https://doi.org/10.1007/978-1-84996-062-5_3.
- [99] Wirth P. Introduction to Industrial Laser Materials Processing 2004:33-7.
- [100] Gupta MC. Laser processing of materials and devices. 2001 Int. Semicond. Device Res. Symp. Symp. Proc. (Cat. No.01EX497), vol. 28, IEEE; 2002, p. 590. <https://doi.org/10.1109/ISDRS.2001.984587>.
- [101] Goswami GL, Kumar D. Laser materials processing. *Bull Mater Sci* 1988;11:213-24. <https://doi.org/10.1007/BF02744555>.
- [102] Nasim H, Jamil Y. Diode lasers: From laboratory to industry. *Opt Laser Technol* 2014;56:211-22. <https://doi.org/10.1016/j.optlastec.2013.08.012>.
- [103] Haiyin S. Guide to Handling Laser Diode Beams. 2015.
- [104] Treusch H-G, Du K, Baumann M, Sturm V, Ehlers B, Loosen P. <title>Fiber-coupling

- technique for high-power diode laser arrays. *Laser Reson* 1998;3267:98–106. <https://doi.org/10.1117/12.308097>.
- [105] Li L. The advances and characteristics of high-power diode laser materials processing. *Opt Lasers Eng* 2000;34:231–53. [https://doi.org/10.1016/S0143-8166\(00\)00066-X](https://doi.org/10.1016/S0143-8166(00)00066-X).
- [106] Vidal E, Quintana I, Azkorbebeitia U, Mendez E, Viera G, Galán M, et al. Fiber coupling of high-power diode laser stack for direct polycarbonate processing. In: Zediker MS, editor. *High-Power Diode Laser Technol. Appl. VIII*, vol. 7583, 2010, p. 75830G. <https://doi.org/10.1117/12.841603>.
- [107] Sercel JP, von Dadelszen M. *Practical UV Excimer Laser Image System Illuminators. Laser Beam Shap. Appl., Second Edition.* | Boca Raton, FL : CRC Press, Taylor & Francis Group, [2017]: CRC Press; 2017, p. 117–57. <https://doi.org/10.1201/9781315371306-4>.
- [108] Liu X, Zhao W, Xiong L, Liu H. *Packaging of High Power Semiconductor Lasers.* New York, NY: Springer New York; 2015. <https://doi.org/10.1007/978-1-4614-9263-4>.
- [109] Cahill B. LASER-BASED FIBRE-OPTIC SENSOR FOR MEASUREMENT OF Project Supervisor 2021. <https://doi.org/10.13140/RG.2.2.10981.73449>.
- [110] Karp JH, Ostroverkhov V, Bogdan D, Graham M, Mccarthy B, Carter W. Area melting with multi-laser arrays to increase build rate for metal powder bed fusion additive manufacturing. In: Helvajian H, Gu B, Chen H, editors. *Laser 3D Manuf. VI*, vol. 1090909, SPIE; 2019, p. 8. <https://doi.org/10.1117/12.2513892>.
- [111] Gaussian T. Propagation of Laser Beam - Gaussian Beam Optics - M² Tutorial n.d.:2–7.
- [112] Yadroitsev I, Bertrand P, Smurov I. Parametric analysis of the selective laser melting process. *Appl Surf Sci* 2007;253:8064–9.

- <https://doi.org/10.1016/j.apsusc.2007.02.088>.
- [113] Sun Z, Tan X, Tor SB, Yeong WY. Selective laser melting of stainless steel 316L with low porosity and high build rates. *Mater Des* 2016;104:197–204. <https://doi.org/10.1016/j.matdes.2016.05.035>.
- [114] Scipioni Bertoli U, Wolfer AJ, Matthews MJ, Delplanque J-PR, Schoenung JM. On the limitations of Volumetric Energy Density as a design parameter for Selective Laser Melting. *Mater Des* 2017;113:331–40. <https://doi.org/10.1016/j.matdes.2016.10.037>.
- [115] Kusuma C, Ahmed SH, Mian A, Srinivasan R. Effect of Laser Power and Scan Speed on Melt Pool Characteristics of Commercially Pure Titanium (CP-Ti). *J Mater Eng Perform* 2017;26:3560–8. <https://doi.org/10.1007/s11665-017-2768-6>.
- [116] Wang L, Wei QS, Shi YS, Liu JH, He WT. Experimental Investigation into the Single-Track of Selective Laser Melting of IN625. *Adv Mater Res* 2011;233–235:2844–8. <https://doi.org/10.4028/www.scientific.net/amr.233-235.2844>.
- [117] Sufiarov VS, Popovich AA, Borisov E V., Polozov IA, Masaylo D V., Orlov A V. The Effect of Layer Thickness at Selective Laser Melting. *Procedia Eng* 2017;174:126–34. <https://doi.org/10.1016/j.proeng.2017.01.179>.
- [118] Suryawanshi J, Prashanth KG, Ramamurty U, Song B, Dong S, Deng S, et al. Competing influence of porosity and microstructure on the fatigue property of laser powder bed fusion Stainless Steel 316L. *Mater Sci Eng A* 2018;8:618–29. <https://doi.org/10.1016/j.jmst.2018.12.011>.
- [119] Wang S, Liu Y, Shi W, Qi B, Yang J, Zhang F, et al. Research on High Layer Thickness Fabricated of 316L by Selective Laser Melting. *Materials (Basel)* 2017;10:1055. <https://doi.org/10.3390/ma10091055>.
- [120] Dong Z, Liu Y, Wen W, Ge J, Liang J. Effect of Hatch Spacing on Melt Pool and As-

- built Quality During Selective Laser Melting of Stainless Steel: Modeling and Experimental Approaches. *Materials* (Basel) 2018;12:50. <https://doi.org/10.3390/ma12010050>.
- [121] Metelkova J, Kinds Y, Kempen K, de Formanoir C, Witvrouw A, Van Hooreweder B. On the influence of laser defocusing in Selective Laser Melting of 316L. *Addit Manuf* 2018;23:161–9. <https://doi.org/10.1016/j.addma.2018.08.006>.
- [122] Thijs L, Verhaeghe F, Craeghs T, Humbeeck J Van, Kruth JP. A study of the microstructural evolution during selective laser melting of Ti-6Al-4V. *Acta Mater* 2010;58:3303–12. <https://doi.org/10.1016/j.actamat.2010.02.004>.
- [123] Nickel AH, Barnett DM, Prinz FB. Thermal stresses and deposition patterns in layered manufacturing. *Mater Sci Eng A* 2001;317:59–64. [https://doi.org/10.1016/S0921-5093\(01\)01179-0](https://doi.org/10.1016/S0921-5093(01)01179-0).
- [124] Seabra M, Azevedo J, Araújo A, Reis L, Pinto E, Alves N, et al. Selective laser melting (SLM) and topology optimization for lighter aerospace components. *Procedia Struct Integr* 2016;1:289–96. <https://doi.org/10.1016/j.prostr.2016.02.039>.
- [125] Xiao Z, Yang Y, Xiao R, Bai Y, Song C, Wang D. Evaluation of topology-optimized lattice structures manufactured via selective laser melting. *Mater Des* 2018;143:27–37. <https://doi.org/10.1016/j.matdes.2018.01.023>.
- [126] Liu YJ, Ren DC, Li SJ, Wang H, Zhang LC, Sercombe TB. Enhanced fatigue characteristics of a topology-optimized porous titanium structure produced by selective laser melting. *Addit Manuf* 2020;32. <https://doi.org/10.1016/j.addma.2020.101060>.
- [127] Ribeiro TP, Bernardo LFA, Andrade JMA. Topology optimisation in structural steel design for additive manufacturing. *Appl Sci* 2021;11:1–66. <https://doi.org/10.3390/app11052112>.

- [128] Abe F, Shiomi M, Osakada K, Liu B, Bean G, Witkin DB, et al. A Review of Additive Manufacturing. *ISRN Mech Eng* 2017;2012:1–10. <https://doi.org/10.5402/2012/208760>.
- [129] Thomas HR, Hopkinson N, Erasenthiran P. High Speed Sintering – Continuing Research into a New Rapid Manufacturing Process. *Proc 17th Solid Free Fabr Symp* 2006:682–91.
- [130] Payne A, Sparkes M, Neill PBO. Multiple Beam , Powder Bed Fusion , Additive Manufacturing n.d.:156.
- [131] Anderson K, Skelly C, Martinson KL, Waite KL, Auwerda PM, Heyboer G. Simultaneous multi-state equine business education program. *J Equine Vet Sci* 2013;33:389. <https://doi.org/10.1016/j.jevs.2013.03.154>.
- [132] Heeling T, Gerstgrasser M, Wegener K. Investigation of selective laser melting spatter characteristics for single- and multi-beam strategies using high speed imaging 2017.
- [133] Ciurana J, Hernandez L, Delgado J. Energy density analysis on single tracks formed by selective laser melting with CoCrMo powder material. *Int J Adv Manuf Technol* 2013;68:1103–10. <https://doi.org/10.1007/s00170-013-4902-4>.
- [134] Peng T, Chen C. Influence of energy density on energy demand and porosity of 316L stainless steel fabricated by selective laser melting. *Int J Precis Eng Manuf - Green Technol* 2018;5:55–62. <https://doi.org/10.1007/s40684-018-0006-9>.
- [135] Zhang S, Pal D, Stucker B, Dilip JJS, Teng C, Zeng K, et al. Influence of processing parameters on the evolution of melt pool, porosity, and microstructures in Ti-6Al-4V alloy parts fabricated by selective laser melting. *Prog Addit Manuf* 2017;2:157–67. <https://doi.org/10.1007/s40964-017-0030-2>.
- [136] Brochu M, Kim K-T, Lee C-W, Choi J-P, Shin G-H, Yang S-S, et al. Densification

- Behavior of 316L Stainless Steel Parts Fabricated by Selective Laser Melting by Variation in Laser Energy Density. *Mater Trans* 2016;57:1952–9. <https://doi.org/10.2320/matertrans.m2016284>.
- [137] Hu Z, Zhu H, Zhang H, Zeng X. Experimental investigation on selective laser melting of 17-4PH stainless steel. *Opt Laser Technol* 2017;87:17–25. <https://doi.org/10.1016/j.optlastec.2016.07.012>.
- [138] Maeda K, Childs THC. Laser sintering (SLS) of hard metal powders for abrasion resistant coatings. *J Mater Process Technol* 2004;149:609–15. <https://doi.org/10.1016/j.jmatprotec.2004.02.024>.
- [139] Abele E, Stoffregen HA, Kniepkamp M, Lang S, Hampe M. Selective laser melting for manufacturing of thin-walled porous elements. *J Mater Process Technol* 2015;215:114–22. <https://doi.org/10.1016/j.jmatprotec.2014.07.017>.
- [140] Sakata S. N-dimensional Berlekamp-Massey algorithm for multiple arrays and construction of multivariate polynomials with preassigned zeros. *Lect Notes Comput Sci (Including Subser Lect Notes Artif Intell Lect Notes Bioinformatics)* 1989;357 LNCS:356–76. https://doi.org/10.1007/3-540-51083-4_72.
- [141] Okunkova A, Volosova M, Peretyagin P, Vladimirov Y, Zhirnov I, Gusarov A V. Experimental approbation of selective laser melting of powders by the use of non-Gaussian power density distributions. *Phys Procedia* 2014;56:48–57. <https://doi.org/10.1016/j.phpro.2014.08.095>.
- [142] Casalino G, Campanelli SL, Contuzzi N, Ludovico AD. Experimental investigation and statistical optimisation of the selective laser melting process of a maraging steel. *Opt Laser Technol* 2015;65:151–8. <https://doi.org/10.1016/j.optlastec.2014.07.021>.
- [143] Yakout M, Cadamuro A, Elbestawi MA, Veldhuis SC. The selection of process

- parameters in additive manufacturing for aerospace alloys. *Int J Adv Manuf Technol* 2017;92:2081–98. <https://doi.org/10.1007/s00170-017-0280-7>.
- [144] Gu H, Gong H, Pal D, Rafi K, Starr T, Stucker B. Influences of energy density on porosity and microstructure of selective laser melted 17- 4PH stainless steel. *Solid Free Fabr* 2013;474–9. <https://doi.org/10.1007/s13398-014-0173-7.2>.
- [145] Aboulkhair NT, Everitt NM, Ashcroft I, Tuck C. Reducing porosity in AlSi10Mg parts processed by selective laser melting. *Addit Manuf* 2014;1:77–86. <https://doi.org/10.1016/j.addma.2014.08.001>.
- [146] Thomas M, Baxter GJ, Todd I. Normalised model-based processing diagrams for additive layer manufacture of engineering alloys. *Acta Mater* 2016;108:26–35. <https://doi.org/10.1016/j.actamat.2016.02.025>.
- [147] Yakout M, Elbestawi MA, Veldhuis SC. On the characterization of stainless steel 316L parts produced by selective laser melting. *Int J Adv Manuf Technol* 2018;95:1953–74. <https://doi.org/10.1007/s00170-017-1303-0>.
- [148] Ion JC, Shercliff HR, Ashby MF. Diagrams for laser materials processing. *Acta Metall Mater* 1992;40:1539–51. [https://doi.org/10.1016/0956-7151\(92\)90097-X](https://doi.org/10.1016/0956-7151(92)90097-X).
- [149] Khan M, Dickens P. Selective laser melting (SLM) of pure gold for manufacturing dental crowns. *Rapid Prototyp J* 2014;20:471–9. <https://doi.org/10.1108/RPJ-03-2013-0034>.
- [150] Abed RN. The thermal management system of laser diode: A review. *ARNP J Eng Appl Sci* 2015;10:5250–60.
- [151] Alsaddah M, Khan A, Groom K, Mumtaz K. Diode area melting of Ti6Al4V using 808 nm laser sources and variable multi-beam profiles. *Mater Des* 2022;215:110518. <https://doi.org/10.1016/j.matdes.2022.110518>.
- [152] Wang YM, Kamath C, Voisin T, Li Z. A processing diagram for high-density Ti-6Al-

- 4V by selective laser melting. *Rapid Prototyp J* 2018;24:1469–78.
<https://doi.org/10.1108/RPJ-11-2017-0228>.
- [153] Spierings AB, Schneider M, Eggenberger R. Comparison of density measurement techniques for additive manufactured metallic parts. *Rapid Prototyp J* 2011;17:380–6. <https://doi.org/10.1108/13552541111156504>.
- [154] Fischer-Cripps AC. Critical review of analysis and interpretation of nanoindentation test data. *Surf Coatings Technol* 2006;200:4153–65.
<https://doi.org/10.1016/j.surfcoat.2005.03.018>.
- [155] Sun S, Brandt M. Laser Beam Machining. In: Davim JP, editor. *Nontradit. Mach. Process.*, London: Springer London; 2013, p. 35–96. https://doi.org/10.1007/978-1-4471-5179-1_2.
- [156] Ehlers B, Herfurth H-J, Heinemann S. Hardening and welding with high-power diode lasers. In: Burnham GT, He X, Linden KJ, Wang SC, editors. *Proc.SPIE*, vol. 3945, 2000, p. 63. <https://doi.org/10.1117/12.380556>.
- [157] Jadhav, Dadbakhsh, Vleugels, Hofkens, Puyvelde, Yang, et al. Influence of Carbon Nanoparticle Addition (and Impurities) on Selective Laser Melting of Pure Copper. *Materials (Basel)* 2019;12:2469. <https://doi.org/10.3390/ma12152469>.
- [158] Jadhav SD, Vleugels J, Kruth J, Van Humbeeck J, Vanmeensel K. Mechanical and electrical properties of selective laser-melted parts produced from surface-oxidized copper powder. *Mater Des Process Commun* 2019:1–8.
<https://doi.org/10.1002/mdp2.94>.
- [159] Shi X, Ma S, Liu C, Chen C, Wu Q, Chen X, et al. Performance of high layer thickness in selective laser melting of Ti6Al4V. *Materials (Basel)* 2016;9:1–15.
<https://doi.org/10.3390/ma9120975>.
- [160] de Formanoir C, Paggi U, Colebrants T, Thijs L, Li G, Vanmeensel K, et al. Increasing

- the productivity of laser powder bed fusion: Influence of the hull-bulk strategy on part quality, microstructure and mechanical performance of Ti-6Al-4V. *Addit Manuf* 2020;33:101129. <https://doi.org/10.1016/j.addma.2020.101129>.
- [161] Pleass C, Jothi S. Influence of powder characteristics and additive manufacturing process parameters on the microstructure and mechanical behaviour of Inconel 625 fabricated by Selective Laser Melting. *Addit Manuf* 2018;24:419–31. <https://doi.org/10.1016/j.addma.2018.09.023>.
- [162] Cordova L, Bor T, de Smit M, Campos M, Tinga T. Measuring the spreadability of pre-treated and moisturized powders for laser powder bed fusion. *Addit Manuf* 2020;32:101082. <https://doi.org/10.1016/j.addma.2020.101082>.
- [163] Zhang J, Gu D, Yang Y, Zhang H, Chen H, Dai D, et al. Influence of Particle Size on Laser Absorption and Scanning Track Formation Mechanisms of Pure Tungsten Powder During Selective Laser Melting. *Engineering* 2019;5:736–45. <https://doi.org/10.1016/j.eng.2019.07.003>.
- [164] Harris DC, Johnson LF, Cambrea L, Baldwin L, Baronowski M, Zelmon DE, et al. Refractive index of infrared-transparent polycrystalline alumina. *Opt Eng* 2017;56:077103. <https://doi.org/10.1117/1.OE.56.7.077103>.
- [165] Koushki E, Mousavi SH, Jafari Mohammadi SA, Majles Ara MH, De Oliveira PW. Optical properties of aluminum oxide thin films and colloidal nanostructures. *Thin Solid Films* 2015;592:81–7. <https://doi.org/10.1016/j.tsf.2015.09.003>.
- [166] Velasco-Castro M, Hernández-Nava E, Figueroa IA, Todd I, Goodall R. The effect of oxygen pickup during selective laser melting on the microstructure and mechanical properties of Ti-6Al-4V lattices. *Heliyon* 2019;5:e02813. <https://doi.org/10.1016/j.heliyon.2019.e02813>.
- [167] Xu W, Brandt M, Sun S, Elambasseril J, Liu Q, Latham K, et al. Additive

- manufacturing of strong and ductile Ti-6Al-4V by selective laser melting via in situ martensite decomposition. *Acta Mater* 2015;85:74–84. <https://doi.org/10.1016/j.actamat.2014.11.028>.
- [168] Shi W, Liu Y, Shi X, Hou Y, Wang P, Song G. Beam Diameter Dependence of Performance in Thick-Layer and High-Power Selective Laser Melting of Ti-6Al-4V. *Materials (Basel)* 2018;11:1237. <https://doi.org/10.3390/ma11071237>.
- [169] Qiu C, Adkins NJE, Attallah MM. Materials Science & Engineering A Microstructure and tensile properties of selectively laser-melted and of HIPed laser-melted Ti – 6Al – 4V. *Mater Sci Eng A* 2013;578:230–9. <https://doi.org/10.1016/j.msea.2013.04.099>.
- [170] Matthews M, Trapp J, Guss G, Rubenchik A. Direct measurements of laser absorptivity during metal melt pool formation associated with powder bed fusion additive manufacturing processes. *J Laser Appl* 2018;30:032302. <https://doi.org/10.2351/1.5040636>.
- [171] Fousová M, Vojtěch D, Doubrava K, Daniel M, Lin C-F. Influence of Inherent Surface and Internal Defects on Mechanical Properties of Additively Manufactured Ti6Al4V Alloy: Comparison between Selective Laser Melting and Electron Beam Melting. *Materials (Basel)* 2018;11:537. <https://doi.org/10.3390/ma11040537>.
- [172] Simonelli M, Tse YY, Tuck C. The formation of $\alpha + \beta$ microstructure in as-fabricated selective laser melting of Ti-6Al-4V. *J Mater Res* 2014;29:2028–35. <https://doi.org/10.1557/jmr.2014.166>.
- [173] Al-Bermani SS, Blackmore ML, Zhang W, Todd I. The origin of microstructural diversity, texture, and mechanical properties in electron beam melted Ti-6Al-4V. *Metall Mater Trans A Phys Metall Mater Sci* 2010;41:3422–34. <https://doi.org/10.1007/s11661-010-0397-x>.

- [174] Facchini L, Magalini E, Robotti P, Molinari A. Microstructure and mechanical properties of Ti-6Al-4V produced by electron beam melting of pre-alloyed powders. *Rapid Prototyp J* 2009;15:171–8. <https://doi.org/10.1108/13552540910960262>.
- [175] Zhang W, Hou W, Deike L, Arnold CB. Using a dual-laser system to create periodic coalescence in laser powder bed fusion. *Acta Mater* 2020;201:14–22. <https://doi.org/10.1016/j.actamat.2020.09.071>.
- [176] Heeling T, Wegener K. Computational Investigation of Synchronized Multibeam Strategies for the Selective Laser Melting Process. *Phys Procedia* 2016;83:899–908. <https://doi.org/10.1016/j.phpro.2016.08.094>.
- [177] Nazami GR, Sahoo S. Influence of hatch spacing and laser spot overlapping on heat transfer during laser powder bed fusion of aluminum alloy. *J Laser Appl* 2020;32:042007. <https://doi.org/10.2351/7.0000157>.
- [178] Yadroitsev I, Smurov I. Surface morphology in selective laser melting of metal powders. *Phys Procedia* 2011;12:264–70. <https://doi.org/10.1016/j.phpro.2011.03.034>.
- [179] Tsai CY, Cheng CW, Lee AC, Tsai MC. Synchronized multi-spot scanning strategies for the laser powder bed fusion process. *Addit Manuf* 2019;27:1–7. <https://doi.org/10.1016/j.addma.2019.02.009>.
- [180] Jiang HZ, Li ZY, Feng T, Wu PY, Chen QS, Feng YL, et al. Factor analysis of selective laser melting process parameters with normalised quantities and Taguchi method. *Opt Laser Technol* 2019;119:105592. <https://doi.org/10.1016/j.optlastec.2019.105592>.
- [181] Brika SE, Letenneur M, Dion CA, Brailovski V. Influence of particle morphology and size distribution on the powder flowability and laser powder bed fusion

- manufacturability of Ti-6Al-4V alloy. *Addit Manuf* 2020;31:100929. <https://doi.org/10.1016/j.addma.2019.100929>.
- [182] Zhang J, Yang Y, Cao S, Cao Z, Kovalchuk D, Wu S, et al. Fine equiaxed β grains and superior tensile property in Ti-6Al-4V alloy deposited by coaxial electron beam wire feeding additive manufacturing. *Acta Metall Sin (English Lett)* 2020;33:1311–20. <https://doi.org/10.1007/s40195-020-01073-5>.
- [183] Yang J, Yu H, Yin J, Gao M, Wang Z, Zeng X. Formation and control of martensite in Ti-6Al-4V alloy produced by selective laser melting. *Mater Des* 2016;108:308–18. <https://doi.org/10.1016/j.matdes.2016.06.117>.
- [184] Wang X, Chou K. EBSD study of beam speed effects on Ti-6Al-4V alloy by powder bed electron beam additive manufacturing. *J Alloys Compd* 2018;748:236–44. <https://doi.org/10.1016/j.jallcom.2018.03.173>.
- [185] Qiu C, Adkins NJE, Attallah MM. Microstructure and tensile properties of selectively laser-melted and of HIPed laser-melted Ti-6Al-4V. *Mater Sci Eng A* 2013;578:230–9. <https://doi.org/10.1016/j.msea.2013.04.099>.
- [186] Cai J, Li F, Liu T, Chen B. Investigation of mechanical behavior of quenched Ti-6Al-4V alloy by microindentation. *Mater Charact* 2011;62:287–93. <https://doi.org/10.1016/j.matchar.2011.01.011>.
- [187] Dong J, Li F, Wang C. Micromechanical behavior study of α phase with different morphologies of Ti-6Al-4V alloy by microindentation. *Mater Sci Eng A* 2013;580:105–13. <https://doi.org/10.1016/j.msea.2013.05.032>.